NON-AXISYMMETRIC INSTABILITIES IN SELF-GRAVITATING STAR-DISK SYSTEMS: BIFURCATION OF RAPIDLY ROTATING PROTOSTARS

by

REBECKA M. TUMBLIN

A DISSERTATION

Presented to the Department of Physics
and the Division of Graduate Studies of the University of Oregon
in partial fulfillment of the requirements
for the degree of
Doctor of Philosophy

September, 2021

DISSERTATION APPROVAL PAGE

Student: Rebecka M. Tumblin

Title: Non-Axisymmetric Instabilities in Self-Gravitating Star-Disk Systems: Bifurcation of Rapidly Rotating Protostars

This dissertation has been accepted and approved in partial fulfillment of the requirements for the Doctor of Philosophy degree in the Department of Physics by:

Gregory Bothun	Chair
James Imamura	Advisor
Graham Kribs	Department Representative
Leif Karlstrom	Institutional Representative

and

Andy Karduna	Interim Vice Provost for Graduate Studies

Original approval signatures are on file with the University of Oregon Division of Graduate Studies.

Degree awarded September, 2021

DISSERTATION ABSTRACT

Rebecka M. Tumblin

Doctor of Philosophy

Department of Physics

September, 2021

Title: Non-Axisymmetric Instabilities in Self-Gravitating Star-Disk Systems: Bifurcation of Rapidly Rotating Protostars

The nonlinear evolution of three-dimensional protostars surrounded by circumstellar disks are numerically investigated to understand the conditions under which short-period binary star systems could form and to probe models of circumbinary Jovian planet formation. This study considers the fission hypothesis for binary star formation, namely, that binary star systems can originate from the bifurcation of one star into two due to rotational instability during the early stages of star formation. The stellar structures investigated are modeled as differentially rotating, compressible fluids and have a specific angular momentum distribution that scales with cylindrical mass. The protoplanetary disks are assumed to rotate with power law angular velocity distributions. The equilibrium star and disk structure is determined from a modified form of the Hachisu self-consistent field method. The density distributions are then perturbed away from equilibrium with low amplitude random noise and evolved forward in time using both linear and nonlinear computational methods. Nonlinear simulations are performed using the radiation-hydrodynamics code CHYMERA.

Previous studies of the fission hypothesis did not investigate the affects circumstellar material would have on stellar evolution. We find that circumstellar material tends to reduce the inward force of gravity which lowers the threshold where dynamic bar-like nonaxisymmetric instabilities develop compared to systems without circumstellar disk material. In the system tested, a bar-like instability develops in the central star. Once instability reaches saturation amplitudes, the star interacts with the disk and the system evolves into two stellar objects which rotate on independent axes and orbit a common center of mass.

Further studies of this system include radiative losses using a constant cooling function with a constant local cooling timescale. For weak cooling, the m=2 Fourier component of the density perturbation reaches maximal amplitude and a short-period, equal mass binary star system forms. For the system with a moderate cooling rate, an m=3 components grows in tandem with the m=2 components and the system develops into an unequal mass pair of central stellar objects. For the fastest cooling rates tested, the disk undergoes fragmentation and within several dynamical timescales an unequal mass binary pair orbited by two smaller over-densities is produced.

This dissertation includes previously published and unpublished co-authored material.

CURRICULUM VITAE

NAME OF AUTHOR: Rebecka M. Tumblin

GRADUATE AND UNDERGRADUATE SCHOOLS ATTENDED:
University of Oregon
Lane Community College

DEGREES AWARDED:
Doctor of Philosophy, Physics, 2021, University of Oregon
Master of Science, Physics, 2016, University of Oregon
Bachelor of Science, Physics, 2014, University of Oregon
Direct Transfer Degree - AAOT, 2012, Lane Community College

AREAS OF SPECIAL INTEREST:
Astrophysics - Circumstellar and Circumbinary Disks

PROFESSIONAL EXPERIENCE:

1. Physics Instructor, Oregon State University, 6/1/2019 -Present
2. Physics/Astronomy Instructor, Lane Community College, 1/1/2018 -Present
3. University of Oregon Graduate Research Assistant, 9/1/2016 -Present
4. National Science Foundation Graduate Research Fellow, 6/1/2014 - 6/1/2019
5. University of Oregon Graduate Teaching Fellow, 1/9/2014 -Present
6. Science Literacy Teaching Program Fellow, 2014 and 2017
7. Los Alamos National Laboratory Computational Physics Summer Internship Fellow, 2013

GRANTS, AWARDS AND HONORS:

1. National Science Foundation Graduate Research Fellowship, 2015
2. Weiser Undergraduate Research Award, 2014
3. Best Poster, Los Alamos Student Symposium, 2013

4. Computational Physics Summer Workshop Fellow, Los Alamos National Lab, 2013

5. Ford Restart Scholarship, 2010

6. REU, Steck Group, 2012

7. NASA Space Grant Scholarship, 2012

8. Scholarship for Oregon Scientists, 2011

9. Undergraduate Catalytic Outreach & Research Experience, 2010

PUBLICATIONS:

1. Hadley et al. Nonaxisymmetric Instabilities and Star-Disk Coupling I: Moderate Mass Disks. Astrophys Space Sci.(2019) 364: 119. DOI:10.1007/s10509-019-3601-5

2. Tumblin, R. et al. Parallel Compact Hash Algorithms for Computational Meshes. SIAM J. Sci. Comput.,37(1),C31C53. (2015), LA-UR-13-26533.

3. Nicholaeff, D. et al. A Survey of Hash-based Algorithms for Scalable Computational Mesh Management Across Heterogeneous Architectures. LLNL-CONF-653580-DRAFT, LA-UR-14-22667.

4. Hadley, K. et al. Nonaxisymmetric Instabilities in Self Gravitating Disks: Linear and Quasi-linear Regimes. AIP Conf. Proc. 1480, 361 (2012), DOI:10.1063/1.4754387

5. Tumblin, R. et al. Nonaxisymmetric Instabilities in Self Gravitating Disks: Angular Momentum Transport. AIP Conf. Proc. 1480, 439 (2012), DOI:10.1063/1.4754413

6. Hadley, K. et al. Nonaxisymmetric Instabilities in Self Gravitating Disks: II Linear and Quasi-linear Analyses. Astrophys. Space Sci. 353, 1 (2014) DOI:10.1007/s10509-014-1994-8

7. Smith, D. et al. The Effects of Internal Stellar Modes on the Evolution of Protoplanetary Star-Disk Systems. American Astronomical Society, AAS Meeting 223, 350.08. 2014.

TABLE OF CONTENTS

Chapter Page

LIST OF FIGURES

Figure Page

Figure Page

LIST OF TABLES

Table Page

CHAPTER I

INTRODUCTION

A fundamental question in astrophysics concerns the origin of the Solar system. How did the star called Sol form, and how did its system of planets come to be? What events have allowed for our species to call this pale blue dot home? In the last few centuries, the scientific revolution has enabled humanity to seek empirical answers to these ancient and fundamental questions. Until very recently, scientists had only a single star system - the Solar system - upon which to base ideas concerning star and planet formation. Furthermore, the formation of the Solar system occurred some 4.6 billion years ago, leaving only a current snapshot in time for scientists to constrain theories about the evolutionary history of our planetary system.

As scientists peer into the twenty-first century using modern precision optics, new instruments such as the Gemini Observatory, Subaru Telescope and the Atacama Large Millimeter/Submillimeter Array (ALMA), are providing observational data which can help illuminate the processes which lead to planetary systems. Furthermore, in the last 25 years, close to 4000 extra-solar planets have been discovered [201]. Given this wealth of new data, we are forced to expand our previous ideas concerning the origin of the Solar system to include the diverse range of systems now observed.

It is now understood that at least half of all sun-like stars occur in multiple systems [47], [218], [169], that binary protostellar objects form early in the star formation process [170] and nearly all massive stars form stellar companions [174]. In addition, over the last decade 156 planets in binary or multiple star systems have been detected [201]. Yet only in the last several years has technology advanced far enough

to permit observing binary star systems in the process of formation. This process is currently being observed around AK Scorpii - a young system in the constellation Scorpius - with unprecedented resolution using the ALMA observatory [5]. Despite the ubiquity of binary and higher order systems, the formation processes leading to multiple star systems - especially those containing planets - remains an outstanding problem in astrophysics.

In the 18th century, Emmanuel Swedenborg [186], Immanuel Kant [111] and Pierre-Simon Laplace [25] independently outlined a general theory to explain the formation of the Solar system. Swedenborg proposed that the Sun developed a dense surface layer that was forced outward by the centrifugal force of its rotation into the equatorial plane of solar rotation, forming a ring like structure. Continuing its outward motion, this ring eventually thinned and broke apart to form all the planets and smaller bodies of the solar system [186],[25]. Laplace argued that our solar system originated from a rotating cloud of fluid-like or gaseous atmosphere and attempted to write down a mathematical framework for this fluid motion [25]. Kant used a Newtonian framework to develop a theory which would go so far as to describe the densities of the planets based on the distance from the central object [111],[25]:

> "Uniform direction of all these movements towards the same area. All particles endeavor to bring themselves to a communal area and accumulate there. Moderate the speed of their movement to an equilibrium with the severity of the distance of their location. Free circulation of all particles around the central body in circles. Formation of the planets from these moving elements. Free movement of the planets composed of it in the same direction in a common plane near the center, almost in circles, and further from it with increasing degrees of eccentricity."

Today, this theory, generally known as *Nebular Hypothesis*, states that stars and planets form from the collapse of dense cores within molecular clouds of gas and dust. Under certain conditions, these molecular clouds become gravitationally unstable, and matter coalesces within to form smaller denser cores. Nothing is truly stationary in space, and so these cores rotate with some nonzero angular momentum. If they are able to cool sufficiently, they will lose pressure support and the cores will further collapse under their own gravity. Due to conservation of angular momentum, the cores will spin faster as they collapse. Conservation of energy causes the gas to heat up under contraction providing the fluid pressure support against further collapse. Collapse in the equatorial plane is disrupted by centrifugal forces. Close to the rotation axis, the collapsing matter forms a protostellar object. Material further from the rotation axis, and in the equatorial plane of the system, develops into a protostellar disk of gas and dust surrounding the protostar.

Planets which form from this disk of gas and dust would tend to orbit in nearly circular, co-planar orbits, and they would orbit in the same sense as the Sun rotates. In this way, nebular hypothesis is able to reproduce the basic observations of planetary orbits and rotation in our solar system. However, if significant redistribution of angular momentum does not occur early in the formation process, the central protostellar object would not be able to accrete enough mass to ignite fusion. Therefore, central to this theory, is a mechanism to redistribute mass and momentum within the young system.

Present Work

Protoplanetary disks are differentially rotating disks of gas and dust subject to gravity, viscous stresses, heating from the central protostar and cooling through

radiation. The mean free path of individual atoms are small compared to the characteristic length scale of the disk, and therefore the physics can be cast in the continuum limit and treated in a fluid dynamics framework. Astrophysical fluid dynamics applies the principles of fluid dynamics to the movement of fluids in space. It is a versatile framework capable of describing a wide range of astrophysical phenomenon ranging from convection cells on the surface of the sun to vortices in Jupiter's atmospheric bands. In addition, computational fluid dynamics offers a way of testing mathematical models which apply the physics and fluid principles of nebular hypothesis to planetary system formation using modern numerical techniques. In this way, we are able to computationally evolve and test theories of planetary system formation, a phenomenon which cannot be observed on human timescales.

Since the discovery of extrasolar planets - a significant fraction of whom orbit multiple stars - thousands of new planetary systems with widely ranging properties must also be explained by *Nebular Hypothesis*. For most of history, science has marched forward on two feet: theory and observation. The technological revolution of the twentieth century has now created a new avenue of scientific endeavor; the ability to computationally solve, simulate and test ideas. Over the past 20 years, leaps and bounds in computing power have facilitated testing theories of star formation and evolution with increasing accuracy. Meanwhile, a flood of observational data not only enables, but demands astrophysicists to constrain theories concerning the origin of the solar system based on the huge array of extra-solar systems we can observe. This present work seeks to understand the formation and evolution of binary star systems and circumbinary protoplanetary disks using modern computational methods.

It has been suggested that binary and multiple star systems form via i) the bifurcation of a rapidly rotating star known as the *fission hypothesis* [24], [107], (See

[187] for discussion). This theory of the origin of double stars was originally proposed by Lord Kelvin (William Thomson, 18241907) and Peter Guthrie Tait (18311901) ii) the gravitational capture of an initially unbound companion [146] (First proposed by George Johnstone Stoney in 1867), iii) large-scale fragmentation of the inital molecular core [76] and iv) fragmentation and clumping of massive protoplanetary disks driven by disk instabilities [144], [189], [138].

The last two theories offer good explanations for wide separation binary and multiple systems and are widely accepted by the astrophysics community. Wide separation binaries can easily form from turbulent fragmentation of the initial nebular cloud [128] or from separate gravitational collapse events driven by disk instabilities [153]. Short separation binaries pose more of a conundrum. One model which is prone to producing close binary systems with regularity is the *fission model*. In the classical fission scenario, as the protostar contracts under self-gravity, the core develops through a series of equilibrium ellipsoidal objects. As core contraction continues, conservation of angular momentum leads to an excess of rotational energy in the young stellar object. The ratio $\beta = T/|W|$ decreases as the contracting star spins faster and at some critical value, the star becomes unstable to nonaxisymmetric perturbations. If the rotational velocity of the stellar core reaches a critical threshold, prompt bifurcation may occur and a short-period close binary pair could form [80], [79], [60], [191], [102]. Since only a small amount of angular momentum can be stored in a star, this mechanism would favor the production of close binaries.

The fission hypothesis is not widely accepted by the astrophysics community [191]. Based on previous nonlinear studies of solitary differentially rotating polytropic stars, it is generally believed that the fission process cannot form binary pairs because the cores may contract on too short of timescales compared to the viscous timescale

of due to gravitational torques from the central object [48], [51], [50], [53]. Instead, nonaxisymmetric instabilities force the star to develop into what is known as a bar mode. The central barlike object that forms does not fission due to the development of spiral arms [101]. Torques from the spiral arms transfer angular momentum outward leading to spin down of the central object. However, these studies only considered isolated polytropic stars. Nebular hypothesis suggests that star formation naturally leads to the formation of a protoplanetary disk of gas and dust surrounding the protostar. Previous studies of the fission process did not include the effects a protostellar disk can have on the evolution of the stellar core, and therefore, dismissed significant physics which naturally take place in the stellar and planetary evolution process. Circumstellar disks produce an outward radial acceleration on material inside the inner edge of the protoplanetary disk. This tends to weaken the average inward pull due to the stellar gravitational field and increase tidal forces at points inside the star. If the mass of the star and disk are comparable, the disk can enhance the fission process.

One possible way to constrain these theories would be to survey the spin-orbit alignment of known binary star systems. One would expect that if close binary pairs formed in the fission hypothesis from one initial stellar object that close binaries systems would have well-aligned orbital and spin angular momenta. However, good alignment is not in any way guaranteed. Disks around young stars might become warped during the last stage of accretion and could torque the orbit while maintaining the orientation of the spins [199], [159]. More generally, star formation may be a chaotic process, with accretion from different directions at different times [18]. There are also many processes that could alter the stellar and orbital spin orientation well after binary formation. A third body orbiting a close binary pair on an inclined orbit

has been known to introduce large oscillations in orbital inclination and eccentricity [150]. Tidal dissipation can cause the system to free itself of Kozai oscillations [120] and become stuck in a high-obliquity state [63]. If dissipation is sufficiently strong then the system will evolve into the double-synchronous state, characterized by spin-orbit alignment [99]. Therefore, whether a close binary or a star-planet system is well-aligned or misaligned depends on its particular history of formation and evolution. One such study made measurements of the relative orientations of the rotational and orbital axes in close binary star systems, most of which harbor early-type stars and found evidence for aligned systems as well as spin-orbit misalignment [4]. (See also [215] for intersting discussion of the Kozai mechanism with respect to hot Jupiters in binary star systems).

This present work serves as proof of concept that a rapidly differentially rotating and compressible protostellar objects surrounded by a massive circumstellar disk under certain initial conditions develop nonaxisymmetric barmode instabilities. When the evolution of the system is followed into the nonlinear regime, the circumstellar material interacts with the star causing the central object to bifurcate and produce a proto-binary star system. Furthermore, if radiative losses are considered, the loss of pressure support causes the disk to fragment, and while some of the fragments fall onto the stellar component, several survive and go into orbit forming a proto-binary system surrounded by proto-planetary objects. This work serves to show that the fission process is a viable method of forming not only multiple star systems, but planets around multiple star systems. This work is by no means a complete picture, but it demands that further studies endeavor to investigate this mechanism as an avenue for forming short-period binary star systems capable of harboring planets.

Organization of Dissertation

The overall framework of my dissertation is organized in the following way. In Chapter 1, I made a compelling case as to why the study of binary star systems and circum-binary disks are of fundamental importance to the astrophysics community. I state the purpose of this study, the research questions I have investigated, and the theoretical and conceptual framework upon which the dissertation is based. I describe the significance of my work and justify it with respect to established theory. In addition, I explain how the work I have performed advances the established theory and comprises a novel research project.

A review of the related research, theory, and professional literature is described in Chapter 2. This chapter serves as the foundation on which my research question rests and as a basis for discussing results and how these results relate to past and current research being performed in my field. It summarizes what is known and identifies what is unknown about star and planet formation, circumbinary disks and binary star formation models. I include major findings from other research groups and address relevant methodological issues in computational fluid dynamics. I review the implications of the previous studies and compare and contrast these with my current investigation.

The methods I have used for investigating astrophysical disks is described in Chapter 3. Each step I have undertaken in the execution of my research is described in detail. Since my research has been performed using the computational fluid dynamics code, CHYMERA, I describe the structure of the code and how each physics module was developed in relation to current theories in star formation and evolution. I include enough detail such that future readers of my work can come away with a clear understanding of how my research was conducted, and what procedures to

follow should they want to replicate my work. I also provide a detailed description of my data analysis toolkit and how I developed these analysis tools. In addition, my assumptions and the limitations of my assumptions are addressed.

Chapter 4 is devoted to reporting the results of my research and how these results pertain to my initial research questions. Chapter 5 provides discussion and comparison to other research projects. Chapter 7 presents conclusions and implications drawn from the results reported in Chapter 4. It describes how my findings answer my questions proposed in Chapter 1 and how they fit into the greater body of work described in Chapter 2. Chapter 6 contains preliminary results and defines goals for future research. I end with a cogent conclusion which summarizes the importance of my work in chapter 7.

CHAPTER II

LITERATURE REVIEW

To motivate my research, I provide a review of related observational and theoretical research and discuss the body of professional literature. This chapter serves as the foundation on which my research question rests and as a basis for discussing results and how they relate to past and current research being performed in my field.

Observational Evidence of Nebular Hypothesis

Recent technological advances have allowed scientists to observe the internal structure of protoplanetary disks [217], [163], [105], [38] and catalogue an extraordinarily diverse set of planetary systems beyond our own [61], [72], [17]. To help answer questions about the birth of planetary systems, the Atacama Large Millimeter/submillimeter Array (ALMA) has conducted one of the deepest surveys ever of protoplanetary disks, the Disk Substructures at High Angular Resolution Project (DSHARP). This undertaking by ALMA and affiliates has yielded the most stunning, never-before-seen, high-resolution images of 20 nearby protoplanetary disks (See Figure 1).

DSHARP is a deep, high resolution (35 mas, or 5 au) survey of the 240 GHz (1.25 mm) continuum emission and 12CO J=2-1 line emission from 20 nearby, bright, and large protoplanetary disks [7]. DSHARP was designed to assess the prevalence, forms, locations, sizes, and amplitudes of small-scale substructures in the mass distributions of the disk material and how they might be related to the planet formation process. For line emission, J refers to the rotational quantum number. Protoplanetary disks

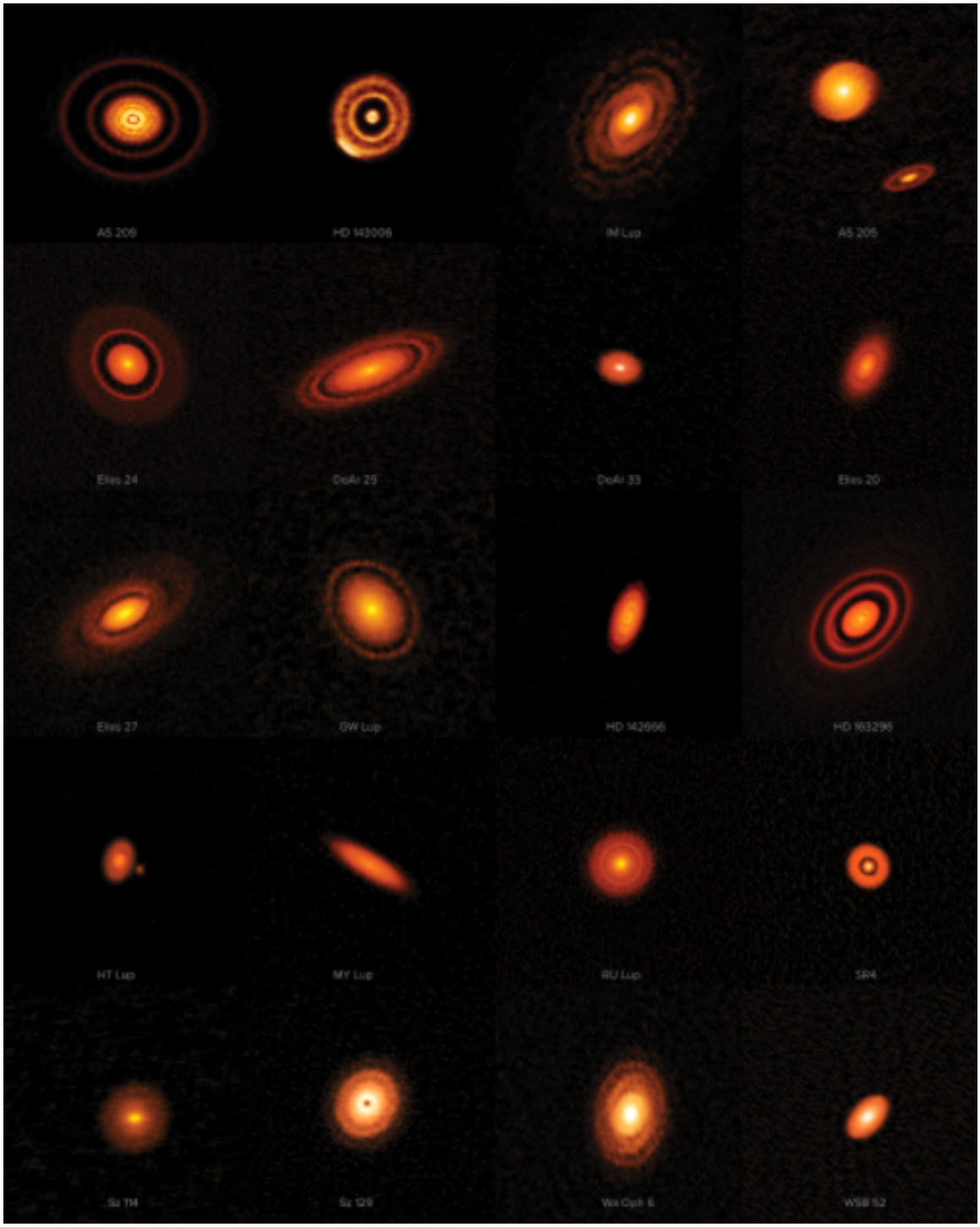

FIGURE 1. Official Data Release for the ALMA Cycle 4 Large Program Disk Substructures at High Angular Resolution Project (DSHARP). Credit: ALMA (ESO/NAOJ/NRAO), S. Andrews et al.; NRAO/AUI/NSF, S. Dagnello

are very difficult to observe, especially in the early stages of evolution, because they are relatively cool collections of molecular hydrogen (H_2) with small percentages of other gasses such as carbon monoxide (CO). One way to image these systems is to look at molecular line spectra.

Polar molecules have nonzero permanent electric dipole moments. Symmetric molecules, such as H_2, have no permanent electric dipole moment. However, asymmetric molecules, such as CO, have asymmetric charge distributions which give them a nonzero electric dipole moment. The electric dipole moments of polar molecules rotating with constant angular velocity ω radiate at their rotational frequency. The intensity of this radiation can be derived from the Larmor formula where permitted rotation rates, and the resulting molecular line frequencies, are determined by the quantization of angular momentum. The quantization of angular momentum to integer multiples of $\hbar$ implies that the rotational energy is also quantized such that

$$E_{rot} = \frac{J(J+1)\hbar^2}{2I}, J = 0, 1, 2... \tag{2.1}$$

Where I is the moment of inertial for the diatomic molecule. Changes in rotational energy are quantized such that the only permitted energy transitions are governed by the quantum-mechanical selection rule

$$\Delta J = \pm 1 \tag{2.2}$$

We can find that going from the J to $J-1$ state releases energy

$$\Delta E_{rot} = [J(J+1) - (J-1)J]\frac{\hbar^2}{2I} = \frac{\hbar^2 J}{I} \tag{2.3}$$

Therefore, the frequency of a photon emitted during this rotational transition is given by,

$$\nu = \frac{\Delta E_{rot}}{h} = \frac{\hbar^2 J}{2\pi I} \tag{2.4}$$

The radio spectrum of a particular polar molecular species in an interstellar cloud or protoplanetary disk will be a ladder whose steps are harmonics of the fundamental frequency. We can see that the frequency will be determined solely by the moment of inertia I of that particular species. The relative intensities of lines in the ladder depend on the temperature of the cloud. Molecules are excited into states where $E_{rot} > 0$ by ambient radiation and collisions in the gas. The minimum gas temperature required for collisional excitation of polar molecules is related to the total rotational energy,

$$T_{min} = \frac{\Delta E_{rot}}{k} \tag{2.5}$$

If the upper-level rotational energy is much higher than kT, few molecules will be collisionally excited to that level and the line emission from molecules in that level will be very weak. The minimum rotational energy of the small and light H_2 molecule is equivalent to a temperature of approximately, $T = 500K$. This is much higher than

the temperatures of most interstellar H_2. Only relatively massive molecules are likely to be detectable in very cold molecular clouds. The lowest frequency of radio line emission depends on the mass and size of the molecule. Large, heavy molecules in cold clouds may be seen at centimeter wavelengths, while smaller and lighter molecules emit only at millimeter wavelengths. ALMA is capable of capturing emission from these small, light molecules in the millimeter/submillimeter wavelengths.

Systematic analysis of annular substructures in 18 single disk DSHARP systems show a remarkably diverse range of structure morphologies. Annular substructures are observed in all 18 of the disks studied, and in a minority of cases, they are observed with other disk substructures such as spiral arms (3/18) and crescent-like azimuthal asymmetries (2/18). The annular substructures observed are hypothesized to be linked to planet-disk interactions [97]. Huang et al. report that annular substructures are observed in disks hosted by stars across a range of luminosities, masses, and accretion rates [97]. They find no immediate relationships between the substructure sizes and locations and the stellar properties. However, they report that underlying relationships may be obscured by selection bias toward bright disks.

In a separate paper, Huang et al. examine the disks around Elias 27, IM Lup, and WaOph 6 [98]. All three disks feature $m = 2$ spiral patterns in addition to observed annular substructures. Gas kinematics are determined by the $12CO\ J = 2 - 1$ line emission and indicate that the continuum spiral arms are trailing the overall motion of the disk material. The Elias 27 spiral pattern extends throughout most of the disk radius, and intersect an annular gap at $R \approx 69$ AU. The spiral pattern in the IM Lup disk extends radially about halfway through the disk. This spiral structure is more complex and contains variation in the pitch angle with disk radius. It also contains interarm features that may be part of ring substructures or spiral arm branches. The

WaOph 6 disk, contains compact spiral arms that extend through most of the radial disk dimension. The disks around Elias 27, IM Lup, and WaOph 6 do not contain high-contrast crescent-like asymmetries or large ($R > 20AU$) emission cavities, which may suggest that multiple spiral formation mechanisms operate in protoplanetary disks [98].

Classification of Young Stellar Objects

The term Young Stellar Object (YSO) typically denotes a star in the early stages of its evolution. Young stars and their protostellar precursors are referred to as young stellar objects [185] since they are often deeply embedded in circumstellar gas and dust and invisible at optical wavelengths. This class of object consists of two main groups those called protostars and those called pre-main-sequence stars. A protostar is in its earliest phase of stellar evolution and is considered to still be gathering mass from it's parent molecular cloud. This stage in stellar evolution typically lasts < 0.5 Myr for low-mass stars $< 1.0 M_{sun}$. YSO's cannot be placed on a Hertzsprung-Russell diagram.

YSOs can be organized along an empirical evolutionary sequence based on the shape of their spectral energy distributions (SED) from near-infrared to submillimeter wavelengths [8]. The peak of the SED shifts from the submillimeter to the optical domain as the star ages. These classifications were formalized into several classes by Adams, Lada & Shu in 1987 [2]. Class 0 objects are protostars who's molecular core is still in the process of collapsing. There is no fusion occurring in the central object and energy being released at this phase is purely gravitational energy. The disk is still puffy and the cores are still slowly rotating. These objects typically emit in the millimeter wavelength continuum. As the core further collapses, it becomes

hot enough to start emitting in the far-infrared spectrum. Class I YSO's start to rotate faster due to conservation of angular momentum, and the disk begins to flatten with dust settling to the mid-plane. The inner part of the cloud core will start fusing hydrogen once enough mass has accreted onto the central object to creates the necessary pressures. The spectrum, however, does not look like that of a star because it is still embedded in a cloud of gas and dusk. Class II YSO's have dissipated their envelope due to strong stellar winds brought on by fusion in the central object. Since the protostellar disk is still dense, the object will still radiate in the IR. Class III objects consist of a young star surrounded by a transparent disk. The disk matter is being depleted by various mechanisms including photo-evaporation and accretion onto the central star. Planet formation under the core accretion scenario is thought to occur during transitions from class II to class III and sometimes the disks during this phase are referred to as transitional disks. In Figure 2 we show the spectral energy distributions for class I, II and III YSO's. It is clear that as the object class progresses from I to III the extent of the IR excess beyond 10 m becomes less extreme. Class III young stellar objects are well approximated by a black-body spectrum. Points and blue lines are data taken from Kenyon and Hartmann (1995) [113], while orange lines are Spitzer spectra from Furlan et al (2006) [69]. Optically thick but physically thin dusty circumstellar disks around T Tauri stars reprocess stellar flux and give rise to excess thermal radiation at wavelengths greater than ≈ 1 μm. Recent observations by Eisner & Carpenter (2006) seem to indicate that a Class I object evolves to a Class II object in about 1 Myr [59].

Following Greene et al. (1994), class I objects have a negative infrared spectral indices α_{IR}, where

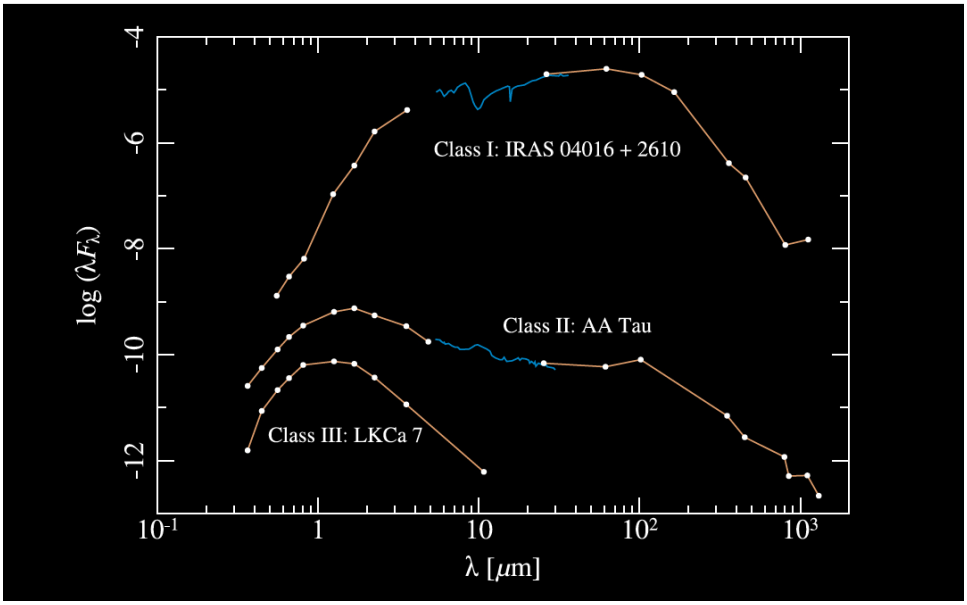

FIGURE 2. Spectral energy distributions for class I, II, and II, Young Stellar Objects. Image adapted from Hartmann (2009).

$$\alpha_{IR} = \frac{dlog(\lambda F_\lambda)}{dlog\lambda} \tag{2.6}$$

where λ is the wavelength and F_λ is the flux at that wavelength, as measured between 2.2 and 10 μm. Class II objects have a flat or rising spectrum with $0 < \alpha_{IR} < 1.6$, and Class III have $\alpha > 1.6$. Classical T Tauri stars span Classes I and II, and Weak T Tauri Stars are Class III objects [77].

A Catalogue of Exo-Planets

In the last 25 years, astronomers have cataloged nearly 4,000 exoplanets in orbit around distant stars [201], [62]. With this wealth of new Solar system data many questions remain about the extraordinarily diverse systems that can form. In Figure 3, we make a scatter plot of all the known exoplanets with the planet's separation distance (semi-major axis) from it's parent star in AU along the horizontal axis

and the planet mass is Jupiter Masses (M_{Jup}) along the vertical axis using data the Exoplanet Orbit Database [62]. The formation processes and initial conditions that lead to the wide array of planets discovered, including so-called hot Jupiters (See Figure 6) living dangerously close to their parent stars, massive rocky worlds with masses that dwarf our rocky Earth, icy dwarf planets, and hopefully soon to be discovered distant analogs of Earth, remains a mystery. For the reader's reference we have also plotted the location of some of the major planets in the Sol system. From the distribution we can visually delineate three distinct groups of planets. Group 1 is composed mainly of a dense grouping of rocky Super Earth's, many times more massive than Earth that orbit close to their parent star ($< 1AU$). Group 2 contains planets with comparable mass to Jupiter, dubbed "Hot Jupiters" due to their high surface-atmosphere temperatures. They orbit at a distance of less than $0.1AU$ and have short orbital periods (generally, $P < 10$ days). Hot Jupiters are the easiest planets to observe using radial-velocity methods because their high mass induces large oscillations in the motion of their parent stars, and they have short orbital periods allowing astronomers to track these motions quickly. The first extra-solar planet, 51 Pegasi b, discovered in 1995 has an orbital period of just 4 days, a mass of about 0.46 M_{jup} and a surface temperature of $1284 \pm 19K$ [139]. Group 3 contains exoplanets which have masses on the order of 1-10 M_{Jup}, and orbit between $0.5 - 5.0$ AU. We can see that none of the planets in the Sol system, with the exception of Jupiter, have masses and separation distances that reside within these three groupings. Given the current data, it seems that although planetary systems are abundant, our Solar system is not the norm for Sun-like stars. We would also like to understand where planets in multiple star systems fall in comparison with these three groups. In Figure 7 we highlight planets in multiple star systems in blue.

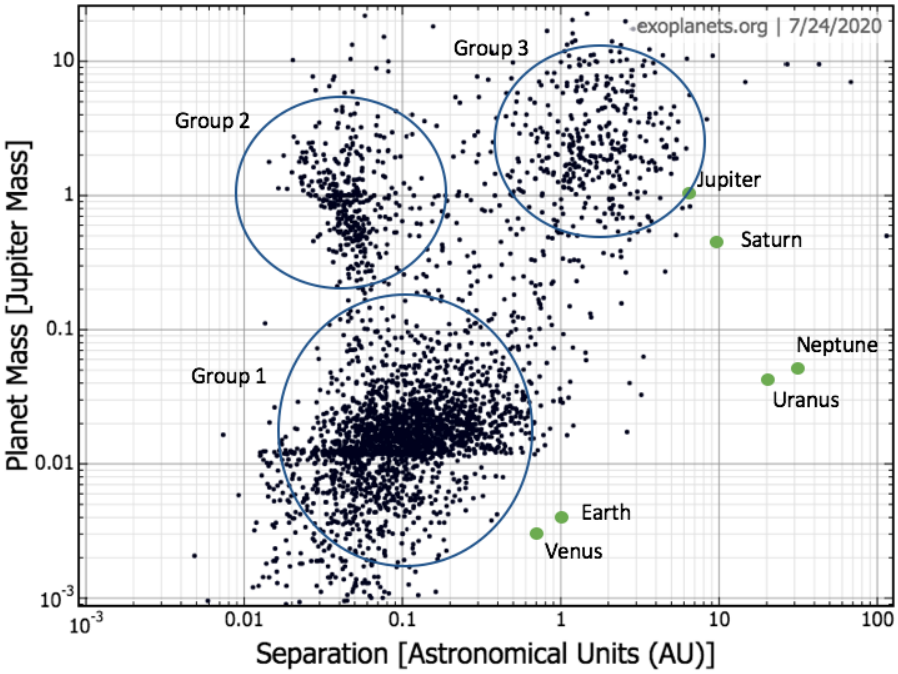

FIGURE 3. Separation distance from parent star versus planet mass for the nearly 4000 exoplanets discovered to date.

In Figure 4 we plot a histogram of exoplanet masses in M_{Jup}. There are two distinct distributions in mass corresponding to the Jovian and rocky planet populations. Further analyses of the distribution of Jovian planets, suggests that there are two distinct populations which may have different formation mechanisms dependent of the metallicity content of the parent molecular cloud [176].

A Catalogue of Exo-Planets in Multiple Star Systems

It is now known that more than 45% of solar type stars occur in binary or multiple star systems [169], [195], [42] [35], [129]. Raghavan (2010) presents the results of a comprehensive assessment of companions to a sample of 454 solar-type stars (with spectral classification F6-K3) within 25 pc using many different observational techniques. They report that the overall observed fractions of single,

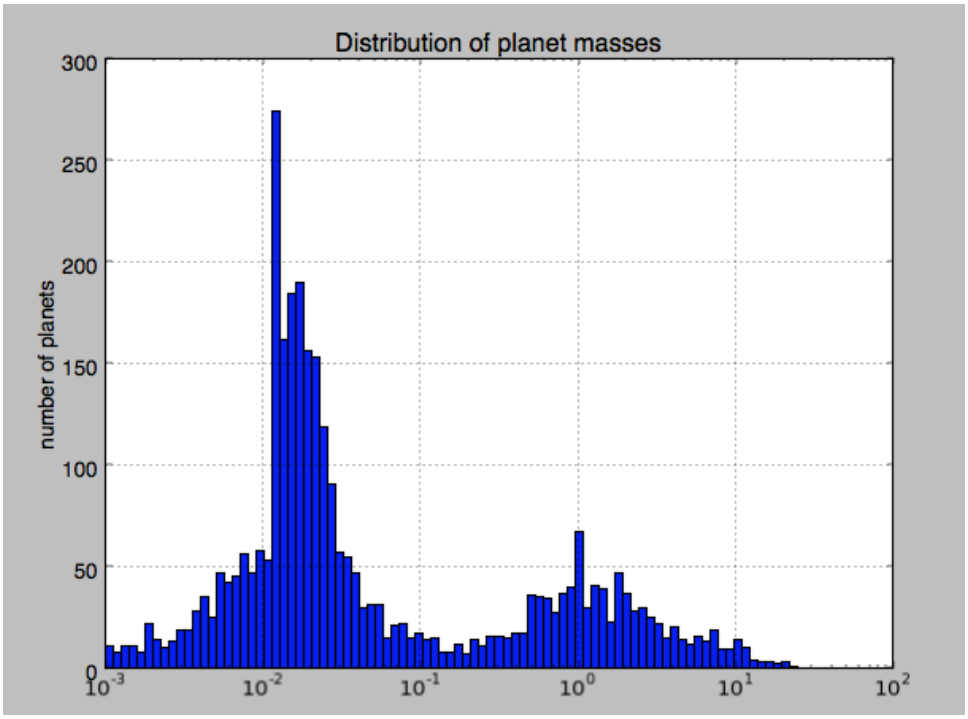

FIGURE 4. Histogram of exoplanet masses.

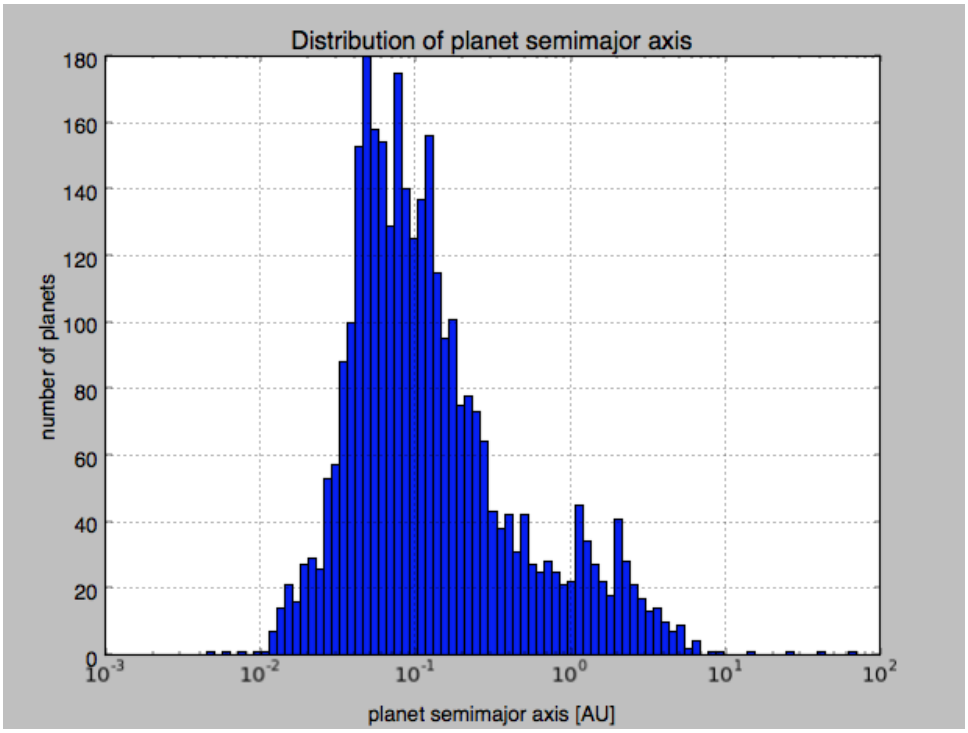

FIGURE 5. Histogram of exoplanet separation distance from parent star.

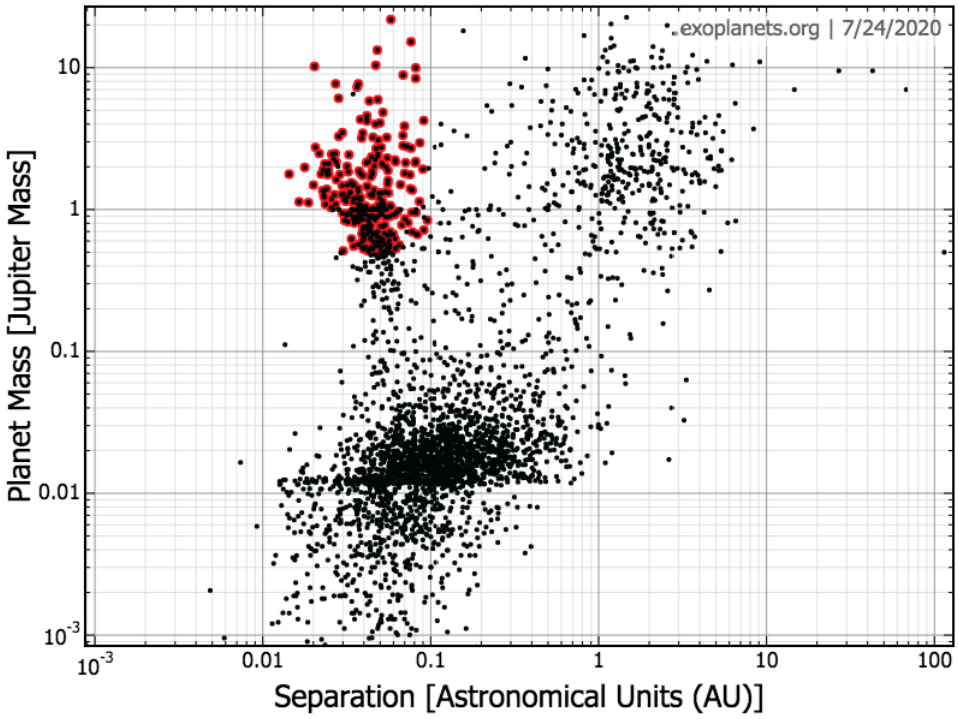

FIGURE 6. Separation distance from parent star versus planet mass for the nearly 4000 exoplanets discovered to date. Hot Jupiters are highlighted in red.

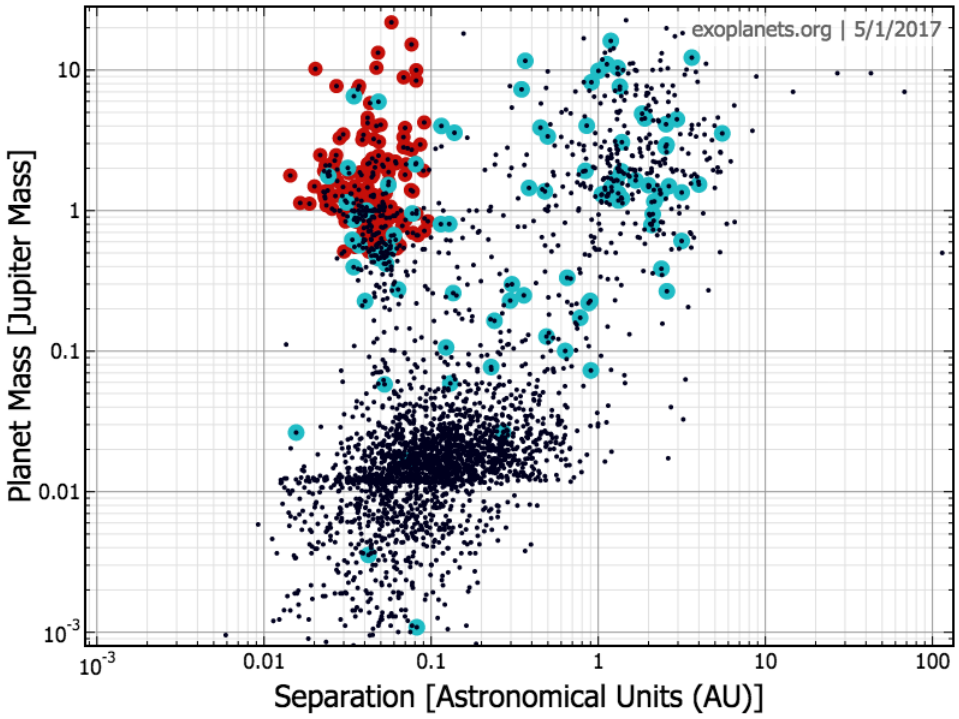

FIGURE 7. Separation distance from parent star versus planet mass for the nearly 4000 exoplanets discovered to date. Hot Jupiters are highlighted in red. Planets in binary star systems highlighted in blue.

double, triple, and higher-order systems are 56% ± 2%, 33% ± 2%, 8% ± 1%, and 3% ± 1%, respectively. De Rosa et al. (2014) [42] were involved in a large scale study of 435 A-type stars and they find the same fractions of single, binary and multiples as Raghavan (2010) to within the errors. For more massive stars, Chini et al. [35] analysed the statistics of multiplicity for 250 O-type and 540 B-type stars and found that 82% of stars with masses above 16 $M_{\odot}$ form close binaries, but this value drops monotonically to 20% at masses around 3 $M_{\odot}$. These studies suggest that binarity is strongly correlated with mass. Determining multiplicity statistics for young stellar objects poses a more observationally difficult problem. Massive Herbig Ae/Be stars were found to have a binary frequency between 31% and 42% [129]. Later, Baines (2006) found Herbig Ae/Be stars to have a much higher binary frequency of 68% ± 11% [11]. A possible reason for this discrepancy is observational bias in different observing methods. Reipurth (2014) describe observations of stellar multiplicity for class 0-III stars. They demonstrate that binary and multiple star systems are the norm at all stellar evolutionary phases. They provide a detailed overview of the stellar multiplicity statistics and describe a boundary condition for models of binary evolution [170]. Duchene & Kraus (2013), review and summarize the current empirical data of stellar multiplicity. They argue that the frequency of stellar multiplicity varies smoothly with primary mass and that multiplicity properties are set for stars at the pre-main sequence phase [47].

In addition, there are now hundres of binary and multiple star systems harboring planets [177]. These results suggests that the formation of massive multiple bodies in Solar system-sized disks must take place on a fairly regular basis.

As of Feb. 13th 2021, the Open Exoplanet Catalogue [201], an open source database of all discovered exoplanets contains data for 4390 planets in 3313 planetary

systems. Out of these, 164 planets are found orbiting in systems with multiple stars. These planets are found using several different methods and it is important to understand the types of observational biases associated with the various methods. To find exoplanets astronomers employ different methods such as looking for transits, radial velocity, microlensing, direct imaging, and pulsar timing.

There are two main types of orbits that planets in binary star systems take, the P-type and the S-type. In the P-type orbit, the planet orbits around both stars, and is a circumbinary planet. In an S-type orbit, the planet orbits only one star (See Figure 8). Using data from the Open Exoplanet Catalogue, I plot the distribution of confirmed planets in binary or multiple star systems based on the planet's mass - in Jupiter masses- and distance from the center of mass of the stellar system in terms of Astronomical Units for planets with the p-type orbit (See Figure 9) and for planets with the s-type orbit (See Figure 10). There are twenty-one planets with the P-type orbit and one-hundred and forty three in the S-type orbit.

Planets with the P-type orbit tend to be found in close binary star systems while planets with the S-type orbit tend to form in wideseparation binary or multiple star systems. There are currently (As of Feb. 2021) twenty-one known circumbinary planets with the P-type orbit. Seven are found from the transit method. Two are found from direct imaging. Most P-type orbits are found from pulsar timing, with a total of twelve planets found by this method (See Figure 9). By comparison, there are no planets in the S-type orbit found from pulsar timing. Most are found by radial velocity method. Those that fall into the hot Jupiter group are mostly found by transit. Those that fall into the Jupiter and super Earth category are all found by radial velocity (See Figure 10).

Most of the known exoplanets have been discovered using the transit method. The transit method was employed by the Kepler Space Telescope and is currently used by Transiting Exoplanet Survey Satellite (TESS). A transit occurs when a planet passes between a star and its observer. As the planet passes in between the star and the observer, it blocks out a small portion of the light from the star. Astronomers can observe the change in brightness. From the periodical nature of this dimming, one can determine the planets orbital period and by looking at the absorption spectra, information about a planets atmosphere can be inferred. In addition, the planets size can be determined. One of its major drawbacks is that to employ this method a distant planet must pass directly between it's partent star and Earth. This requires very specific orbital alignments.

The radial velocity method - also known as Doppler Spectroscopy - consists of observing a star for signs of "wobble" where the star is moving toward or away from the observer. This is deduced by using a spectometer to measure the way in which the stars spectral lines are displaced due to the Doppler Effect and how light from the star is redshifted or blueshifted end of the spectrum. One of the main advantages is that it allows for the eccentricity of the planets orbit to be measured directly. The radial velocity signal is distance-independent, but requires a high signal-to-noise-ratio spectra to achieve a high degree of precision. As such, it is generally used to look for low-mass planets around stars that are within 160 light-years from Earth.

A pulsar is a neutron star, the dense, rapidly rotating remnant of a supernovae. Pulsars are also rotate with very precise regularity. As they rotate they emit radio waves and slight anomalies in the timing of it's radio pulses are used to track motion of their orbit and reveal gravitational perturbations to that orbit. Like regular stars, these perturbations are evidence of a planetary companion. In addition,

information about the orbital parameters of the perturbing planet can be inferred. In addition, pulsar timing methods can be used to find planets that are very far away. Unfortunately, pulsars are relatively rare and the special circumstances that would lead to planets around pulsars are not well understood.

Direct Imaging is a method by which a planet is directly imaged by looking at the light reflected from the atmosphere in infrared wavelengths. This method works best for young planets that emit infrared light and are located at large separation distances from their parent star. Since the stars are usually missions ot bissions of times brighter than the light reflected from a planets atmosphere, the planet must be far from its parent star so that the light is now drowned out by radiation coming from the star.

Another method used to find extra solar planets relies on gravitational microlensing. this method relies on the gravitational force of a planet to bend and focus light coming from a star. The path of the light from tha distant star will be altered by the presence of a massive planet. Microlensing can be used to find planeta at very large distances from Earth - hundreds to thousands of light years away. For comparison, The radial velocity method can only be used to find planets at distances of 100 light years away. In addition, the microlensing method can find low mass planets in wide orbits. Microlensing is one of the most effective method for finding Earth-like planets around Sun-like stars. Unfortunately, microlensing is also unable to yield accurate estimates of a planets orbital properties, since the only orbital characteristic that can be directly determined with this method is the planets current semi-major axis.

Kurtovic et al. (2018) characterize the substructures induced in protoplanetary disks by the interaction between stars in multiple systems for the triple systems HT-

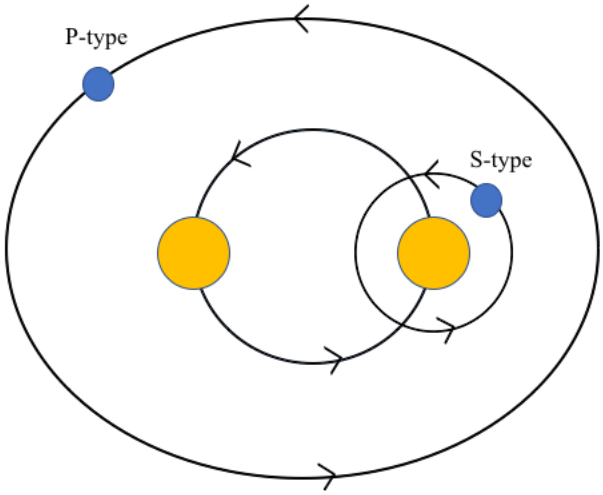

FIGURE 8. Illustration of P and S-type orbits for planets in binary star systems.

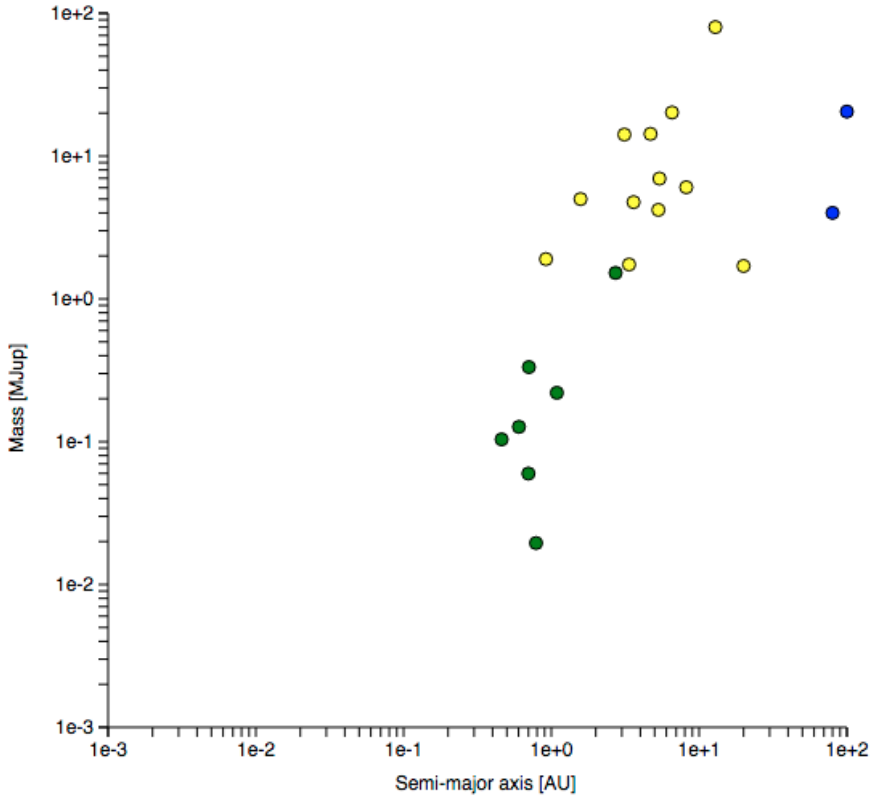

FIGURE 9. Distribution of circumbinary planets with P-type orbits. Planets found from the transit method are plotted in green, planets found from pulsar timing are plotted in yellow and planets found from direct imaging are plotted in blue.

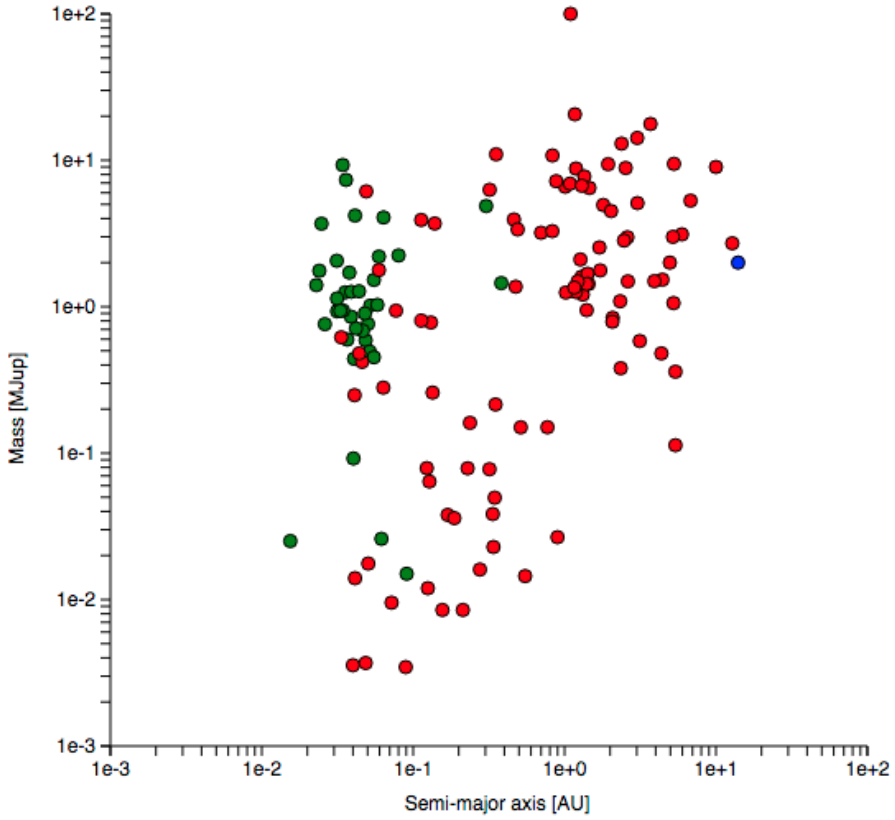

FIGURE 10. Distribution of planets in multiple star systems with S-type orbits. Planets found using the transit method are plotted in green, planets found by the radial velocity method are plotted in red and one planet found by direct imaging is plotted in blue.

Lup and AS-205, at scales of ≈ 5 AU, as part of the DSHARP project [122]. In the continuum emission, they find an two-armed spiral structure with a pitch angle of 14° in the disk around AS-205 N, a spectroscopic binary. The southern component of AS-205 S is surrounded by a compact inner disk and a bright ring at a radius of 34 AU. The 12CO line exhibits clear signatures of tidal interactions, with spiral arms, extended arc-like emission, and high velocity gas, possible evidence of a recent close encounter between the disks in the AS-205 system. In the triple system HT-Lup, the primary disk, HT-Lup A, shows a two-armed symmetric spiral structure with a pitch angle of 4°, while HT Lup B and C, located at 25 and 434 AU separation from HT-Lup A, are barely resolved with ≈ 5 and ≈ 10 AU diameter disks, respectively. The gas kinematics for the closest pair indicates a different sense of rotation for each disk, which could be explained by either a counter rotation of the two disks in different, close to parallel, planes, or by a projection effect of these disks with a close to 90° misalignment between them [122].

Angular Momentum Transport and Instability Theory

The process by which angular momentum redistribution in disks occurs remains an outstanding problem in astrophysics. In order for astrophysical disks to accrete enough material onto the central object to ignite fusion, significant redistribution of mass and momentum must occur in the disk after the initial core collapse occurs in giant molecular clouds. If angular momentum can be redistributed from an inner to an outer region of the disk, then azimuthal fluid speed decreases in the inner region and fluid flows inward toward the central protostar. Models that assume disks evolve driven by molecular viscosity alone cannot sustain the accretion rates observed during star formation. Many theorists propose that turbulent viscosity

could accelerate angular momentum transport within disks, but now there arises the problem of determining the origin and nature of this turbulence. Fluid instabilities are a proposed mechanism for generating turbulence and theoretical models are often realized by performing an eigenvalue analysis of linear and nonlinear perturbations superimposed on some base flow (See reviews [54], [180], [9]).

A typical approach in physics modeling is to start with a highly simplified system, gain some traction, and add increasing complexity in incremental steps. Thus, the stability analyses of astrophysical systems began with highly simplified models.

Chandrasekhar showed that if the collapsing cores are treated as self-gravitating incompressible systems with uniform vorticity that their equilibrium configurations are spheroids or ellipsoids. He explores these theoretical investigations in his seminal works works Introduction to the Study of Stellar Structure, Hydrodynamic and Hydromagnetic Stability, and Ellipsoidal Figures of Equilibrium [32], [33], [34]. It has long been understood that these systems are applicable to the structure of stellar and planetary systems. Later, in the 1970s and 1980s the ability to model the evolution of self-gravitating fluid systems using numerical techniques allowed for a wide range of circumstances to be studied [197],[198], [196], [126], [127], [154], [187], [49].

Gravitational instabilities are instabilities which grow on dynamic timescales and are driven by the self-gravity of a fluid system. Toomre (1964) developed a relationship between relevant quantities in differentially rotating, infinitesimally thin gaseous disks which determine the gravitational stability of the system [197]. Toomre found that a gravitationally unstable disk has

$$Q \equiv \frac{c_s \Omega}{\pi G \Sigma} < 1 \tag{2.7}$$

$$c_s^2 \equiv \frac{dP}{d\Sigma} \tag{2.8}$$

where Q is the Toomre-Q parameter, c_s is the sound speed, κ is the epicyclic frequency, G is Newton's universal gravitational constant, and Σ is the surface density of the disk. Stated another way, when $Q > 1$ the system is stable against gravitational collapse. In the case of a stationary gas, the Jean's stability criterion plays a similar role as the Toomre Q parameter for rotating systems. The Jean's stability criterion compares the relative strength of gravity with that of the thermal pressure. Jeans considered the process of gravitational collapse within an interstellar cloud of gas beginning with hydrostatic equilibrium configuration where

$$\frac{dp}{dr} = -\frac{G\rho(r)M_{enc}}{r^2} \tag{2.9}$$

where $M_{enc}(r)$ is the mass enclosed, p is the pressure, $\rho(r)$ is the density of the gas at radius r and G is the universal gravitational constant. When pressure dominates the system, we get oscillations in the form of sound waves in the medium. When gravity dominates the system, we get gravitational collapse. Cooling the system lowers the pressure and can trigger collapse. Jeans was able to show that there is a critical mass for which gravitational instability leads to the collapse of an interstellar cloud of molecular gas and dust

$$M_J = -\frac{4\pi}{3}\rho\lambda_J^3 \tag{2.10}$$

where M_J is the mass contained in a sphere of radius λ_J and λ_J is the Jeans length. The Jeans length

$$\lambda_J = (\frac{15k_BT}{4\pi GM_p\mu\rho})^{1/2} \tag{2.11}$$

Where k_B is the Boltzman constant, T is the temperature of the gas cloud, μ is the mass per particle, M_p is the mass of a proton. Large, cool, dense regions collapse under gravity while small, warm diffuse regions will oscillate.

Papaloizou & Pringle (1984, I and II) first showed that thick, differentially rotating disks with uniform entropy and constant specific angular momentum are unstable to global nonaxisymmetric hydrodynamic instabilities, the Papaloizou-Pringle instability (PPI), which can redistribute angular momentum within an accretion disk [161]. The PPI is a purely hydrodynamic instability which selects the large-scale $m = 1$ azimuthal mode as the fastest growing, non-linearly dominant mode. In black hole torus systems, the PPI instability leads to nonaxisymmetric features which remain intact for time scales much longer than the dynamical timescale of the system and can lead to large amplitude, quasiperiodic gravitational waves, and significant redistribution of mass and momentum [114].

Ostriker and Peebles (1973) found that for systems that are self-gravitating and rapidly rotating, where rapid means the star's ratio of gravitational potential energy to the absolute value of the rotational energy $\beta = T/|W| > 0.14$ become unstable to an

$m = 2$ nonaxisymmetric instability. This was a condition different from the threshold $\beta > 0.2738$ which had been established for incompressible Maclaurin spheroids [154].

Star formation takes place in Giant Molecular clouds where collapse of small embedded cloud cores is triggered by external mechanisms such as shock waves or stellar winds. For nonrotating cloud cores, our understanding of the star formation process is well in-hand. However, it is clear that in general, rotation must be taken into account. Observations show that molecular cloud cores typically have specific angular momenta $\sim 10^{21-22}$ cm^2 s^{-1} [191]. Clouds with such high specific angular momenta cannot collapse directly into stars. Only a few percent of the cloud matter, that nearest the rotation axis, goes directly into the formation of the central object; the rest forms a massive circumstellar disk [181], [191]. Star formation thus hinges on how mass from the disk finds its way onto the nascent star. Molecular viscosity as a mechanism is ineffective at transporting angular momentum in astrophysical disks. Other mechanisms are needed to enhance transport above that which results from binary particle collisions [9]. Hydrodynamic and/or magnetohydrodynamic nonaxisymmetric instabilities have been proposed as ways to supply the needed dissipation, either directly through wave transport or indirectly as mechanisms that generate turbulence which supplies the needed effective viscosity [14]. We model the redistribution of angular momentum through global nonaxisymmetric hydrodynamic instabilities in this and follow-up papers. Reviews of the fluid mechanics involved in young stellar objects by Shariff (2009) and Armitage (2011) include summaries of observed characteristics of various classes of objects, as well as discussions of various mechanisms involved, and focus on magnetic field effects, radiation transport and turbulence [180],[9].

The stability of nonmagnetic disks has been of interest since the late nineteenth century when Dyson (1893) first investigated what he called â̂nchor rings [57]. As with many systems in physics, the stability analyses began with simplified models, and added increasing complexity over time. Serious attempts at the stability analysis of non-self-gravitating (NSG) thick disks began with Papaloizou & Pringle (1984) who studied isentropic disks with power law differential rotation [157], [158]. They made the important discovery that disks may be dynamically unstable to global nonaxisymmetric modes with azimuthal dependence given by $e^{im\phi}$. For the special cases of a thin cylindrical shell and a thin isothermal ring, a threshold of instability was found for low-m modes and slender tori such that disks were found to be unstable for a range of angular momentum profiles. For disks with power law angular rotation distributions with exponent q, Kelvin-Helmholtz-like instabilities were found to dominate disks for low q while sonic instability dominates systems near a constant specific angular momentum profile, $q = 2$. These sonic instabilities were later named P modes. Papaloizou & Pringle (1987) subsequently performed work on higher order modes, studying modes trapped near the inner and outer disk boundaries by an evanescent region around corotation, modes for which the fluid speed equals the speed of the perturbation [157]. Kojima (1986) further analyzed non-self-gravitating isentropic thick disks for $q = 2$ and $n = 0$, 1.5, and 3.0, where n is the polytropic index [118], [119]. Kojima found the disks were unstable for almost all cases calculated and that the growth rate decreased for either sufficiently large or small radial widths, and also decreased with decreasing q. The growth rates showed little dependence on compressibility, with only small differences between his $n = 1.5$ and $n = 3.0$ calculations.

The effect of self-gravity was first included in the analytic and numerical investigations of long wavelength modes found in slender, incompressible tori by Goldreich, Goodman & Narayan (1986) [74]. Their theory used a thin ribbon approximation to investigate the two-dimensional incompressible limit of the narrow torus. They showed that two new modes emerged, one with corotation at the density maximum, called the J mode (for the Jeans instability) and a second with corotation outside the ribbon, called the I mode (intermediate between P and J modes). Goodman & Narayan (1988) further investigated I modes and J modes adding self-gravity to their calculations of 3D slender incompressible tori with $q = 2$ and 2D slender incompressible tori with varying q. They found that I and J modes were strongly influenced by self-gravity showing character different from the P modes [75].

Papaloizou & Lin (1989) used a variational principle approach to study thin (flat) self-gravitating disks [160]. They found modes which fell into three categories determined by the distribution of vortensity (See also [156]). One kind of mode is associated with extrema in vortensity, corresponding to a disk where corotation is located at the radius of the maximum density. A second mode is generated by the gradient of vortensity on the disk boundaries, corresponding to the existence of the corotation radius outside the disk. A third mode is associated with internal variations in the vortensity gradient. These modes show corotation inside the disk, but not necessarily at the density maximum.

An important development in the study of disks occurred when Adams, Ruden, & Shu (1989) showed that the *indirect* stellar potential could couple the star and disk, and drive spiral one-armed $m = 1$ modes in disks [2]. Symmetry arguments showed that multi-armed modes with $m \geq 2$ could not drive the central star off

the disk center of mass and so could not contribute to the indirect stellar potential. Adams, Ruden & Shu (1989) found that $m = 1$ modes were unstable for high mass disks ($M_*/M_d \approx 1$), attributing instability to SLING amplification. Noh, Vishniac & Cochran (1992) studied $m = 1$ modes in Keplerian ($q = 1.5$) disks for high and low disk masses with emphasis on sensitivity to the outer disk boundary conditions. They found that low mass disks, down to $M_*/M_d \approx 2.0$, were unstable to $m = 1$ modes only when a reflecting outer boundary existed, with growth rates increasing rapidly with an increase in disk mass [151]. They also found that there were two types of $m = 1$ modes (See also [81]).

Mathematically simple systems, such as infinitesimally thin disks, self-gravitating annuli and tori with constant mass density and circular cross-sections, have been studied extensively. Fully 3D, self-gravitating disks have received much less attention. Tohline & Hachisu (1990) performed nonlinear calculations for $n = 1.5$, varying q, for extremely small mass stars, $10^{-9} < M_*/M_d < 10^{-6}$, making these disks fully self-gravitating. Their analysis included eight models but was extended in a second paper, Woodward, Tohline & Hachisu (1994) where a more extensive study was performed, this time including models where the star-to-disk ratio was much larger [194].

An incompressible inviscid fluid disk is stable, however, with respect to both centrifugal instability (Rayleighs circulation criterion) and shear instability (Rayleighs inflection point criterion and its variants). Disks with magnetic fields exhibit a linear magneto-rotational instability [13], and radial entropy gradients can lead to a linear baroclinic instability [116] or, in a different arrangement, to a linear Rossby instability, a type of inflection point instability [134].

Protostars that are axisymmetric beyond the point of dynamic bar-like mode instability do not fission due to gravitational torques [101], [104], [135]. However, in

the presence of a massive disk, a polytropic star unstable to the bar-like instability may fission due to tidal forces from the disk if the stars are sufficiently flattened. The nonlinear effects of how these mechanisms manifest are still unknown and this current study seeks to investigate the fission model of binary star formation.

T Tauri Stars

T Tauri stars (TTS) are a class of young variable stars with ages of $< 10^6$ years. They are typically found near star forming regions of large molecular clouds. The first TTS discovered in the Taurus molecular cloud 140 pc away from Sol, which hosts a stellar nursery with hundreds of newly forming stars and protoplanetary disks. TTS are pre-main-sequence stars with $M < 3M_{sun}$ that are in the process of contracting to the main sequence along the Hayashi track. They are divided into two classes based on the shape of their spectral energy distributions [2]. Weak emission T Tauri stars (WTTS) resemble normal main-sequence stars with some emission from an active chromosphere while classical T Tauri stars (CTTS) emit excess infrared (IR) and ultraviolet (UV) radiation compared to a stellar photosphere [205], [92].

TTS comprise the youngest visible F, G, K and M spectral type stars whose surface temperatures are similar to those of main-sequence stars of the same mass. Due to the fact that they are still in the proces of contracting, they have much larger radii and therefore, are significantly more luminous than main-sequence stars. Their central temperatures are too low for hydrogen fusion with effective temperatures of 202000 K [39]. They are powered by gravitational energy released as the stars contract toward the main sequence, which they reach after about 100 million years. They typically rotate with a period between one and twelve days, compared to a month for the Sun. Many TTS have extremely powerful stellar winds and eject gas

in high-velocity bipolar jets. TTS increase their rotation rates as they age, through contraction and spin-up, as they conserve angular momentum. Roughly half of TTS have protoplanetary disks. Since discs are estimated to dissipate on timescales of up to 10 million years, this puts an upper limit on the timescales of planet formation. Another interesting characteristic of TTS is that they tend to be binary star systems. Circumstellar disks are popular explanations for many properties of CTTS, including temperatures, variability, the IR and UV excess emission [1], [112]. Another source of brightness variability could be from clumps (protoplanets and planetesimals) in the disks surrounding T Tauri stars.

Higher mass analogues (3-9 M_{sun}) of TTS for A and B spectral type premain-sequence stars, are called Herbig Ae/Be-type stars. More massive (¿8 solar masses) stars in premain sequence stage have not been observed, most likely because they evolve very quickly. Once they become visible, they are already burning hydrogen in their cores and are considered main sequence stars.

Magnetic Fields

Magnetic fields are expected to play a large role in the dynamics and evolution of protoplanetary disks. Magnetic fields can efficiently transport angular momentum by magentohydrodynamic (MHD) turbulence or through magnetocentrifugal acceleration of outflows from the disk surface. Optical and near-infrared images of circumstellar disks often reveal bipolar outflows, normal to the disk plane [26]. Hydrodynamic models fail to account for the observed jets collimation and ejection efficiency [27]. Magnetized Keplerian disks have been shown to exhibit the magneto-rotational instability which can drive turbulent accretion [15]. Magnetically-driven mixing can alter disk chemistry and evolution of the dust grain population.

Magnetic stresses can also change the effective fluid viscosity (making the $\alpha - disk$ approximation invalid [179]).

It is known that the effective viscous response of the disk determines whether planets migrate inwards or outwards. However, young protoplanetary disks are expected to be weakly ionized due to their optical thickness and low temperatures [70]. Weak ionisation of protoplanetary disks means that magnetic fields may not be able to effectively couple to the matter. In addition, very young stellar objects may need to shed magnetic field before further collapse is possible. Diffusive effects can damp magnetic structures, and potentially quench the MRI [109] [121], as supported by numerous non-linear simulations [89], [65], [10]. Reduction of ionization can be taken into account by incorporating non-ideal MHD effects: ohmic diffusion, ambipolar diffusion, and the Hall drift [149], [206].

Discourse on Planet Formation: Core Accretion versus Disk Instability

Currently there are two main theories of planet formation: the core-accretion scenario and disk instability. Here I describe the details of each theory and discuss the theoretical and observational evidence, and related research which supports them. While it is sometimes presented in the literature that either core accretion or disk instability is the "correct" theory of planet formation, in fact one must delineate between what type of planet is under consideration, rocky or gaseous, how metal rich the stellar component is, and where in the disk the planet forms. Both theories have merits and in truth planet formation probably involves aspects of both theories (and currently unknown theories) to produce the wide range of planets discovered to date.

The Core Accretion Scenario

The formation of planets in the core-accretion scenario from micron-sized dust particles requires growth through at least 12 orders of magnitude. The process begins when sub-micron sized particles begin to collide and stick together. Such small particles are well coupled to the gas, and subject to Epstein Drag, felt by solid particles that are smaller than the mean free path of gas in the disk. Consider a spherical particle of radius s. To understand how such a particle might evolve in a protoplanetary disk we need to understand the drag force experienced by the particle when it moves at some velocity relative to the local velocity of the gas. If $s \lesssim \lambda$ where λ is the mean free path of gas molecules within the disk we are in what is known as the Epstein drag limit. This drag regime is most relevant for small particles which effectively act as a collision-less ensamble with a Maxwellian velocity distribution. If $s \gtrsim \lambda$ then the gas in the disk flows as a fluid around the dust particles as if they were an obstruction. This is known as the Stokes regime. In either regime, the force will scale with the area πs^2 which faces the gas, and the acceleration caused by the gas drag decreases with particle size and eventually becomes negligible once bodies of planetesimal size are formed. Coagulation to form planetesimals will then be determined by the frequency of particle collisions and how efficiently the particles can adhere together. As the particles collide and stick together, they grow larger and can decouple from the gas, and begin to interact with it because of the differential rotation between solids and gas. Once particles grow to a size much larger than the mean free path of the gas, the interaction can be treated in classical fluid terms and Stokes drag becomes important.

The gas rotates about the star at a slower velocity than the solids due to a radial pressure gradient that partially counteracts the gravitational attraction of the gas

toward the star. If the radial and azimuthal velocities of the particle are v_r and v_ϕ respectively, than the equations of motion including the aerodynamic drag forces can be written as

$$\frac{dv_r}{dt} = \frac{v_\phi^2}{r} - \Omega_K^2 r - \frac{1}{t_{fric}}\left(v_r - v_{r,gas}\right) \tag{2.12}$$

$$\frac{d}{dt}\left(rv_\phi\right) = -\frac{r}{t_{fric}}\left(v_\phi - v_{\phi,gas}\right) \tag{2.13}$$

where r is the radial coordinate, Ω_K is the Keplerian angular velocity, and t_{fric} is the friction timescale, which quantifies the coupling between the gas and the dust, and is written,

$$t_{fric} = \frac{mv}{|F_D|} \tag{2.14}$$

where F_D is the drag force for either the Epstein or Stokes limit. Friction via gas drag produces an acceleration proportional to and in the direction opposite of the relative velocity between the particle and the gas. Friction generally removes angular momentum from the solid particles causing them to drift radially towards the star [207],[86]. In addition, considering the Epstein friction timescale for dust settling, and using a simple model of hydrostatic equilibrium in the vertical direction,

$$\frac{dz^2}{dt^2} + \frac{1}{t_{fric}}\frac{dz}{dt} + z\Omega_K^2 = 0 \tag{2.15}$$

suggests that micron-sized particles would take millions of orbital periods to settle to the mid-plane, a timescale too long for this to ever occur before the gas component was dispersed. This suggests that dust particles first need to aggregate and grow into larger particles. Centimeter sized particles in this same model would only require on the order of thousands of orbits to approach the disk mid-plane [41]. However, this simple model assumes that there are no turbulent motions in the gas. Planetesimals will be able to grow from sub-micron sized solids only if their relative velocities are less than $\sim 1ms^{-1}$ [20]. Turbulent motions in protoplanetary disks can result in relative velocities for cm-m sized particles which exceed this limit [209]. Growth beyond the cm regime presents a physical challenge in the core accretion process.

One proposed scenario to overcome these issues suggests that long lived vortices within the protoplanetary disk could act as dust traps accelerating the growth of planetesimals [117], [115]. Once dust was trapped inside the vortex, particles would be concentrated within the trap, the relative velocities of particles inside the vortex would be reduced, and particles within the trap would not experience orbital drift because they would be at a local pressure maxima. Another method of averting this issue of particle growth proposed by Safronov (1969) [173] and later by Goldreich and Ward (1973) [73], suggests that prompt formation of planetesimals may occur through gravitational instability in the dust layer at the disk mid-plane. If gas can settle to the mid-plane of the disk, we can adopt a two-dimensional (2D) fluid approach where the basic equations describing the dynamics of the particle disk are the continuity and momentum equations together with Poisson's equation for the gravitational field,

$$\frac{\partial \Sigma}{\partial t} + \nabla \cdot (\Sigma \mathbf{v}) = 0 \tag{2.16}$$

$$\frac{\partial \mathbf{v}}{\partial t} + (\mathbf{v} \cdot \nabla)\mathbf{v} = -\frac{1}{\Sigma}\nabla P - \nabla \Phi_g \tag{2.17}$$

$$\nabla^2 \Phi_g = 4\pi G \rho \tag{2.18}$$

where Σ is the surface density, $\mathbf{v}$ is the velocity, P is the pressure, Φ_g is the gravitational potential, G is the gravitational constant and ρ is the density. Local analysis of axisymmetric instability for a thin 2D disk requires that the Toomre Q parameter $Q < 1$. Turbulent effects in the background gaseous disk and radial drift can disrupt dust settling, halting or extending the timescales on which this hybrid process could form planetesimals [40]. However, self-gravity between particles within a dust-trapping vortex may trigger local gravitational instability leading to prompt formation of planetesimals. The formation and stability of dust trapping vortices has been under active research since this scenario was first proposed [16].

Recent observational evidence lends credence to the idea that dust trapping vortices may be physical mechanisms occurring in protoplanetary systems. The Atacama Large Millimeter/sub-millimeter Array (ALMA) has recently revealed the existence of dust cavities and azimuthal asymmetries in protoplanetary disks [162]. In addition, direct observations have shown that gas is still present within the vortices [221], [30], [204], [188]. The Oph IRS 48 transition disk is one such example of a disk exhibiting an asymmetric structure that has been interpreted as a dust trap (See Figure 11).

Assuming that the solid component has had time to agglomerate into rocky/icy cores of about a kilometer in diameter, these cores can begin to gravitationally

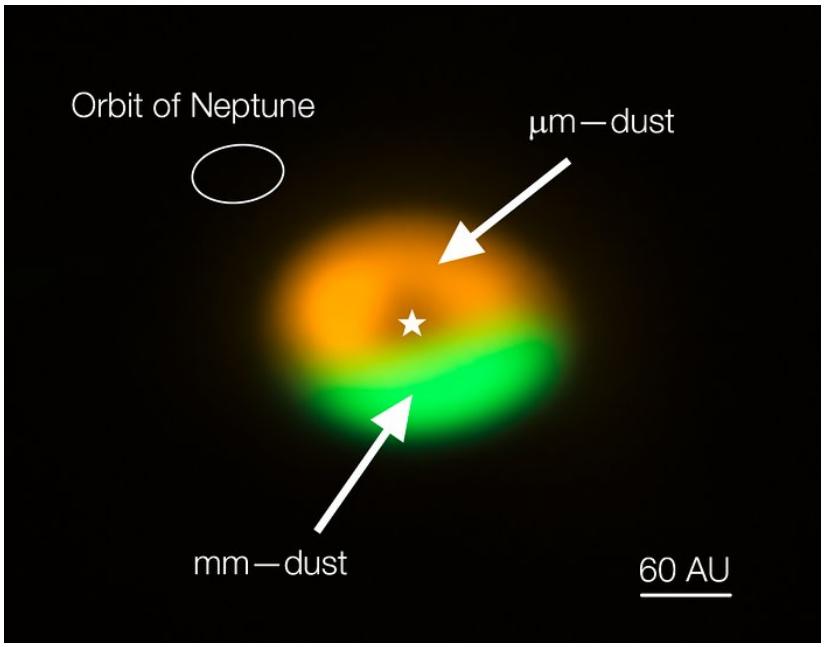

FIGURE 11. Annotated image from the Atacama Large Millimeter/submillimeter Array (ALMA) showing the dust trap in the disc that surrounds the system Oph-IRS 48. The green area is the dust trap, where the bigger particles accumulate. The size of the orbit of Neptune is shown in the upper left corner to show the scale. Credit: ALMA (ESO/NAOJ/NRAO)/Nienke van der Marel.

interact with their neighbors. The gravitational field of the planetesimals can add a enhancement factor to the growth rate of the planetesimal,

$$\frac{dm_s}{dt} = \pi R^2 v_{rel} \rho_s F_g \tag{2.19}$$

where v_{rel} is the relative velocity between impacting bodies, ρ_s is the density of the solid component of the disk, and F_g is the gravitational enhancement factor. During the growth of planetary embryos from swarms of planetesimals, relative velocities play a crucial role in determining accretion rates. The velocity distribution of planetesimals is determined by processes such as elastic and inelastic collisions, gravitational scattering, and frictional drag by the gas.

There is a region around any planet where that planet's gravity dominates the gravity of the star that it orbits. This region is called the Hill sphere if the planet. If the radial oscillations of planetesimals is within several Hill radii of the planet embryo, this process can lead to runaway growth, and this growth continues until its neighborhood has been cleared of planetesimals [132], [41]. Once the feeding zone has become depleted, the planet embryo becomes nearly isolated. The isolation timescale is several tens of thousand of orbital periods. To form a Jupiter like planet, the planet embryo must accrete gas from the gas component of the disk. Gas can accrete onto a planet when the thermal energy is smaller than the gravitational binding energy of the planet , or when the escape velocity from the surface of the planet embryo exceeds the local thermal speed of the gas in the disk. Growth of gas envelopes is regulated by gravitational contraction, pressure and gas opacity. It is still uncertain if growth through so many orders of magnitude and gas capture can occure before the

gas componenet of the disk has dispersed due to T-Tauri winds and fission ignition within the central young stellar object.

Disk Instability Theory

Gravitational instabilities could trigger prompt formation of planetary embryos on timescales which align with stellar evolution. That is, gravitational instabilities offer a mechanism of planet formation in tandem, and on the same timescales, as star formation. One of the major drawbacks of the core accretion scenario is the timescale on which Jupiter like planets form. If the star enters the T-Tauri phase of its evolution before the gas giants have accumulated gas from the protoplanetary disk, the star fusion ignition produces stellar winds that could deplete the disk of its gas before a giant planet has time to form.

Gravitational Instabilities can occur in any region of a protoplanetary disk which becomes sufficiently cool or develops a high enough surface density. In the early phase of the disks lifetime (pre T-Tauri), disks are expected to be weakly ionized, massive, and relatively cool; conditions under which disk self-gravity is expected to play a large role in stellar and planetary evolution [130], [125]. Disk instability theory suggests that Jupiter like planets are formed through gravitational collapse of the the material in the disk in a process similar to the initial disk formation model. The gas becomes unstable to fragmentation and clumping, driven by gravity (perhaps through Jeans-like instabilities)[66]. Once a clump forms in the disk, dust sediments to the center forming a planetary core. As the protoplanet orbits, it clears a gap in the disk (see DSHARP observations). This process is quick, taking place on time scales as short as hundreds to thousands of years.

It is now generally understood that fluid instabilities can give rise to nonaxisymmetric spiral structures which are efficient at transporting angular momentum, redistributing mass, and fragmenting the disk into dense clumps, as well as, producing self-gravitating turbulences [14], [12], [180], [9], [214], [81], [82], [203], [83]. While instabilities can lead to disks which fragment, it is still not known if disk fragmentation occurs in physical systems, and if fragments do form, are they long lived and gravitationally bound to the system.

An important point now recognized is that disk thermodynamics plays a large and, perhaps, the dominant role in the longterm behavior of nonaxisymmetric instabilities and consequently on the mechanisms responsible for angular momentum redistribution and disk fragmentation. Cooling limits the growth of instability by dissipating energy gained from the nonlinear development of instabilities and removes pressure support from the gas [155], [133], [140], [23], [67]. Modern numerical simulations approach the problem of disk thermodynamics by either (i) specifying a simple equation of state to study isentropic, isothermal and adiabatic limits [166], [168], [137] (ii) specifying a simple cooling rate per unit volume [71], [138], [141] or (iii) modeling radiative cooling based on gas opacities and dust compositions [21], [140], [29]. Modeling radiative cooling using opacities and dust composition becomes a difficult problem due to transitions from optically thin to optically thick gas within protoplanetary disks. In addition, modeling dust requires making assumptions about collisional growth and destruction rates, size distributions and how strongly the dust is coupled to the gas.

Strong observational evidence for disk instability theory comes from the existence of hot Jupiter's combined with the short lifetimes of protoplanetary disks. Most protoplanetary disks are thought to have lifetimes of about 3 Myr at which time,

planet formation must already have occured due to gas depletion from T-Tauri winds [214], [58]. The recent discovery of the young planet k2-33b throws the plausibility that orbital migration could be responsible for the plethora of hot Jupiter's into question [200]. The timescales on which core accretion can form planets does not appear to be a viable mechanism for forming gas giants unless some other physical process can accelerate planetesimal growth.

Hadley et al. have (See [81], [82], [203], [83]) completed an extensive study of nonaxisymmetric instabilities in self-gravitating disks in which they mapped the stability space occupied by typical protostellar and protoplanetary star/disk systems and investigated the mass and angular momentum transport properties of nonaxisymmetric disk modes in the linear, quasi-linear, and in some instances into the nonlinear regime. Hadley et al. showed that circumstellar disks are unstable over a wide range of conditions and usually dominated by one-armed spiral modes, $m = 1$ modes, where m was the azimuthal mode number defined by the azimuthal dependence of the modes $e^{im\phi}$. Here, $i = \sqrt{-1}$ and ϕ is the azimuthal angle.

Disks susceptible to one-armed spirals behave differently from those dominated by multi-armed modes, $m \geq 2$ modes, because coupling between the central star and disk allows angular momentum transfer between the star and disk even when instability is in the linear regime [83]. Adams (1989) argued that one-armed spirals may play the dominant role in stellar and planetary formation processes while others claim that despite the star being displaced from the system's center of mass, one armed modes do not play the dominant role in [3], [29]. Hadley et al. have found that in some cases, when an $m = 1$ disk fragments, the resulting asymmetric structures produced at saturation could be interpreted as dust trapping vortices (See Figure 12).

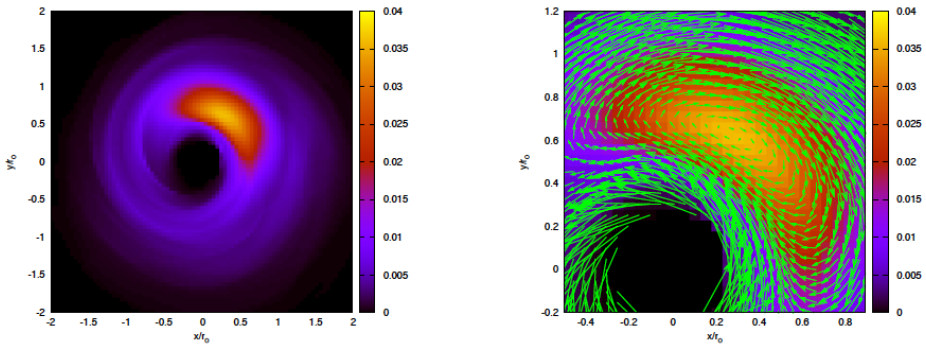

FIGURE 12. The density structure in the disk mid plane for an m=1 dominant non-cooled model. The densities are in polytrope units in which the equilibrium density maximum is $\rho_0 = 0.0284$. The density peak is $\sim 1.5\rho_0$. Superimposed on the density contour are arrows showing the velocity field in the frame of the density clump. The arrows show relative velocities but have arbitrary normalization.

Despite capturing the essential physics of how planetary systems can form, not one computational model has been able to reproduce the mass and orbital distribution of both the terrestrial planets and the asteroids [202], much less the formation of the gas giant and terrestrial planets. In the standard core accretion scenario, planetary embryos the size of mars and swarms of km sized planetessimals follow nearly circular co-planar orbits in the inner region of the disk, and their number density decreases with distance to the sun. The giant planets in the outer region of the disk perturb these orbits and a cascade of collisions ensues. These collisions form the rocky planets, and the leftover material becomes the asteroid belt. Despite simulations producing systems which broadly capture the properties of the inner solar system, the detailed mass and orbital distributions have not been reproduced, and some argue that it is not possible [106].

Standard formation scenarios don't consider that orbital migration of the gas giants can alter the density profile of the inner planetesimal swarm. In order for this to fix the problems of reproducing the solar system, there must be a match between the growth and migration times of the giant planets. This has yet been unrealizable

in simulations which assume the gas giants formed via the core accretion scenario. Models of giant planet formation by disk instability can form jupiter like objects on short timescales. However, no hybrid model of core accretion and disk instability has been performed, and it may not be possible given that the relevant timescales for each process differ drastically. As of now, standard models of planet formation do not satisfy the major constraints of the planet formation processes.

Jovian planets are thought to form in protoplanetary disks either through slow growth described by core accretion theory, or promptly from direct collapse as predicted by disk instability theory. The astrophysics community has a hard time agreeing on which model accurately describes giant planet formation, although, in reality, a mixture of the two theories is most likely at work. Statistical evidence now suggests that there are two different populations of giant planets $> 1M_J$. Santos (2017) in *Observational Evidence for Two Distinct Giant Planet Populations*, uses statistical analyses to investigate mass distributions of giant planets compared to solar-type stars and determine two regimes, planets that are above and below $4M_{jup}$, where M_{jup} is the mass of Jupiter. Then they compare the metallically and mass distributions for planets that are above and below $4M_{jup}$. They apply a Kolomgorov-Smirnov test on their two samples to determine if they come from the same parent population. The data shows that the more massive planets orbit stars that are more metal poor and the less massive planets orbit stars that are more metal rich [176].

CHAPTER III

METHODS

Equilibrium Methods

To investigate the stability properties of star-disk systems it is important to begin from an equilibrium mass density and angular momentum structure where the fundamental quantities are unchanging in time. These equilibrium structures will be used as an initial state for time-evolving linear and non-linear models. For equilibrium structures, we begin by assuming axisymmetry about the rotation axis and mirror symmetry across the equatorial plane. Equilibrium structures of differentially axisymmetric rotating inviscid polytropic stars surrounded by inviscid polytropic disks are calculated using the inviscid, axisymmetric mass and momentum conservation equations

$$\partial_t \rho = -\nabla \cdot (\rho \mathbf{v}) \tag{3.1}$$

$$\partial_t (\rho \mathbf{v}) = -\nabla \cdot (\rho \mathbf{v}\mathbf{v}) - \nabla P - \rho \nabla \Phi_g \tag{3.2}$$

which are solved on an Eulerian, cylindrical grid. Here ρ is the mass density, $\mathbf{v}$ is the velocity P is the pressure and Φ_g is the gravitational potential. The stars and disks are assumed to rotate on cylinders with $\mathbf{v} = \Omega(\varpi)\varpi\hat{\phi}$ and $\Omega(\varpi) = \Omega_0(\frac{\varpi}{r_0})^{-q}$ a power law angular velocity distribution with Ω_0 the frequency of fluid at the density maximum in the disk r_0, ϖ the cylindrical radial coordinate and q the power. Setting $q = 1.5$ allows one to recover the familiar Keplerian rotation law and $q = 2.0$ is a limiting case of constant specific angular momentum. An energy equation is not

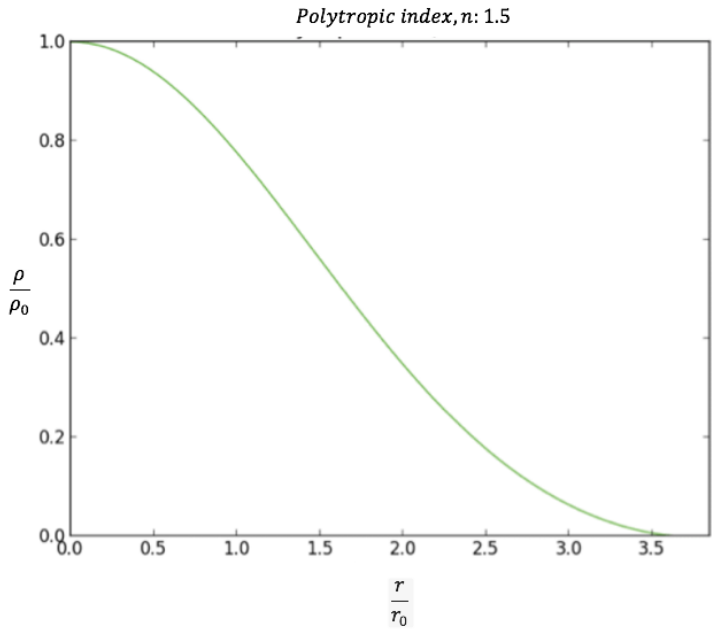

FIGURE 13. The normalized density as a function of scale length for a polytrope with n = 1.5.

needed because the energy of the gas is assumed to be isentropic for which we use a polytropic relationship between pressure and density $P = K\rho^{1+\frac{1}{n}}$ where P is the pressure, ρ is the density, K is the polytropic constant and is related to the entropy per baryon and n is the the polytropic index. A polytropic index of $n = 1.5$ is generally a good model for stellar cores such as those of red giants, or even brown dwarfs and giant gaseous planets. In figure 13 we show how density scales with radius for an $n = 1.5$ polytrope. Using this index, one can find that the polytropic exponent is $\gamma = 1 + \frac{1}{n} = 5/3$, which gives the specific heat capacity for a monatomic gas. A polytrope with index $n = \infty$ is that of an isothermal sphere with exponent equal to unity. For an ideal gas, an infinite n corresponds to constant temperature. In general, increasing the polytropic index makes the gas more compressible and pushes the density distribution to one more heavily weighted toward the center of the fluid body [32], [87].

Equilibrium shapes of rotating bodies of incompressible fluids are well known and are generally composed of spheres, oblate spheroids, and ellipsoids. A Maclaurin spheroid is an oblate, incompressible, uniformly rotating spheroid. The Maclaurin spheroid is considered to be one of the simplest models of rotating ellipsoidal figures in equilibrium since it assumes uniform density [33]. For our equilibrium models we can assume a compressible central star that is in differential rotation with the specific angular momentum distribution of a Maclaurin spheroid

$$h_{\mathrm{M}}(m_{\varpi}) = 2.5\big[1 - (1 - m_{\varpi})^{\frac{2}{3}}\big] \tag{3.3}$$

or with the specific angular momentum distribution

$$h_M(\varpi) = 2m_{\varpi} \tag{3.4}$$

where m_{ϖ} is the cylindrical mass fraction

$$m_{\varpi} = \frac{4\pi \int_0^{\varpi} \varpi \mathrm{d}\varpi \int_0^{Z_{\varpi}} \rho(\mathbf{r})\mathrm{dz}}{M_*} \tag{3.5}$$

(See Bodenheimer & Ostriker (1973) [154]), $\rho(\mathbf{r})$ is the mass density, and Z_{ϖ} is the height of the star at cylindrical radius ϖ. Here. we refer to the later case as the L-distribution.

In steady-state, the mass and momentum conservation equations become

$$\nabla\cdot(\rho\mathbf{v}) = 0 \tag{3.6}$$

and

$$\rho \mathbf{v} \cdot \nabla \mathbf{v} + \nabla \mathrm{P} + \rho \nabla \Phi_g = 0 \tag{3.7}$$

The gravitational potential Φ_g is found through solution of the Poisson equation,

$$\nabla^2 \Phi_g = 4\pi G \rho \tag{3.8}$$

where G is the gravitational constant. In axisymmetry with circular motion, the mass conservation equation is satisfied identically. For rotation on cylinders and a polytropic equation of state the momentum equation can be integrated once to yield the star-disk equilibrium equation

$$C = (n+1) K \rho^{1/n} + \Phi_g + \Phi_c \tag{3.9}$$

where C is the integration constant related to energy conservation (i.e. Bernoulli equation) and Φ_c is the centrifugal potential, which takes the form

$$\Phi_c = -\int^{\varpi} \Omega^2(\varpi) \varpi \mathrm{d}\varpi. \tag{3.10}$$

Central star families are defined by their polytropic indices and rotational structures, with family members defined by ratio of their equatorial radius r_e and polar radius r_p. This ratio determines a flattening parameter for the initial stars. Disk families are defined by their polytropic indices n and exponents q of their angular velocity distributions, with disk family members defined by the ratios of the inner and outer radii of the disk r_- and r_+, respectively. Star-disk families are defined by the ratio of the maximum density of the disk $\rho_\circ$ to the central density of the star ρ_c, $\eta = \rho_\circ / \rho_c$, and the ratio of the stellar equatorial radius to the radius of the inner edge

of the disk, r_e/r_-. The parameter η controls the relative stellar mass M_* to the disk mass M_d, $\mathcal{M} = M_*/M_d$, for given r_-/r_+. Specifying η allows the star and disk to lie along different adiabats. The solutions are normalized using modified polytropic units where G = K_* = M_*+M_d = 1. For systems with pointlike stars, the polytropic constant is set to 1 everywhere (*e.g.,* see Williams & Tohline (1987) [211], [212]). In this work, the disk polytropic constant K_d may differ from 1. With the inclusion of their respective constants, the equations for the star and disk take identical form.

We solve Equation 3.8 using the Hachisu self-consistent field algorithm (Hachisu 1986). In the description that follows, we denote stellar quantities with the subscript $*$ and disk quantities with the subscript d. We employ the following strategy: (i) guess the initial density distributions for the star and disk, ρ_* and ρ_d, respectively. (ii) Find C_* and C_d, the integration constants for the star and disk, and $h^2_{\circ,*}$ and $h^2_{\circ,d}$, the scales for the star and disk centrifugal potentials, where we defined

$$\Phi_c(\varpi) = -\int^{\varpi} \Omega^2(\varpi)\varpi \mathrm{d}\varpi = h^2_\circ \Psi(\xi). \tag{3.11}$$

In the above, $\Psi(\xi)$ is the dimensionless centrifugal potential,

$$\Psi(\xi) = -int_0^{t_0}\Omega_0^2(\xi)(\xi)^{-q} r_0^2 \xi d\xi \tag{3.12}$$

and $\xi = (\varpi/r_\circ)$. To find C_* and h_{0*} equation [3.9] is evaluated at the polar radius (ϖ,z) = (0,r_p) and at the equatorial radius (r_e,0). At both locations, $\rho_* = 0$. This yields

$$h^2_{\circ,*} = \frac{\Phi_g(0, r_p) - \Phi_g(r_e, 0)}{\Psi(0) - \Psi(r_e)} \tag{3.13}$$

a measure of how much angular momentum is in the system, and

$$C_* = \begin{cases} \Phi_g(0, r_p) + \Phi_c(0) \\ \\ \Phi_g(r_e, 0) + \Phi_c(r_e) \end{cases} \tag{3.14}$$

For the disk, C_d and $h^2_{\circ,d}$ are found in a similar manner but with Equation [3.9] evaluated at (r_-,0) and at (r_+,0),

$$h^2_{\circ,d} = \frac{\Phi_g(r_-, 0) - \Phi_g(r_+, 0)}{\Psi(r_-) - \Psi(r_+)}, \tag{3.15}$$

and

$$C_d = \begin{cases} \Phi_g(r_-, 0) + \Phi_c(r_-) \\ \\ \Phi_g(r_+, 0) + \Phi_c(r_+) \end{cases} \tag{3.16}$$

(iii) Equation 3.9 with $(C_*, h^2_{\circ,*})$ and $(C_d, h^2_{\circ,d})$ as defined in (ii), is inverted to yield ρ_*, ρ_d, K_*, and K_d. If the guessed and calculated structures are consistent, the calculation is halted and the model declared converged. If not, new guesses for ρ_* and ρ_d are made, and steps (ii) and (iii) repeated. Consistency is defined when C_*, C_d, $h^2_{\circ,*}$, and $h^2_{\circ,d}$ each varies by less than 1 part in 10^{10} in successive iterations.

The accuracy of the model is defined by the virial test. The virial theorem relates the total kinetic energy T, both rotational and thermal, to the gravitational potential energy of a self-gravitating body W as $2T + W = 0$. In practice, this quantity does not equal zero for our calculations, and so we discard models in which $(2T + W)/|W| > 10^{-3} - 10^{-4}$.

Linear Methods

Fluid flows, which are governed by the Navier-Stokes equations, are spatio-temporal systems that are inherently nonlinear. These systems often exhibit complex behaviors whose modeling and physical understanding are still the object of ongoing research. Many challenges arise when modeling such systems due to their high dimensionality and nonlinear nature. For nonlinear systems, a small change in the initial conditions can lead to drastically different outcomes. One could say that the output is not proportional to changes in the input. The dynamical behavior of nonlinear fluid systems is often chaotic and unpredictable. Weather systems are a good example of this chaotic behavior, where a simple change in one part of the system will often produce complex effects throughout. Nonlinearity is one of the main reasons why accurate long-term weather forecasts are virtually impossible with current technology. The behavior of a nonlinear fluid system is mathematically described by a set of simultaneous partial differential equations in which the unknown functions appear as variables of a polynomial of degree higher than one. As nonlinear dynamical equations are difficult to solve, nonlinear systems are commonly approximated by a set f linearized equations. Linearization serves as a useful approximation for understanding the behavior, however important information is often lost and interesting phenomenon such as chaos, feedback and turbulent motions are hidden.

The linear stability of equilibrium star-disk systems to infinitesimal perturbation are investigated by imposing a set of Eulerian perturbations of the form,

$$A = A_\circ + \delta A(\varpi, z, t)e^{im\phi} \tag{3.17}$$

to the relative fluid quantities. Here, $A_\circ$ is the equilibrium solution and $\delta A(\varpi, z, t)$ is the perturbed amplitude where the condition

$$|\frac{\delta A(\varpi, z, t)}{A_\circ(\varpi, z)}| << 1 \tag{3.18}$$

is imposed. In cylindrical coordinates, the linearized equations are

$$\begin{aligned}
\partial_t \delta\rho &= -im\Omega\delta\rho - \rho_\circ \frac{\delta v_\varpi}{\varpi} - \delta v_\varpi \partial_\varpi \rho_\circ - \delta v_z \partial_z \rho_\circ \\
&\quad -\rho_\circ \left(\partial_\varpi \delta v_\varpi + \frac{im}{\varpi}\delta v_\phi + \partial_z \delta v_z \right) && (3.19) \\
\partial_t \delta v_\varpi &= -im\Omega\delta v_\varpi + 2\Omega\delta v_\phi - \frac{\gamma P_\circ}{\rho_\circ^2}\partial_\varpi \delta\rho \\
&\quad -(\gamma - 2)\frac{\delta\rho}{\rho_\circ^2}\partial_\varpi P_\circ - \partial_\varpi \delta\Phi, && (3.20) \\
\partial_t \delta v_\phi &= -im\Omega\delta v_\phi - \frac{1}{\varpi}\partial_\varpi(\Omega\varpi^2)\delta v_\varpi - \frac{im}{\varpi}\frac{\gamma P_o}{\rho_o^2}\delta\rho \\
&\quad -\frac{im}{\varpi}\delta\Phi, && (3.21) \\
\partial_t \delta v_z &= -im\Omega\delta v_z - \frac{\gamma P_o}{\rho_o^2}\partial_z \delta\rho - (\gamma - 2)\frac{\delta\rho}{\rho_o^2}\partial_z P_o \\
&\quad -\partial_z \delta\Phi && (3.22)
\end{aligned}$$

(See Hadley (2014) [83]). The perturbed gravitational potential $\delta\Phi$ is found from solution of the perturbed Poisson equation,

$$\nabla^2(\Phi_0 + \delta\Phi e^{im\phi}) = 4\pi \mathrm{G}(\rho_0 + \delta\rho e^{im\phi}) \tag{3.23}$$

which includes the equilibrium solution Φ_0 and the small perturbed quantity $\delta\Phi$. We then integrate once. Boundary conditions consist of: (i) mirror symmetry about the equatorial plane; (ii) perturbed velocities in the ϖ and z directions and $\delta\rho$ which go

to zero on the surface of the disk and the surface of the star; and (iii) perturbed gravitational potentials on the outer grid boundaries computed using an expansion in spherical harmonics including l-values up to 16.

We use a random white noise perturbation of the density

$$\rho = \rho_0 + \delta\mathcal{R}e^{im\phi} \tag{3.24}$$

where $\mathcal{R}$ is a random number ($1 > \mathcal{R} > 0$) and ($\delta << \rho_0$) and solve the linearized hydrodynamic equations 3.19-3.22 and Poisson's equation (equation 3.8). Time derivatives are left continuous, but the spatial derivatives are approximated using finite differencing. We solve the initial value problem (IVP) using a fourth-order Runge-Kutta method to advance the equations in time. We extract the eigenvalues from the system after it reaches global steady exponential growth. The growth rates and frequencies of the density perturbation determined are the fastest growing mode for a given m-symmetry characterizing instability in the system. Our numerical code is described in detail in Hadley *et al.* (2014, 2015) [83], [84].

Non-Linear Methods

To follow the evolution of unstable star-disk systems into the nonlinear regime, we employ the radiation hydrodynamics code CHYMERA (See [190],[216], [164] [140], [28], [22]). Here I describe the structure of the code and how each physics module was developed in relation to current theories in star formation and evolution and modern numerical technique. I seek to include enough detail such that future readers of my work can come away with a clear understanding of how my research was conducted, and what procedures to follow should they want to replicate my work.

CHYMERA numerically solves a set of partial differential equations from a set of initial conditions, *ie.* CHYMERA solves an an initial value problem. CHYMERA employs a finite differencing scheme to numerically solve differential equations. This method of numerical modeling is widely used in fluid flow, and plasma physics problems. The equilibrium density and momentum structure is loaded onto a 3D grid and serves as the initial condition. CHYMERA solves the hydrodynamic equations together with self-gravity on a fixed, Eulerian, cylindrical grid (r, ϕ, z). A cylindrical grid is chosen because it most closely matches the symmetry of a protostellar system. The r-direction is broken into J-discrete elements, the ϕ-direction into L-discrete elements and the z-direction into K-discrete elements. By fixed, we mean that the cells (volume elements in the computational grid) do not change size nor move with the fluid in time. Eulerian meaning the Eulerian specification of the flow field as opposed to the Lagrangian computational fluid dynamics methods commonly used which focuses on particle transport rather fluxing and sourcing. The Lagrangian description of a fluid flow follows individual fluid parcels as they move through space and time. These parcels/particles are marked and their trajectories are described as a function of time. The Eulerian description is a way of tracking the fluid motion by focusing on a fixed volume in space through which the fluid moves in time (see Landau and Lifshitz (1987) [124]).

The numerical code CHYMERA has gone through several iterations to reach its current form. The original version was the hydrodynamics code developed by Dr. Tohline at UC Santa Cruz in the 1970s [190]. At the time the code was first order in space. Subsequently, the code was made second order in time and space using a van Leer advection scheme for flux transport [216]. The code went through another set of modifications in 1995 to include an energy equation, artificial viscosity and some *ad*

hoc cooling prescriptions [164]. Radiation physics were added in 2004, and in 2006 those radiation algorithms were improved upon [140] [28]. The code was extended to parallelization using openMP methods in 2007 [22] and ported to the University of Oregon computing cluster in 2012.

The nonlinear hydrodynamic equations consist of mass conservation in pure conservative form (mass continuity), an equation of motion and an energy equation which consists of conservative terms and source/sink terms. The mass continuity equation can be written,

$$\frac{\partial \rho}{\partial t} + \nabla \cdot (\rho \mathbf{v}) = 0 \tag{3.25}$$

where ρ is the mass density and $\mathbf{v}$ is the fluid velocity. The continuity equation describes how the mass density within some volume element changes in time due to the flux of the mass through that element. We do not include explicit mass creation or destruction. The equation of motion can be cast into a similar form as the time rate of change of momentum plus the divergence of the flux of momentum within some volume element is equal to explicit sources or sinks of momentum, e.g momentum changed by pressure gradients and gravitational forces. The explicit equation of motion is written,

$$\frac{\partial \rho \mathbf{v}}{\partial t} + \nabla \cdot \rho \mathbf{v}\mathbf{v} = -\nabla P - \rho \nabla \Phi_g - \nabla \cdot (\rho \mathcal{Q}) \tag{3.26}$$

where P is the pressure and Φ_g is the total gravitational potential with the last term included to handle artificial viscosity. $\mathcal{Q}$ is a tensor where elements

$$Q_{jj} = \begin{cases} C_Q(\Delta v_j)^2 & \Delta v_j \leq 0 \\ 0 & \Delta v_j > 0 \end{cases} \tag{3.27}$$

and is a von Neuman & Richtmeyer artificial viscosity Scheme [152]. The constant, C_Q is parameter that spreads shocks over several cells to stabilize the shocks against ringing while generating the appropriate amount of entropy in the system [164]. C_Q is an experimentally determined parameter which we set $C_Q = 3$ in our simulations (See Hawley (1984) [90]). The gravitational potential and therefore the self-gravity of the system is again found from solution of Poisson's equation

$$\nabla^2 \Phi_g = 4\pi G\rho \tag{3.28}$$

The energy equation takes a similar form with the time rate of change of the energy density within a finite volume plus the divergence of the energy flux through that element being equal to any sources or sinks of energy. The energy equation can be written,

$$\frac{\partial \epsilon}{\partial t} + \nabla \cdot \epsilon \mathbf{v} = -P\nabla \cdot \mathbf{v} + \Gamma_Q + \Lambda \tag{3.29}$$

where $\epsilon = \rho e$ and e is the specific internal energy of the gas, and the source term $(-P\nabla \cdot \mathbf{v})$ represents gas compressions. The artificial viscosity contribution to the energy equation is

$$\Gamma_Q = -\rho \left(Q_{\varpi\varpi}\partial_\varpi v_\varpi + Q_{\phi\phi}\frac{1}{\varpi}\partial_\phi v_\phi + Q_{zz}\partial_z v_z \right), \tag{3.30}$$

and Λ is the radiation heating/cooling term which I describe in more detail in the next section.

The hydrodynamics equations are solved within each volume element in the grid where the fluxing and sourcing of each quantity in space and time is handled in such a way as to try and conserve mass, momentum and energy as efficiently as possible. Boley (Thesis) provides a detailed description of how CHYMERA achieves these goals computationally and describes stability tests performed using the finite differencing methods employed [22]. Using an ideal gas equation of state with a constant γ (i.e. the ratio of specific heats $\gamma = C_p/C_v$)

$$P = (\gamma - 1)\epsilon \tag{3.31}$$

allows the energy equation to be recast into the form

$$\frac{\partial \epsilon^{1/\gamma}}{\partial t} + \nabla \cdot \epsilon^{1/\gamma}\mathbf{v} = \nabla \cdot \left(\epsilon^{\mathbf{1}/\gamma}\mathbf{v}\right) + \frac{\epsilon^{\mathbf{1}/\gamma-\mathbf{1}}}{\gamma}\mathbf{\Gamma_Q} + \mathbf{\Lambda} \tag{3.32}$$

This form of the energy equation has been implemented into the code and shown to produced better numerical stability [164]. Rather than using velocities, CHYMERA uses momentum densities to flux quantities in the equation of motion. Therefore, to evolve the fluid flow in space and time the code fluxes and sources the radial momentum density $S = \rho v_\varpi$, the vertical momentum density $T = \rho v_z$ and the angular momentum density $A = \rho v_\phi \varpi$. For each finite element in the system (i.e. grid cell within the 3D discretized space), the array values ρ, ϵ and A are set at the cell center and S and T are set at the centers of cell faces (See Figure 15). It has been shown that solving quantities in a *staggered grid* formalism is more numerically stable than solving all quantities at the centers of cells. In most staggered grid schemes, scalar quantities are set at cell centers and vector quantities are set at cell faces. We can re-write the equation of motion in terms of the momentum densities S, T, and A using

cylindrical coordinates by letting $\rho\mathbf{v} = S\hat{r} + \frac{A}{r}\hat{\phi} + T\hat{z}$. Now consider the divergence term in the equation of motion

$$\nabla \cdot \rho\mathbf{v}\mathbf{v} = \rho\mathbf{v}\nabla \cdot + \mathbf{v} \cdot \nabla\rho\mathbf{v} \tag{3.33}$$

and position vector $\mathbf{r} = r\hat{r} + z\hat{z}$. The radial component of the equation of motion then becomes,

$$\begin{aligned} \nabla \cdot \rho\mathbf{v}\mathbf{v} \cdot \hat{r} &= r^{-1}\partial_r\left(rSv_r\right) + r^{-1}\partial_\phi\left(Sv_\phi\right) + \partial_z\left(Sv_z\right) - r^{-2}v_\phi A & (3.34) \\ &= \nabla \cdot S\mathbf{v} - \frac{A^3}{\rho r^3} & (3.35) \end{aligned}$$

the azimuthal component becomes

$$\begin{aligned} r\nabla \cdot \rho\mathbf{v}\mathbf{v} \cdot \hat{\phi} &= r^{-1}\partial_r\left(rAv_r\right) + r^{-1}\partial_\phi\left(Av_\phi\right) + \partial_z\left(Av_z\right) & (3.36) \\ &= \nabla \cdot A\mathbf{v} & (3.37) \end{aligned}$$

continuing this calculation for the z-component we can find

$$\nabla \cdot \rho\mathbf{v}\mathbf{v} \cdot \hat{z} = \nabla \cdot T\mathbf{v} \tag{3.38}$$

This allows us to write the equation of motion in terms of the divergence of the flux of the momentum in each spatial direction

$$\frac{\partial_T}{\partial_t} + \nabla \cdot T\mathbf{v} = -\rho\frac{\partial_P}{\partial_z} - \rho\frac{\partial_\Phi}{\partial_z} - \frac{\partial_{\rho Q_{zz}}}{\partial_z} \quad (3.39)$$

$$\frac{\partial_A}{\partial_t} + \nabla \cdot A\mathbf{v} = -\rho\frac{\partial_P}{\partial_\phi} - \rho\frac{\partial_\Phi}{\partial_\phi} - \frac{\partial_{\rho Q_{\phi\phi}}}{\partial_\phi} \quad (3.40)$$

$$\frac{\partial_S}{\partial_t} + \nabla \cdot S\mathbf{v} = -\rho\frac{\partial_P}{\partial_r} - \rho\frac{\partial_\Phi}{\partial_r} - \frac{\partial_{\rho Q_{rr}}}{\partial_r} + \frac{A^2}{\rho r^3} \quad (3.41)$$

The CHYMERA code uses a method of operator splitting to evolve the hydrodynamic equations, using two operations called sourcing $\mathcal{S}$ and fluxing $\mathcal{F}$. Looking at the hydrodynamic equations, fluxing handles the right-hand flux terms and sourcing handles the left-hand advection terms. In figure 14 we explicitly show the second order accuracy computation scheme. First, the momentum densities from the previous step, $t_\circ$, are used by the source routine to calculate provisional ϵ, S, T, and A values at a half step $t_{1/2} = t_\circ + 1/2\Delta t$ (See Williams and Tohline 1987 [212],1988 [213]), where Δt is the size of the computational time step. There are no source terms for the density. Next, the new quantities with the source terms plus the original density are used to calculate velocities in all three directions at the half step. Using these velocities, the previous output of the source routine and the density are fluxed again by one full time step, thus giving the flux terms and the density for the next step, t_1. The gravitational potential and the pressure are now updated by the Poisson solver and the equation of state routines. Finally, another half step source is needed to calculate the source terms at one full step, followed by an update of the pressure by the equation of state routine. The time step size is determined by the Courant condition [164], which forces Δt to be equal to the shortest cell-crossing or sound-crossing time of a fluid element in the grid. The 3-D hydrodynamics code also assumes mirror symmetry across the equatorial plane, so the equatorial plane of the

disk is situated along the lowest z zone. Boundary conditions on the axis consist of velocities and density gradient set to zero.

Non-Linear Cooling

It is well known that thermodynamics strongly changes the outcome of a simulation [155], [166], [167], [133], [171], [141], [21], [23], [67], [145], [183]. The amplitude of the instability which gives a quantitative measure of the strength of influence that the instability has on the disk is regulated by the active heating and cooling processes in the system. A gravitationally unstable disk without sources of heating will cool until it loses pressure support and becomes unstable. Gravitationally unstable disks eject spiral arms and heat the disk through shocks as these spiral disturbances interact with lower density fluid. Thus there is a feedback loop between these two processes. Gammie (2001) derived a cooling criteria for 2D thin disks which states that if the timescale for the local internal energy to dissipate is more or less equivalent to the local orbital timescale, clump production will follow [71]. Cooling on the order of a dynamical timescale causes the disk to fragment before it can react to the gravitational stabilities and heat up. Given the importance of cooling to disk evolution, we include cooling using a parameterized cooling function Λ for which the local cooling timescale τ_c is constant and the same across the disk. We use this Λ to assess quantitatively the effects cooling has on our star-disk system.

For this current study, our cooling function Λ has the form,

$$\Lambda = \left(\frac{\epsilon}{\tau_c} \right) \tag{3.42}$$

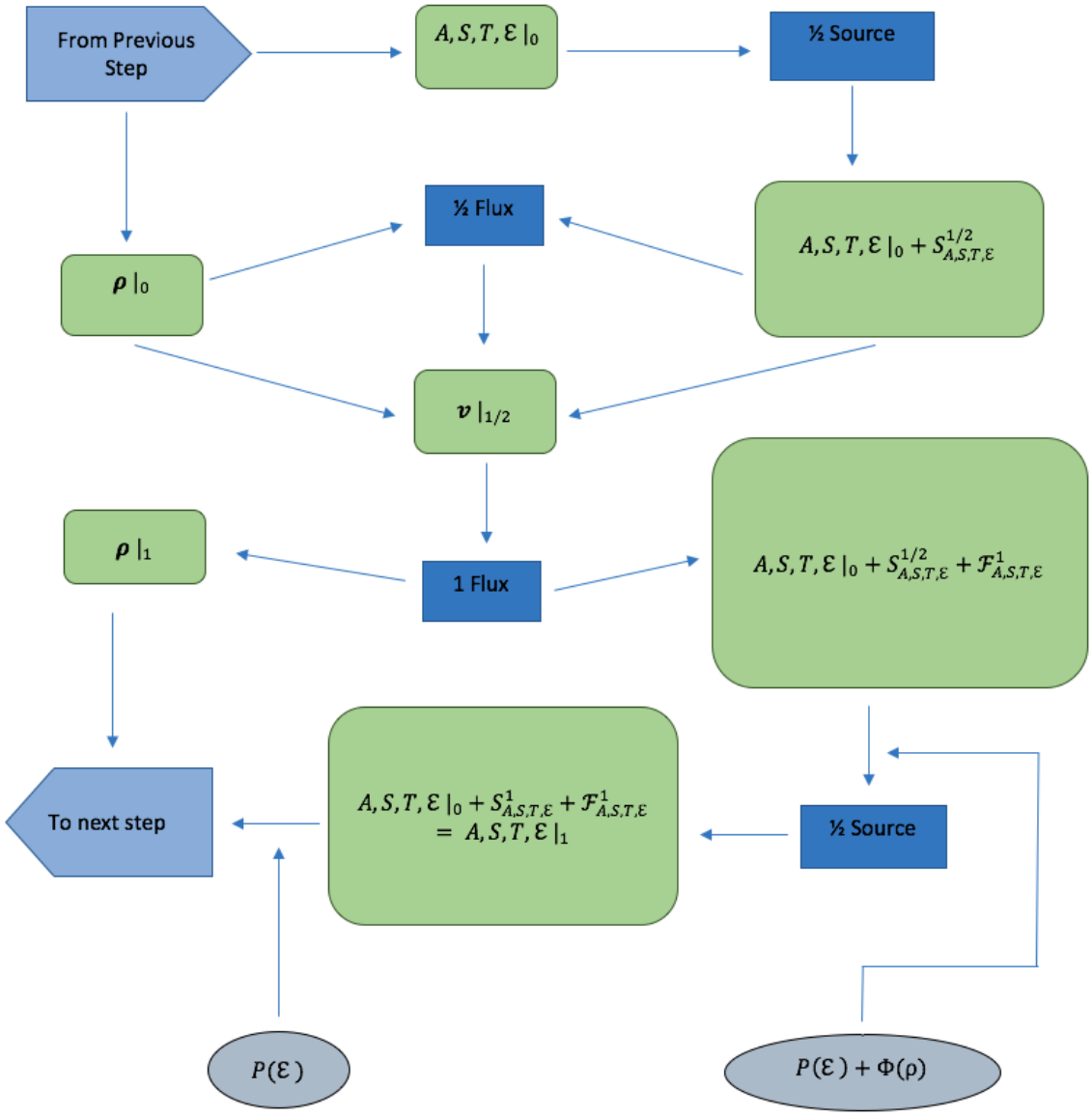

FIGURE 14. A flow chart which illustrates the method of operator splitting showing the second-order time integration scheme for the CHYMERA code. This chart was reproduced from Boley (2007).

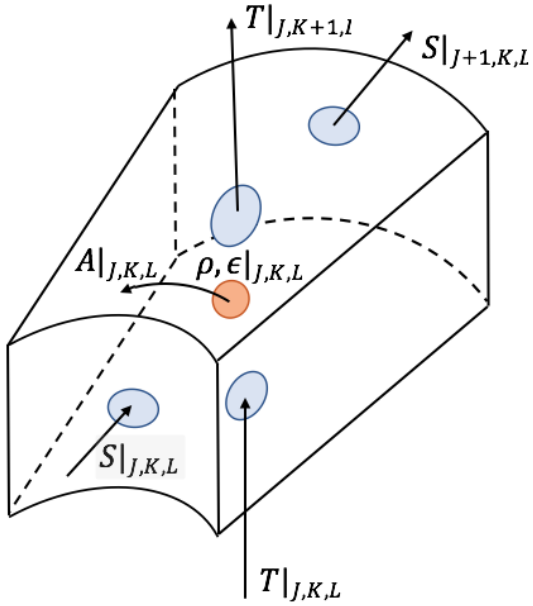

FIGURE 15. Location of the values for the five principle hydrodynamic arrays. The indexing for the cylindrical grid $(r, \phi, z) = (J, L, K)$ is illustrated. This chart was reproduced from Boley 2007.

where $\tau_c = C_\Lambda \tau_\circ$, and C_Λ is a constant. We define weak cooling to be cases where $\tau_c \gg \tau_\circ$ where the energy dissipation is much less than the characteristic timescale of the system. A moderate cooling rate is defined as $\tau_c \approx 5\tau_\circ$ and fast cooling $\tau_c \approx 1\ \tau_\circ$ where energy dissipation in the system is on order with the dynamical timescale of the system.

Quasi-linear Torques

The transition from the linear regime to the nonlinear regime can be modeled using quasi-linear (QL) theory in which torques are found from substitution of

$$\rho = \rho_\circ + \delta\rho e^{im\phi}, \tag{3.43}$$

$$\mathbf{v} = \mathbf{v}_\circ + \delta\mathbf{v} e^{im\phi}, \tag{3.44}$$

and

$$\Phi = \Phi_\circ + \delta\Phi e^{im\phi} \tag{3.45}$$

into the torque density equation $\mathbf{N} = \mathbf{r} \times \mathbf{f}$. Here $\mathbf{N}$ is the torque density, $\mathbf{r}$ is the position vector, and $\mathbf{f}$ is the force density (See Hadley *et al.* 2014 [83], 2015 [84]). The gravitational torque on the annulus between ϖ and $(\varpi + \Delta\varpi)$ is given by

$$\Gamma_{g,m}(\varpi) = \pi m \int_{\varpi}^{\varpi+\Delta\varpi} \int_0^{Z_\varpi} |\delta\rho_m||\delta\Phi_m| \sin\varphi \, \varpi \mathrm{d}\varpi \mathrm{d}z \tag{3.46}$$

where $\delta\rho_m$ and $\delta\Phi_m$ are the m-th Fourier components of the perturbed density and gravitational potential, respectively, $\varphi = \phi_{\rho,m} - \phi_{\Phi,m}$, and $\phi_{\rho,m}$ and $\phi_{\Phi,m}$ are the phases of the density and gravitational perturbations, respectively.

We calculate the star-disk gravitational torques, $\gamma_{*d,m} = \sum_j \Gamma_{*d,m}(\varpi_j)$ where ϖ_j is the coordinate of the *j-th* radial cell and the sum is taken over the disk. The Reynolds stress torque on the annulus between ϖ and $(\varpi + \Delta\varpi)$ is given by

$$\Gamma_{R,m}(\varpi) = -\mathcal{F}_m(\varpi + \Delta\varpi) + \mathcal{F}_m(\varpi), \tag{3.47}$$

where

$$\mathcal{F}_m(\varpi) = 2\pi m \int_0^{Z_\varpi} \rho_\circ |\delta v_{\varpi,m}||\delta v_{\phi,m}| \cos\varphi \, \varpi^2 \mathrm{d}z, \tag{3.48}$$

$\delta v_\varpi, m$ and $\delta v_\phi, m$ are the m-th Fourier components of the perturbed velocity components, $\varphi = \phi_{v_\varpi,m} - \phi_{v_\phi,m}$, and $\phi_{v_\varpi,m}$ and $\phi_{v_\phi,m}$ are the phases of the velocity perturbations. The $\Gamma_{g,m}(\varpi)$ and $\Gamma_{R,m}(\varpi)$, Equations [3.46] and [3.47], scale with the square of the amplitude of the perturbed mode $\mathcal{M}_m^2$, where

$$\mathcal{M}_m = \int |\delta\rho| \mathrm{d}^3\mathrm{x}. \tag{3.49}$$

Unless stated otherwise, QL torques are presented for $\mathcal{M}_m = 1$.

Analysis Methods

In this section we introduce variables and equations used to analyze the linear and nonlinear model results. The measure of the perturbed mass given by Equation (33) is different from that used in our nonlinear simulations where the Fourier coefficients for the density distribution, $\mathcal{A}_m$, are defined as $\mathcal{A}_m = \sqrt{a^2 + b^2}$ where

$$a = \int \rho(\mathbf{r}) \cos(m\phi) \mathrm{d}^3\mathrm{x} \;\text{ and }\; b = \int \rho(\mathbf{r}) \sin(m\phi) \mathrm{d}^3\mathrm{x} \tag{3.50}$$

(See Pickett, Durisen, & Davis (1996) [165]). The relationship between $\mathcal{M}_m$ and $\mathcal{A}_m$, is calculated for each disk and m under consideration.

To analyze the β dependence in the star and disk, β parameters are defined for the star and disk,

$$\beta_* = \frac{0.5 \int_* \rho_*(\mathbf{r}) \left[\Omega(\varpi)\varpi\right]^2 \mathrm{d}^3\mathrm{x}}{\left| \int_* \rho_*(\mathbf{r}) \left[0.5\Phi_*(\mathbf{r}) + \Phi_d(\mathbf{r})\right] \mathrm{d}^3\mathrm{x} \right|} \tag{3.51}$$

and

$$\beta_d = \frac{0.5 \int_d \rho_d(\mathbf{r}) \left[\Omega(\varpi)\varpi\right]^2 \mathrm{d}^3\mathrm{x}}{\left| \int_d \rho_d(\mathbf{r}) \left[\Phi_*(\mathbf{r}) + 0.5\Phi_d(\mathbf{r})\right] \mathrm{d}^3\mathrm{x} \right|}, \tag{3.52}$$

respectively.

To compare with point mass models, the gravitational multipole fields for the equilibrium stars are calculated using,

$$\Phi_l(\mathbf{r}) = -\frac{G}{r}\int \rho(\mathbf{r}')\left(\frac{r'}{r}\right)^l \mathrm{P}_l(\theta')\mathrm{d}^3\mathrm{x}', \tag{3.53}$$

In $\Phi_l(\mathbf{r})$, r is the radial coordinate, θ is the polar angle, and $\mathrm{P}_l(\theta)$ is the Legendre polynomial of order l. The multipole fields are given compared to the monopole field, Φ_l/Φ_0, with the ratio evaluated at $(r, z) = (r_e, 0)$. The magnitudes of the quadrupole potentials are all < 6 % that of the monopole field at $(r_e, 0)$.

J_{rot}, the angular momentum of the star in the star's center-of-mass frame, is found from

$$J_{rot} = \hat{z} \cdot \int (\mathbf{r} - \mathbf{r}_{cm}) \times \rho(\varpi)(\mathbf{v} - \mathbf{v}_{cm})\mathrm{d}^3\mathrm{x} \tag{3.54}$$

where the center-of-mass of the star, $\mathbf{r}_{cm}$, and the center-of-mass velocity, $\mathbf{v}_{cm}$ are

$$\mathbf{r}_{cm} = \frac{\int \rho(\mathbf{r}')\mathbf{r}'\mathrm{d}^3\mathrm{x}'}{M_*}, \text{ and } \mathbf{v}_{cm} = \frac{\int \rho(\mathbf{r}')\mathbf{v}(\mathbf{r}')\mathrm{d}^3\mathrm{x}'}{M_*}, \tag{3.55}$$

with the integrals taken over the star.

The z-component of the orbital angular momentum of the star, J_{orb}, is the z-component of $\mathbf{r}_{cm} \times M_* \mathbf{v}_{cm}$. Using J_{orb} we define the *orbital* star-disk couple $\gamma_{cm} = 2\langle J_{orb}\rangle/\tau_1$ where the average is taken over an oscillation cycle.

Polytropic Units

Results of our calculations are presented in polytropic units. To convert to other dimensional systems, use

$$r_{dim} = r_{pu}\left(\frac{K_{dim,*}}{G}\mathrm{M}_\circ^{-1/3}\right) \tag{3.56}$$

$$\rho_{dim} = \rho_{pu}\left(\frac{G}{K_{dim,*}}\right)^3 \mathrm{M}_\circ^2 \tag{3.57}$$

$$\Omega_{dim} = \Omega_{pu}(\frac{G}{K_{dim,*}})^{3/2}\sqrt{G}\mathrm{M}_\circ \tag{3.58}$$

for given total system mass $\mathrm{M}_\circ$ and stellar polytropic constant $K_{dim,*}$ (See Williams & Tohline (1987) [211]). In the above, r_{dim}, ρ_{dim}, and Ω_{dim} are dimensional quantites and r_{pu}, ρ_{pu}, and Ω_{pu} are quantities in polytropic units.

Alternatively, we can recast the relationships in terms of $M_\circ$ and the radius of the location of the maximum density in the disk midplane $R_\circ$,

$$K_{dim,*} = K_* R_\circ G M_\circ^{1/3} \tag{3.59}$$

$$\rho_{dim} = \rho_{pu}\frac{M_\circ}{R_\circ^3} \tag{3.60}$$

$$\Omega_{dim} = \Omega_{pu} G^{7/2} R_\circ^{3/2} M_\circ^{3/2} \tag{3.61}$$

where $K_{dim,*}$ is now an output. Other quantities may be expressed as above, *e.g.*, dimensional angular momenta are $J_{dim} = M_\circ \Omega_{dim} r_{dim}^2$ and dimensional pressures are

$$P_{dim,*} = K_{dim,*}\rho_{dim}^\gamma \tag{3.62}$$

$$P_{dim,d} = K_d K_{dim,*}\rho_{dim}^\gamma \tag{3.63}$$

for the star and disk, respectively.

Unit Conversions

For the readers ease, we have calculated conversion factors to tranform quantities reported in polytrope units to *cgs* units in Table 1. Here, we assume a value for the initial total mass $M_\circ$ and a characteristic radius $R_\circ$ for several different "typical" systems. Recall that what constitues a "typical" system is not well defined. Many researchers have attempted to calculate the minimum mass protoplanetary disk from which the star Sol and all the planets in the Solar system were born from. This initial disk is referred to as the minimum mass solar nebula (MMSN).

The most famous version of the MMSN was provided by Weidenschilling (1977) [207] and Hayashi (1981) [91].

They assumed that the planets accreted all material in the initial disk and that the planets formed where they presently orbit. However, there is strong evidence that Jupiter and the other gas giants may have migrated from a position much further from the Sun than their present locations. There is also strong evidence that mass may be ejected from the system by stellar outflows or strong stellar winds, or by shockwaves in the protoplanetary disk. In addition, from current extra-solar planetary data (See *Literature Review*), the Sol system is not a typical planetary system, nor is it a binary star system, whose formation mechanisms are the focus of this current study. Therefore, from a theoretical standpoint, non-dimensional units are a more natural system to use.

In Table 1, we present coversions for four different choices of $M_\circ$ and $R_\circ$ to give the reader an idea of how our modeled system *may* compare to other known systems. The first row corresponds to choosing $M_0 = 1.989 \times 10^{33}$ g $= M_{sun}$ the value of one solar mass in grams and $R_0 = 1.494 \times 10^{14}$ cm $= 10$ AU, roughly the location of saturn in the solar system. The second row corresponds to choosing $M_0 = 1.989 \times 10^{34}$ g

$= 10M_{sun}$ the value of ten solar masses and $R_0 = 4.488 \times 10^{14}$ cm $= 30$ AU, roughly the location of Neptune.

In rows $3-4$ of table 1, we report conversion factors informed from data, using estimated values of M_0 and R_0 for the binary planetary system GGTau-A and the young proto-binary system Bernard 59 [BHB2007] 11, respectively. Only several multiple star systems have been observed in the process of formation. A circumbinary disk surrounds the young $1-5$ Myr low-mass triple stellar system GGTau-A which is located 140 pc away in the Taurus molecular cloud. The estimated values of M_0 and R_0 used for the GGtau system were reported in [88] and [210]. The main binary GGTau-A (Aa-Ab) and the close-binary GGTau-Ab (Ab1-Ab2) have an apparent separation of 35 AU and 4.5 AU, respectively [46]. The outer disc mass is 0.15 M_{sun} and GGTau-Aa and Ab each have a mass of about 0.65 M_{sun} [210]. The outer circumbinary Keplerian disc of gas and dust surrounding GGTau-A consists of a ring extending from radius r 190 to 280 AU and an outer disc extending up to 800 AU from the central stars with a total mass 0.15 M_{sun} [56]. Approximating the initial mass of the system to be 1.5 solar masses and the characteristic radius to be near the location of the inner disk, we choose $M_0 = 1.6M_{sun} = 3.1824 \times 10^{33}$ g and $R_0 = 280$ AU $= 4.189 \times 10^5$ cm.

Bernard 59 [BHB2007] 11, a young binary protostar system, is the youngest (0.1-0.2 Myr) member of the small cluster of young stellar objects in the Barnard 59 molecular core which is part of the greater Pipe Nebula molecular cloud. It is still growing mass through dust and gas accretion. It is classified as a class 0/I young stellar object (YSO). Previous observations of this object show an envelope surrounding a circumbinary disk of radius 90 AU, with prominent bipolar outflows launched near the disk edge [5]. The Bernard 59 proto-binary

Table 1. Unit Conversions from Polytropic Units to cgs units

M_0 (g)	R_0 (cm)	ρ (g/cm^3)	v (cm/s)	τ_0 (s)	K_*
1.989e33	1.494e14	5.94073e-10	941887.03	158830090.41	1.255369e18
1.989e34	4.488e14	2.20027e-10	1719642.62	260984453.31	8.113829e18
3.1824e33	4.189e15	4.32935e-14	225148.69	18605481976.69	4.11140e19
2.9835e33	1.346e15	1.2234e-12	384580.90	3499913548.80	1.2929e19

system was observed at 225.3 GHz (wavelength 1.3 mm) with the Atacama Large Millimeter/submillimeter Array. Dust maps reveal two compact sources that are interpreted as circumstellar disks around both components of the proto-binary system. The two stellar components have a projected separation of $\approx$ 28 AU. From the continuum emission, the masses of the circumstellar disks are estimated to be within an order of magnitude of a Jupiter mass M_{Jup}, with the [BHB2007] $11A$ disk slightly more massive than the [BHB2007] $11B$ disk. The larger circumbinary disk has a total estimated mass of $M_d = 0.08 \pm 0.03 M_{sun}$. Because this value represents $\approx$ 260 earth masses of dust, Alves *et al* (2019) speculate that the circumstellar disks may later form rocky terrestrial planets. Approximating the initial mass of the system to be on the order of 1.5 solar masses and the initial density maximum to be the location of the circumbinary disk [BHB2007] 11, we choose $M_0 = 1.5 M_{sun} = 2.9835 \times 10^{33}$ g and $R_0 = 90 AU = 1.346 \times 10^{15}$ cm and report conversion factors using these values in Table 1, column 4.

CHAPTER IV

RESULTS

This chapter is devoted to reporting the results of my research and how these results pertain to my initial research questions: Can the fission hypothesis produce short-period binary stars, and what initial conditions lead to the formation of binary stars and circumbinary planets? To motivate the results of this investigation I first present related results from previous linear stability analyses of star-disk systems where we considered the central star to be a pointmass object. This previous work serves as a foundation for understanding nonaxisymmetric instabilities in protostellar disks and for informing how and why I chose the particular initial conditions for the Fission Model.

Previous Studies and Results of Nonaxisymmetric Instabilities in Protostellar Disks surrounding Pointmass Stars

An extensive library of equilibrium disk models was compiled covering the parameter space occupied by typical protostellar and protoplanetary disks [83]. Disk models were grouped into families defined by n and q, where family members were parameterized by r_-/r_+, the ratio of the inner and outer radii of the disk, and M_*/M_d, the ratio of the star to disk mass. We modeled $q = 1.5$, 1.75 and 2 disks for $r_-/r_+ = 0.05$ to 0.75, and $M_*/M_d = 0$ to 10^3. Density contours in meridional slices for representative equilibrium models are shown in Figure 16 to qualitatively illustrate the effects of varying M_*/M_d, q and r_-/r_+. Large star masses, small inner radii and shallow rotation curves all have the effect of flattening the disk. Small stellar masses, large inner radii and steep rotation curves have the opposite effect leading to values

of $h/r \approx 1$ where h is the disk thickness at radius r. The latter is where we expect thin-disk approximations to break down.

We investigated disk stability based on local and global macroscopic properties of the equilibrium disks. Some examples of parameters used in our previous investigations include the well-known Toomre Q parameter which indicates local instability in thin disks if Q falls below unity, where

$$Q = \frac{c_s \kappa}{\pi \mathrm{G} \Sigma}, \tag{4.1}$$

and c_s is the local sound speed, and κ is the epicyclic frequency,

$$\kappa^2 = (4 - 2q)\Omega^2 \tag{4.2}$$

for power law rotation [197]. For a Keplerian disk, $\kappa = \Omega$. The epicyclic frequency is the frequency at which a radially displaced parcel of fluid will oscillate and can be used to determine the stability properties of the orbital motion at a particular radius. If κ becomes negative, this indicates that small perturbations to the original symmetric, circular orbit will grow and become unstable. For nonaxisymmetric instability, a corresponding necessary and sufficient condition does not exist but it has been suggested that systems which have $Q \lesssim 1.5 - 1.7$ anywhere in the disk are unstable to nonaxisymmetric instability [54].

For $q = 2$, Q = 0 identically due to the fact that the epicyclic frequency goes to zero for this value of q. For $q = 1.5$, disks with small M_*/M_d show large regions where $Q < 1.5 - 1.7$ while for large M_*/M_d, $q = 1.5$ disks show $Q > 1.5 - 1.7$ everywhere. An additional effect of Q arises in regions where $Q < 1$. In such regions, traveling waves damp. For $q \approx 2$, the disk has $Q \approx 0$ because $\kappa^2 \approx 0$. Qualitatively similar

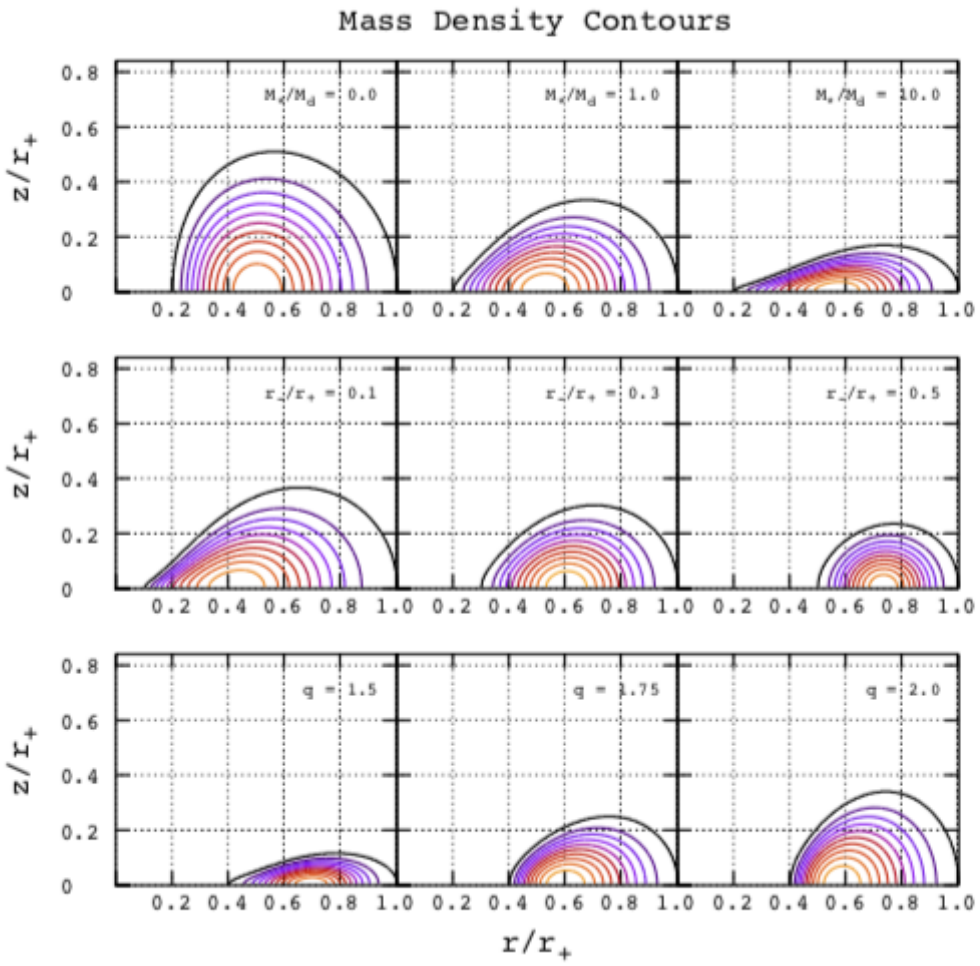

FIGURE 16. Top row: Mass density contours for models of varying values of M_*/M_d with $q = 1.5$ and $r_-/r_+ = 0.20$. Contours trace ten divisions between the arbitrary low density of 10^{-30} and the max density. Middle row: Contours for models with $q = 1.5$ and $M_*/M_d = 1$, sweeping r_-/r_+. Bottom row: Contours for models with $M_*/M_d = 25$ and $r_-/r_+ = .4$, sweeping q.

behavior between $q = 1.5$ and 1.75 is seen. The region where $Q < 1$ begins wide, decreases in width monotonically with increasing M_*/M_d and finally disappears. On grounds of the Q-parameter, disks near $q = 2$ are likely to be much more unstable than $q = 1.5$ and 1.75 disks. For $q = 1.5$ and 1.75, systems with large M_*/M_d are likely to be stable based on Q.

Another parameter commonly used in the analysis of equilibrium disks is the ratio of the rotational kinetic energy to the absolute value of the gravitational potential energy, $T/|W|$. $T/|W|$ is particularly useful in the analysis of gravito-rotation driven nonaxisymmetric modes in star-like objects. $q = 1.5$ disks, Kepler-like disks, show higher values of $T/|W|$ for large M_*/M_d than do $q = 2$ disks. $T/|W| \to 0.5$ for the largest M_*/M_d and r_-/r_+ for all q and varying q and r_-/r_+ has little effect on $T/|W|$ for large M_*/M_d. $T/|W|$ also varies differently across parameter space for different q making it less useful as a universal stability indicator for star/disk systems than has been found for toroids and *spheroidal* objects [81], [187].

Two local measures of the importance of self-gravity,

$$p^2 = \frac{4\pi \mathrm{G}\rho_\circ}{\Omega_\circ^2}, \tag{4.3}$$

and

$$\eta = \frac{\Omega_k^2}{\Omega_\circ^2} \tag{4.4}$$

are useful indicators of stability in thin-disks [36], [6]. Andalib, Tohline, & Christodoulou (1997) present a survey of the principle modes of instability, the so-called P, I and J modes, for *slender incompressible torus with constant specific angular momentum*. Their survey was a natural extension of the work done by Goodman and Narayan (1988) [75]. Here, Ω_k is the Keplerian angular velocity given by Ω_k

$= \sqrt{GM_*/r_\circ^3}$. Although p and η show different behavior and also vary with q, individually, each may be a useful indicator for the stability properties of thick, self-gravitating disk systems.

A foundation is presented for the understanding of nonaxisymmetric disk modes, beginning with the linearized evolution equations. This is followed by detailed descriptions of the character of the several types of modes observed (J, E/P, I, m=1) in thick self-gravitating disk systems, followed by laying out, in $(r_-/r_+, M_*/M_d)$ space for given q, the eigenvalues and character of the dominant m-modes.

Pointmass Linearized Evolution

Linearly unstable modes for thick, self-gravitating disk systems surrounding pointmass stars are found from solution of an Initial Value Problem (IVP) formulated from the hydrodynamics equations evaluated using Eulerian perturbations of the form,

$$A = A_\circ + \delta A(\varpi, z, t)e^{im\phi}, \tag{4.5}$$

where $A_\circ$ is the equilibrium solution and δA is the perturbed amplitude in the meridional plane. For all complex perturbed quantities, the physical solution corresponds to the real part.

From the perturbations and the hydrodynamic equations, a set of linearized evolution equations is formed as presented in Chapter III of this present work [83]. The equilibrium and perturbed gravitational potentials Φ_g and $\delta\Phi_g$ are found by solving the Poisson equation

$$\nabla^2\Phi_d = 4\pi \mathrm{G}\rho. \tag{4.6}$$

We superimpose the star's point-like contribution

$$\Phi_* = -\frac{\mathrm{G}M_*}{|\mathbf{r} - \mathbf{r}_*|}, \tag{4.7}$$

where $\mathbf{r}$ is the field point and $\mathbf{r}_*$ is the position of the star, with the perturbed disk self-gravity potential found by solving the Poisson equation as

$$\nabla^2(\delta\Phi_g e^{im\phi}) = 4\pi\mathrm{G}\delta\rho e^{im\phi} \tag{4.8}$$

for the azimuthal mode m under consideration.

The star follows a spiral trajectory giving rise to an increasing *indirect potential*,

$$\delta\Phi* = -\frac{\mathrm{GM}_*}{r}\left(\frac{\delta_* \cdot \mathbf{r}}{r^2}\right) \tag{4.9}$$

where δ_* is the perturbed location of the star. $\delta\Phi_*$ is included in the evolution equations in addition to the disk potential. We find δ_* from solution of the linear evolution equation for the perturbed position of the star,

$$\partial_{tt}\delta_* = \pi\mathrm{G}(\hat{\mathbf{x}} + \mathbf{i}\hat{\mathbf{y}})\int \frac{\delta\rho}{r^3}\varpi^2 \mathrm{d}\varpi\mathrm{dz} + \pi\mathrm{G}\delta_* \int \frac{\rho_\circ}{r^3}\left(3(\frac{\varpi^2}{r^2}) - 2\right)\varpi^2\mathrm{d}\varpi\mathrm{dz}, \tag{4.10}$$

simultaneously with the linearized evolution equations. The Cartesian coordinates of the star are related as $\delta_{*,y} = i\delta_{*,x}$ so that the perturbed stellar potential is

$$\delta\Phi_* = -\frac{\mathrm{GM}_*}{r}\left(\frac{\delta^R_{*,x} + i\delta^I_{*,x}}{r^2}\right)\varpi e^{i\phi} \tag{4.11}$$

where $\delta^R_{*,x}$ and $\delta^I_{*,x}$ are the real and imaginary parts of the perturbed $\hat{x}$ component of the stellar position.

Equilibrium values for ρ and $\mathbf{v}$ are used as the background for solution of the IVP equations. The IVP is evolved on the same grid as the equilibrium models. Spatial derivatives are given in finite difference form and time derivatives left continuous. The perturbed solutions are advanced in time using a fourth order Runge-Kutta method. The numerical code is described in detail in [81]. We usually used grid sizes of $n_{\varpi} \times n_z = 512 \times 512$ although for disks with large r_-/r_+ and $q = 1.5$, we sometimes used grids of size 1024×1024. Boundary conditions consist of mirror symmetry about the equatorial plane. Perturbed velocities are set to zero on the surface of the disk while the mass density perturbation is unconstrained. The gravitational potential is set at the outermost grid boundaries through solution of the integral form of the Poisson equation.

The evolution of the perturbed disk was followed by monitoring $|\delta\rho|/\rho_\circ$ at three points in the disk midplane to ensure that instability is global in nature. A model is deemed dynamically stable if it shows no global growth after 30 - 40 $\tau_\circ$ where $\tau_\circ$ is the rotation period at the radius of the density maximum. We monitor growth until time dependence has settled into stable exponential behavior,

$$f(t) = f_0 e^{-i\omega_m t} \tag{4.12}$$

for any perturbed quantity f. We choose these and other sign conventions to be consistent with previous workers in the field (*e.g.,* see Kojima (1986) [118]). Growth rates and oscillation frequencies are determined from least squares fits to the logarithm of the amplitude and the phase, respectively. For our definition, the real part of ω refers to the frequency of the perturbation while the imaginary part refers to the growth rate. Prograde modes have $\mathcal{R}(\omega) < 0$. For our choice of the form for the

azimuthal eigenfunction, normalized eigenvalues are defined as

$$y_1(m) = -\left(\frac{\mathcal{R}(\omega_m)}{\Omega_\circ} + m\right) \text{ and } y_2(m) = \frac{\mathcal{I}(\omega_m)}{\Omega_\circ}. \tag{4.13}$$

Here $\mathcal{R}$(z) and $\mathcal{I}$(z) take the real and imaginary parts of complex functions z = f+ig where f and g are real functions.

The corotation radius, r_{co}, is where the pattern frequency of the mode equals the orbital frequency of the fluid. The $y_1(m)$ are defined so that if $y_1(m) < 0$, $r_{co} > r_\circ$ and if $y_1(m) > 0$, $r_{co} < r_\circ$. For power-law Ω, r_{co} is given by:

$$\frac{r_{co}}{r_\circ} = \left(\frac{y_1(m)}{m} + 1\right)^{1/q} \tag{4.14}$$

The inner and outer Lindblad resonances r_{ilr} and r_{olr}, are located where the real part of ω_m equals $\pm\kappa$. For power-law Ω, r_{ilr} and r_{olr} are related to r_{co} by:

$$\frac{r_{lr}}{r_{co}} = \left(1 \pm \frac{\sqrt{4-2q}}{m}\right)^{1/q} \tag{4.15}$$

The vortensity is defined as

$$\mathbf{\Lambda} = \frac{\nabla \times \mathbf{v}}{\Sigma} \tag{4.16}$$

where Σ is the column density. For axial disks that rotate on cylinders with power law angular velocity, the only nonzero component of $\mathbf{\Lambda}$ is

$$\Lambda_z = (2-q)\left(\frac{\Omega}{\Sigma}\right). \tag{4.17}$$

Vortensity modes arise when corotation falls at extrema in Λ_z [156].

For analysis purposes, we calculate the work done locally by the perturbed kinetic energy, and the perturbed enthalpy which also accounts for the perturbation in the acoustic energy [119]. The perturbed kinetic energy and acoustic energy are designated as E_k and E_h, respectively and, for a polytrope, are given by:

$$\mathrm{E}_k = \frac{1}{2}\rho\langle\delta v_\varpi^2 + \delta v_\phi^2 + \delta v_z^2\rangle \tag{4.18}$$

$$\mathrm{E}_h = \frac{1}{2}\gamma\frac{P}{\rho^2}\langle\delta\rho^2\rangle \tag{4.19}$$

Here, the brackets represent time-averaged perturbed quantities. The total energy of the mode is the sum of the two. The time rate of change of the perturbed energy may be broken down into the time rate of change of the stresses:

$$\partial_t\sigma_R = -\rho_\circ\varpi\partial_\varpi(\delta v_\phi\delta v_\varpi) \tag{4.20}$$

$$\partial_t\sigma_G = -\rho_\circ(\delta\mathbf{v}\cdot\nabla)(\delta\Phi_d + \delta\Phi_*) \tag{4.21}$$

$$\partial_t\sigma_h = -\nabla\cdot(\delta P\delta v) \tag{4.22}$$

where σ_R is the Reynolds stress, σ_G is the gravitational stress, and σ_h is the acoustic stress.

Classification of Nonaxisymmetric Disk Modes

Modes are identified from their morphological and dynamical properties. We use characteristics including the winding of their arms, the regions in the disk where

they have the largest amplitude, locations of corotation and vortensity extrema, and the self-gravity parameter p to classify modes. We have also examined the ratio of gravitational and Reynolds stress rates integrated over the disk,

$$\mathcal{R} = \frac{\int \partial_t \sigma_G \mathrm{d}^3 x}{\int \partial_t \sigma_R \mathrm{d}^3 x} \tag{4.23}$$

and found that it tracks mode type almost exactly as p does for $m \geq 2$. While this is useful in suggesting that the importance of self-gravity to the perturbation and equilibrium track each other, we find it does not reveal much about the modes that other parameters (like p, y_1 and y_2) do not.

No one characteristic is sufficient or necessary to define a particular mode type. In the following subsections we present representative models that characterize each mode type in an effort to provide a predictive classification based on the initial equilibrium parameters for the linear evolution. The reader may find it helpful to reference this section to understand which azimuthal mode number dominates respective modes (J, E/P, I) discussed.

J Modes

J modes, the Jeans-like modes, are driven by self-gravity. They dominate systems with narrow, $r_-/r_+ > 0.30$, and high mass disks, $M_*/M_d < 0.2$, where the self-gravity parameter $p \gtrsim 7.5$. For given M_*/M_d, J modes with successively higher m dominate as r_-/r_+ increases. In the limiting case, one can imagine an extremely narrow tube fragmenting with azimuthal wavelength comparable to its thickness.

The properties of typical J modes are illustrated in Figure 17 and Table 2. We show constant phase loci for $\delta\rho/\rho_\circ$ and $\mathcal{W}$, amplitudes of $\delta\rho/\rho_\circ$, work integrals, and

Table 2. Representative J Modes

	r_-/r_+	$r_+/r_\circ$	$r_\circ$	$\tau_\circ$	J	m	y_1, y_2	$r_{ilr}/r_\circ, r_{olr}/r_\circ$	$r_{co}/r_\circ$
J1	0.402	1.51	6.47	187	1.43	2	-0.344,0.110	0.714,1.49	1.13
J2a	0.600	1.27	14.8	560	2.49	2	0.0297,0.840	$\cdots$,1.30	0.990
J2b	”	”	”	”	”	3	-0.0271,1.57	0.768,1.22	1.01
J2c	”	”	”	”	”	4	-0.0844,1.85	0.837,1.18	1.01

Note. — Examples of J modes and their properties, giving (left to right) the radial aspect ratio of the disk, the disk outer radius, radius of density max, characteristic rotation time at density maximum τ_0 in polytrope units, total angular momentum, azimuthal mode number m, oscillation frequencies and growth rates of perturbed density, the radii of the inner and outer Lindblad resonances and the corotation radius.

stress rates in the disk midplane for $q = 1.5$ disks with $M_*/M_d = 0.01$ and large r_-/r_+. Here

$$\mathcal{W} = \gamma \frac{P_\circ}{\rho_\circ^2} \delta\rho + \delta\Phi \tag{4.24}$$

is an alternative eigenfunction formed from the sum of the perturbed enthalpy and gravitational potential [157]. $\mathcal{W}$ is a more natural eigenfunction for disks than is $\delta\rho$ [81]. Here, this can be seen in the location of corotation which more closely tracks minima in $\mathcal{W}$ than minima in $\delta\rho$. This result is consistent with the suggestion that the corotation singularity at threshold is removed by $\mathcal{W} = 0$ rather than by $\delta\rho = 0$. This behavior is also clear for the $m \geq 2$ I and J modes.

J modes do not show large variation in their properties. The $\delta\rho/\rho_\circ$ eigenfunctions are barlike for $r < r_\circ$, and show trailing spiral arms that extend for $\sim \pi/m$ radians for $r > r_\circ$. The arms shown by $\mathcal{W}$ lead those of $\delta\rho$ indicating that the gravitational perturbation leads the enthalpy perturbation. The work integrals for the $m = 2$

modes show two distinct peaks in E_h, the first peak larger than the second. E_k has one peak which is much lower in amplitude than the E_h peaks, near the center of the disk for large r_-/r_+ models and skewed toward the inner edge for models with small r_-/r_+. For the $m = 3$ mode, the minimum between the peaks does not go to zero, and the $m = 4$ mode has only one peak each for E_k and E_h, with the E_k at higher amplitude. As for the stress rates, $\partial_t \sigma_h$ dominates near the inner edge with higher amplitude for the $r_-/r_+ = 0.40$ model than for the $r_-/r_+ = 0.60$ model. In the central part of the disk, $\partial_t \sigma_G$ is positive while $\partial_t \sigma_h$ is negative. For the $m = 2$ mode, the amplitudes of $\partial_t \sigma_G$ and $\partial_t \sigma_h$ are roughly comparable, while for the $m = 2$ mode, the amplitude of $\partial_t \sigma_G$ is higher than that of $\partial_t \sigma_h$. $\partial_t \sigma_R$ is positive, but significantly lower in amplitude than either $\partial_t \sigma_G$ or $\partial_t \sigma_h$, and is skewed toward the inner edge in the $r_-/r_+ = 0.60$ model. The stress rates for the $m = 2$, 3 and 4 are similar to each other.

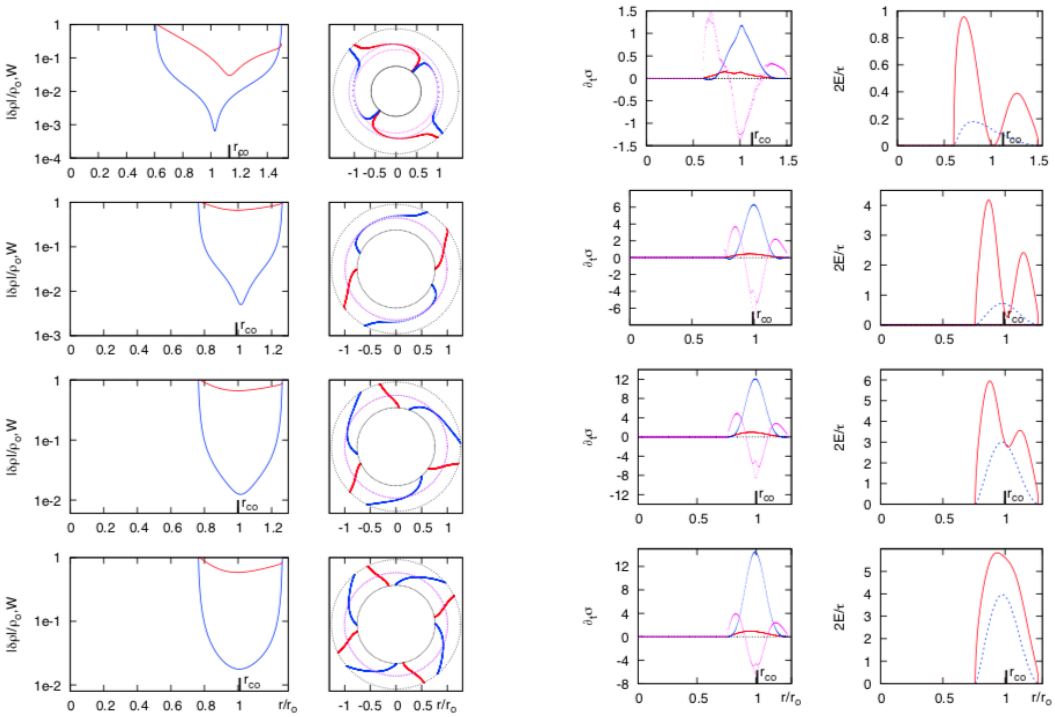

FIGURE 17. $m = 2$, 3, and 4 J modes for $q = 1.5$ and $M_*/M_d = 0.01$ systems with $r_-/r_+ = 0.4$ and 0.6, models J1, J2a, J2b, and J2c from top-to-bottom. We show $\delta\rho$ and $\mathcal{W}$, $\partial_t\sigma$, and δJ. For the eigenfunctions, the blue curve is for $|\delta\rho/\rho_\circ|$ and the red curve for $\mathcal{W}$. For the $\partial_t\sigma$, the Reynolds stress is the red curve, the gravitational stress the blue curve, and the acoustic stress rate the magenta curve. For the perturbed energies, the kinetic energy is the blue curve and the enthalpy the red curve.

Table 3. Representative P and Edge $m = 2$ Modes

	r_-/r_+	$r_+/r_\circ$	$r_\circ$	$\tau_\circ$	J	y_1, y_2	$r_{co}/r_\circ$
P1	0.452	1.60	0.254	0.0808	5.05	-0.0649,0.0956	1.02
P2	0.500	1.49	0.403	0.161	6.35	-0.227,0.151	1.06
P3	0.600	1.33	1.09	0.712	10.4	-0.152,0.212	1.04
P4	0.700	1.21	3.37	3.88	18.4	-0.0736,0.126	1.02
E1	0.101	5.52	6.13×10^{-3}	3.03×10^{-4}	0.786	0.428,0.067	0.908
E2	0.202	2.99	0.0229	2.18×10^{-3}	1.51	0.177,0.0833	0.959
E3	0.402	1.74	0.159	0.04	3.99	-0.0524,0.141	1.01

P & Edge Modes

P and edge modes are driven by coupling of inertial waves across corotation. For both, corotation and the minimum in $\mathcal{W}$ sit at $\sim r_\circ$. P and edge modes are dominant in the region in $(r_-/r_+, M_*/M_d)$-space to the far right and below the J mode corner (see Figure 22 and 23). We identify three characteristic behaviors. For given M_*/M_d and increasing r_-/r_+, P and edge modes show: (i) bars near the inner edge of the disk with short forward phase shifts at $r_\circ$ which switch to long trailing arms outside $r_\circ$, sometimes winding around the disk repeatedly. (ii) A similar mode with central bars and short leading phase shifts but with short trailing arms outside $r_\circ$. And (iii) another mode with smoothly winding leading spiral arms. The instabilities with large winding number are referred to as edge modes. Edge modes are associated with the low r_-/r_+ and high M_*/M_d regime. The modes in (ii) and (iii) are associated with the humps shown in the NSG y_2 plot discussed in §3.2.3.

There is a narrow transition region between the edge modes and P modes with characteristic behavior illustrated in Figures 18 and 19 where a sequence of figures of $m = 2$ modes for $q = 2$, $M_*/M_d = 10^2$, and $r_-/r_+ = 0.70$ to 0.10 systems are

shown (see also Table 3). These models strongly resemble corresponding NSG disks. Threshold behavior occurs at $r_-/r_+ = 0.50$, with the $r_-/r_+ = 0.48$ model just below the threshold exhibiting a less rapid switch from leading to trailing arm. At transition, corotation moves across $r_\circ$ but does not coincide with the extension of the arms. For example, $r_{co} = 1.01 r_\circ$ for the model at $r_-/r_+ = 0.45$, even though it has extended arms. The first forward phase shift falls near $r_\circ$, with a rapid switch to a trailing arm. As r_-/r_+ decreases from 0.60, $r_\circ$ moves further inside the geometric center of the disk, leaving more room for the trailing arm to extend. Note that there is a change in y_1, as seen in Figure 22 (y_1 plotted for $q = 2$, $m = 2$, M_*/M_d *vs.* r_-/r_+) in that models exhibiting P mode behavior have $y_1 < 0$, while edge modes have $y_1 > 0$. In edge modes, the number of wraps increases with decreasing r_-/r_+. The corresponding eigenfunctions in Figure 19 indicate that a second minimum appears when the trailing arm extends beyond the inner bar. For low r_-/r_+, the winding of the arms increases. The minima occur with more frequency toward the outer edge of the disk. The P mode work integral plot has two peaks in E_h, one lying close to the inner and one closer to the outer edge of the disk. As r_-/r_+ decreases, a broad valley develops between them. E_k has a peak which lies inside the inner E_h peak, with a shoulder across the central region, going to zero at the outer edge of the disk. The edge mode work integral plot also has a narrow E_h peak near the inner edge which contains the peak in E_k, but both have very low amplitude except near the inner edge. The work integrals become oscillatory for smaller r_-/r_+. The stress plots show acoustic flux dominating near the inner and outer edges while Reynolds stress dominates the inner disk region, carrying opposite sign. Stress due to self-gravity is negligible for the P and edge modes.

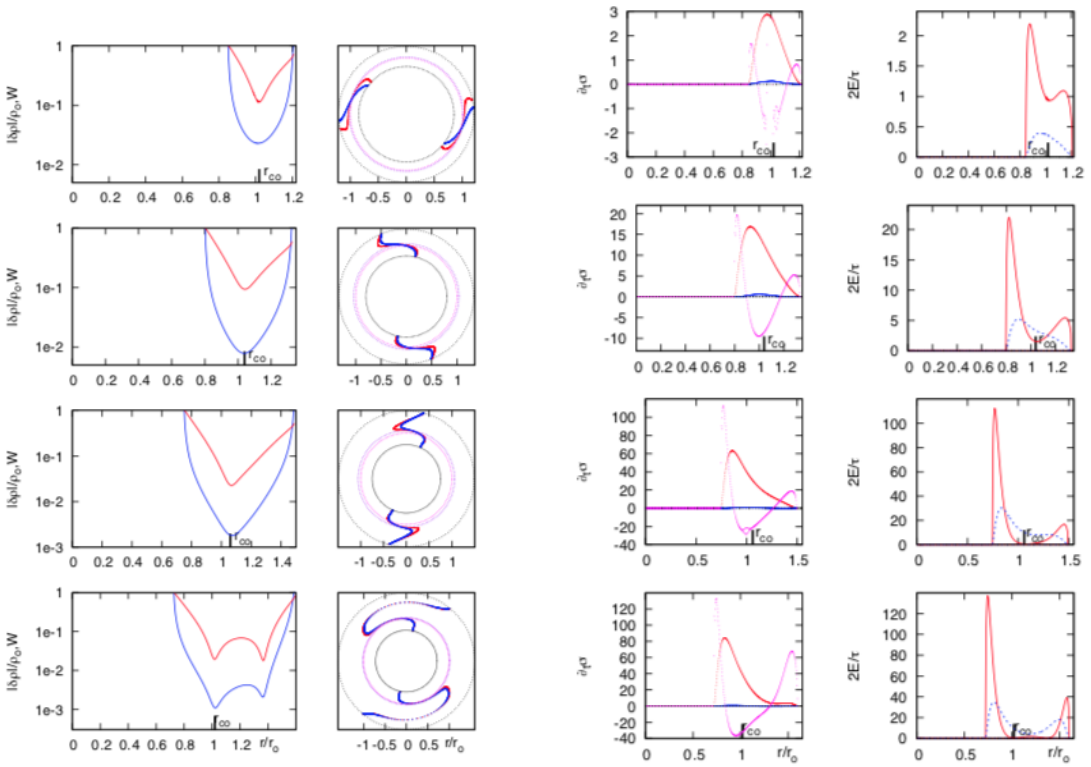

FIGURE 18. Barlike P modes, $m = 2$, for disks with $q = 2$ and $M_*/M_d = 10^2$ for $r_-/r_+ > 0.45$, models P4, P3, P2, and P1 from top-to-bottom. We show $\delta\rho$ and $\mathcal{W}$, $\partial_t\sigma$, and δJ. For the eigenfunctions, the blue curve is for $|\delta\rho/\rho_\circ|$ and the red curve for $\mathcal{W}$. For the $\partial_t\sigma$, the Reynolds stress is the red curve, the gravitational stress the blue curve, and the acoustic stress the magenta curve. For the perturbed energies, the kinetic energy is the blue curve and the enthalpy the red curve.

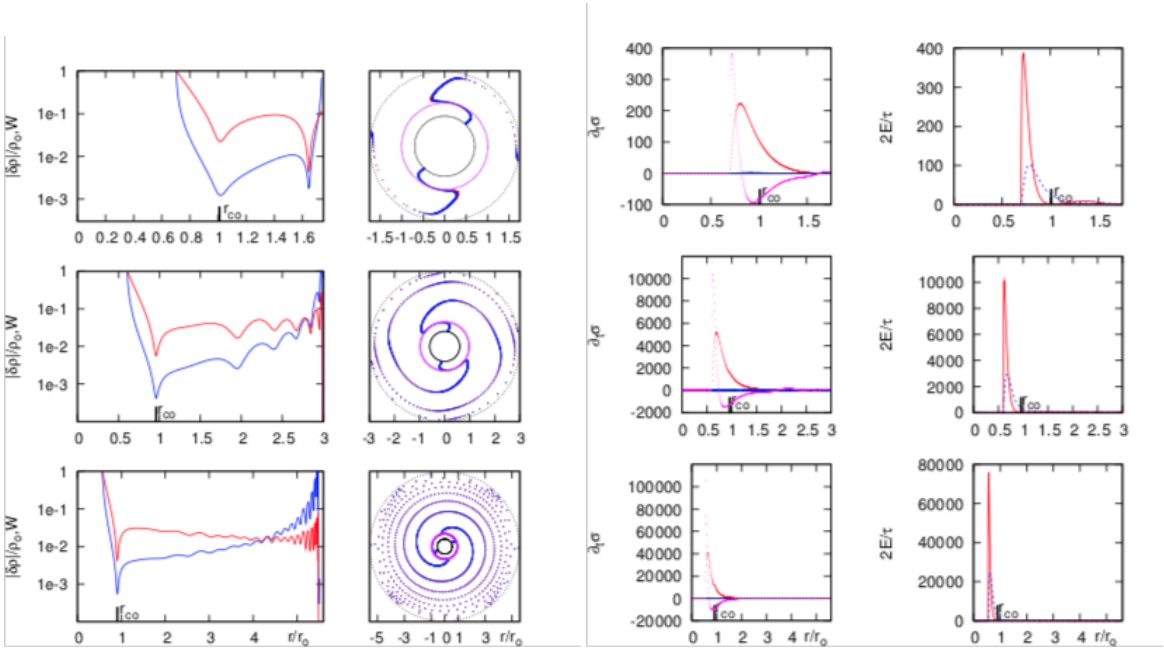

FIGURE 19. Barlike edge modes, $m = 2$, for disks with $q = 2$ and $M_*/M_d = 10^2$ for $r_-/r_+ < 0.45$, models E3, E2, and E1 from top-to-bottom. We show $\delta\rho$ and $\mathcal{W}$, $\partial_t\sigma$, and δJ. For the eigenfunctions, the blue curve is for $|\delta\rho/\rho_\circ|$ and the red curve for $\mathcal{W}$. For the $\partial_t\sigma$, the Reynolds stress is the red curve, the gravitational stress the blue curve, and the acoustic stress the magenta curve. For the perturbed energies, the kinetic energy is the blue curve and the enthalpy the red curve.

Table 4. Representative I^- and I^+ $m = 2$ Modes

	M_*/M_d	q	r_-/r_+	$r_+/r_\circ$	$r_\circ$	$\tau_\circ$	J	y_1, y_2	$r_{co}/r_\circ$
I1	0.1	1.5	0.600	1.27	14.9	511	2.75	0.905,0.504	0.780
I2	5	1.5	0.600	1.26	16.2	176	9.41	0.784,0.432	0.802
I3	7	2	0.600	1.30	7.68	49.8	7.47	-0.747,0.169	1.26
I4	0.2	1.5	0.402	1.50	6.60	152	1.84	-0.993,0.601	$> r_+$
I5	7	1.5	0.500	1.36	11.6	91.6	9.32	-0.737,0.274	1.36

I^- & I^+ Modes

The I modes are modes with properties intermediate between those of the J and P modes. There are two types of I modes, fast I modes with corotation inside $r_\circ$, sometimes inside r_-, the I^- modes, and slow I modes with corotation outside $r_\circ$, sometimes outside r_+, the I^+ modes. The I mode region is seen in Figure 22 as a wide arc extending to the right and below the J mode corner previously defined, ending in stable models curving from $(r_-/r_+, M_*/M_d) = (0.70,10.0)$ to $(r_-/r_+, M_*/M_d) = (0.20,0.01)$. Equilibrium disks which show I modes have $7.5 \gtrsim p \gtrsim 3$ with density contours nearly concentric for small M_*/M_d disks, becoming somewhat flatter for high M_*/M_d disks.

Figure 20 depicts and Table 4 presents relevant properties for typical I^- modes. Corotation falls well inside $r_\circ$. $\mathcal{W}$ shows a minimum near $r_\circ$ while $|\delta\rho/\rho_\circ|$ shows a minimum near $r_\circ$. The phase plots show a central bar and an outer bar connected by a trailing π/m phase shift in $\delta\rho/\rho_\circ$ slightly outside $r_\circ$. $\mathcal{W}$ is out of phase with $\delta\rho/\rho_\circ$ at the inner edge, with a short leading arm that switches to trailing at r_{co}, coming into phase with $\delta\rho/\rho_\circ$ at the outer edge. Models where $M_*/M_d < 1$ exhibit bars near the inner and outer edges of the disk, while in higher M_*/M_d models, the bars become

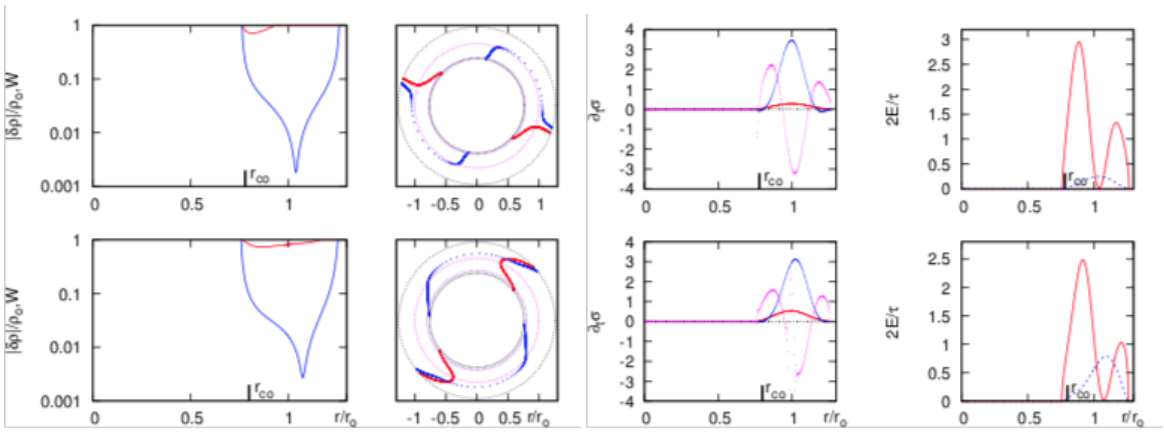

FIGURE 20. Barlike I^- modes, $m = 2$ modes, with corotation inside $r_\circ$ and sometimes inside r_- for disks with $q = 1.5$ and $M_*/M_d = 0.1$ and 5 for $r_-/r_+ = 0.6$, models I1 and I2 from top-to-bottom. We show eigenfunctions, $\partial_t\sigma$, and δJ. For the eigenfunctions, the blue curve is for $|\delta\rho/\rho_\circ|$ and the red curve for $\mathcal{W}$. For the $\partial_t\sigma$, the Reynolds stress is the red curve, the gravitational stress the blue curve, and the acoustic stress the magenta curve. For the perturbed energies, the kinetic energy is the blue curve and the enthalpy the red curve.

less perpendicular to the disk edges with $\delta\rho/\rho_\circ$ and $\mathcal{W}$ in phase and trailing at the outer edge. For the $M_*/M_d = 5$ model pictured here, $\delta\rho/\rho_\circ$ and $\mathcal{W}$ come into phase at $r/r_\circ = 1.09$. These trends are also seen in $q = 1.75$ and 2, in that the $M_*/M_d < 1$ models exhibit bars and the bars are less perpendicular in higher M_*/M_d models. $\delta\rho/\rho_\circ$ amplitudes are similar to J modes, but the $\mathcal{W}$ amplitudes of I^- modes typically have a dip near the inner edge of the disk. The work integrals for these models are similar in character to those of the J modes. The $M_*/M_d = 5$ model shows stronger dominance of E_k in the disk, especially outside $r_\circ$. Stress plots are generally similar to those seen in the J modes.

I^+ modes are illustrated in Figure 21 and Table 4. Equilibrium density contours are nearly concentric for small M_*/M_d disks, becoming somewhat flatter for high M_*/M_d disks. Corotation falls outside r_+ or, for model I5, just at r_+. $\mathcal{W}$ does not show extrema when $r_{co} > r_+$. $\mathcal{W}$ is in phase with $\delta\rho/\rho_\circ$ near the inner edge of the

disk, becoming out-of-phase for $\varpi > r_\circ$. There is roughly a π/m trailing phase shift in $\delta\rho/\rho_\circ$ that lies close to $r_\circ$. $q = 1.5$ models have bars near the inner and outer disk edges, becoming less perpendicular for higher M_*/M_d. The work integral of these models all show two peaks in E_h with the inner peak higher, and a region in the middle of the disk that is dominated by E_k. Unlike the I^- mode, where the peak in E_k lies at the zero between the two E_h peaks, the peak in E_k for the I^+ mode lies within the region of the inner E_h peak. Notably, the $q = 1.5$, $r/r_\circ = 0.50$, $M_*/M_d = 7$ model is dominated more strongly by E_k for much of the disk inside $r_\circ$. The stress plots show domination in the inner and outer regions by $\partial_t\sigma_h$ while $\partial_t\sigma_G$ dominates in the center of the disk. The Reynolds stress is positive with relatively low amplitude. The notable exception here is the $q = 2$, $r/r_\circ = 0.60$, $M_*/M_d = 7$ model, which has a region inside $r_\circ$ that is dominated by the Reynolds stress.

There is a region of parameter space that lies between I^+ modes and edge modes where the characteristics of the models resemble neither. Unlike I modes, corotation lies near $\mathrm{r}_\circ$ and unlike edge modes, the $\mathcal{W}$ phase lies significantly away from that of $|\delta\rho/\rho_\circ|$, indicating that self-gravity is important. There is a large variance in appearance of the models, with no strong characteristic identifying modes in this region.

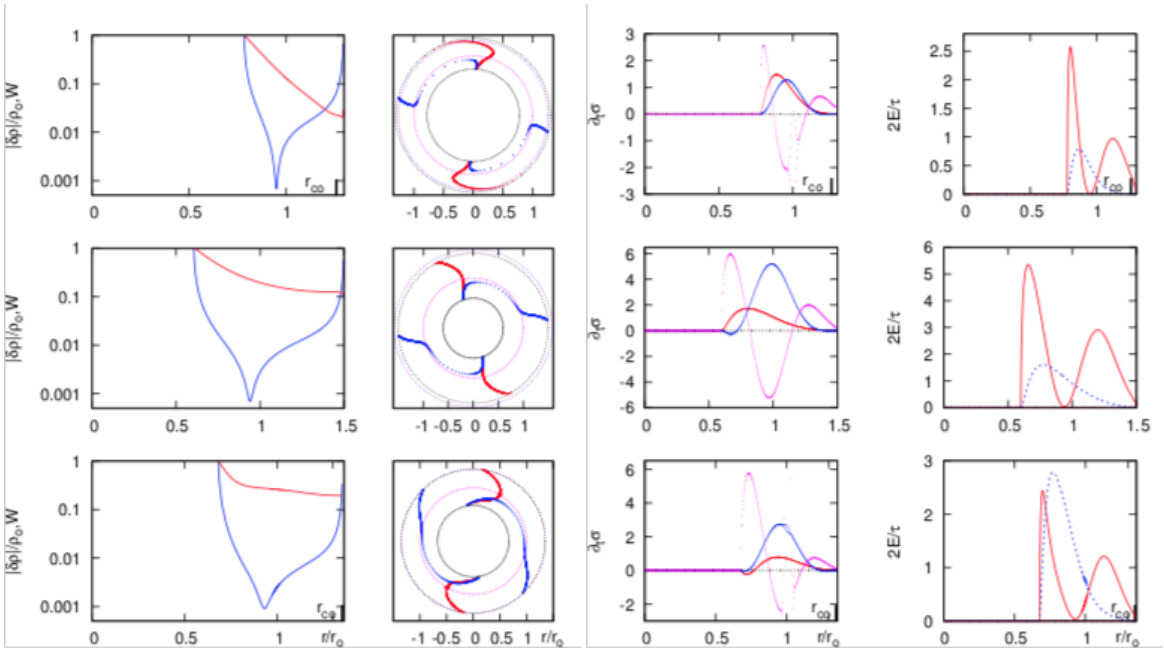

FIGURE 21. Barlike I^+ modes, $m = 2$ modes, with corotation outside $r_\circ$ and sometimes outside r_+ for disks with $q = 2$, $M_*/M_d = 7$, and $r_-/r_+ = 0.6$, model I3, $q = 1.5$, $M_*/M_d = 0.2$, and $r_-/r_+ = 0.402$, model I4, and $q = 1.5$, $M_*/M_d = 7$, and $r_-/r_+ = 0.5$, model I5, from top-to-bottom. We show $\delta\rho$ and $\mathcal{W}$, $\partial_t\sigma$, and δJ. For the eigenfunctions, the blue curve is for $|\delta\rho/\rho_\circ|$ and the red curve for $\mathcal{W}$. For the $\partial_t\sigma$, the Reynolds stress is the red curve, the gravitational stress the blue curve, and the acoustic stress the magenta curve. For the perturbed energies, the kinetic energy is the blue curve and the enthalpy the red curve.

A Summary of the Eigenvalue Parameter Space for Pointmass Models

Our results are highlighted in Figure 22 where we show y_1 values for $m = 1$ and 2 modes for $q = 1.5$ and 2 disks, and in Figure 23 where we show y_2 values for $m = 1$ and 2 modes and the self-gravity parameters p and η for $q = 2$ disks. Star/disk systems are generally unstable. For $q = 2$ disks, disks where the Toomre Q parameter Q = 0, are usually dominated by $m = 1$ modes. Multi-armed modes, $m \geq 2$ modes are only dominant at large r_-/r_+, with some exceptions. Similar behavior is seen in the $q = 1.75$ and 1.5 disks except that the range over which multi-armed modes dominate cover larger portions of the parameter space. For $q = 1.5$ disks, the region stretches from high r_-/r_+ to $r_-/r_+ \sim 0.1$ for systems with moderate to low disk mass, $M_*/M_d \approx 1$ to 20. Protostellar and protoplanetary disks are expected to show nearly *Keplerian* rotation with $M_*/M_d \approx 1$ to 20 and are thus expected to be dominated by $m = 2$, 3, and 4 modes. If they, however, are closer to constant specific angular momentum disks, $q = 2$ disks, they are are then expected to be dominated by $m = 1$ modes.

The instability regimes for multi-armed modes in $(r_-/r_+, M_*/M_d)$ space track the strength of self-gravitational effects as measured by the parameter p (independent of q). This can be seen in Figure 23. The most unstable modes are in the upper left hand corner of the plot where p is largest. In this region, modes show corotation near $r_\circ$ (see Figure 22). These models are confined mainly over $0.20 < M_*/M_d \leq 10$ for $r_-/r_+ \geq 0.60$. Growth rates decrease away from this corner, then increase and decrease forming a bulls eye pattern. Two stable regions where y_2 goes to 0 are seen. There is a short arc sweeping from $r_-/r_+ \approx 0.425$, $M_*/M_d = 0.01$ to $r_-/r_+ \approx 0.475$, $M_*/M_d = 0.05$, and a long arc sweeping through parameter space from $0.1 \leq r_-/r_+ \leq 0.20$, $0.01 \leq M_*/M_d \leq 0.1$ to $r_-/r_+ \approx 0.70$, $17.5 \leq M_*/M_d = 50$. The two

arcs roughly follow $p \approx 7.5$ and 3. Sometimes strips of stability or near-stability are present at the boundary between regions where the dominant mode has a different character. This is seen in the NSG plots with $r_-/r_+ = 0.5$, where y_1 jumps while the growth rate y_2 goes to zero near the transition. Usually, however, changes in mode type are marked by more subtle changes in the time eigenvalue. The changes are usually more distinct in y_1 than in y_2.

For one-armed spirals, $m = 1$ modes, the instability regimes more closely follow the constant η curves than constant p curves. One-armed spirals are more unstable at large η than small η. For $q = 2$ disks, a tongue of weak instablity extends from intermediate M_*/M_d to high $M_*.M_d$ at intermediate r_-/r_+. This feature is not as prominent in $q = 1.5$ disks. Outside of this feature, the instability regimes for the $m = 1$ modes are similar for q 1.5 and 2 disks. This does not mean the same types of $m = 1$ modes populate the regions, however. For $q = 1.5$ disks, $m = 1$ modes are slow for small M_*/M_d and nearly stationary for large M_*/M_d. For $q = 2$ disks, $m = 1$ modes are also slow for small M_*/M_d, but show faster modes, modes with corotation near $r_\circ$ and just outside $r_\circ$ at large M_*/M_d. For Keplerian disks, $q = 1.5$ disks, $m = 1$ modes show r_{co} just outside $r_\circ$ for systems with small r_-/r_+ and $M_*/M_d \approx 0.5$-3.

Fission Model: Equilibrium Properties

To investigate the fission hypothesis of binary star formation we begin with an equilibrium state where the stellar configuration, based on previous studies, is unstable and known to form a central bar [108], [184], [172], [126], [127]; [52], [193], [53],[213], [101], [104], [55], [192], [135], [191]. The fission hypothesis is not widely accepted by the astrophysics community as a viable way to produce close-binary stars due to the failure of past numerical studies involving single stars with no

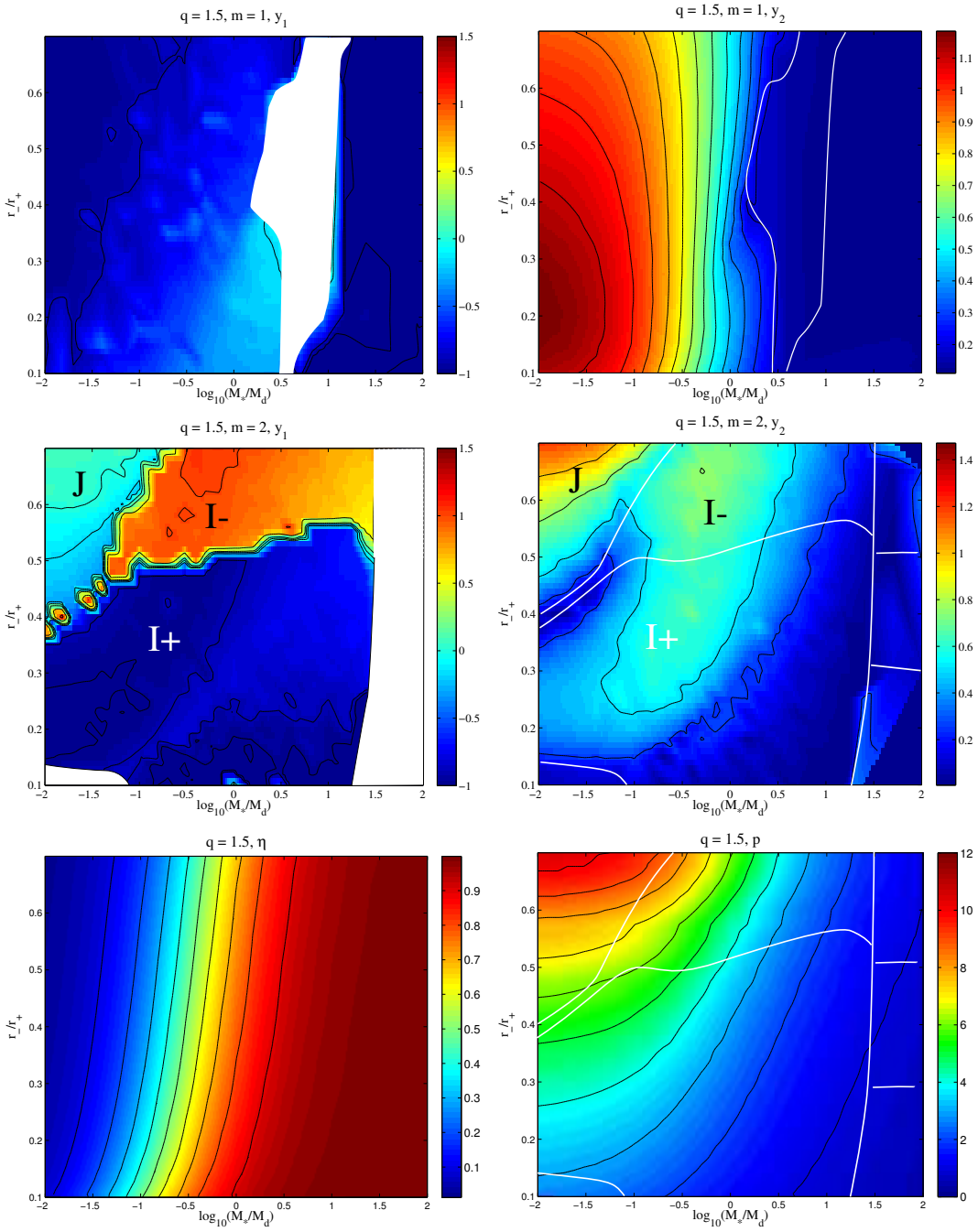

FIGURE 22. Oscillation (y_1) and growth rate (y_2) eigenvalues, η and p for $q = 1.5$ disks. η contours step by .1, p contours step by 1 (smallest $p \approx .5$). Regions without a resolved pattern frequency are whited out. For $m = 2$ at $M*/M_d > 30$, the boxed regions extrapolate stable, I^+ and I^- modes, bottom to top, based on 0, 3 and 3 unstable models respectively.

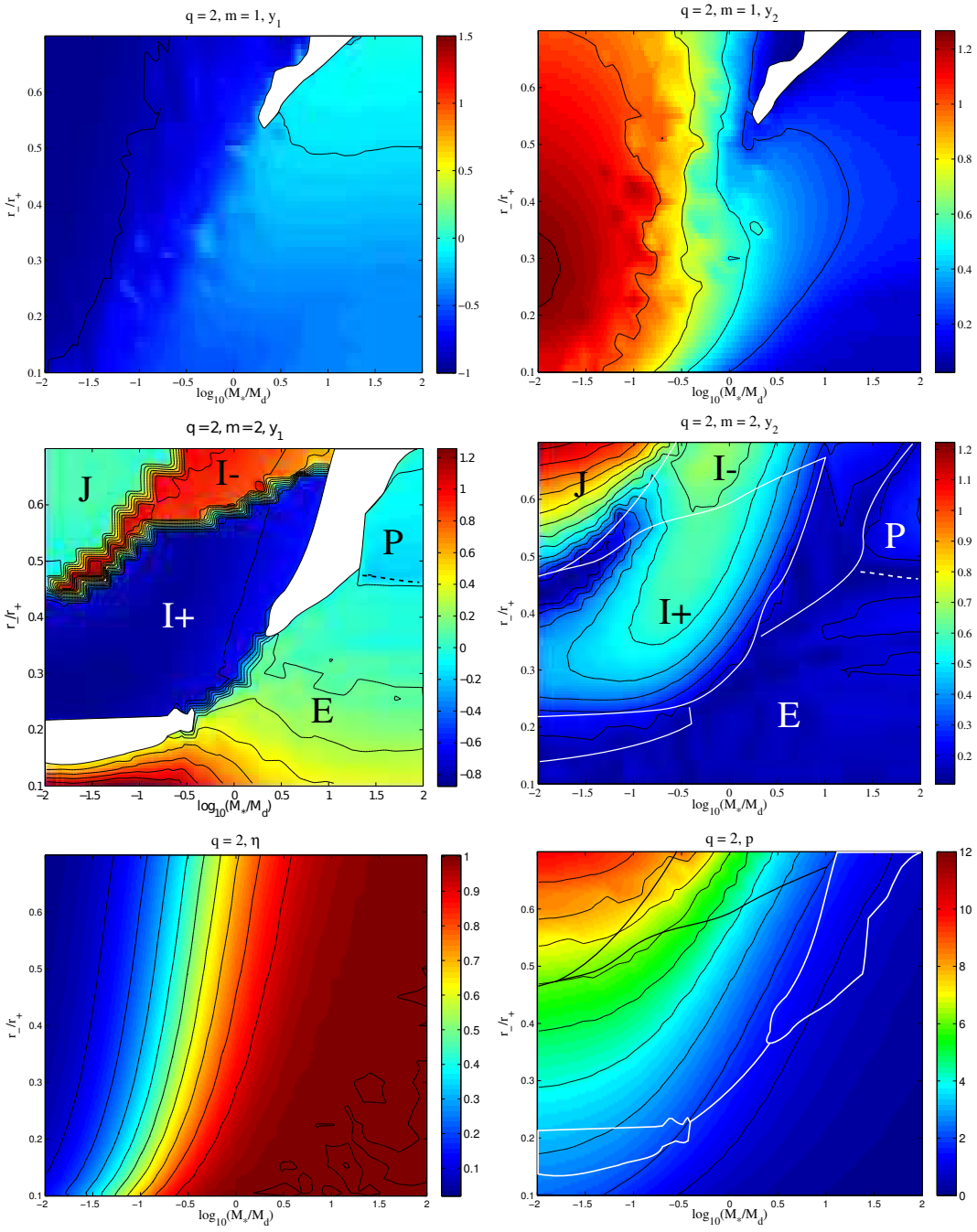

FIGURE 23. Oscillation (y_1) and growth rate (y_2) eigenvalues, η and p for $q = 2$ disks. η contours step by .1, p contours step by 1 (smallest $p \approx .05$). Regions without a resolved pattern frequency are whited out;

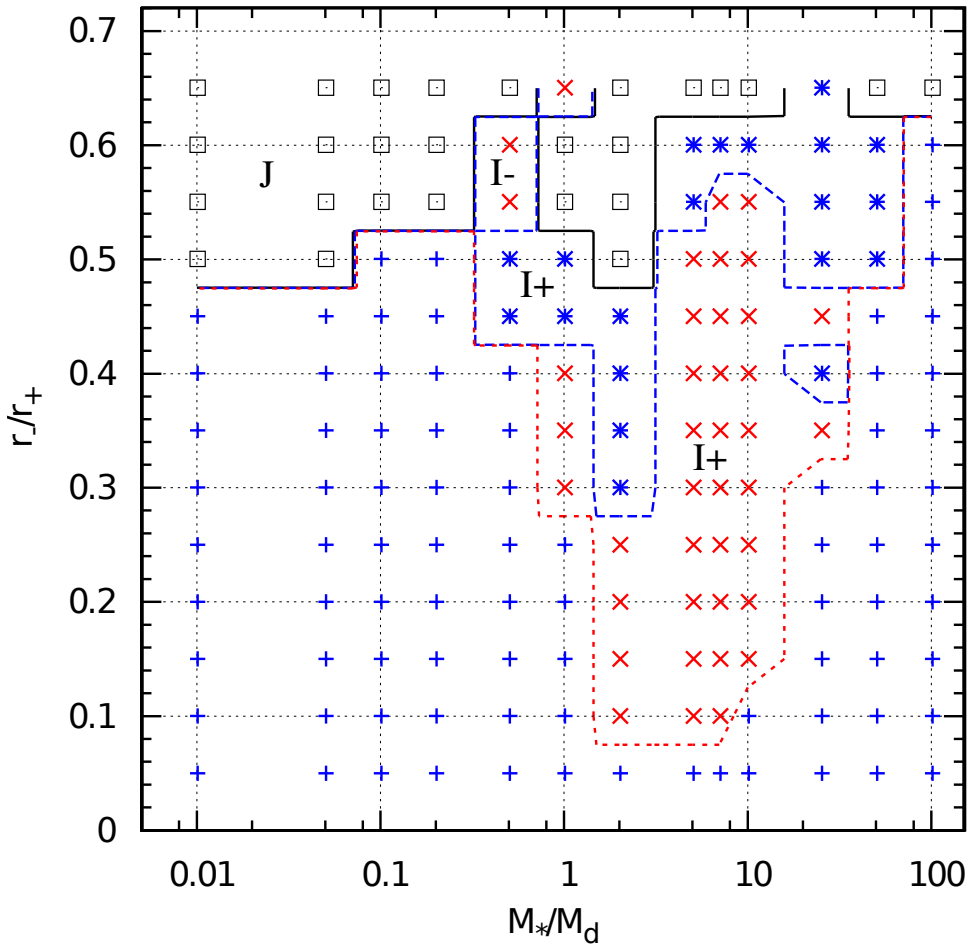

FIGURE 24. Dominant modes in $(r_-/r_+, M_*/M_d)$ space for $q = 1.5$ disks. The modes are denoted as follows: $m = 1$ blue crosses, $m = 2$ red Xs, $m = 3$ blue asterisks, and $m = 4$ black squares. Stable models are filled black squares. Note that the large $m = 2$ I^+ region showed numerical difficulties with $m = 1$ at $q = 1.5$, and $m = 1$ may in fact dominate here.

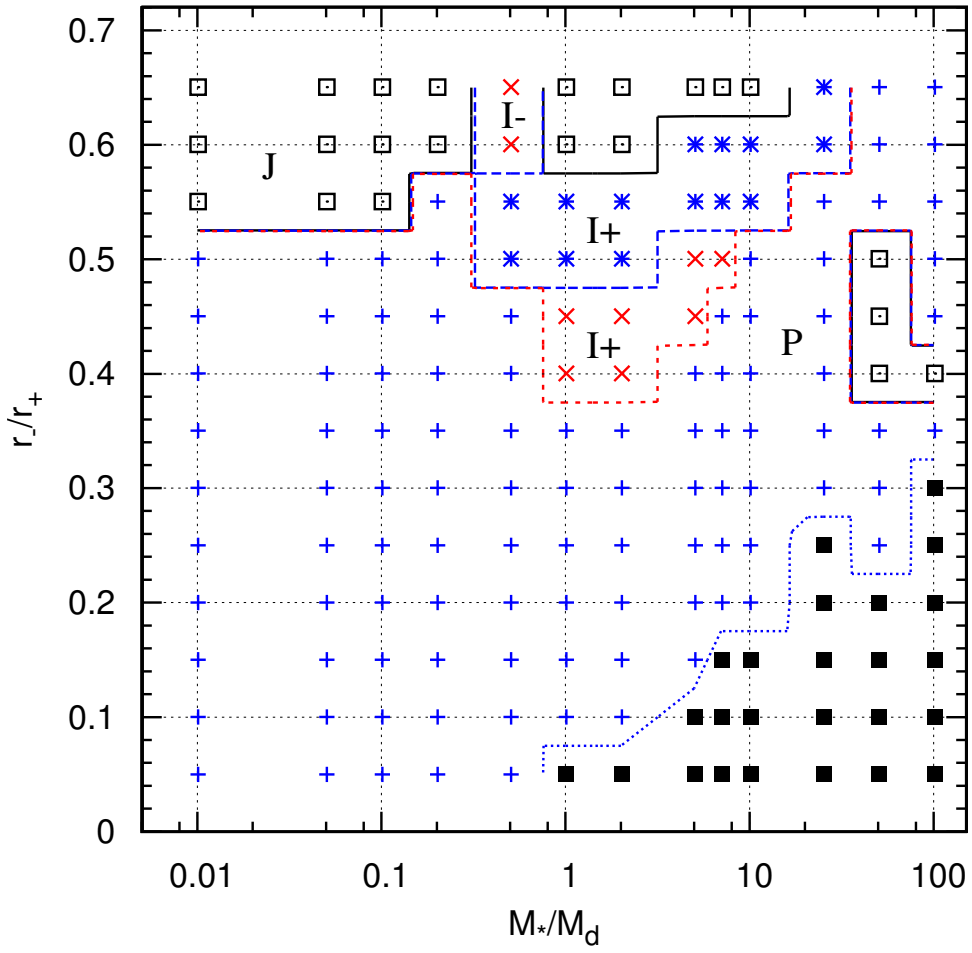

FIGURE 25. Dominant modes in $(r_-/r_+, M_*/M_d)$ space for $q = 1.75$ disks. The modes are denoted as follows: $m = 1$ blue crosses, $m = 2$ red Xs, $m = 3$ blue asterisks, and $m = 4$ black squares. Stable models are filled black squares.

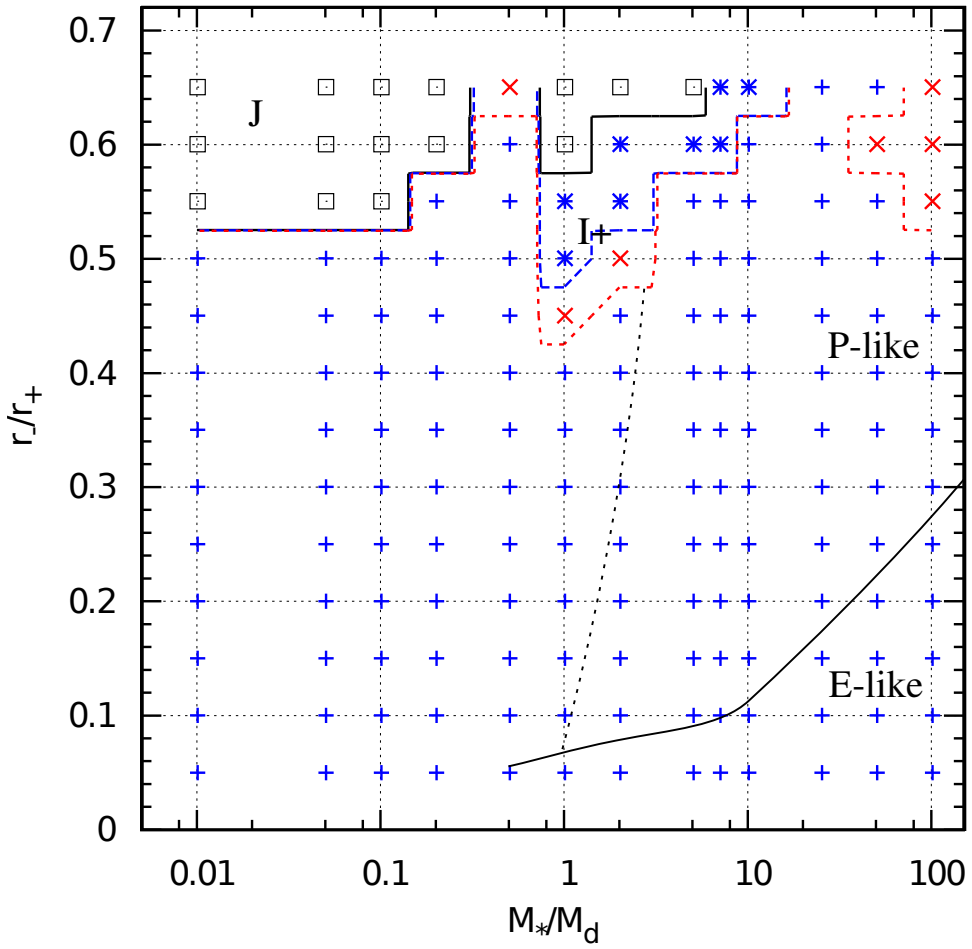

FIGURE 26. Dominant modes in $(r_-/r_+, M_*/M_d)$ space for $q = 2$ disks. The modes are denoted as follows: $m = 1$ blue crosses, $m = 2$ red Xs, $m = 3$ blue asterisks, and $m = 4$ black squares. Stable models are filled black squares.

accretion disks. Based on previous nonlinear studies of solitary differentially rotating polytropic stars, the unstable central star develops through a nonaxisymmetric barmode instability which does not directly lead to fission. The system first develops of spiral arms and torques from central star on the spiral arms transfers angular momentum outward in the system leading to spin-down of the central object [101]. Williams and Tohline (1988) found that within $\approx 10\tau_{cen}$, a rapidly rotating polytrope of index $n = 0.8$ and $\beta = 0.31$ develops spiral arms which exert a torque on the central object leading to a more slowly rotating central star plus a ring. Previous studies of the fission process did not include the effects a protostellar disk can have on the evolution of the stellar core, and therefore, dismissed significant physics which naturally take place in the stellar and planetary evolution process [213]. We investigate the effects of including circumstellar material into the calculation. Here we present the equilibrium properties/results of our fission model. Once the equilibrium configuration is calculated, linear and nonlinear stability analysis are performed using the equilibrium model as the initial condition.

The central star is highly flattened and has ratio $r_p/r_e = 0.180$ and $r_e/r_- = 0.790$ and is in rapid differentital rotation with $\beta_* = 0.220$, while the disk has $r_-/r_+ = 0.66$ and $\beta_d = 0.455$. The star and disk have nearly equal mass with $M_*/M_d = 1.18$ and the angular velocity distribution is Keplerian with $q = 1.5$. By rapid rotation, we mean that the star has $\beta = T/|W|$ above the Maclaurin spheroid barlike mode secular instability threshold, $\beta_{sec} = 0.137$ (See Tassoul (1978) [187]). The star, however, has β_* below the dynamic barmode instability threshold $\beta_{dyn} = 0.274$ where dynamic barlike instabilities have been shown to develop for incompressible Maclaurin spheroids. In this case, the dynamically stable star according to the β_{dyn} criterion, may be driven unstable by the coupling of the secularly unstable stellar mode to the

dynamically unstable disk mode [103], [219]. Alternatively, the disk may alter the central star configuration greatly enough so that the star is unstable to the dynamic bar instability even though $\beta_* < \beta_{dyn}$ [85].

The model parameters were chosen: (i) in large part because the disk is massive and expected to have a large effect on the star, and because the model falls into the region of parameter space where the $m = 2$ coefficient is expected to dominate the disk leading to a two-fold symmetry conducive to the excitation of the barmode in the star. (ii) The star and disk gas properties have $n = 1.5$ making the gas compressible (See Figure 13). Using this index, one can find that the polytropic exponent is $\gamma = 5/3$, which gives the specific heat capacity for a monatomic gas. The star is also in differential rotation with the L-distribution $h_M(\varpi) = 2m_\varpi$.

Equilibrium properties of the star-disk systems are summarized in Table 5 and Table 6 where J is the total angular momentum of the system, τ_{cen} is the central rotation period for the star, and K_d is the polytropic constant in the disk. The polytropic constant for the star is $K_* = 1$. All other parameters have been previously defined. A meridional density map for the star and disk are shown in Figure 29. We see that the star is highly flattened due to its rapid rotation and that the disk has a roughly circular cross-section. Looking at figure 24 we see that for $q = 1.5$ a disk around a pointmass stellar object with $M_*/M_d = 1.18$ and $r_-/r_+ = 0.66$ falls on the cusp of where $m = 2$ and $m = 4$ are the fastest growing coefficients of the density perturbation.

In figure 27 we show the effect of varying the flattening of the central star. We do this by plotting $T/|W|$ versus M_*/M_d for the star and disk varying initial conditions. Equilibrium configurations were calculated using $q = 1.5$, $n = 1.5$, $r - /r+ = 0.66$, $r_e/r_- = 0.790$ and several different values of the ratio $r_p/r_e = 0.18$, 0.2, 0.25, 0.375,

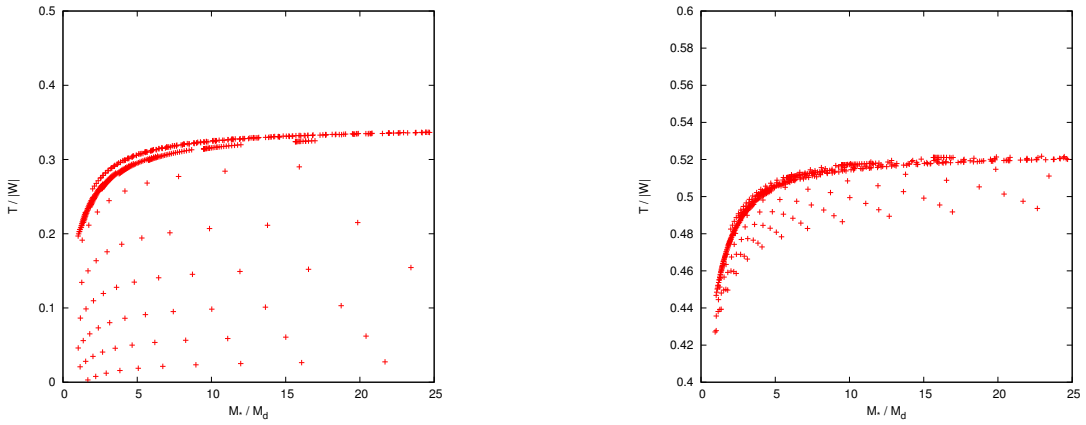

FIGURE 27. $T/|W|$ versus M_*/M_d for the star (left) and disk (right) varying the relative flattening parameter r_p/r_e of the central star.

0.5, 0.625, 0.75, 0.857, 1.0. The angular momentum distribution chosen for this study was the L-distribution. In addition, we slowly varied the density distribution in the star and disk producing a large range of the ratios M_*/M_d. There are eight curves representing the values of r_p/r_e. All of these curves have an asymptotic character as M_*/M_d increases. The largest ratio, $r_p/r_e = 1.0$, yields the lowest values of $T/|W|$ and is seen as the bottom most curve in figure 27. The flattening does not uniquely predict $T/|W|$, however, the relative flattening of the central star could be used as a measure for determining stability thresholds. It is a good indicator for when rotation becomes a large fraction of the gravitational binding energy of the system. The disk gravity acts in the same direction as the stellar centrifugal force, therefore, $T/|W|$ in the star is reduced as the disk mass increases. In figure 28 we show $T/|W|$ versus r_e/r_p for the star and the disk.

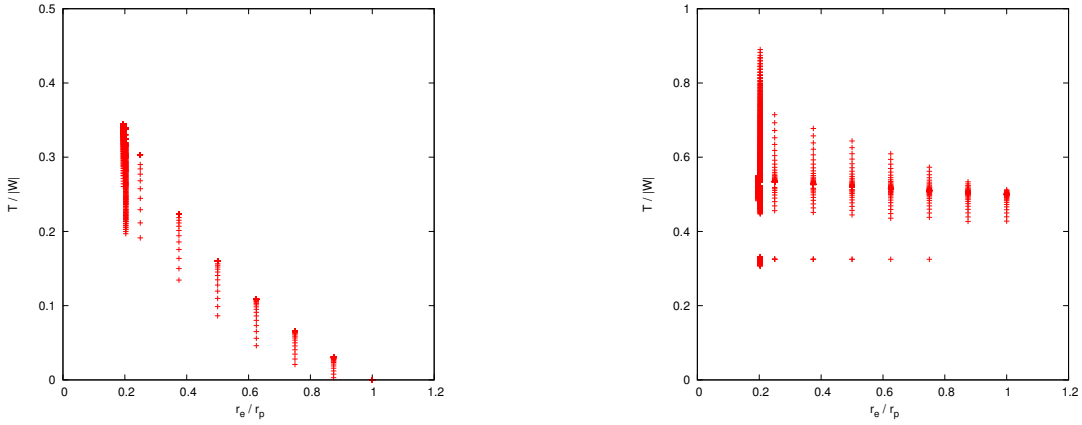

FIGURE 28. $T/|W|$ versus r_e/r_p for the star (left) and disk (right) varying the ratio M_*/M_d.

Table 5. Equilibrium Properties of Fission Model

Model	M_*/M_d	r_-/r_+	β_d	β_*	$\frac{r_p}{r_e}$
M2	1.18	0.66	0.455	0.220	0.180

Table 6. Equilibrium Properties of Fission Model

Model	J	r_+	K_d	$r_\circ$	τ_{cen}	$\tau_\circ$
M2	2.96	35.60	0.0435	29.5	373.4	1133.4

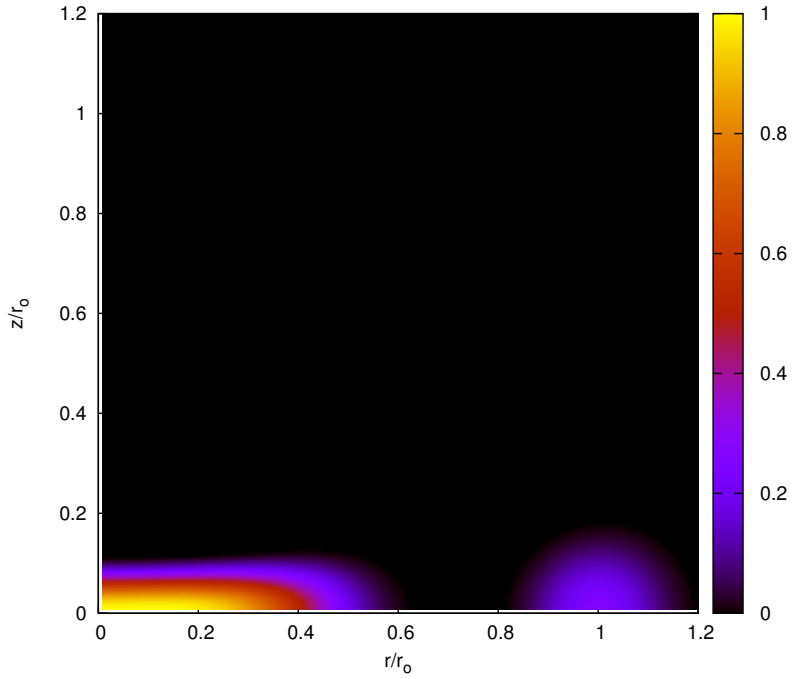

FIGURE 29. Equilibrium density contours in a meridional slice. The contours are normalized to ρ_{cen}, the central density of the star. The rz-coordinates are normalized to the radius of density max $r_\circ$ in the disk.

Table 7. Linear Properties for the Fission Model M2

y_1	y_2	$r_{ilr}/r_\circ$	$r_{olr}/r_\circ$	$\delta\rho_{min}/r_\circ$	$W_{min}/r_\circ$	$r_{co}/r_\circ$	m
0.842	1.628	0.498	1.037	1.025	1.175	0.791	2
2.405	1.358	0.515	0.818	1.045	1.155	0.675	3
3.689	0.883	1.105	1.553	1.135	1.130	1.338	4
4.076	0.797	0.987	1.294	0.965	1.150	1.145	5

Fission Model: Linear Results

For this present linear stability analysis, we use a fully resolved central star and begin with the equilibrium configuration described in the previous section. For the fission model, from hereon referred to as model $M2$, components with $m = 1 - 5$ were tested. For nonlinear simulations beginning with the same initial equilibrium parameters, the $m = 2$ Fourier component of the density perturbation presents the fastest growth-rate. For different cooling rates in the nonlinear regime, excitation of the $m = 3$ component changes the evolutionary behavior of the system. Here I present results of linear calculations for the $m = 2$ and 3 components. In Table 7, I present the y_1 and y_2 eigenvalues for the $m = 2$ and 3 components, the locations of the inner and outer Linblad resonances r_{ilr} and r_{olr}, and the location of corotation r_{co} as well as the the location of minima in $\delta\rho$ and $\mathcal{W}$.

Results for the $m = 2$ and 3 Components

In Figure 30 we plot the growth of the density perturbation at three radii in the disk and in Figure 31 we show the frequencies of the density perturbation. In the early part of the calculation, the growth plots show an initial organizational period where the perturbation is fluctuating rapidly followed by steady exponential growth. The

$m = 2$ component spends very little time $\approx 0.5\tau_\circ$ in this organizational phase while the $m = 3$ Fourier component takes considerably longer to reach steady exponential growth $\approx 1.5\tau_\circ$. This behavior is also observed in nonlinear simulations (See Nonlinear Results). The y_1 and y_2 eigenvalues are listed in Table 7 with $y_1 = 0.842, 2.405$ and $y_2 = 1.63, 1.36$ for the $m = 2$ and 3 components, respectively. Locations of the inner and outer Linblad resonances are also shown in Table 7. The Linblad resonances are places in the disk where the real part of ω_m matches the epicyclic frequency. The inner Linblad resonance $r_{ilr}/r_\circ = 0.498, 0.515$ and the outer linblad resonance $r_{olr}/r_\circ = 1.037, 0.818$ for the $m = 2$ and 3 components, respectively.

Recall that I-modes have properties intermediate between those of the J and P modes. There are two types of I-modes, (i) fast I-modes with corotation inside $r_\circ$, sometimes inside r_-, the I^- modes, and (ii) slow I-modes with corotation outside $r_\circ$, sometimes outside r_+, the I^+ modes. For the model under current study, corotation falls inside $r_\circ$ and within r_- with $r_{co}/r_\circ = 0.791, 0.675$ for the $m = 2$ and 3 components, respectively. Based on this criteria, we categorize $m = 2$ mode of the $M2$ model as an I^- barmode.

Phase plots (Figure 32) show the location in the disk midplane of constant phase in a topdown view of $\mathcal{W}$ and $\delta\rho$ for the $m = 2$ and 3 components. Rotation is in the counterclockwise direction. The outer edge of the star r_* is shown in red, while the inner r_- and outer r_+ edge of the disk are shown in blue. The maximum density in the disk is plotted in magenta and falls dead center in the disk. Corotation can be seen to fall inside $r_\circ$ and within r_-. The $\delta\rho$ phase shows a central bar and $\delta\rho/\rho_\circ$ has roughly constant phase inside the star which extends into trailing spiral arms similar to the bar mode structures seen by Imamura (1999) [101]. The disk phases in $\delta\rho$ show a bar in the inner part of the disk connected to a trailing π/m phase shift slightly

outside $r_\circ$ which then extends to a outer bar. The alternative eigenfunction formed from the perturbed enthalpy and gravitational potential, $\mathcal{W}$, is out of phase with $\delta\rho$ inside the central star and shows a bar-like feature which extends beyond the $\delta\rho$ bar and then quickly transitions to a leading arm at the edge of the star. The $\mathcal{W}$ in the disk is out of phase with the inner bar in $\delta\rho$, but after the π/m phase shift in $\delta\rho$, $\mathcal{W}$ falls nearly on top of the outer bar in $\delta\rho$.

In figure 33 we see that $\mathcal{W}$ has a minimum near $r_\circ$ but slightly outside with $\mathcal{W}_{min}/r_\circ = 1.175, 1.155$ for the $m = 2$ and 3 components, respectively. $\delta\rho$ also has a minimum near $r_\circ$ with $\delta\rho_{min}/r_\circ = 1.175, 1.155$ for the $m = 2$ and 3 components, respectively.

In Figure 34 we show the gravitational torque and the Reynolds torque over the star and disk for the $m = 2$ and 3 components. For the $m = 2$ component, the inner region of the star $r/r_\circ < 0.44$ has negative total torque due to a large negative Reynolds torque and very little contribution from the gravitational torque, while the outer region of the star $0.44 < r/r_\circ < 0.63$ has a large positive total torque due to a large contribution from the Reynolds torque and a small contribution from the gravitational torque. The minimum lies at approximately $r/r_\circ \approx 0.38$. Material experiencing a negative Reynolds torque is losing pressure support, and therefore angular momentum, and so we would expect this material to move inward, or spin-down. Material with a positive total torque is gaining angular momentum and should either move to a larger orbit or spin-up. Imamura (1999) found that the central bar exerted a torque on the disk which led to angular momentum transfer between the central bar and outer layers of the star [101]. This caused the spin-down in the central part of the star and and ejected spiral arms which inhibited the star from undergoing bifurcation. At $r/r_\circ = 0.80$ at the inner edge of the disk, we again see a negative

total torque. Here, the Reynolds torque is negative and the gravitational torque is positive. At $r/r_\circ \approx 1.05$ slightly outside $r_\circ$ and approximately at the minimum in $\delta\rho$ the total disk torque changes sign. For the $m = 3$ component, we see similar overall trends with the one difference being in the sign of the gravitational torque.

In Figure 35 we show the perturbed kinetic energy E_k, and the perturbed enthalpy (acoustic energy) E_h across the star and the disk (see Kojima 1989). For the $m = 2$ component, a maxima in E_k occurs at $r \approx 0.22$ and a maxima in E_h at $r \approx 0.40$. Comparing these to the phase plots in Figure **??** we see that the maxima in E_k falls where $\delta\rho$ in the star transitions from a bar to spiral arms. The maxima in E_h falls approximately where the $\mathcal{W}$ transitions from a barlike structure to leading spiral arms. We see similar behavior for the $m = 3$ Fourier component, with the maxima in E_h reaching a slightly higher amplitude. For both components, E_k and E_h are close to zero in the disk. In Figure 36 we show the Reynolds stress σ_R, the gravitational stress σ_G, and the acoustic stress σ_h over the star and the disk. A common astrophysical approximation for the viscous stress in a disk is the α-disk model [179]. In α-disk model, the ϕ-r component of the stress tensor $T_{\phi r}$ is assumed to b proportional to the local gas pressure where the constant of proportionality is α such that,

$$T_{\phi r} = \alpha P \tag{4.25}$$

For our models, an effective α can be locally defined. It is clear that $\alpha_{eff} \neq$ constant and that the α-disk model is not applicable to our simulations.

Fission Model: Non-linear Results

In this investigation we considered the 3D nonlinear evolution of our M2 equilibrium star-disk system described in the previous section. Here we present the

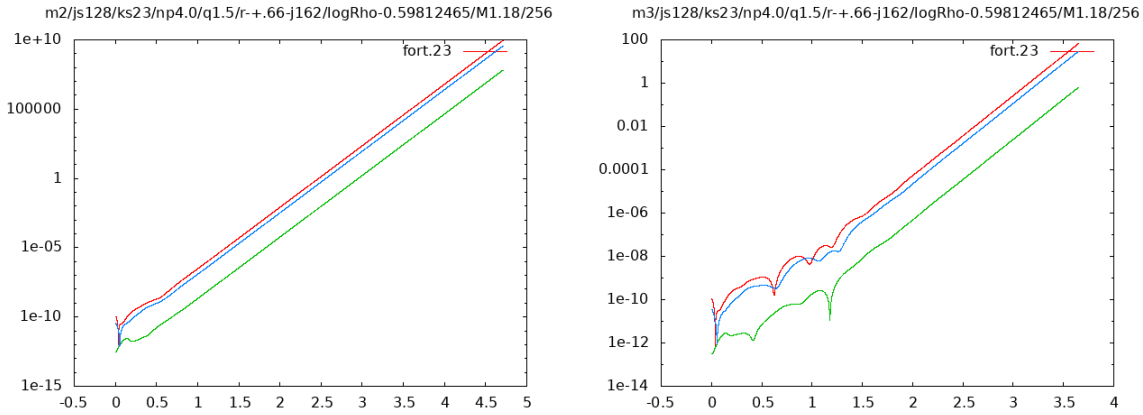

FIGURE 30. The growth rates of the density perturbation for the $m = 2$ Fourier component is plotted on the left and the $m = 3$ on the right. These are measured at three different radii in the disk.

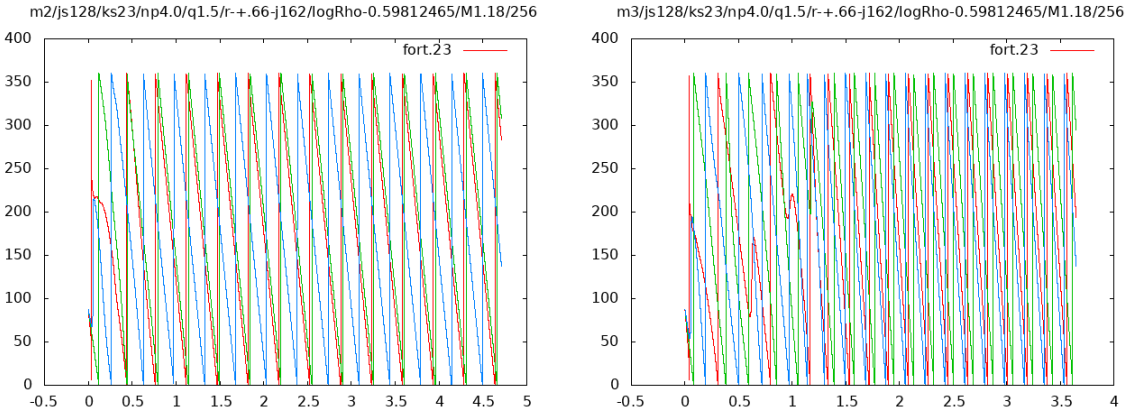

FIGURE 31. The frequencies of the density perturbation for the $m = 2$ Fourier component is plotted on the left and the $m = 3$ on the right. These are measured at three different radii in the disk to make sure there is convergence.

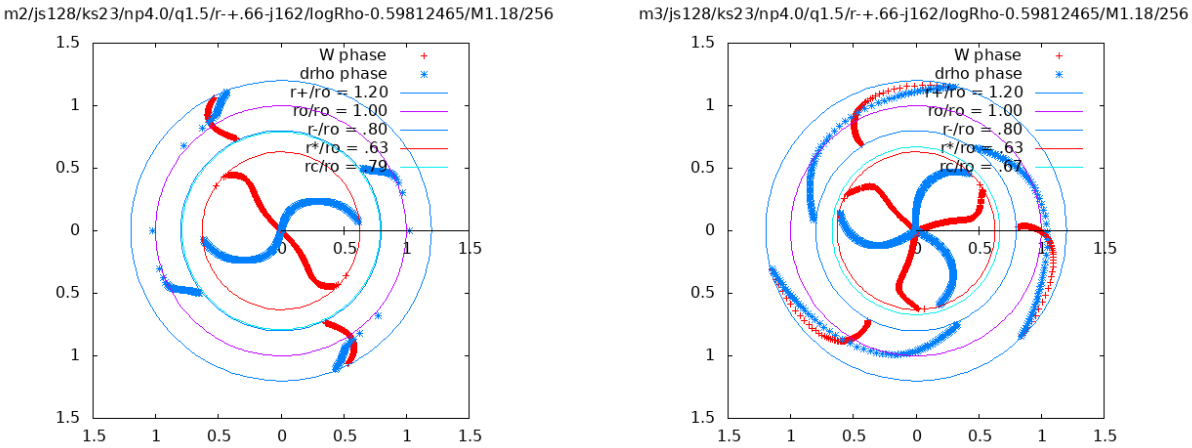

FIGURE 32. Constant phase loci for the M2 model. $\mathcal{W}$ phases are shown with red + symbols while $\delta\rho$ phases are shown with blue + symbols. The outer edge of the star is plotted in red, while the inner and outer edge of the disk are plotted in blue. The maximum density in the disk is plotted in magenta while corotation is plotted in teal. The $m = 2$ Fourier component is plotted on the left and the $m = 2$ on the right.

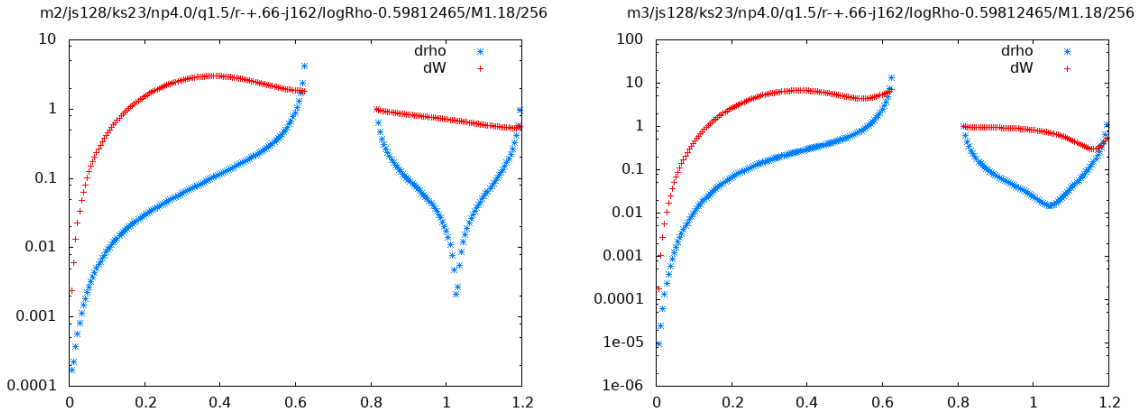

FIGURE 33. $\mathcal{W}$ and $\delta\rho$ eigenfunctions normalized by $r_\circ$ for the M2 Model. The $m = 2$ Fourier component is plotted on the left and the $m = 3$ on the right.

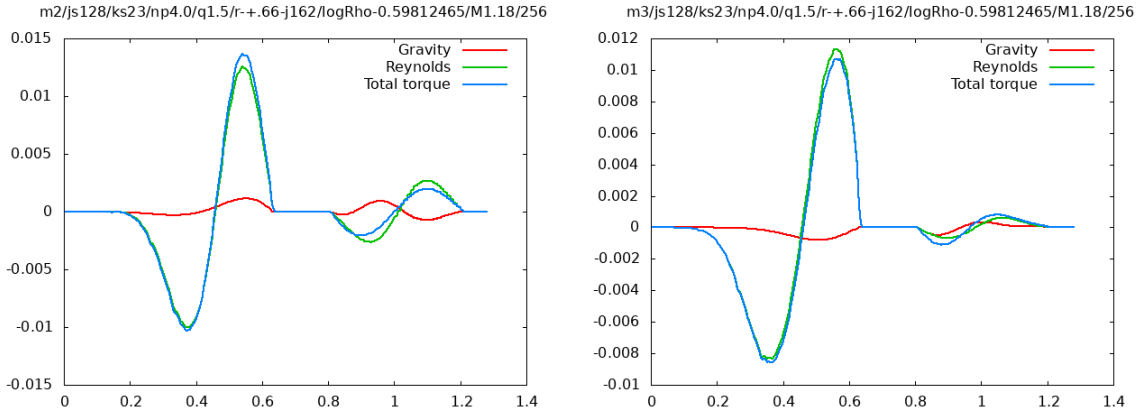

FIGURE 34. Torque plots for the the $m = 2$ Fourier component is plotted on the left and the $m = 3$ on the right. The gravitational torque is shown in red, the Reynolds torque in green and the total torque in blue.

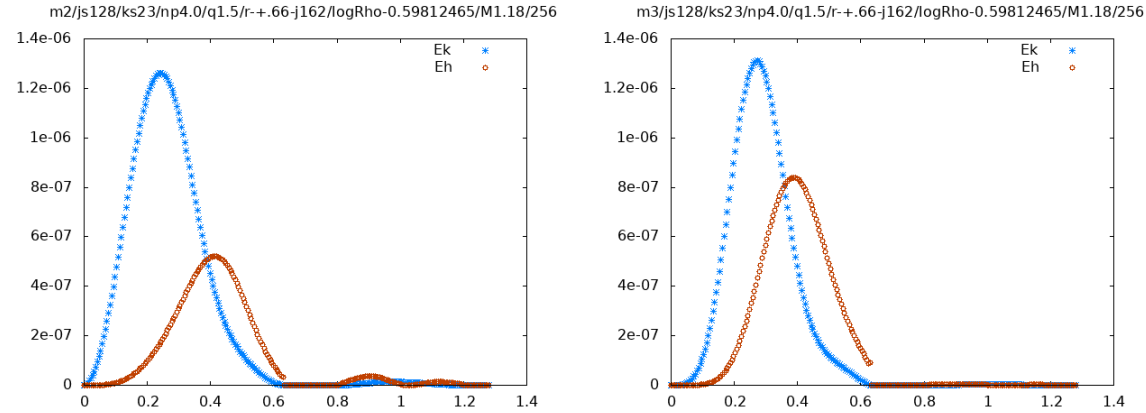

FIGURE 35. The perturbed kinetic energy E_k is plotted with blue asterisks and the perturbed acoustic energy E_h is plotted with red circles in the upper panels with the $m = 2$ Fourier component plotted on the left and the $m = 3$ on the right. The total energy of the mode is plotted in the bottom panel in red.

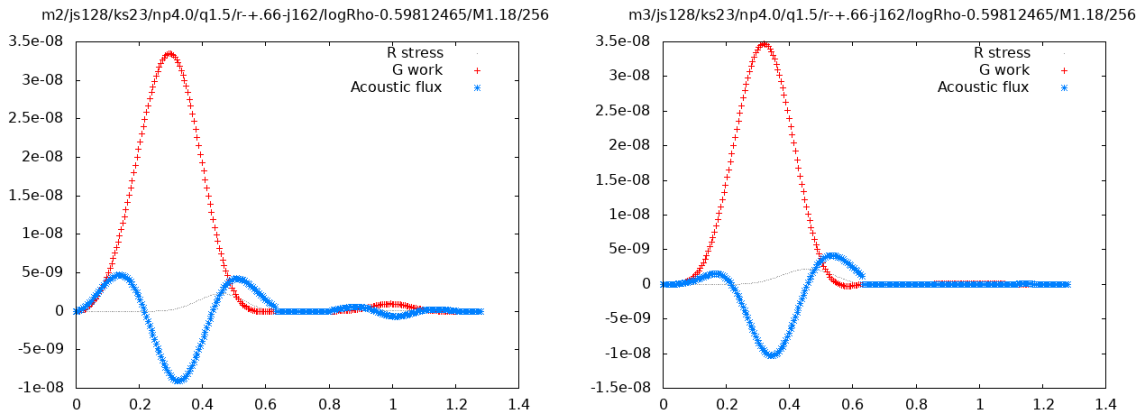

FIGURE 36. The Reynolds stress σ_R is shown in gray dots, the gravitational stress σ_G is shown with red $+'s$, and the acoustic stress σ_h are shown with blue asterisks with the $m = 2$ Fourier component plotted on the left and the $m = 3$ on the right.

results of the nonlinear evolution of this system. We first consider the model without any radiative losses. We compare these results to the results of our linear stability analysis. We then consider the effects of radiative losses to the system by exploring the effects of three different cooling rates scaled to the characteristic timescales of the star and/or disk. We investigate how cooling changes the growth-rates of the fastest growing modes and what effect this has on the nonlinear evolution of the $M2$ system. We make density maps, velocity maps and temperature maps and present quantitative and qualitative analyses of the results of our simulation.

Non-Cooling Case

In Figure 37 we show the integrated Fourier amplitudes of the density perturbation, the A_m, as the system evolves in time. Times are normalized in units of $\tau_\circ$, the equilibrium rotation period for material at density maximum in the disk mid-plane. We can see four distinct stages of evolution for the system: (i) After the initial perturbation is applied to the disk, there is an organizational/settling stage

between $0.0 < t/\tau_\circ < 0.6$. Once the disk has settled the $m = 2$ component goes into steady exponential growth and maintains the highest amplitude throughout the evolution of the system. The initial settling phase closely matches for the linear and nonlinear calculations (See Figure 30). (ii) The system next transitions into steady exponential growth of the $m = 2$ component, the linear stage of evolution, between $0.6 < t/\tau_\circ < 1.6$. During this state we find good agreement with linear calculations. From Figure 37 we estimate that $m = 2$ grows at a rate of $\approx 9.2\tau_\circ^{-1}$ and $m = 3$ grows at a rate of $\approx 7.7\tau_\circ^{-1}$. Comparing to Figure 30, there is very good agreement with the linear calculations which predicted that $m = 2$ grows at a rate of $\approx 9.0\tau_\circ^{-1}$ and $m = 3$ grows at a rate of $\approx 7.7\tau_\circ^{-1}$. The $m = 3$ component begins to grow exponentially around $t/\tau_\circ = 0.8$ followed by $m = 4$ at a rate of $\approx 24.3\tau_\circ^{-1}$. near $t/\tau_\circ = 1.3$ with $m = 6, 7, 8$ near $t/\tau_\circ = 1.4 - 1.6$ at rates $\approx 29.6, 23.0, 51.7\tau_\circ^{-1}$, respectively. The odd-$m = 1, 5$ components never settle into steady exponential growth. (iii) Between $1.6 < \tau_\circ < 2.3$ growth of the perturbations saturate. Here, we expect our quasi-linear theory to apply, initially. We see that even-m components saturate at a much higher amplitude $A_{even} \approx 1.0$ while the odd components initially peaking at $A_{odd} \approx 0.01$ around $\tau_\circ = 1.6$ but eventually settling around $A_{odd} \approx 0.1$ with the $m = 1$ component reaching the highest amplitude $A_1 = 0.34$ for the odd modes. (iv) Beyond saturation $\tau_\circ > 2.3$, the system reaches a new steady state. The model is halted at $\tau_\circ = 2.6$ after 5.2% of the material has flowed off the grid. At this point $A_2 = 1.47$, $A_4 = 0.98$, $A_6 = 0.78$ and $A_6 = 0.55$. Continuing to perform fluxing after material has flowed off the computational grid poses a problem due to the fact that mass and momentum are no longer being conserved. The radial dimension of the computational grid was expanded up $J = 1024$ cells, however, expanding beyond this number of cells becomes too computationally expensive to continue the simulation.

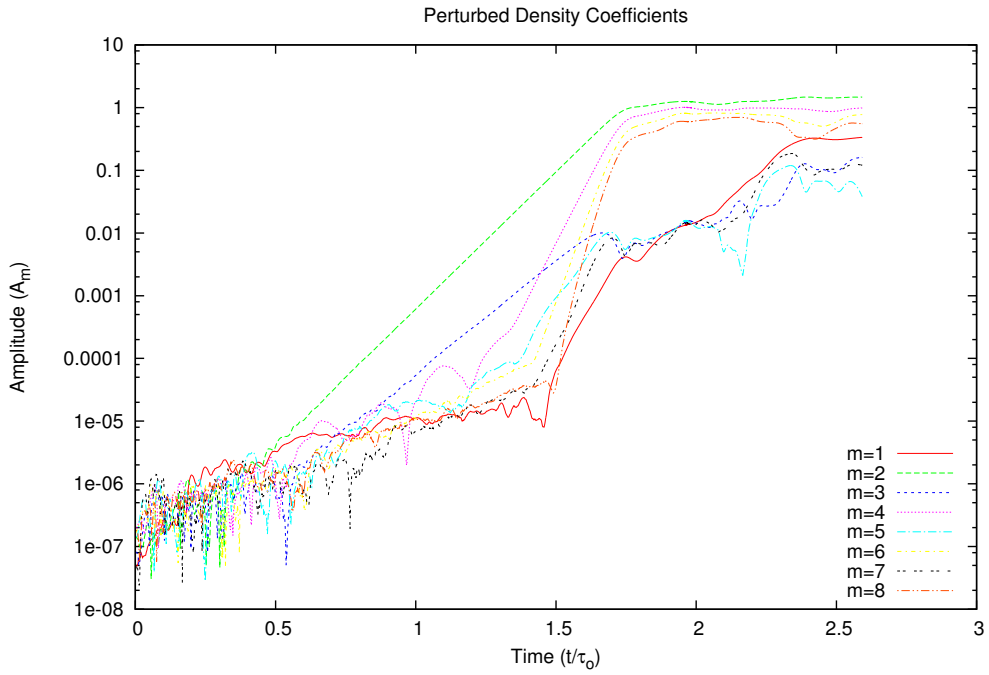

FIGURE 37. Integrated Fourier amplitudes $\mathcal{A}_m$ for $m = 1$ to 8 in the disk midplane for model M2 in the absence of cooling. Times are normalized in units of $\tau_\circ$, the rotation period for material at density maximum in the disk midplane.

Figure 38 gives a time series of integrated midplane density maps for the nonlinear evolution of the $M2$ model showing development of the central stellar bar. Distances are normalized to $r_\circ$ the location of density maximum in the equilibrium disk. Note that the colorbar changes depending on the maximum density. The upper left panel shows the initial system after perturbations have been applied but while the system is still in the settling phase at $t/\tau_{circ} = 0.18$. In the upper right panel, taken at $t/\tau_\circ = 1.6$ when $A_2 = 0.46$ the star develops a central bar with trailing spiral arms near the outer edge while the disk begins to become more eccentric in shape deviating from axisymmetry. Major changes to the density structure of the disk only become apparent to the eye once the instability enters the saturation phase. In the lower left panel when $t/\tau_\circ = 1.7$ and $A_2 = 0.83$ the central bar intersects the disk forming two dense lobes which begin accreting material from the disk. In the lower right panel at $t/\tau_\circ = 1.9$ and $A_2 = 1.2$, the lobes continue to accrete material from the disk and we see that the central object is beginning to bifurcate. Figure 39 gives the subsequent density evolution of the $M2$ model showing the bifurcation of the central object and subsequent formation of the binary system. The upper left panel, is taken at $t/\tau_\circ = 2.1$ when $A_2 = 1.1$ shows the central object undergoing bifurcation. Mass is being transferred to the stars in beautiful twirling loops reminiscent of a cosmic pretzel. (See Discussion section for a comparison with the Bernard 59 dark nebula [BHB2007] 11 forming binary system). The upper right panel shows the system at $t/\tau_\circ = 2.35$ when $A_2 = 1.4$ just after bifurcation, the lower left panel is take at $t/\tau_\circ = 2.5$ when $A_2 = 1.4$ and the lower right is at $t/\tau_\circ = 2.6$ when $A_2 = 1.47$. At this point the system has evolved into two unequal mass binary stars that are still accreting material from the disk. When the system is halted, the binary stars sit at a separation of roughly $\varpi = 1.6r_\circ$.

Figures 40 and 41 show the same time series of integrated midplane density maps with overlaid velocity vectors for the nonlinear evolution of the $M2$ model and Figures 42 and 43 show midplane temperature maps. Velocity vectors are calculated by transforming into the rotating frame of the binary system. Velocity vectors are scaled such that they are visible in the figure, and so only present relative velocities rather than actual values. Temperature maps are created by dividing the internal energy density array $\epsilon(J, L, K)$ by the mass density array $\rho(J, L, K)$ and plotting the result. With this definition,

$$\frac{\epsilon}{\rho} = \frac{kT}{(\gamma - 1)\mu m_p} \tag{4.26}$$

where k is Boltzman's constant, T is the temperature, $\gamma = 5/3$, μ is the mean molecular weight and m_p is the mass of a proton. We can also find kinetic temperature from the average molecular kinetic energy of the gas. In Figure 40, we see that circulation of the fluid is counterclockwise. In the upper right panel of Figure 40, we see the development of the central bar. In the lower left panel, when the central star intersects with the disk, a shockwave is launched away from the forming lobes. Looking at the lower right and left panels of the temperature maps (Figure 42) for the system, we can see the shockwaves being launched and spreading away from the star-disk system. Significant heating occurs at the shockfronts. In the lower right panel of Figure 41 we can see that there is counterclockwise circulation in each of the stellar objects, that they rotate on independent axes and rotate in the same sense. At this point, the maximum density in the primary star is $\rho = 0.12$ and the maximum temperature is $T = 0.2$. The maximum temperature in the shockwave reached $T = 0.7$ when $t/\tau_\circ = 1.7$ and $A_2 = 0.83$.

In Table 8 we calculate the total mass of the stellar "clumps" formed after saturation when $\tau_\circ = 2.6$ and the simulation was halted. In column 1, we label the two clumps. In column 2, we give the value of the maximum density in each clump ρ_{max} in polytrope units. In section *Methods – Unit Conversions* we describe how to transform from polytrope units to any unit system and in Table **??** we give conversion factors for transforming into cgs units for several different choices of initial mass $M_\circ$ for the system and location of density maximum $r_\circ$. Columns 3-4 give the J, L-cell location of density max and columns 5-7 give the cells where density was integrated to approximate the total mass contained in the volume. Note that this is a difficult calculation to do precisely due to the size/shape of the computational grid because cells on the grid are not uniform, they are cylindrical wedges and do not match the spherical symmetry of the stellar clumps. In column 8 we give the total volume in polytrope units and in column 9 we give the total mass contained within that volume. Note that CHYMERA performs calculations in a dimensionless unit system where $G = K = M = 1.0$, therefore values are presented for systems where the total mass $M = 1.0$. At $t/\tau_\circ = 2.6$ a total of 5.2% of the material had flowed off the computational grid. At this point, we find that the two stellar components are unequal in mass with the primary stellar component containing roughly 46% of the initial mass of the system and the secondary stellar component containing roughly 27%. The remaining 21.8% of the mass on the computational grid is contained in the remaining disk filaments.

In Figure 44 shows the location of constant $\delta\rho$-phase in the disk midplane for the $m = 2$ component of the $M2$ model at $t/\tau_\circ = 1.57$ just before saturation. The equilibrium values for the outer edge of the star r_*, location of corotation r_{co}, inner edge of the disk r_-, location of density maximum in the disk $r_\circ$ and the disk outer

edge r_+ are shown with all values normalized by $r_\circ$. We find very good agreement with the linear calculations (See Figure **??**). Rotation is in the counter clockwise direction. The central star exhibits a bar with trailing spiral arms. The disk $\delta\rho$-phase shows a bar at the inner edge of the disk connected to a trailing π/m phase shift slightly outside $r_\circ$ which then extends to a outer bar. At the inner edge of the disk, the $\delta\rho$-phase is $2/9\pi$ ahead of the star.

In Figure 45 we plot the cosine of the $\delta\rho$-phase for the $m = 2$ component taken inside the central star at $r/r_\circ = 0.32$. A fitting function $f(t) = cos(18.1 * t + 4.3)$ overlaid the nonlinear data. Times are normalized by $\tau_\circ$. We can see that the star goes through an initial settling phase in which the perturbation is still organizing itself until $t/\tau_\circ \approx 0.9$ when the perturbation goes into steady oscillation. In figure 46 we plot the cosine of the $\delta\rho$-phase for the $m = 2$ component taken inside the disk at $r/r_\circ = 1.0$. A slightly shifted function $f(t) = cos(18.1 * t + 5.1)$ is overlaid with the nonlinear data. The disk takes less time to organize, with steady oscillation beginning at $t/\tau_\circ \approx 0.6$. The period of this oscillation is $0.347t/\tau_\circ$ from the fitting function which corresponds to a frequency of 2.88.

In figures 47, 48, 49 and 50, we plot the total angular momentum contained in a cylindrical annulus as a function of the disk radius normalized by $r_\circ$ (top) and the total mass contained in a cylindrical annulus as a function of the disk radius (bottom) at $t/\tau_\circ = 0.18$ (red) corresponding to the upper left panel of Figure 38 compared to four different later times in the system's evolution (green). Figure 47 shows the momentum and mass at time $t/\tau_\circ = 1.57$ just before saturation of the instability when we would expect good agreement with the linear calculations. Recall that the time rate of change of angular momentum is equal to torque and so these plots can be used to (roughly) visualize how torques affect the mass transport in the system. In

regions where $0.20 > r/r_\circ = 0.45$ there is negative torque, between $0.45 > r/r_\circ = 0.70$ torque changes sign and becomes positive, and between $0.90 > r/r_\circ = 1.05$ torque is again negative and finally for $1.05 > r/r_\circ = 1.20$ torque is positive. Comparing these to figure 34 confirms that the linear calculations provide a good prediction of the nonlinear results during this stage in the evolution of the system. A positive torque corresponds to fluid material speeding up in its orbit. Roughly speaking, to conserve angular momentum, we would expect material experiencing positive torque to move outward to larger radii while material experiencing a negative torque would tend to move inward. Figure 48 shows the momentum and mass at time $t/\tau_\circ = 1.7$ and corresponds to the lower left panel of 38. At $t/\tau_\circ = 1.7$ just after the linear phase of the evolution has ended and saturation of the instability is taking hold, significant mass redistribution occurs in the system. The central star has positive torque inside $r/r_\circ = 0.2$ and negative torque between $0.2 > r/r_\circ = 0.5$. Between $0.5 > r/r_\circ = 0.8$, torque is again negative, while the central part of the disk from $0.8 > r/r_\circ = 1.2$ again experiences positive torque. Figures 49 and 50 show the mass and momentum at times $t/\tau_\circ = 2.1$ and $t/\tau_\circ = 2.6$, respectively, corresponding to the upper left and lower right panels of Figure 39.

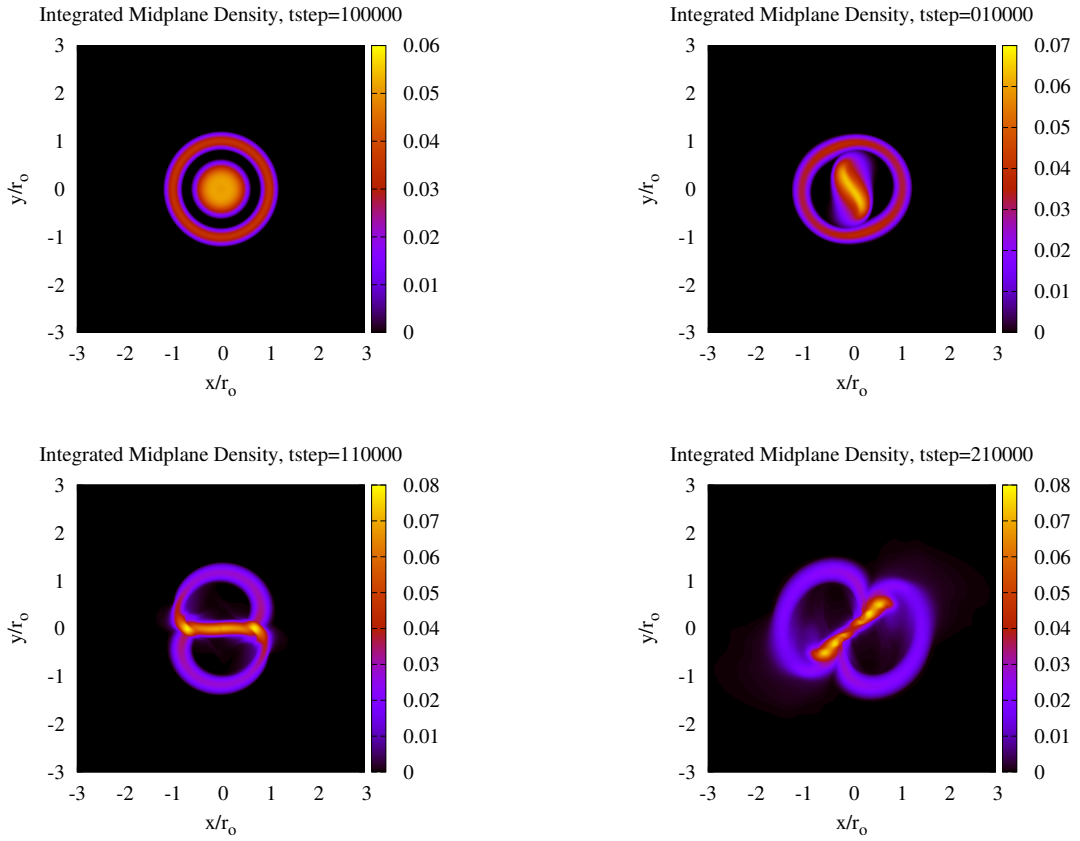

FIGURE 38. Integrated midplane density map for the nonlinear evolution of the $M2$ model in the absence of cooling showing the formation of the central stellar bar. Distances are normalized to $r_\circ$ the location of density maximum in the equilibrium disk.

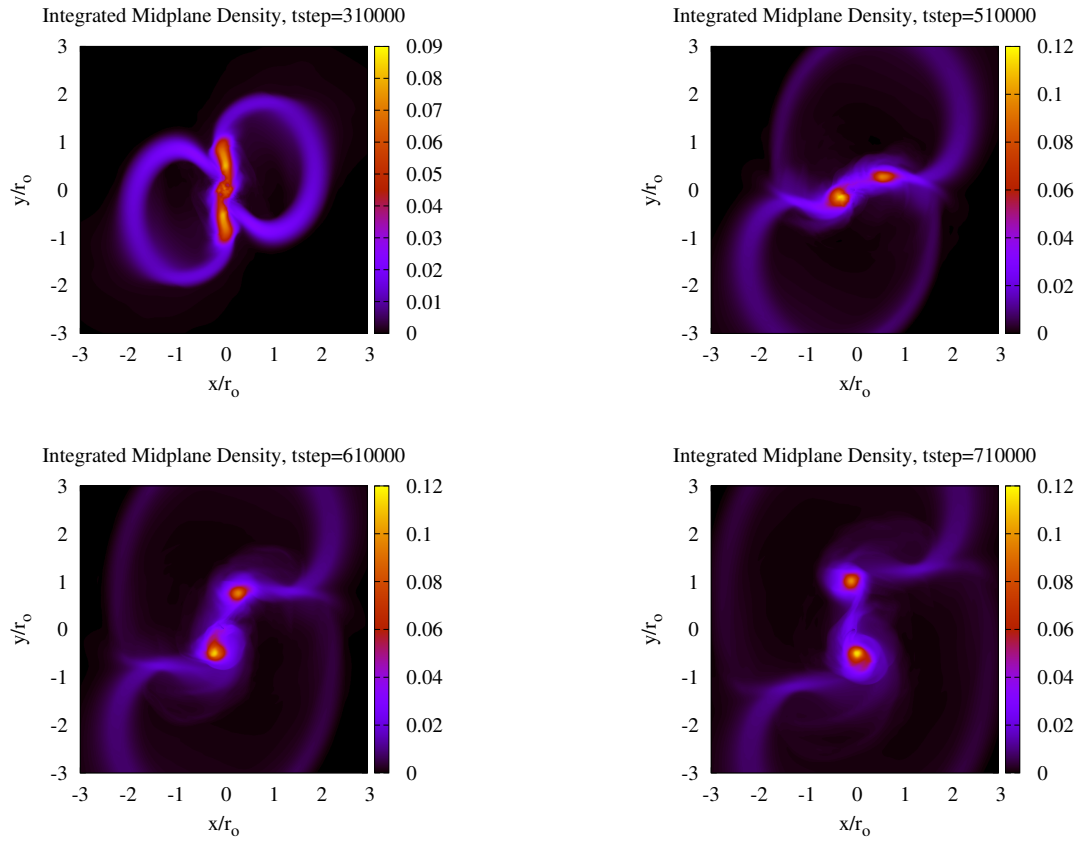

FIGURE 39. Integrated midplane density map of the nonlinear evolution of the $M2$ model in the absence of cooling showing stellar bifurcation and subsequent evolution of the binary system. Distances are normalized to $r_\circ$ the location of density maximum in the equilibrium disk.

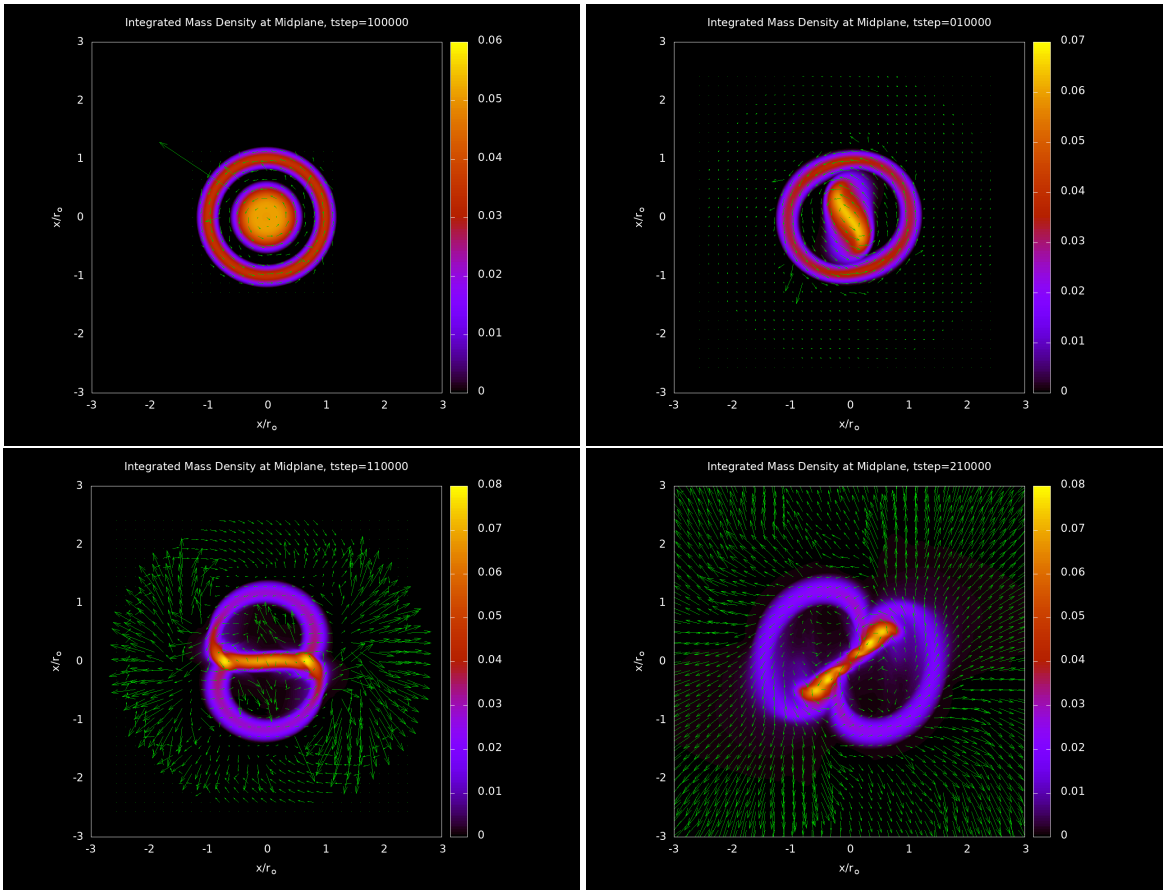

FIGURE 40. Integrated midplane density map with overlaid velocity vectors for the nonlinear evolution of the $M2$ model in the absence of cooling showing the formation of the central stellar bar. Distances are normalized to $r_\circ$ the location of density maximum in the equilibrium disk.

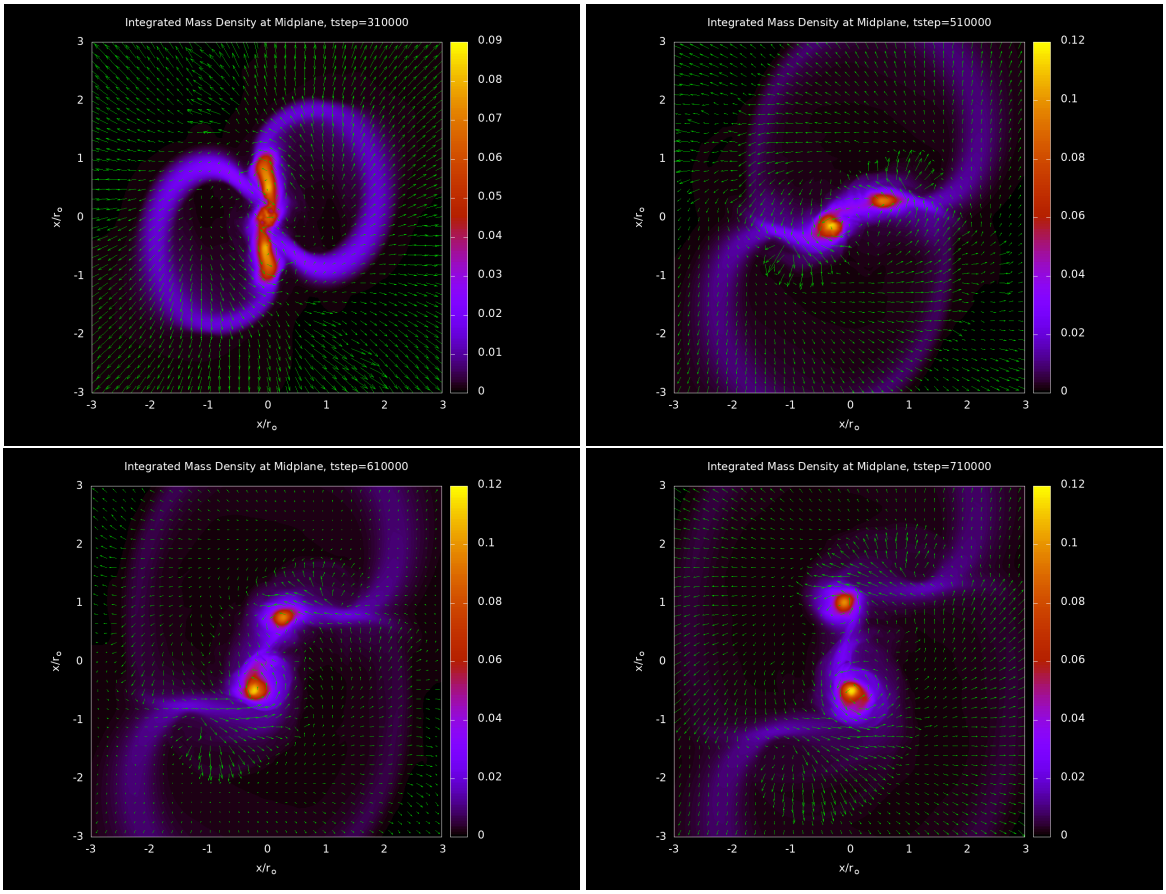

FIGURE 41. Integrated midplane density map with overlaid velocity vectors for the nonlinear evolution of the $M2$ model in the absence of cooling showing stellar bifurcation and subsequent evolution of the binary system. Distances are normalized to $r_\circ$ the location of density maximum in the equilibrium disk.

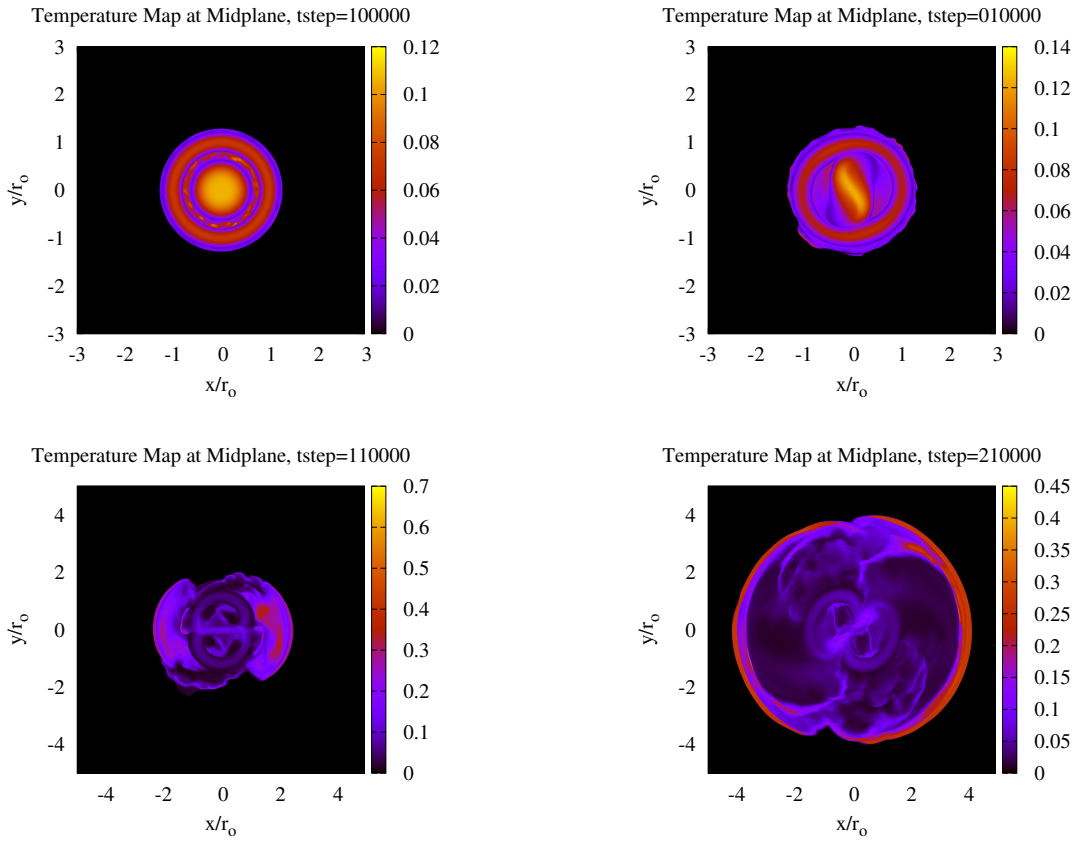

FIGURE 42. Midplane temperature map for the nonlinear evolution of the $M2$ model in the absence of cooling showing the formation of the central stellar bar. Distances are normalized to $r_\circ$ the location of density maximum in the equilibrium disk.

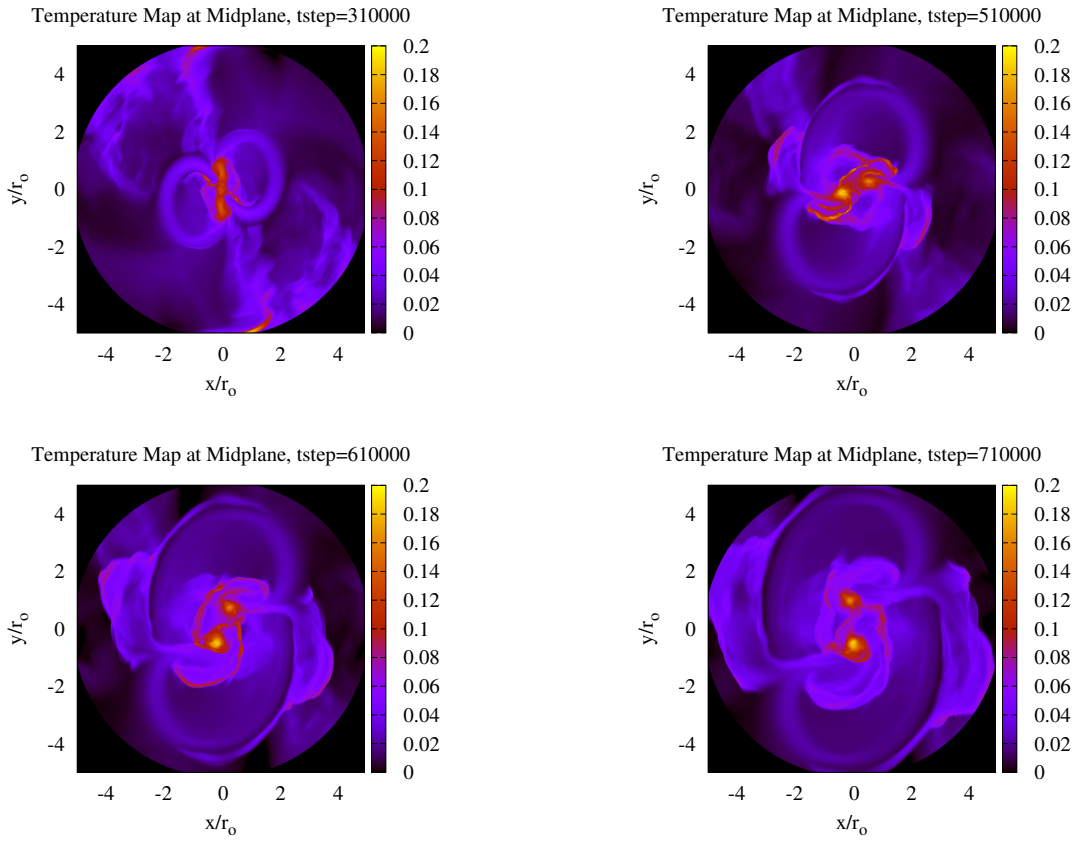

FIGURE 43. Midplane temperature map for the nonlinear evolution of the $M2$ model in the absence of cooling showing stellar bifurcation and subsequent evolution of the binary system. Distances are normalized to $r_\circ$ the location of density maximum in the equilibrium disk.

Weak Cooling, $\tau_c \gg \tau_\circ$

Here we present the results of our nonlinear calculations including weak cooling where $\tau_c = 5\tau_\circ = 15.2\tau_{cen}$. With this definition the volumetric cooling rate used in the energy equation becomes $\Lambda = \epsilon/5\tau_\circ$. Weak cooling is defined to be on a timescale slower than the timescale over which the instability is growing/oscillating. For non-cooling case the instability saturates after 1.6 $\tau_\circ$. Recall that Gammie (2001) derived a cooling criteria for 2D thin disks which states that if the timescale for the local

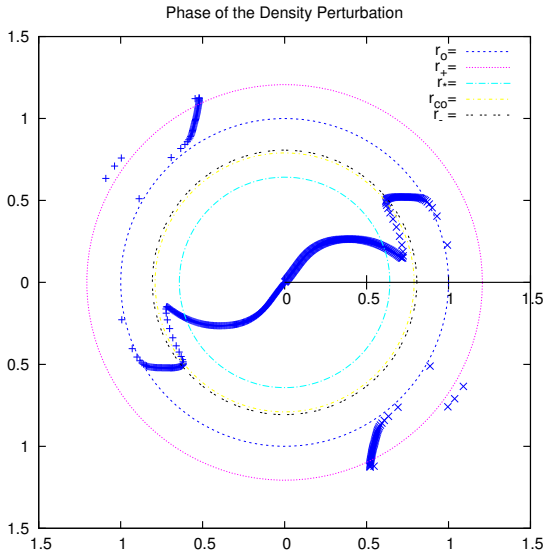

FIGURE 44. Constant phase loci for the $M2$ model in the absence of cooling showing $\delta\rho$ phase of the $m = 2$ component at $t/\tau_\circ = 1.57$. The equilibrium values for the outer edge of the star r_*, location of corotation r_{co}, inner edge of the disk r_-, location of density maximum in the disk $r_\circ$ and the disk outer edge r_+ are shown. Values are normalized by $r_\circ$.

Table 8. Clump analysis for the $M2$ model in the absence of cooling

Clump	ρ_{max}	J	L	ΔJ	ΔL	ΔK	Volume	Mass
1	1.7757e-3	104	196	166-236	24-184	0-64	0.02935	0.45890
2	4.3419e-3	200	67	150-250	37-97	0-64	0.03986	0.27201

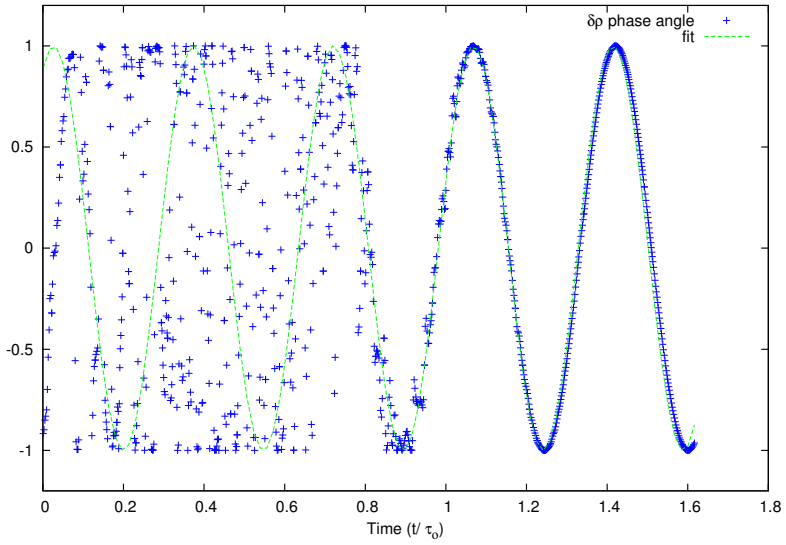

FIGURE 45. Phase angle plot for the $M2$ model in the absence of cooling showing the cosine of the $\delta\rho$ phase angle for the $m = 2$ component in blue taken inside the central star at $r/r_\circ = 0.32$. A fitting function $f(t) = cos(18.1 * t + 4.3)$ is plotted in green. Times are normalized by $\tau_\circ$.

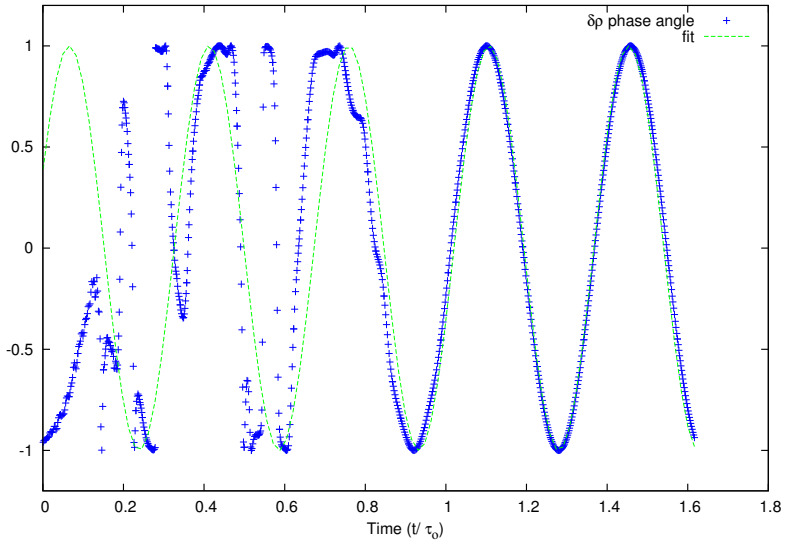

FIGURE 46. Phase angle plot for the $M2$ model in the absence of cooling showing the cosine of the $\delta\rho$ phase angle for the $m = 2$ component in blue taken inside the disk at $r/r_\circ = 1.0$. A fitting function $f(t) = cos(18.1 * t + 5.1)$ is plotted in green. Times are normalized by $\tau_\circ$.

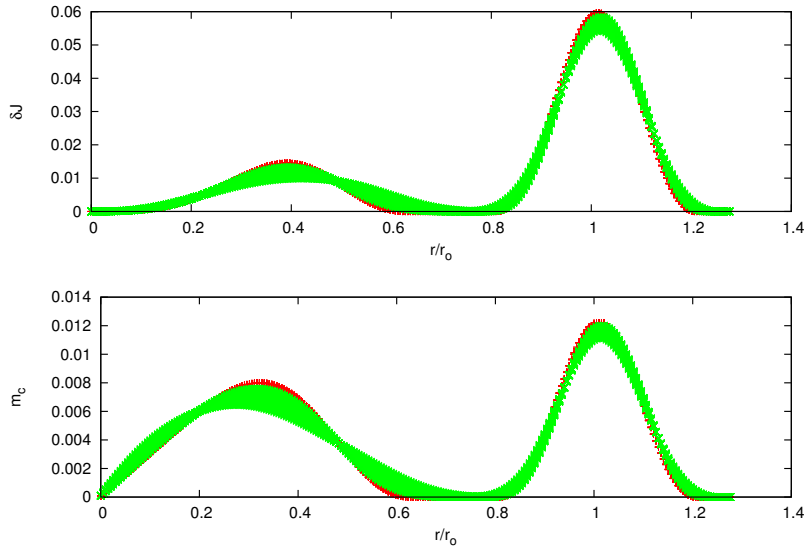

FIGURE 47. Angular momentum δJ and cylindrical mass fraction m_c for the $M2$ model in the absence of cooling at times $\tau_\circ = 0.18$ (red) and 1.57 (green).

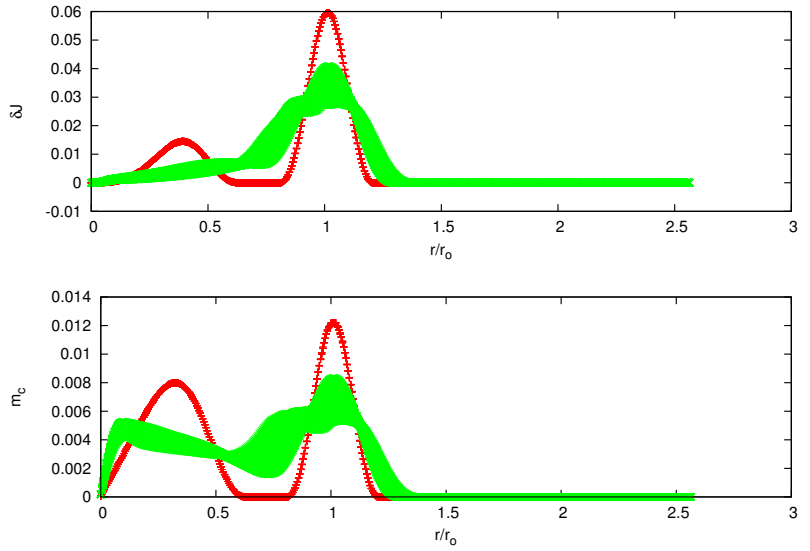

FIGURE 48. Angular momentum δJ and cylindrical mass fraction m_c for the $M2$ model in the absence of cooling at times $\tau_\circ = 0.18$ (red) and 1.7 (green).

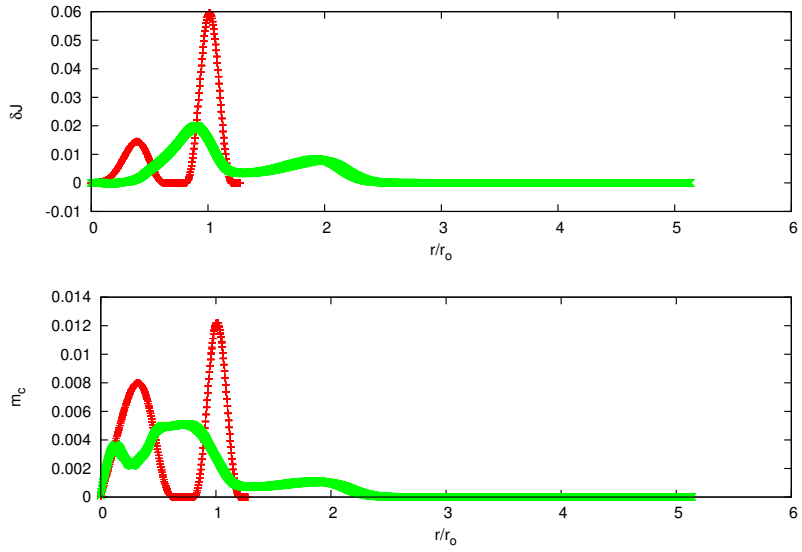

FIGURE 49. Angular momentum δJ and cylindrical mass fraction m_c for the $M2$ model in the absence of cooling at times $\tau_\circ = 0.18$ (red) and 2.1 (green).

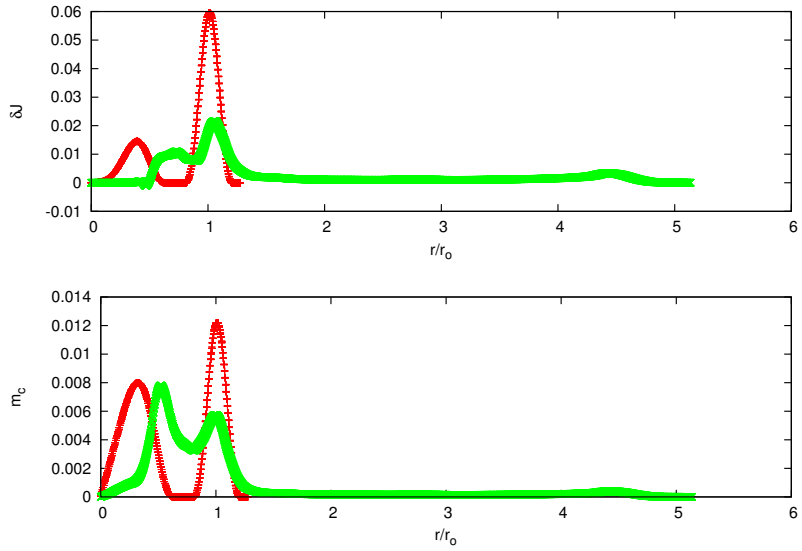

FIGURE 50. Angular momentum δJ and cylindrical mass fraction m_c for the $M2$ model in the absence of cooling at times $\tau_\circ = 0.18$ (red) and 2.60 (green).

internal energy to dissipate is more or less equivalent to the local orbital timescale, clump production will follow [71].

We show the integrated Fourier amplitudes of the density perturbation for the nonlinear evolution of the $M2$ model with the inclusion of weak cooling in (See Figure 51). Again, there are four distinct stages in the evolution of the system. (i) After the initial perturbation is applied to the disk, there is a organizational/settling stage between $0.0 < \tau_\circ < 0.4$ after which the $m = 2$ Fourier component goes into steady exponential growth maintaining the highest amplitude throughout the evolution of the system. In the presence of weak cooling, the model spends less time in organizational/settling phase of its evolution as compared to the non-cooling case. (ii) The system next transitions into steady exponential growth of the $m = 2$ component, the linear stage of evolution, between $0.4 < t/\tau_\circ < 1.3$. Compared to the non-cooling case, exponential growth in the $m = 3$ component begins at $\tau_\circ = 0.6$ again, followed by the $m = 4$ near $\tau_\circ = 1.2$. The growth rate in the $m = 3$ component is larger with the addition of weak cooling compared to the case where no radiative losses were considered. From figure 51, we estimate that $m = 2$ grows at a rate of $\approx 10.8\tau_\circ^{-1}$ and $m = 3$ grows at a rate of $\approx 10.1\tau_\circ^{-1}$. This represents a 17.4% difference for $m = 2$ and 31.2% difference for the $m = 3$ growth rate as compared to the non-cooling case. The $m = 4$ grows at a rate of $\approx 24.3\tau_\circ^{-1}$. near $t/\tau_\circ = 1.2$ with all other even and odd components reaching steady exponential growth between $t/\tau_\circ = 1.2 - 1.4$ at rates $\approx 20.7, 29.6, 29.6, 51.8\tau_\circ^{-1}$, for the $m = 5 - 8$ components, respectively. (iii) Between $1.3 < \tau_\circ < 1.7$ growth of the perturbation saturates. We see that even-m components saturate at a much higher amplitude $A_{even} \approx 1.0$ while the odd components initially peaking at $A_{odd} \approx 0.01$ around $\tau_\circ = 1.6$, then briefly increasing in amplitude around $\tau_\circ = 1.9$ to $A_{odd} \approx 0.05$. (iv) Beyond saturation

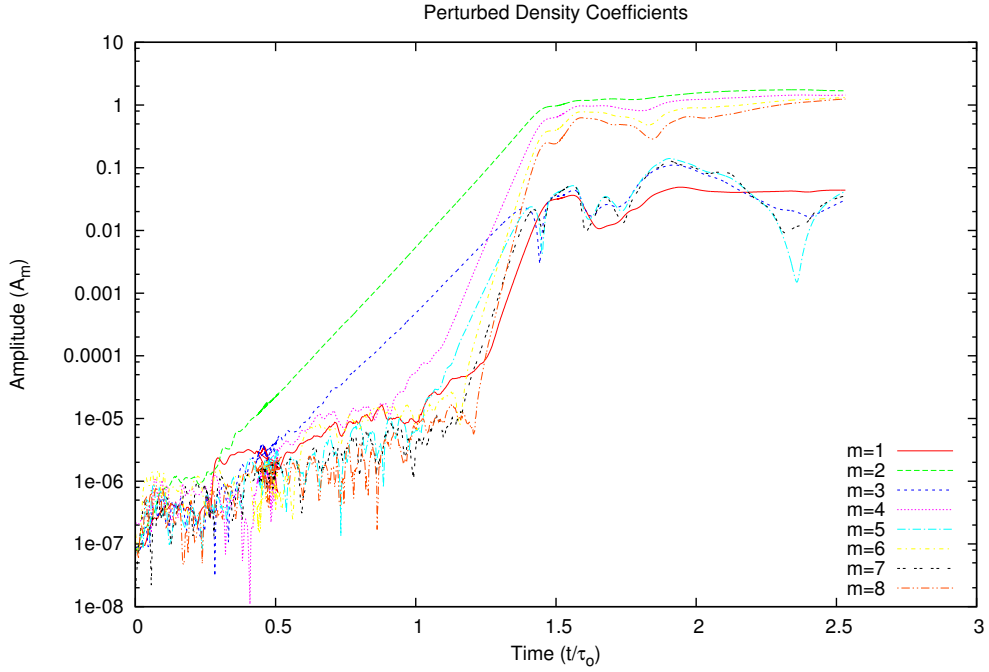

FIGURE 51. Integrated Fourier amplitudes $\mathcal{A}_m$ for $m = 1$ to 8 in the disk midplane for model $M2$ including weak cooling. Times are normalized in units of $\tau_\circ$, the rotation period for material at density maximum in the equilibrium disk midplane.

$\tau_\circ > 1.7$, the system reaches a new steady state in which the even-m remain at $A_m \approx 1.0$ and odd-m at $A_m \approx 0.5$. The model is halted at $\tau_\circ = 2.53$ after 5.5% of the material has flowed off the grid. At this point $A_2 = 1.68$, $A_3 = 0.03$, $A_4 = 1.44$, $A_5 = 0.42$, $A_6 = 1.32$, $A_7 = 0.36$, $A_8 = 1.24$.

In Figure 52 we present integrated midplane density maps for the nonlinear evolution of the $M2$ model including weak cooling showing the formation of the central stellar bar and in Figure 53 showing stellar bifurcation and subsequent evolution of the binary system. Distances are normalized to $r_\circ$ the location of density maximum in the equilibrium disk. The upper left panel shows the initial system after perturbations

have been applied but while the system is still in the settling phase at $t/\tau_{circ} = 0.12$. In the upper right panel, taken at $t/\tau_\circ = 1.36$ when $A_2 = 0.33$, when the star begins to develop a central bar with trailing spiral arms near the outer edge. The disk becomes more eccentric in shape deviating from axisymmetry. Major changes to the density structure of the disk only begin once the instability enters the saturation phase. In the lower left panel when $t/\tau_\circ = 1.42$ and $A_2 = 0.67$ the central bar becomes more compact/slender due to the loss of pressure support from cooling. In the lower right panel at $t/\tau_\circ = 1.56$ with $A_2 = 1.13$, the central stellar bar intercepts the disk forming two dense lobes which begin accreting material from the disk. When this happens, shock waves are again launched. Figure 39 gives the subsequent density evolution of the $M2$ model showing the bifurcation of the central object and subsequent formation of the binary system. The upper left panel, is taken at $t/\tau_\circ = 1.73$ when $A_2 = 1.24$ and shows the central object undergoing bifurcation. Again, the disk is reminiscent of the [BHB2007] 11 proto-binary system. The upper right panel shows the system at $t/\tau_\circ = 1.85$ when $A_2 = 1.32$ just after bifurcation of the stellar object. The lower left panel is taken at $t/\tau_\circ = 2.11$ when $A_2 = 1.65$ and shows the system evolving into to equal mass binary pairs with a separation of approximately $\varpi = 1.8r_\circ$. The stars are still accreting mass from the remaining disk. The lower right is at $t/\tau_\circ = 2.53$ when $A_2 = 1.68$. At this point the system has evolved into two equal mass binary stars. The disk at this point is very diffuse. When weak cooling is included the odd-m Fourier components never reach the saturation amplitudes of the even-m components. This may account for the even symmetry of the system's evolution. When the simulation is halted, the binary stars sit at a separation of roughly $\varpi = 2.5r_\circ$.

We show the integrated midplane density after saturation of the instability at $\tau_\circ = 2.53$ after the star has fissioned into two stellar objects and when the simulation

was halted in Figure 58 and the integrated midplane density map with overlaid velocity vectors in Figure 59. The velocity vectors show that there is circulation about a rotation axis in each stellar object. We can also see that material continues to accrete from the disk onto the two stars.

Figures 54 and 55 show the same time series of integrated midplane density maps with overlaid velocity vectors for the nonlinear evolution of the $M2$ model including weak cooling and Figures 56 and 57 show midplane temperature maps. In Figure 54 we see that circulation of the fluid is counterclockwise. In the upper right and lower left panels of Figure 54, we see the development of the central bar. In the lower right panel, when the central star intersects with the disk, a shockwave is launched away from the forming lobes. Looking at the lower right panel of figure 56 we can see shockwaves being launched and spreading away from the star-disk system. Significant heating occurs at the shockfront. In the upper left panel of 57 the shockwave has steepened forming a circular wave with very high temperatures $T = 3.5$ that spreads away from the disk located at roughly $4r_\circ$. These are temperatures 14 times higher than that of the final stellar temperatures. The next three panels show temperature evolution of the central stellar objects after the shockwave has left the computational grid. In the lower right panel of Figure 55 we can see that there is counterclockwise circulation in each of the stellar objects that forms nearly circular streamlines. At this point, the maximum density in the primary star is $\rho = 0.06$ and the maximum temperature is $T = 0.25$.

In Table **??** we calculate the total mass of the stellar "clumps" formed after saturation when $\tau_\circ = 2.53$ and the simulation has been halted. In column 1, we label the two clumps. In column 2, we give the value of the maximum density in each clump ρ_{max} in polytrope units. In section *Methods – Unit Conversions* we describe

how to transform from polytrope units to any unit system and in Table **??** we give conversion factors for transforming into cgs units for several different choices of initial mass $M_\circ$ for the system and location of density maximum $r_\circ$. Columns 3-4 give the J, L-cell location of density max and columns 5-7 give the cells where density was integrated to approximate the total mass contained in the volume. Note that this is a difficult calculation to do precisely due to the size/shape of the computational grid because cells on the grid are not squares, they are wedges and do not match the spherical symmetry of the stellar clumps. In column 8 we give the total volume in polytrope units and in column 9 we give the total mass contained within that volume. Note that CHYMERA performs calculations in a dimensionless unit system where $G = K = M = 1.0$, therefore values are presented for systems where the total mass $M = 1.0$. At $\tau_\circ = 2.5$ a total of 5.5% of the material had flown off the grid. At this point we find that the two stellar components are roughly equal in mass with the primary stellar component containing roughly 43% of the initial mass of the system and the secondary stellar component containing roughly 40%. The remaining 11.5% of the mass on the computational grid is contained in the disk filaments.

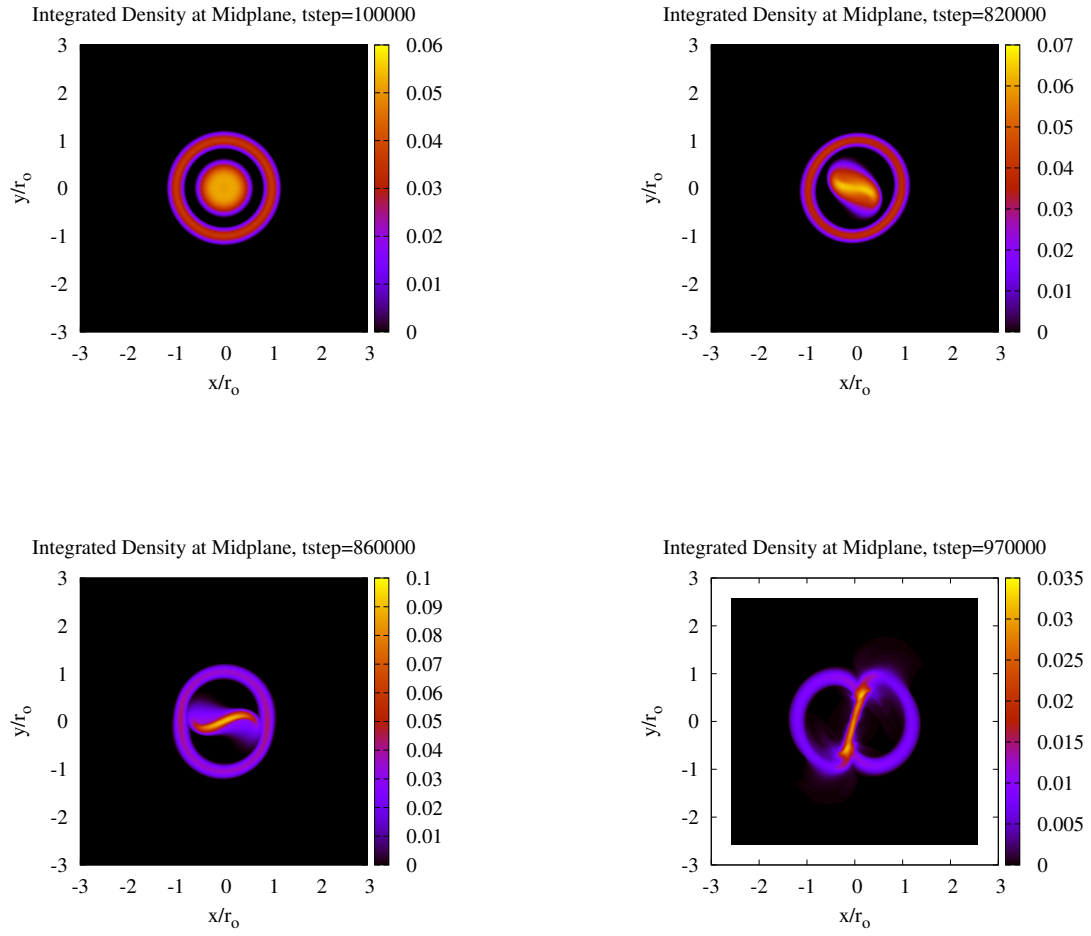

FIGURE 52. Integrated midplane density map for the nonlinear evolution of the $M2$ model including weak cooling showing the formation of the central stellar bar. Distances are normalized to $r_\circ$ the location of density maximum in the equilibrium disk.

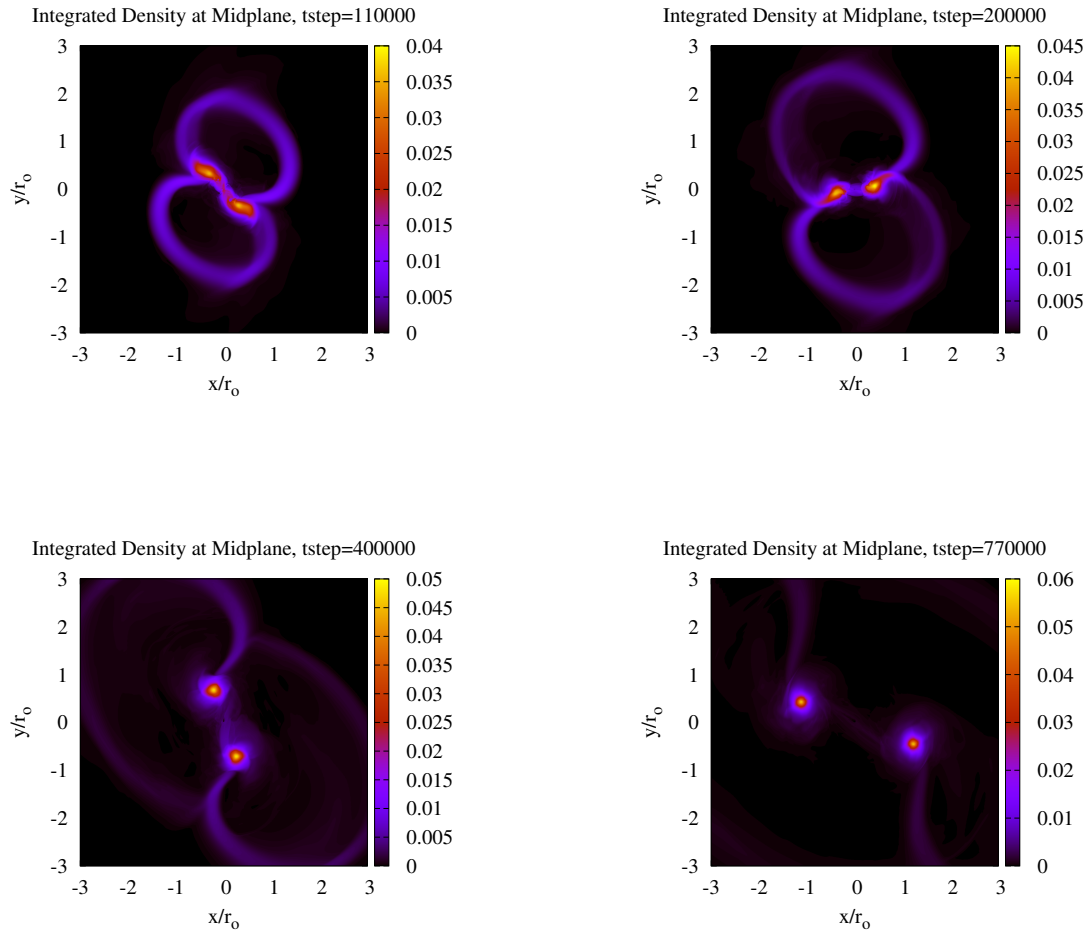

FIGURE 53. Integrated midplane density map of the nonlinear evolution of the $M2$ model including weak cooling showing stellar bifurcation and subsequent evolution of the binary system. Distances are normalized to $r_\circ$ the location of density maximum in the equilibrium disk.

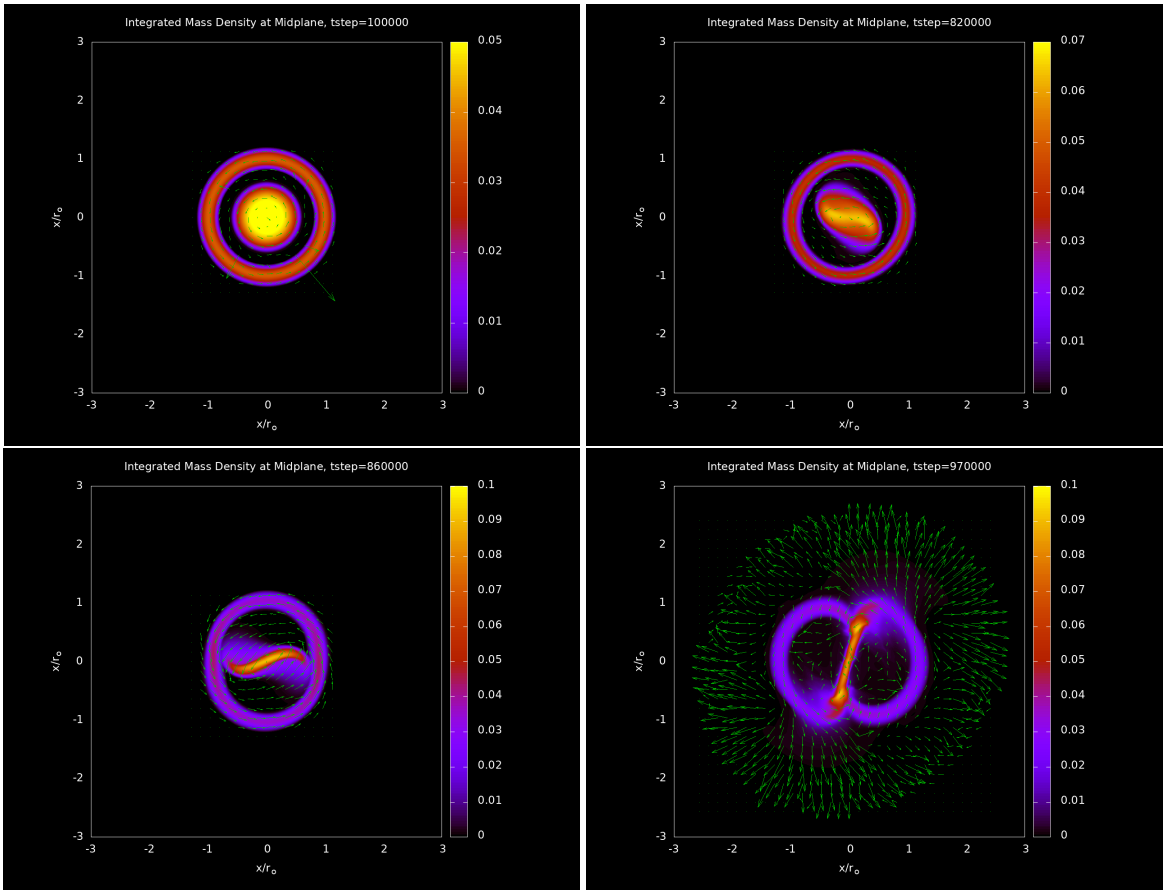

FIGURE 54. Integrated midplane density map with overlaid velocity vectors for the nonlinear evolution of the $M2$ model including weak cooling showing the formation of the central stellar bar. Distances are normalized to $r_\circ$ the location of density maximum in the equilibrium disk.

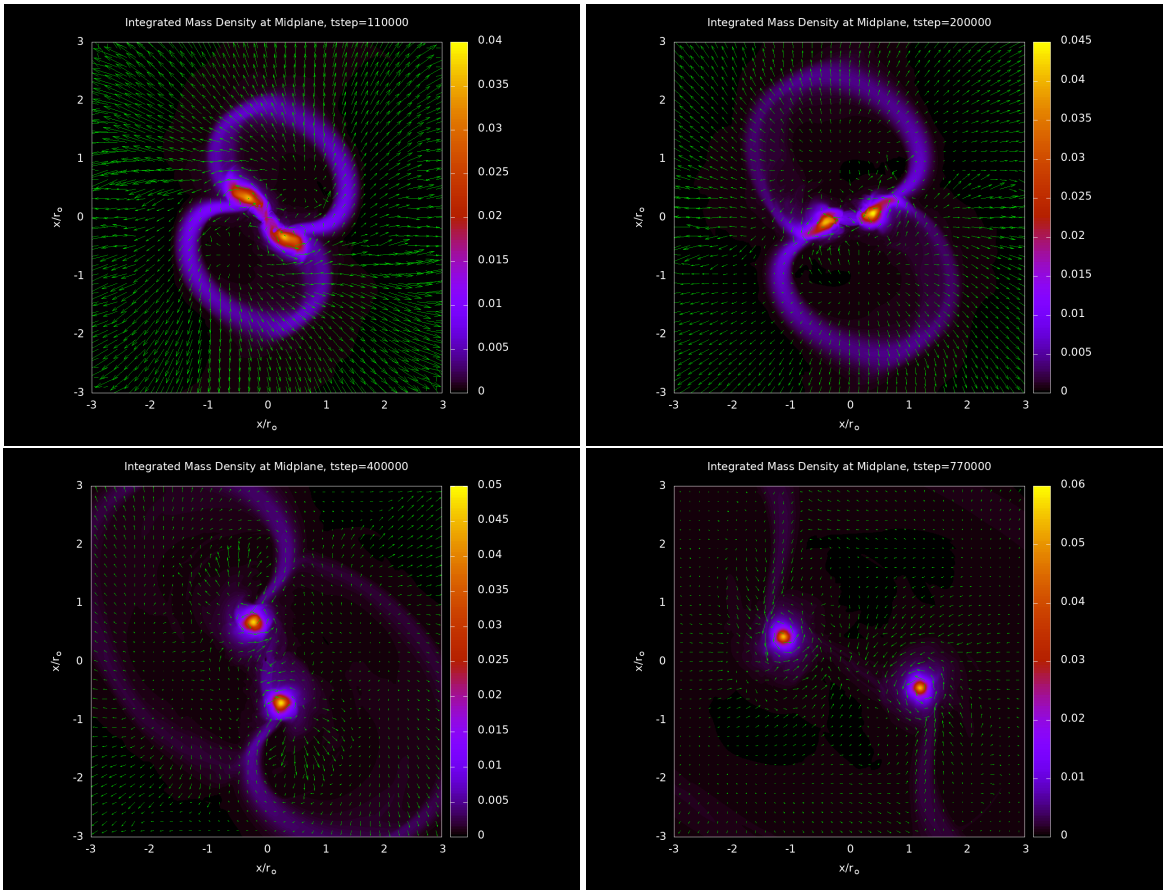

FIGURE 55. Integrated midplane density map with overlaid velocity vectors for the nonlinear evolution of the $M2$ model including weak cooling showing stellar bifurcation and subsequent evolution of the binary system. Distances are normalized to $r_\circ$ the location of density maximum in the equilibrium disk.

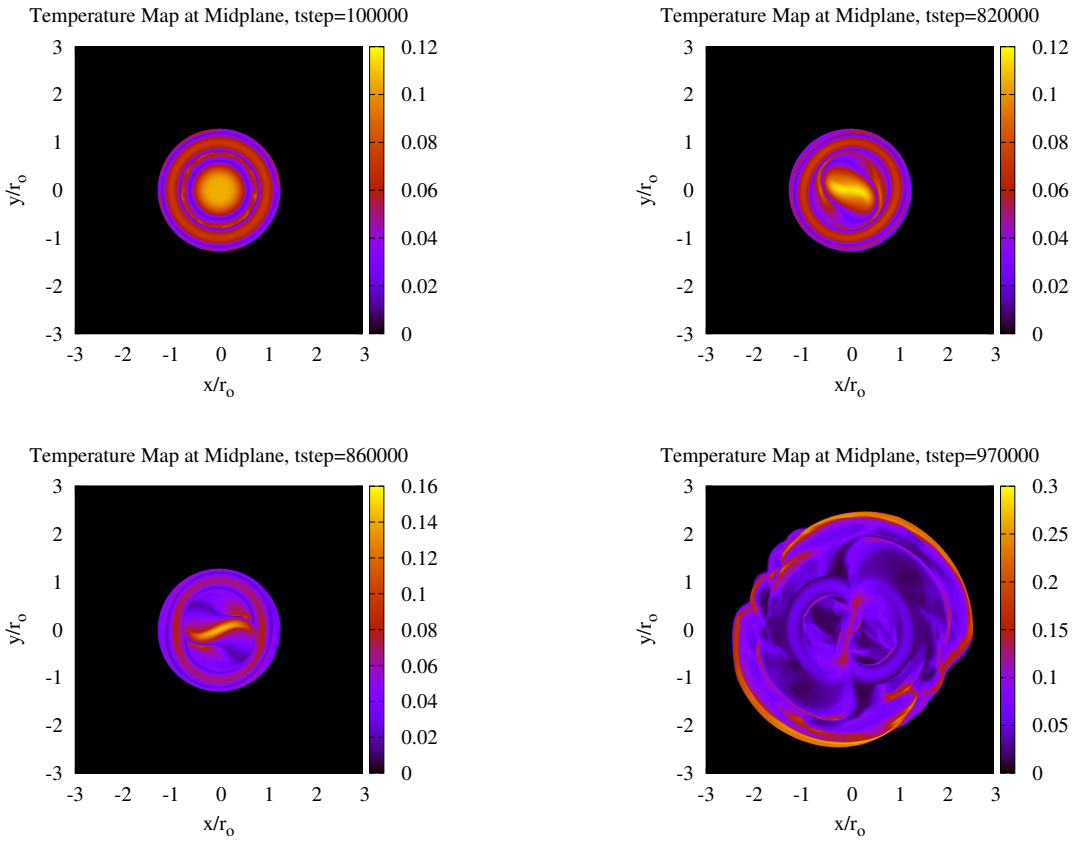

FIGURE 56. Midplane temperature map for the nonlinear evolution of the $M2$ model including weak cooling showing the formation of the central stellar bar. Distances are normalized to $r_\circ$ the location of density maximum in the equilibrium disk.

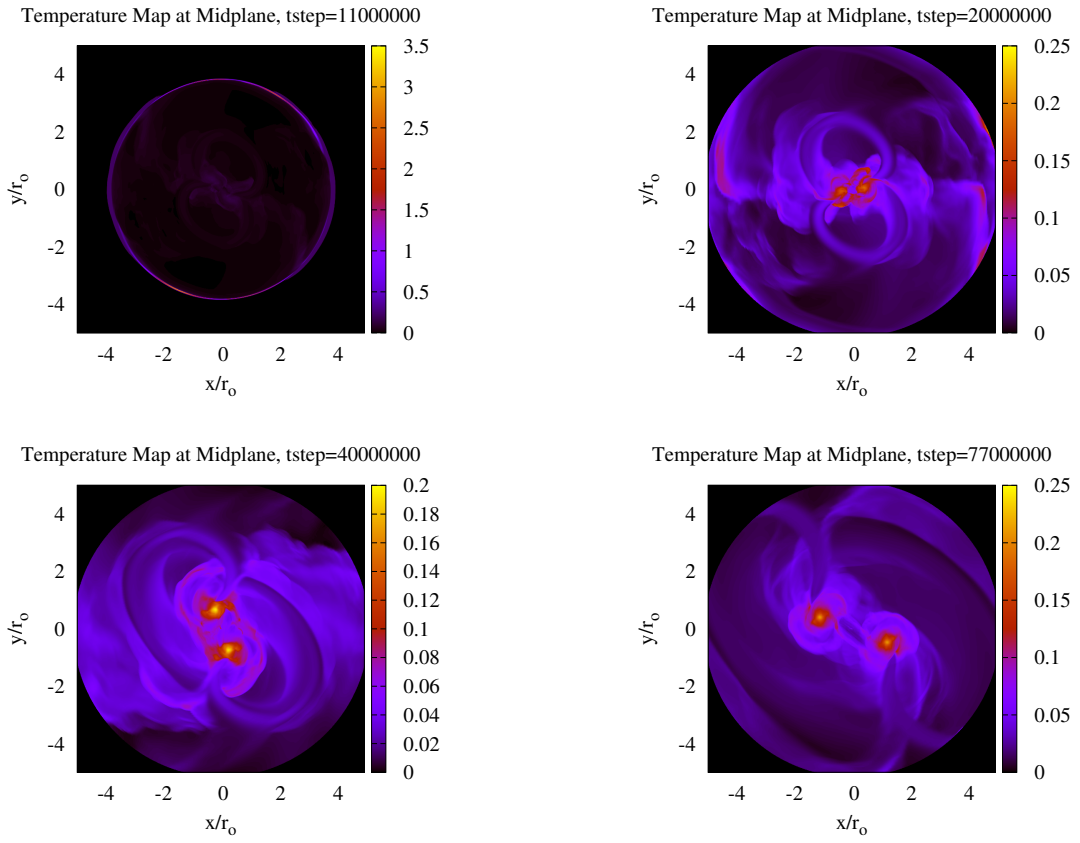

FIGURE 57. Midplane temperature map for the nonlinear evolution of the $M2$ model including weak cooling showing stellar bifurcation and subsequent evolution of the binary system. Distances are normalized to $r_\circ$ the location of density maximum in the equilibrium disk.

Moderate Cooling – $\tau_c = 5\tau_\circ$

Here we present the results of our nonlinear calculations including moderate cooling where $\tau_c = 1.7\tau_\circ = 5.0\tau_{cen}$. We show the integrated Fourier amplitudes of the density perturbation for the nonlinear evolution of the $M2$ model with the inclusion of moderate cooling in (See Figure 65). Again, there are four distinct stages in the evolution of the system. (i) After the initial perturbation is applied to the disk, there is a organizational/settling stage between $0.0 < \tau_\circ < 0.4$ after which the $m = 2$ Fourier component goes into steady exponential growth maintaining the highest amplitude

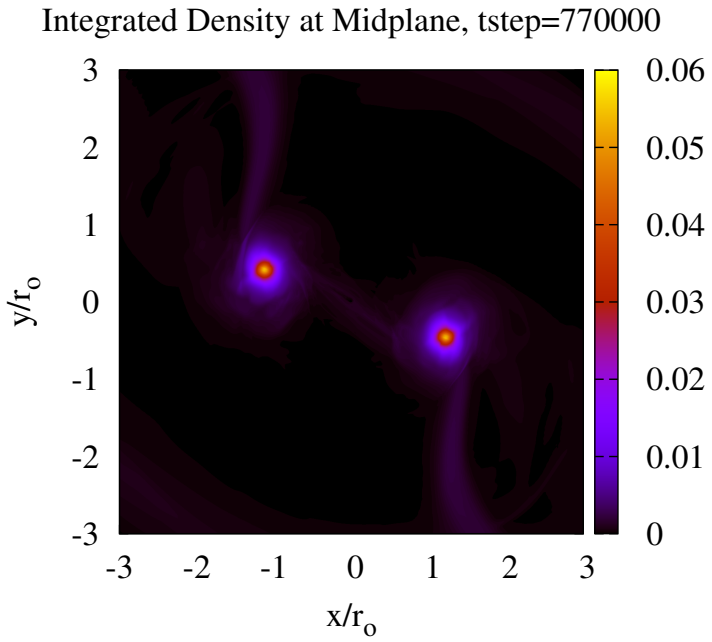

FIGURE 58. Integrated midplane density map of the $M2$ model including weak cooling after saturation of the barlike instability when $\tau_\circ = 2.53$ and $A_2 = 1.68$. Distances are normalized to $r_\circ$ the location of density maximum in the equilibrium disk.

Table 9. Clump analysis for the $M2$ model including weak cooling

Clump	ρ_{max}	J	L	ΔJ	ΔL	ΔK	Volume	Mass
1	4.3562e-3	239	113	139-339	63-163	0-80	0.05403	0.4290
2	4.3419e-3	259	241	159-359	170-255	0-80	0.05721	0.40345

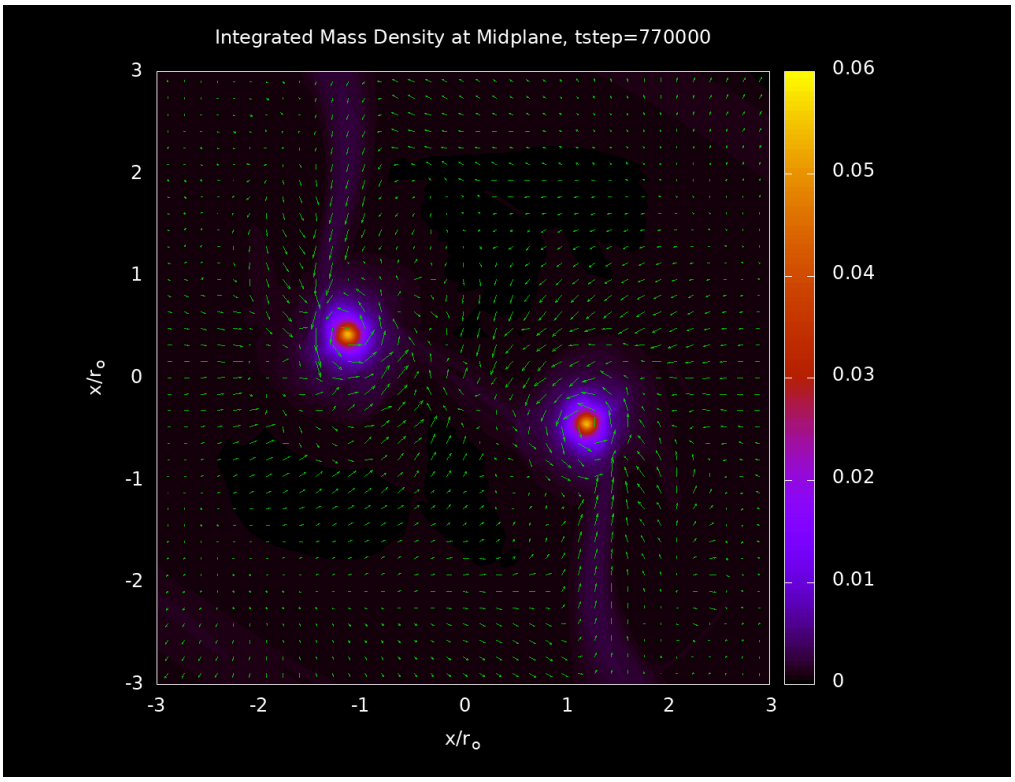

FIGURE 59. Integrated midplane density map with overlaid fluid velocity vectors for the nonlinear evolution of the $M2$ model including weak cooling after saturation of the barlike instability showing the binary system when $\tau_\circ = 2.53$ and $A_2 = 1.68$. Distances are normalized to $r_\circ$ the location of density maximum in the equilibrium disk.

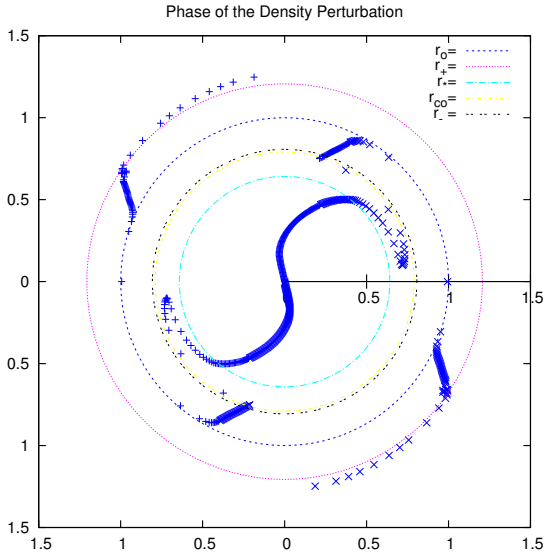

FIGURE 60. Constant phase loci for the $M2$ model including weak cooling showing $\delta\rho$ phase of the $m = 2$ component at $t/\tau_\circ = 1.36$. The equilibrium values for the outer edge of the star r_*, location of corotation r_{co}, inner edge of the disk r_-, location of density maximum in the disk $r_\circ$ and the disk outer edge r_+ are shown. Values are normalized by $r_\circ$.

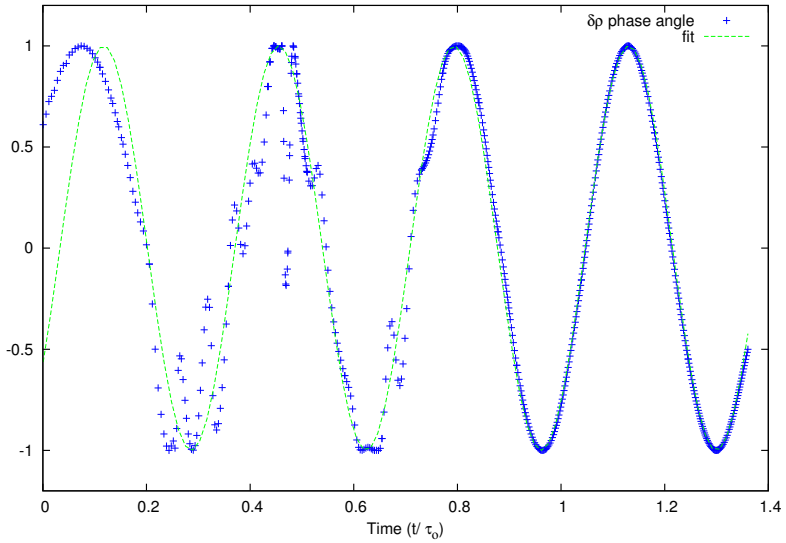

FIGURE 61. Phase angle plot for the $M2$ model including weak cooling showing the cosine of the $\delta\rho$ phase angle for the $m = 2$ component in blue taken inside the central star at $r/r_\circ = 1.0$. A fitting function $f(t) = cos(18.6 * t + 4.1)$ is plotted in green. Times are normalized by $\tau_\circ$.

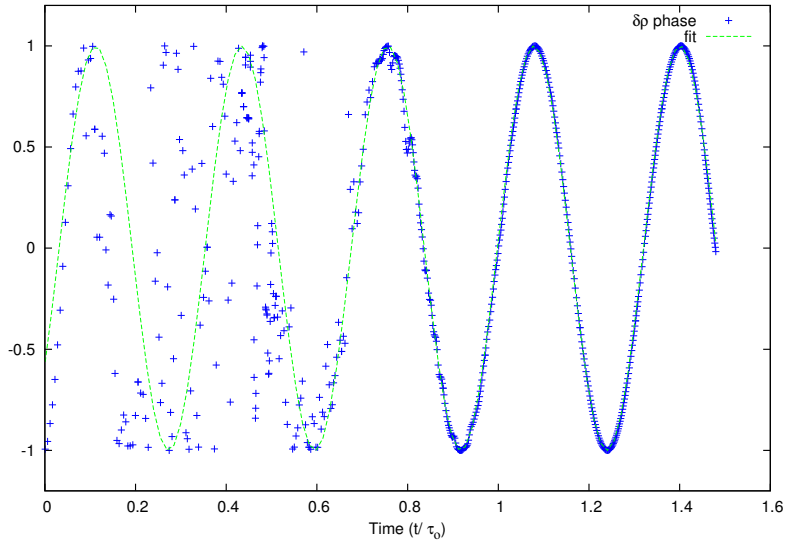

FIGURE 62. Phase angle plot for the $M2$ model including weak cooling showing the cosine of the $\delta\rho$ phase angle for the $m = 2$ component in blue taken inside the central star at $r/r_\circ = 0.32$. A fitting function $f(t) = cos(19.6 * t + 4.1)$ is plotted in green. Times are normalized by $\tau_\circ$.

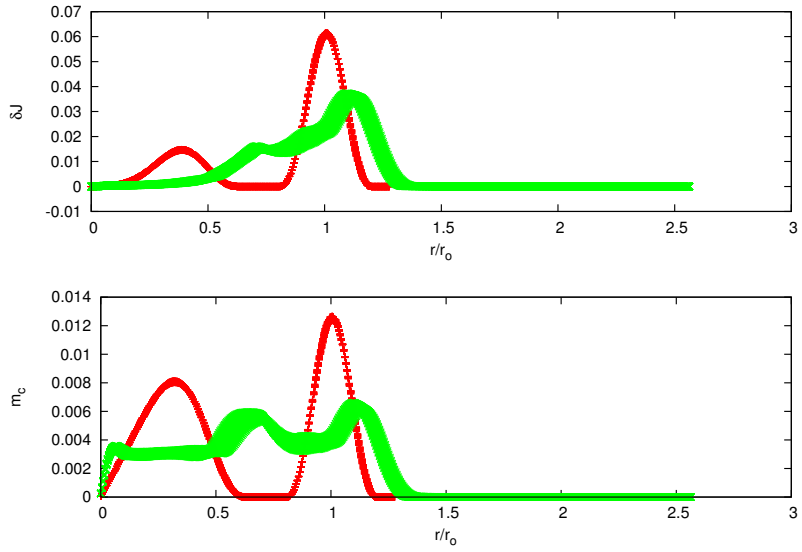

FIGURE 63. δJ and cylindrical mass fraction m_c for the $M2$ model including moderate cooling at times $\tau_\circ = 0.12$ (red) and 1.56 (green).

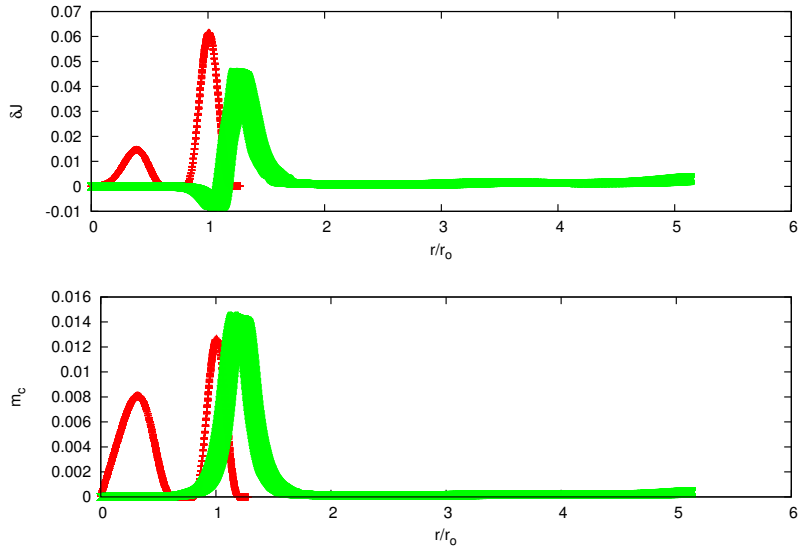

FIGURE 64. δJ and cylindrical mass fraction m_c for the $M2$ model including moderate cooling at times $\tau_\circ = 0.12$ (red) and 2.53 (green).

throughout the evolution of the system. With moderate cooling, the model spends less time in organizational/settling phase of its evolution as compared to the non-cooling case, but similar to the weak cooling case. (ii) The system transitions into the linear phase of its evolution with steady exponential growth of the $m = 2$ component between $0.4 < t/\tau_\circ < 1.2$. Compared to the non-cooling case, exponential growth in the $m = 3$ component begins at $\tau_\circ = 0.6$ followed by the $m = 4$ near $\tau_\circ = 1.2$, at which point the growth rate of the $m = 3$ changes character. This could be evidence of mode mixing where power from one mode is transferred to another mode. coupling between the even and odd modes may be responsible for the differences we see in the evolution of the system. The growth rate in the $m = 3$ component is larger with moderate cooling than weak cooling and on order with the $m = 2$ component until $\tau_\circ = 1.2$ when $m = 4$ starts growing exponentially. From figure 65, we estimate that $m = 2$ grows at a rate of $\approx 12.3\tau_\circ^{-1}$ and $m = 3$ grows at a rate of $\approx 12.5\tau_\circ^{-1}$ but then changes to $\approx 9.2\tau_\circ^{-1}$ at $t/\tau_\circ = 1.2$. This represents a 33.7% difference for $m = 2$ and 62.3% difference for the $m = 3$ growth rate as compared to the non-cooling case. The $m = 4$ grows at a rate of $\approx 20.7\tau_\circ^{-1}$. near $t/\tau_\circ = 1.2$. The rest of the modes do not clearly reach steady exponential growth as they did in the weak cooling model. (iii) Between $1.3 < \tau_\circ < 1.7$ growth of the perturbation saturates. We see that even-m components saturate at a much higher amplitude $A_{even} \approx 1.0$ while the odd components peaking at $A_{odd} \approx 0.1$ around $\tau_\circ = 1.7$. (iv) Beyond saturation $\tau_\circ > 1.7$, the system reaches a new steady state in which the even-m remain at $A_m \approx 1.0$ and odd-m at $A_m \approx 0.1$. The model is halted at $\tau_\circ = 2.48$ after 4.7% of the mass has flowed off the grid. At this point $A_2 = 1.61$, $A_3 = 0.27$, $A_4 = 1.29$, $A_5 = 0.20$, $A_6 = 1.17$, $A_7 = 0.316$, $A_8 = 1.08$.

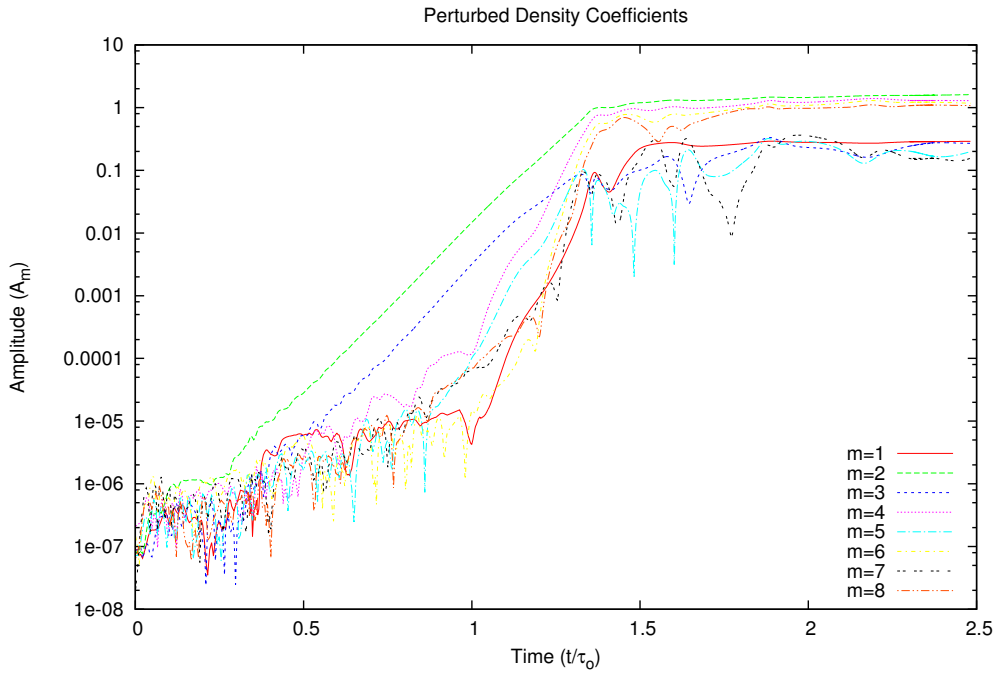

FIGURE 65. Integrated Fourier amplitudes $\mathcal{A}_m$ for $m = 1$ to 8 in the disk midplane for model M2 with moderate cooling. Times are normalized in units of $\tau_\circ$, the rotation period for material at density maximum in the disk midplane.

In Figure 66 we present integrated midplane density maps for the nonlinear evolution of the $M2$ model including moderate cooling showing the evolution of the central star into a bar-like object and in Figure 67 showing stellar bifurcation and subsequent evolution of the binary system. The upper left panel shows the initial system after perturbations have been applied but while the system is still in the settling phase at $t/\tau_{circ} = 0.11$. In the upper right panel, taken at $t/\tau_\circ = 1.31$ when $A_2 = 0.51$, when the star begins to develop into a bar-like object that is qualitatively different in form than the non-cooling of weak cooling case. The disk becomes more eccentric in shape deviating from axisymmetry with density higher in parts of the disk where it is closest to the bar-like object. Major changes to the density structure of the disk only begin once the instability enters the saturation phase. In the lower left panel when $t/\tau_\circ = 1.39$ and $A_2 = 1.00$ the central barlike object thins and elongates due to the loss of pressure support from cooling. It also intercepts the disk forming two dense lobes which begin accreting material from the disk. In the lower right panel at $t/\tau_\circ = 1.53$ with $A_2 = 1.22$, the central object bifurcates. There is evidence of disk fragmentation as we can see one clump falling onto the lower star. Figure 67 gives the subsequent density evolution of the $M2$ model showing further fragmentation of the disk and formation of the binary system. The upper left panel, is taken at $t/\tau_\circ = 1.55$ when $A_2 = 1.26$. The upper right panel shows the system at $t/\tau_\circ = 1.72$ when $A_2 = 1.32$. We see two more fragments have formed in the disk and the lower star has absorbed the fragment visible in the upper left panel. The lower left panel is taken at $t/\tau_\circ = 1.94$ when $A_2 = 1.45$, shows the system evolving into to unequal mass binary pairs. The disk fragments are being absorbed by the stars and they have become very nearly circular in shape. At this point they sit with a separation of approximately $\varpi = 2.0 r_\circ$. The stars are still accreting mass from the remaining

disk. The lower right is at $t/\tau_\circ = 2.20$ when $A_2 = 1.55$. At this point the system has evolved into two unequal mass binary stars. At this point, the binary stars sit at a separation of roughly $\varpi = 2.3 r_\circ$.

Figures 70 and 71 show the same time series of integrated midplane density maps with overlaid velocity vectors for the nonlinear evolution of the $M2$ model including weak cooling and Figures 68 and 69 show midplane temperature maps. In Figure 70 we see that circulation of the fluid is counterclockwise. In the upper right panel of Figure 70, we see the development of the central bar-like object. In the lower left panel, when the central star intersects with the disk, a shockwave is launched away from the forming lobes. Looking at the lower left panel of Figure 68 we can see shockwaves being launched and spreading away from the star-disk system. Significant heating occurs at the shockfront. In the upper left panel of 69 the shockwave has steepened forming a circular wave with very high temperatures $T = 3.0$ that spreads away from the disk located at roughly $3.5 r_\circ$. These are temperatures 12 times higher than that of the final stellar temperatures. The next three panels show temperature evolution of the central stellar objects after the shockwave has left the computational grid. In the lower right panel of Figure 71 we can see that there is counterclockwise circulation in each of the stellar objects that forms nearly circular streamlines. At this point, the maximum density in the primary star is $\rho = 0.2$ and the maximum temperature is $T = 0.25$.

We show the density structure in the disk mid-plane after saturation of the instability when the simulation was halted in Figure 72 and overlaid velocity vectors in Figure 73 at $t/\tau_\circ = 2.48$ when $A_2 = 1.61$. The star has fissioned into two unequal mass stellar objects which rotate on independent axes and show nearly circular stramlines.

In Table 10 we calculate the total mass of the stellar "clumps" formed after saturation when $\tau_\circ = 2.48$ and the simulation has been halted. In column 1, we label the two clumps. In column 2, we give the value of the maximum density in each clump ρ_{max} in polytrope units. In section *Methods – Unit Conversions* we describe how to transform from polytrope units to any unit system and in Table **??** we give conversion factors for transforming into cgs units for several different choices of initial mass $M_\circ$ for the system and location of density maximum $r_\circ$. Columns 3-4 give the J, L-cell location of density max and columns 5-7 give the cells where density was integrated to approximate the total mass contained in the volume. Note that this is a difficult calculation to do precisely due to the size/shape of the computational grid because cells on the grid are not squares, they are wedges and do not match the spherical symmetry of the stellar clumps. In column 8 we give the total volume in polytrope units and in column 9 we give the total mass contained within that volume. Note that CHYMERA performs calculations in a dimensionless unit system where $G = K = M = 1.0$, therefore values are presented for systems where the total mass $M = 1.0$. At $\tau_\circ = 2.48$ a total of 4.7% of the material had flown off the grid. At this point we find that the two stellar components are unequal in mass with the primary stellar component containing roughly 49.7% of the initial mass of the system and the secondary stellar component containing roughly 32.8%. The remaining 12.8% of the mass on the computational grid is contained in the disk filaments.

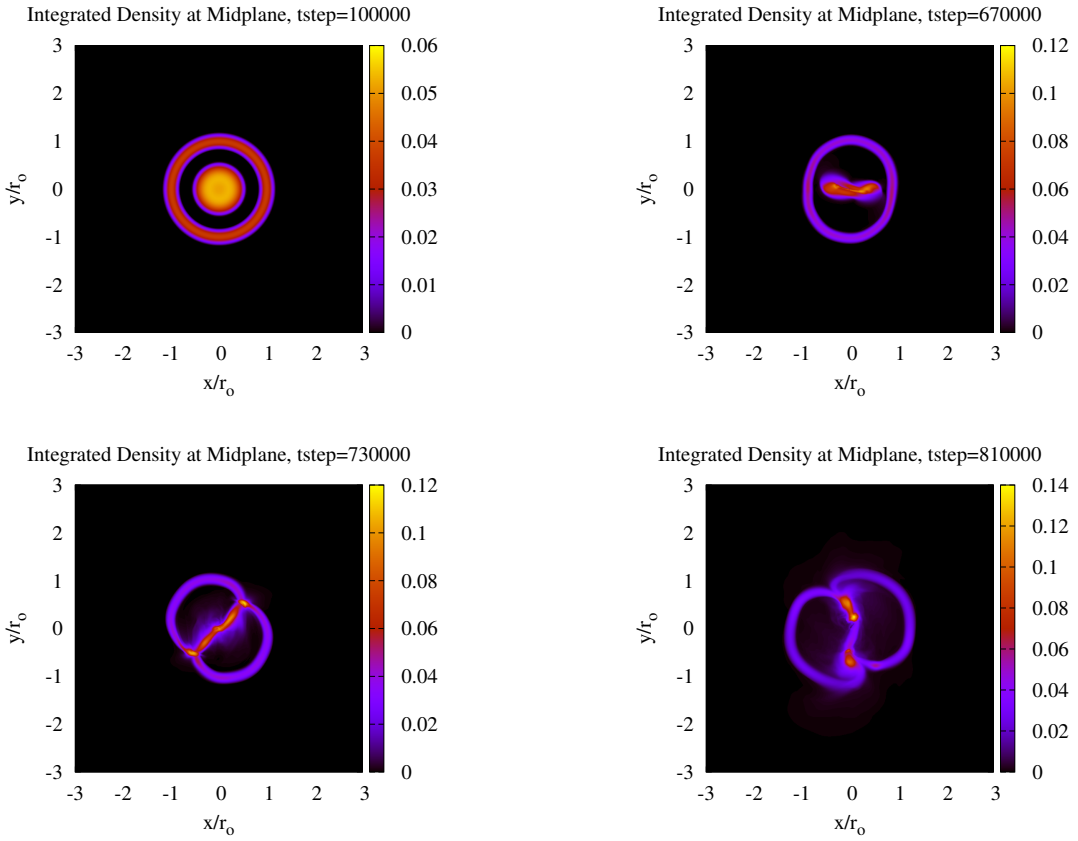

FIGURE 66. Integrated midplane density map for the nonlinear evolution of the $M2$ model including moderate cooling showing the formation of the central stellar bar. Distances are normalized to $r_\circ$ the location of density maximum in the equilibrium disk.

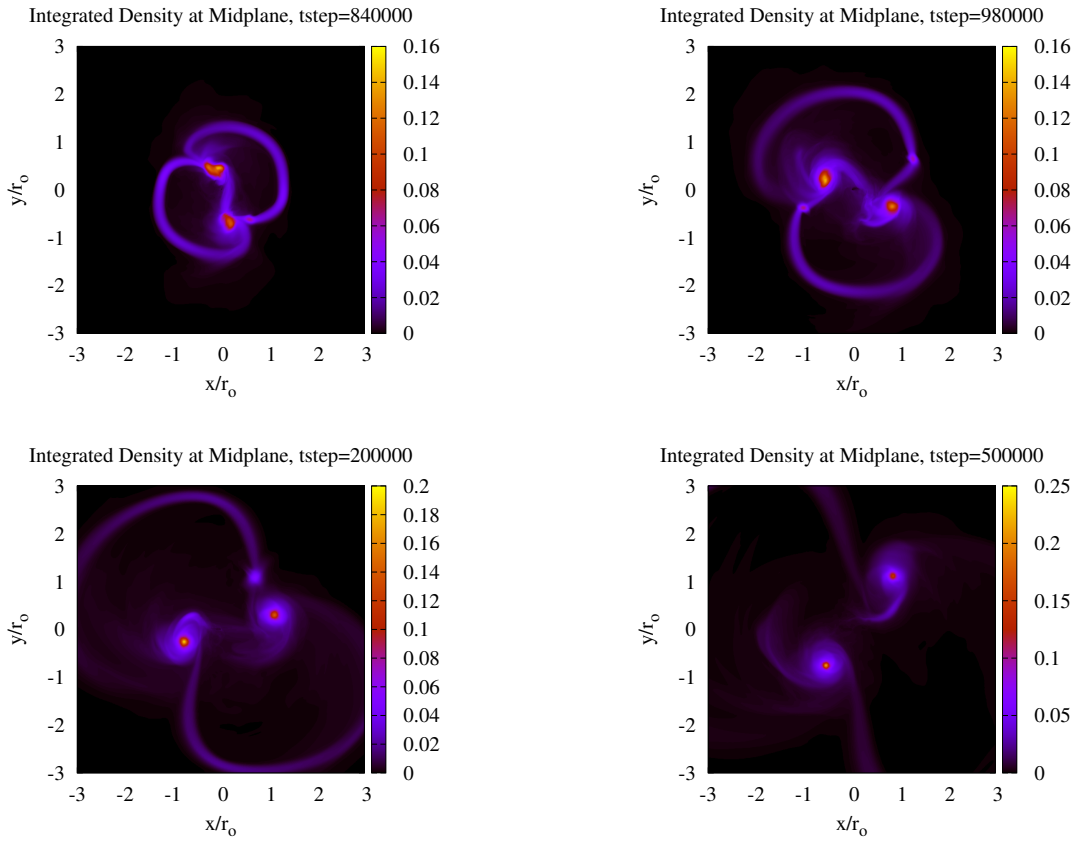

FIGURE 67. Integrated midplane density map of the nonlinear evolution of the $M2$ model including moderate cooling showing stellar bifurcation and subsequent evolution of the binary system. Distances are normalized to $r_\circ$ the location of density maximum in the equilibrium disk.

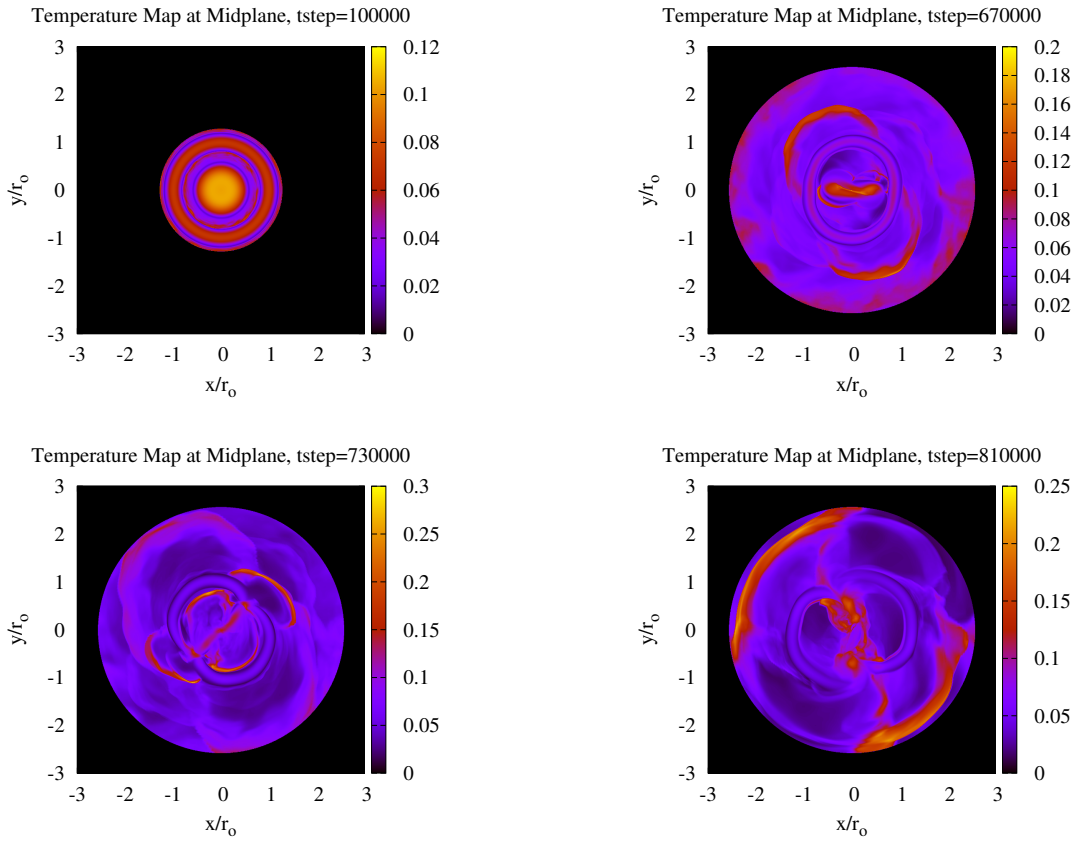

FIGURE 68. Midplane temperature maps for the nonlinear evolution of the $M2$ model including moderate cooling showing the formation of the central stellar bar. Distances are normalized to $r_\circ$ the location of density maximum in the equilibrium disk.

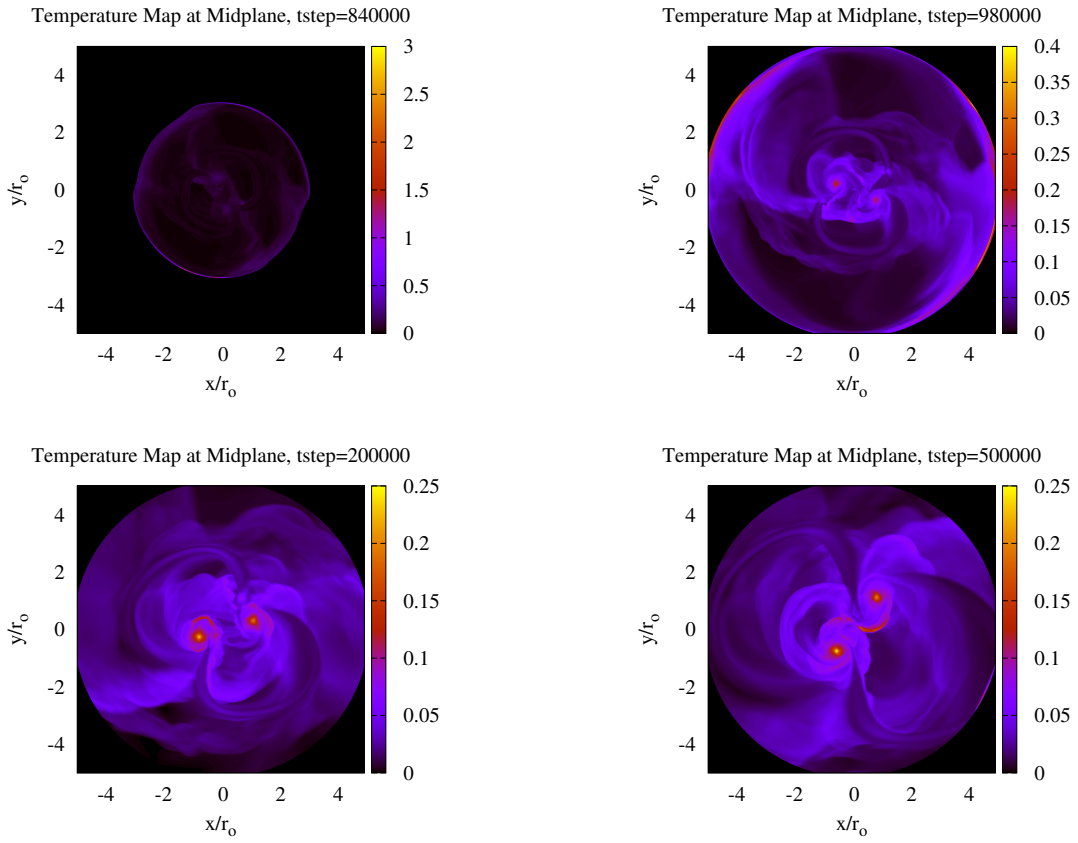

FIGURE 69. Midplane temperature map of the nonlinear evolution of the $M2$ model including moderate cooling showing stellar bifurcation and subsequent evolution of the binary system. Distances are normalized to $r_\circ$ the location of density maximum in the equilibrium disk.

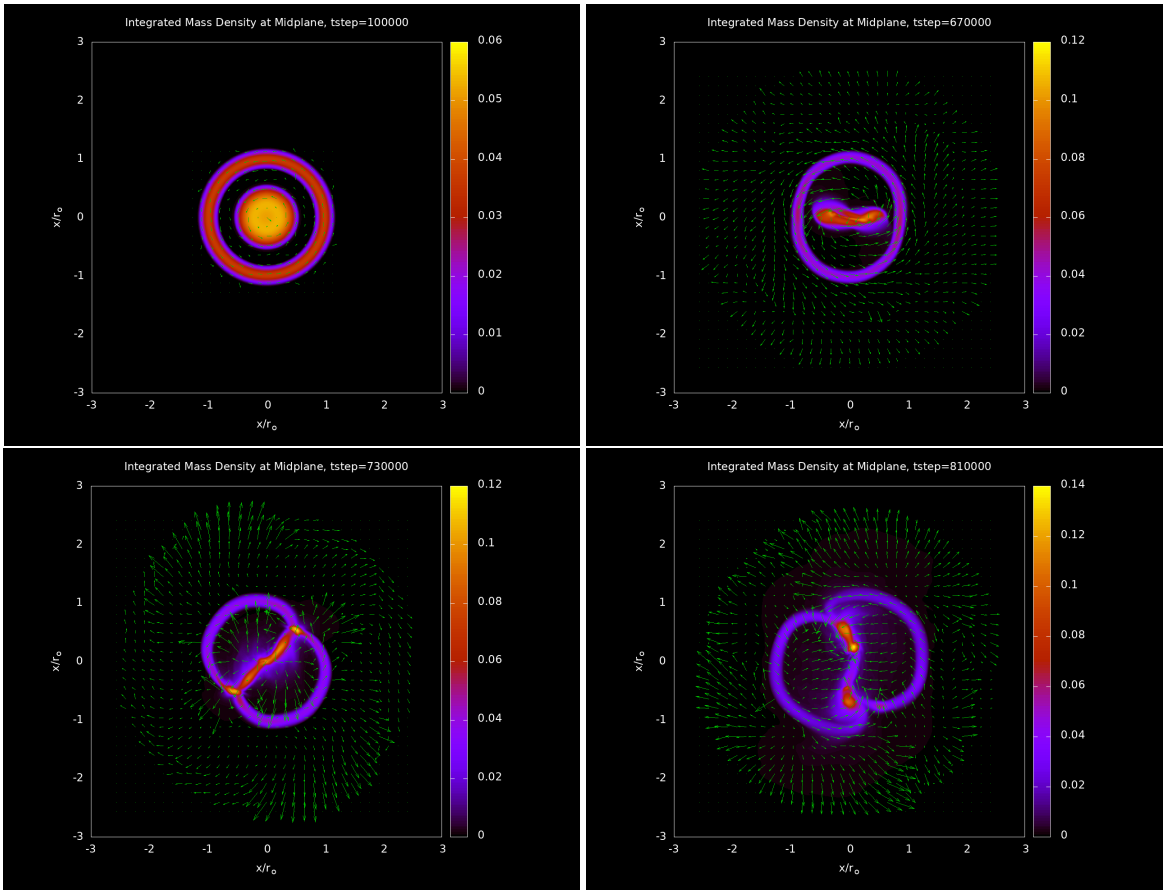

FIGURE 70. Integrated midplane density map with overlaid velocity vectors for the nonlinear evolution of the $M2$ model including moderate cooling showing the formation of the central stellar bar. Distances are normalized to $r_\circ$ the location of density maximum in the equilibrium disk.

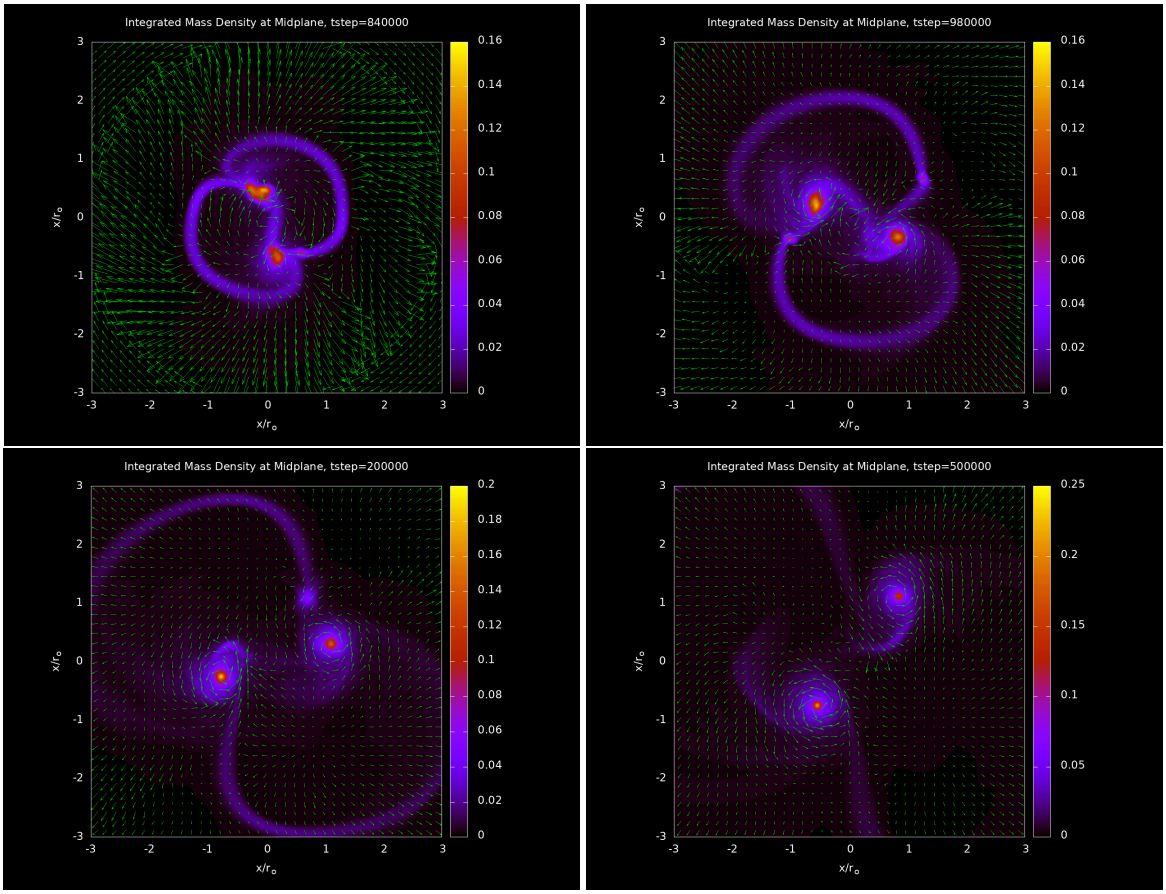

FIGURE 71. Integrated midplane density map with overlaid velocity vectors for the nonlinear evolution of the $M2$ model including moderate cooling showing stellar bifurcation and subsequent evolution of the binary system. Distances are normalized to $r_\circ$ the location of density maximum in the equilibrium disk.

Table 10. Clump analysis for the M2 model including modelrate cooling

Clump	Max ρ	J-val	L-val	ΔJ	ΔL	ΔK	Volume	Mass
1	5.4467e-3	120	114	0-300	64-164	0-80	0.04967	0.4967
2	3.3882e-3	181	241	20-320	171-256	0-80	0.05100	0.3281

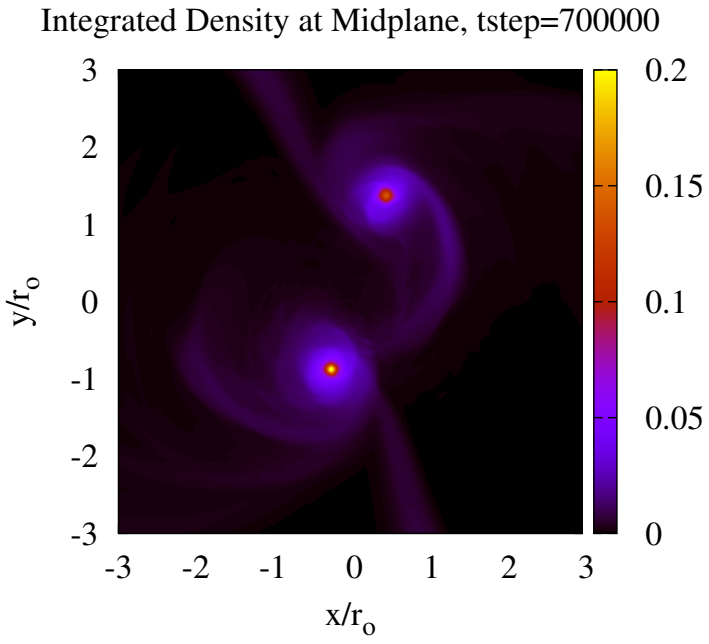

FIGURE 72. Integrated midplane density map of the M2 model including moderate cooling after saturation of the barlike instability when $\tau_\circ = 2.48$ and $A_2 = 1.61$

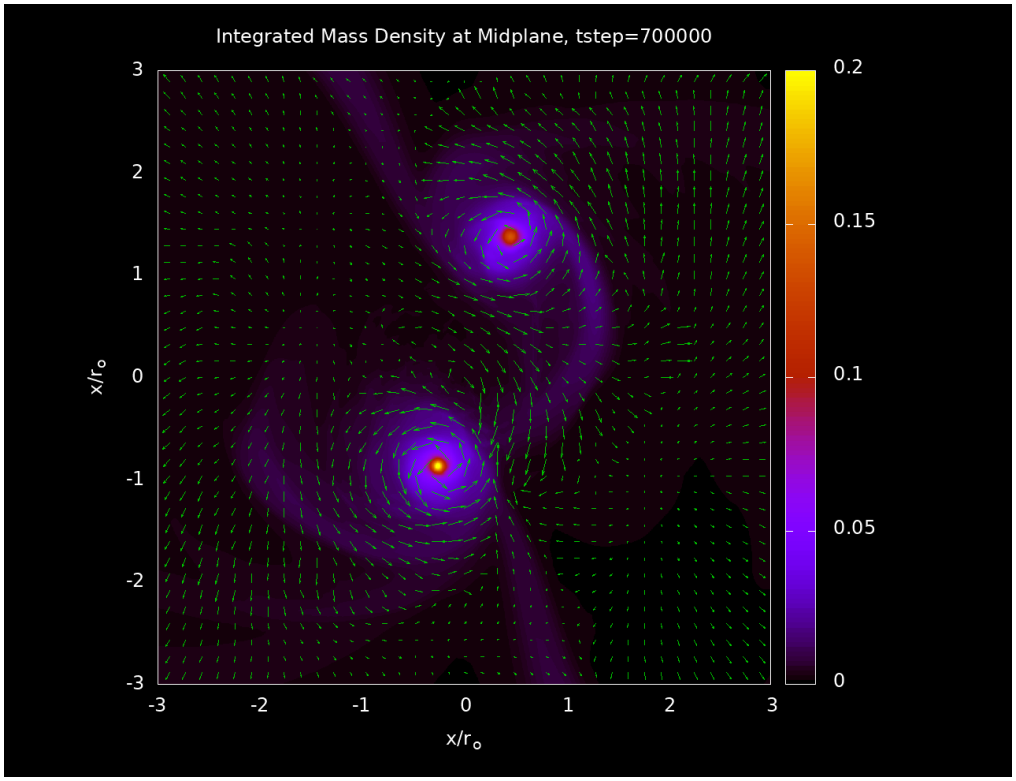

FIGURE 73. Integrated midplane density map of the M2 model including moderate cooling after saturation of the barlike instability when $\tau_\circ = 2.48$ and $A_2 = 1.61$

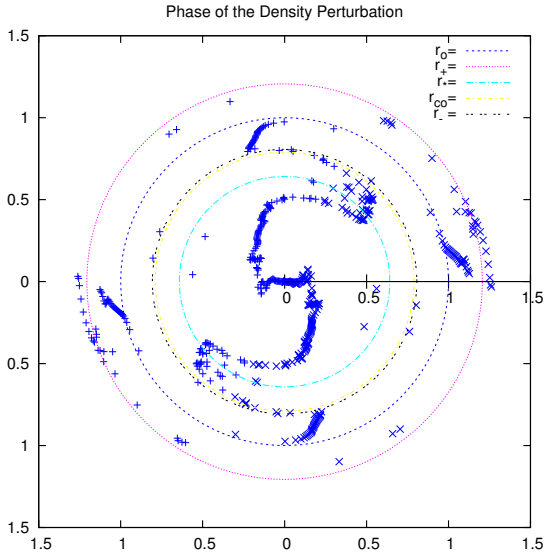

FIGURE 74. Constant phase loci for the $M2$ model including moderate cooling showing $\delta\rho$ phase of the $m = 2$ component at $t/\tau_\circ =$. The equilibrium values for the outer edge of the star r_*, location of corotation r_{co}, inner edge of the disk r_-, location of density maximum in the disk $r_\circ$ and the disk outer edge r_+ are shown. Values are normalized by $r_\circ$.

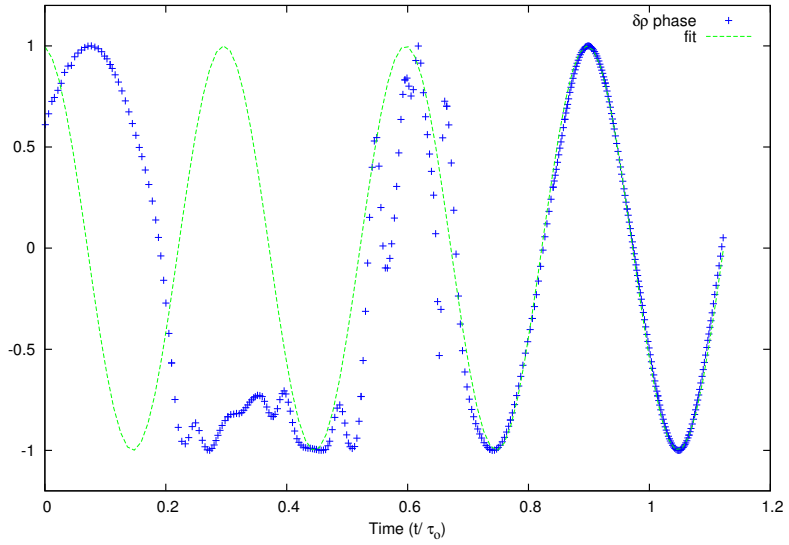

FIGURE 75. Phase angle plot for the $M2$ model including moderate cooling showing the cosine of the $\delta\rho$ phase angle for the $m = 2$ component in blue taken inside the disk at $r/r_\circ = 1.0$. A fitting function $f(t) = cos(20.9 * t + 0.1)$ is plotted in green. Times are normalized by $\tau_\circ$.

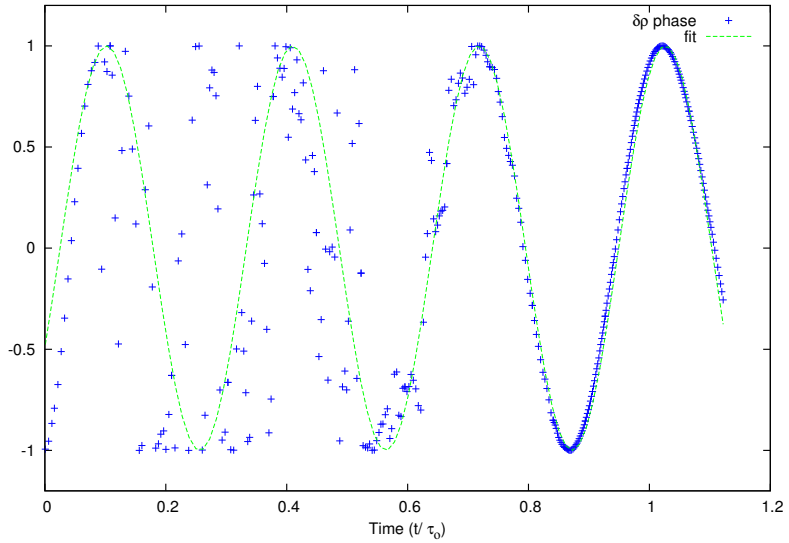

FIGURE 76. Phase angle plot for the $M2$ model including moderate cooling showing the cosine of the $\delta\rho$ phase angle for the $m = 2$ component in blue taken inside the disk at $r/r_\circ = 0.32$. A fitting function $f(t) = cos(20.4 * t + 4.2)$ is plotted in green. Times are normalized by $\tau_\circ$.

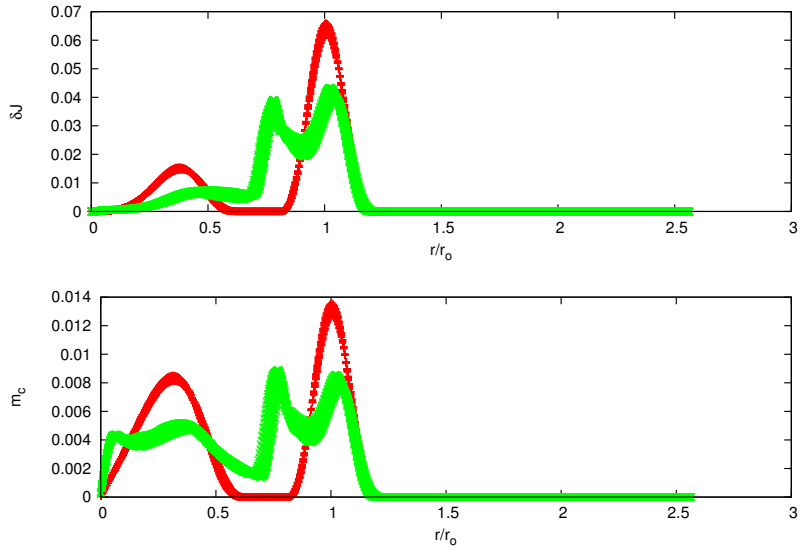

FIGURE 77. δJ and cylindrical mass fraction m_c for the $M2$ model including moderate cooling at times $\tau_\circ = 0.11$ (red) and 1.39 (green).

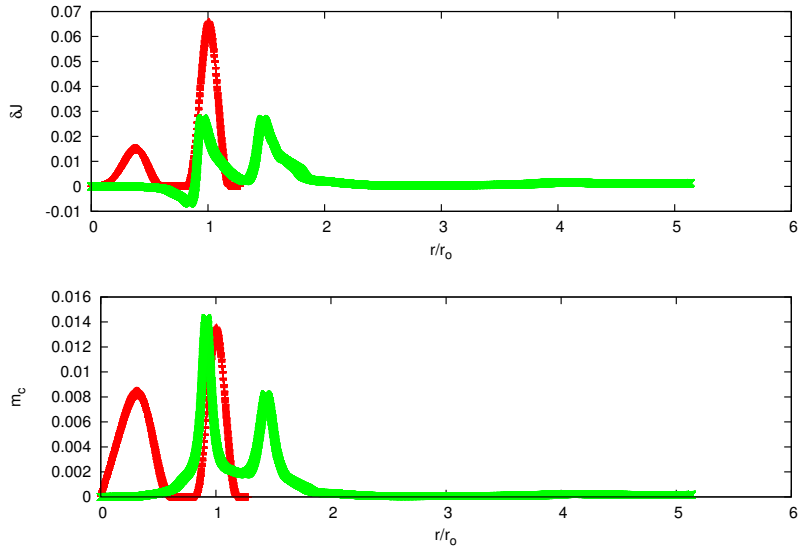

FIGURE 78. δJ and cylindrical mass fraction m_c for the $M2$ model including moderate cooling at times $\tau_\circ = 0.11$ (red) and 2.48 (green).

Fast Cooling – $\tau_c = 1.0\ \tau_\circ$

Here we present the results of our nonlinear calculations including fast cooling where $\tau_c = 1.0\tau_\circ = 3.0\tau_{cen}$. This cooling rate is expected to result in disk fragmentation based on the Gammie criterion. The qualitative evolution of this model is markedly different in character than for the previous cooling rates tested. We show the integrated Fourier amplitudes of the density perturbation for the nonlinear evolution of the $M2$ model with the inclusion of moderate cooling in (See Figure 79). Again, there are four distinct stages in the evolution of the system. (i) After the initial perturbation is applied to the disk, there is a organizational/settling stage between $0.0 < t/\tau_\circ < 0.3$ after which the $m = 2$ Fourier component goes into steady exponential growth maintaining the highest amplitude until $t/\tau_\circ < 1.2$ where the $m = 8$ briefly reaches the same amplitude. With fast cooling, the model spends less time in organizational/settling phase of its evolution as compared to the non-cooling, weak and moderate cooling cases. (ii) The system transitions into the linear phase of its evolution with steady exponential growth of the $m = 2$ component between $0.3 < t/\tau_\circ < 1.2$. Compared to the non-cooling, weak and moderate cooling case, exponential growth in the $m = 3$ component briefly appears at $\tau_\circ = 0.6$ at which point the this mode begins to dampen and around $t/\tau_\circ = 0.7$ growth in the $m = 7$ and $m = 8$ components begin to grow. Cooling causes the disk to narrow which changes the value of r_-/r_+. The results of many linear calculations across parameter space show that higher m-modes grow for narrower disks. From figure 79, we estimate that $m = 2$ grows at a rate of $\approx 11.9\tau_\circ^{-1}$ and $m = 3$ briefly grows at a rate of $\approx 11.9\tau_\circ^{-1}$ but then changes character completely at which point the $m = 7$ and $m = 8$ components grow at a rate of $\approx 12.2\tau_\circ^{-1}$ and $\approx 12.1\tau_\circ^{-1}$, respectively. This represents a 29.3% difference for $m = 2$ as compared to the non-cooling case. The $m = 4$ grows at a

rate of $\approx 25.9\tau_\circ^{-1}$ followed by the he $m = 4$ with a rate of $\approx 25.9\tau_\circ^{-1}$ near $t/\tau_\circ = 1.2$. (iii) Between $1.2 < \tau_\circ < 1.7$ growth of the perturbation saturates. We see that even-m components saturate at at nearly the same amplitude $A_{even} \approx 1.0$ as the odd components around $\tau_\circ = 1.7$. (iv) Beyond saturation $\tau_\circ > 1.7$, the system reaches a new steady state in which the even-m and odd-m stay around $A_m \approx 1.0$ with the exception of the $m = 8$ component. Coupling between the even and odd modes may be responsible for the differences we see in the evolution of the system. The model is halted at $\tau_\circ = 2.30$ after 6.5% of the mass has flowed off the grid. At this point $A_1 = 0.79$, $A_2 = 1.46$, $A_3 = 0.82$, $A_4 = 1.00$, $A_5 = 0.91$, $A_6 = 0.60$, $A_7 = 0.98$, $A_8 = 0.28$.

In Figure 80 we present integrated midplane density maps for the nonlinear evolution of the $M2$ model including moderate cooling showing the evolution of the central star into a bar-like object and in Figure 81 showing stellar bifurcation and subsequent evolution of the binary system. The upper left panel shows the initial system after perturbations have been applied but while the system is still in the settling phase at $t/\tau_{circ} = 0.16$. In the upper right panel, taken at $t/\tau_\circ = 1.16$ when $A_2 = 0.09$ at this point we already see evidence of fragmentation in the disk with corresponding to growth of the $m = 7$ and $m = 8$ components of the density perturbation which begin steady growth around this time. We see evacuation of the central star, a new feature of the fast cooling model. This could be due to the rapid rotation combined with the fast cooling rate and the fact that the star's outer edge and the disk inner edge $r_e/r_- = 0.79$ are very close to one another and the inward force of gravity in the star is reduced. The disk is pulling the stellar material outward and at the same time cooling is causing the loss of pressure support. In the lower left panel when $t/\tau_\circ = 1.28$ and $A_2 = 0.31$ the disk fragments into ten clumps, and the

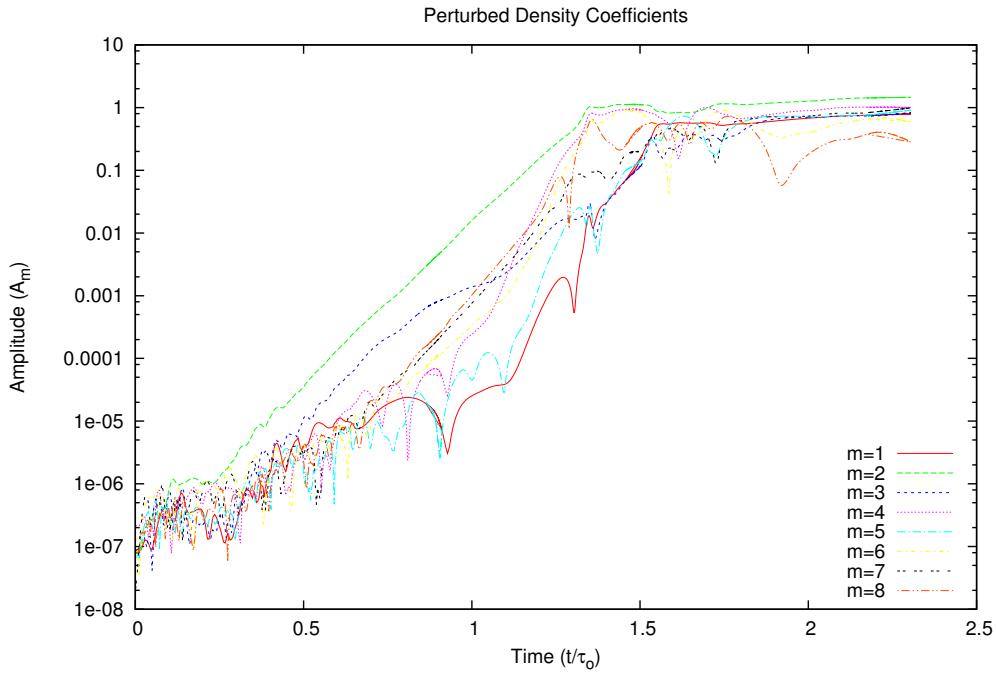

FIGURE 79. Integrated Fourier amplitudes $\mathcal{A}_m$ for $m = 1$ to 8 in the disk midplane for model M2 with fast cooling. Times are normalized in units of $\tau_\circ$, the rotation period for material at density maximum in the disk midplane.

evacuated stellar object folds over on itself with two distinct dense objects forming. In the lower right panel at $t/\tau_\circ = 1.37$ with $A_2 = 1.0$, the central object has evolved into a bar-like object and intercepted the disk absorbing two of the ten clumps initially formed. Figure 81 gives the subsequent density evolution of the $M2$ model showing further absorption of disk fragments by the stellar object and subsequent formation of the binary system. The upper left panel, is taken at $t/\tau_\circ = 1.43$ when $A_2 = 1.10$. The central bar-like object is in the process of absorbing several more clumps. The upper right panel shows the system at $t/\tau_\circ = 1.56$ when $A_2 = 0.88$ the central bar-like object has split with one component much more massive than the other. There are several disk clumps which remain. The lower left panel is taken at $t/\tau_\circ = 1.67$ when $A_2 = 0.87$, shows more disk fragments being absorbed by the primary stellar object. The lower right panel is taken at $t/\tau_\circ = 1.77$ when $A_2 = 1.13$. At this point the system has evolved into two unequal mass binary stars and two disk fragments remain.

Figures 82 and 83 show the same time series of integrated midplane density maps with overlaid velocity vectors for the nonlinear evolution of the $M2$ model including fast cooling and Figures 84 and 85 show midplane temperature maps. In Figure 82 we see that circulation of the fluid is counterclockwise. The upper left panel shows the initial system after perturbations have been applied but while the system is still in the settling phase. In the upper right panel of Figure 82, we see growth of the $m = 7$ and $m = 8$ components of the density perturbation which lead and development of high order instability in the disk. In the lower left panel, the disk fragments into $n = 10$ fragments. In the lower right panel, when the central star intersects with the disk, a shockwave is launched. This shockwave does not disrupt the disk fragments. Looking at the upper left and right panels of Figure 85 we can see evolution of the

shockwave as it spreads away from the star-disk system. Significant heating occurs at the shockfront. In the upper right panel of 85 the shockwave has steepened forming a circular wave with a high temperature of $T = 0.9$ at roughly $4.0r_\circ$ on the right hand side of the shockfront. These are temperatures 3 times higher than that of the final stellar temperatures. The next two panels show temperature evolution of the central stellar objects after the shockwave has left the computational grid. In the lower right panel of Figure 83 we can see that there is counterclockwise circulation in each of the stellar objects that forms nearly circular streamlines. In addition, the two remaining disk fragments also show evidence of circulation. At this point, the maximum density in the primary star is $\rho = 0.16$ and the maximum temperature is $T = 0.3$.

We show the density structure in the disk mid-plane after saturation of the instability when the simulation was halted in Figure 86 and overlaid velocity vectors in Figure 87 at $t/\tau_\circ = 2.30$ when $A_2 = 1.45$. The system has evolved into two unequal mass stellar sized objects which rotate on independent axes and show nearly circular stramlines. These are orbited by two fragments which remain from the disk. These fragments also show evidence of fluid circulation lending credence to the possibility that they are not just transient objects.

In Table 11 we calculate the total mass of the clumps formed after saturation when $\tau_\circ = 2.48$ and the simulation has been halted and a total of 4.7% of the material had flown off the grid. At this point we find that the two stellar components are unequal in mass with the primary stellar component containing roughly 58.1% of the initial mass of the system and the secondary stellar component containing roughly 16.6%. The two substellar clumps contain 3.9% and 3.8% of the initial mass of the system. The remaining 3.9% of the mass on the computational grid is contained in the disk filaments.

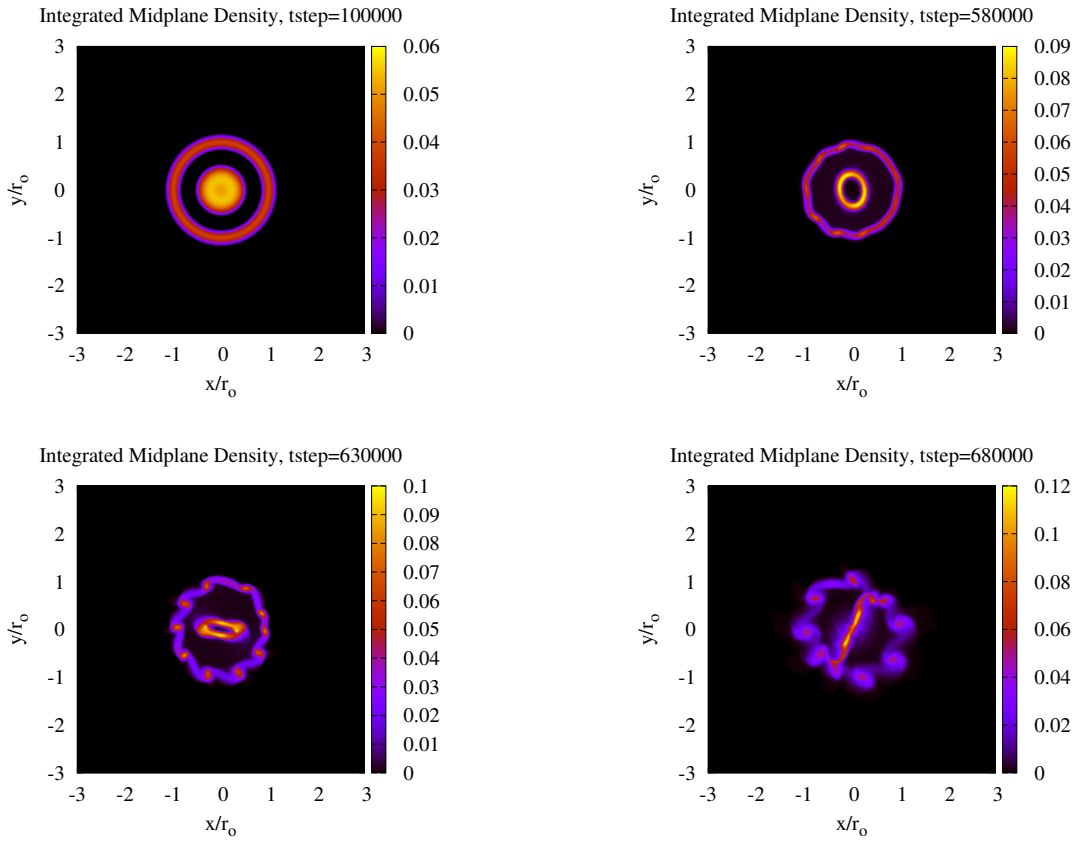

FIGURE 80. Integrated midplane density maps for the nonlinear evolution of the $M2$ model including fast cooling showing the formation of the central stellar bar and fragmentation of the disk. Distances are normalized to $r_\circ$ the location of density maximum in the equilibrium disk.

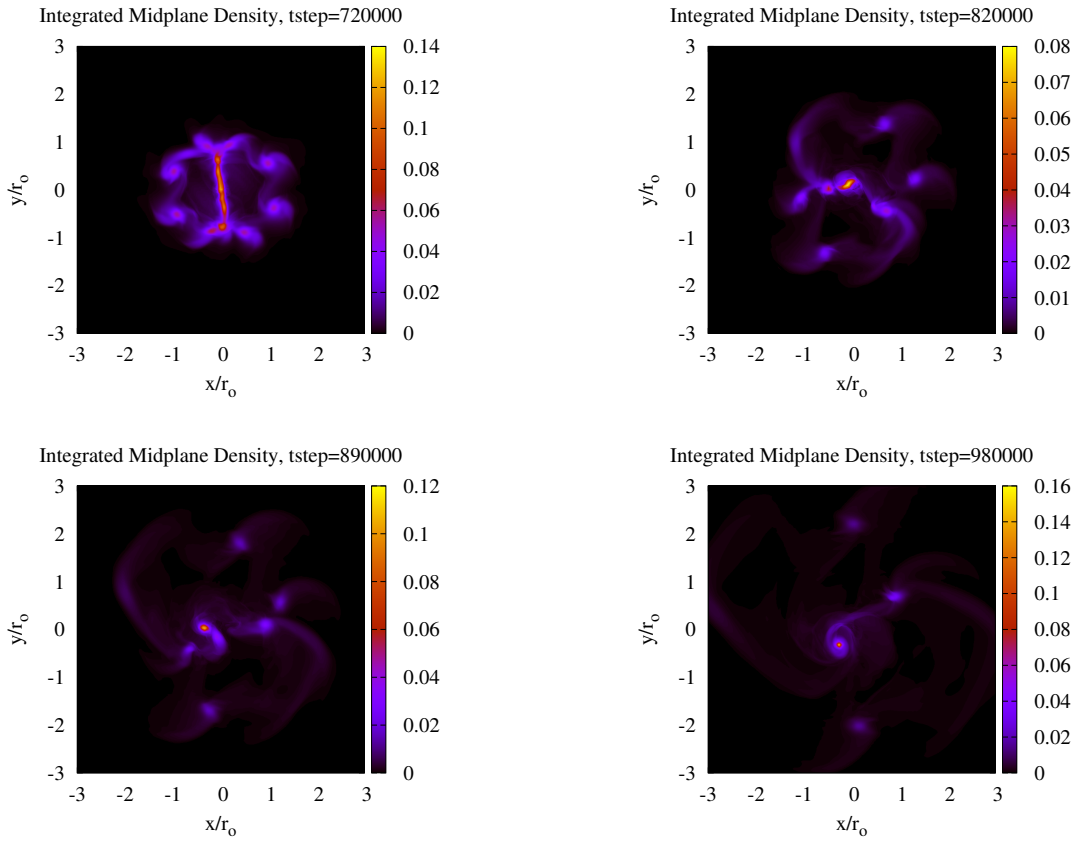

FIGURE 81. Integrated midplane density map for the nonlinear evolution of the $M2$ model including fast cooling showing stellar bifurcation and subsequent evolution of the binary system. Distances are normalized to $r_\circ$ the location of density maximum in the equilibrium disk.

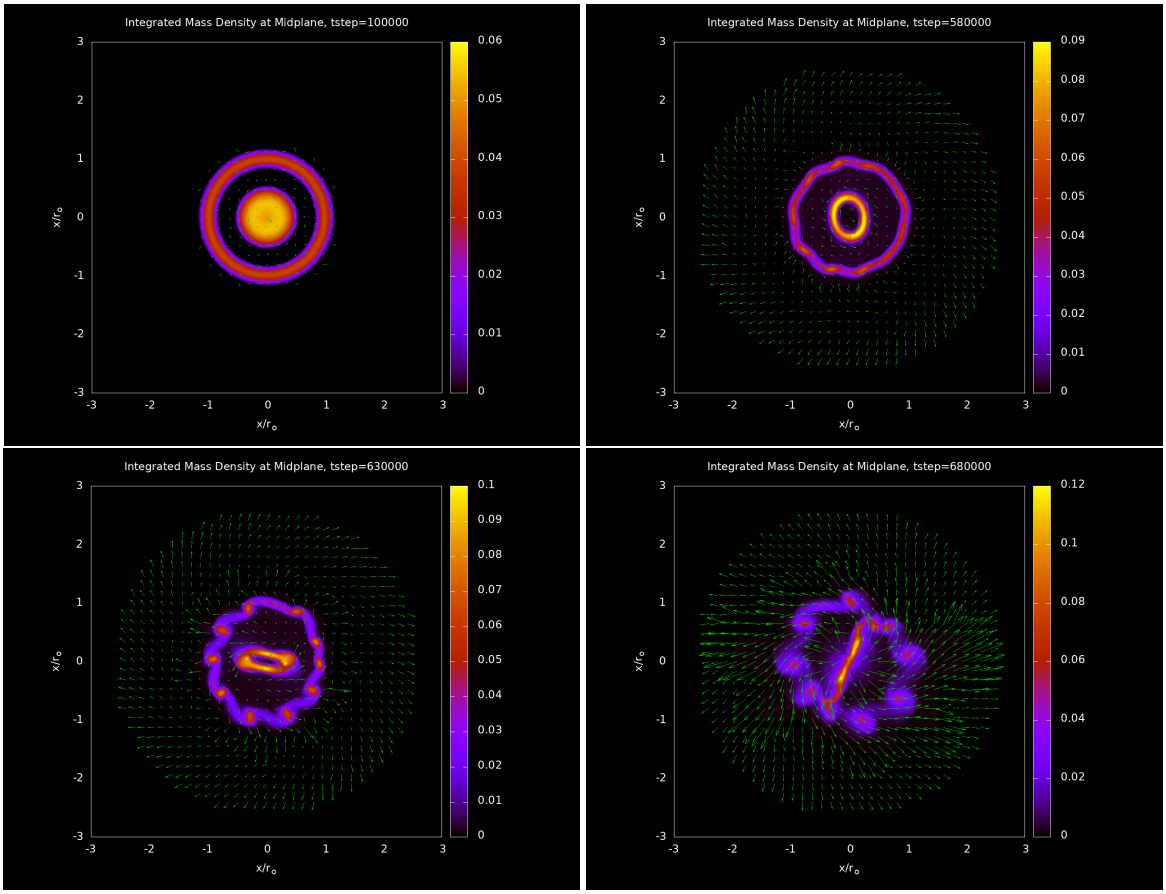

FIGURE 82. Integrated midplane density maps with overlaid velocity vectors for the nonlinear evolution of the $M2$ model including fast cooling showing the formation of the central stellar bar and fragmentation of the disk. Distances are normalized to $r_\circ$ the location of density maximum in the equilibrium disk.

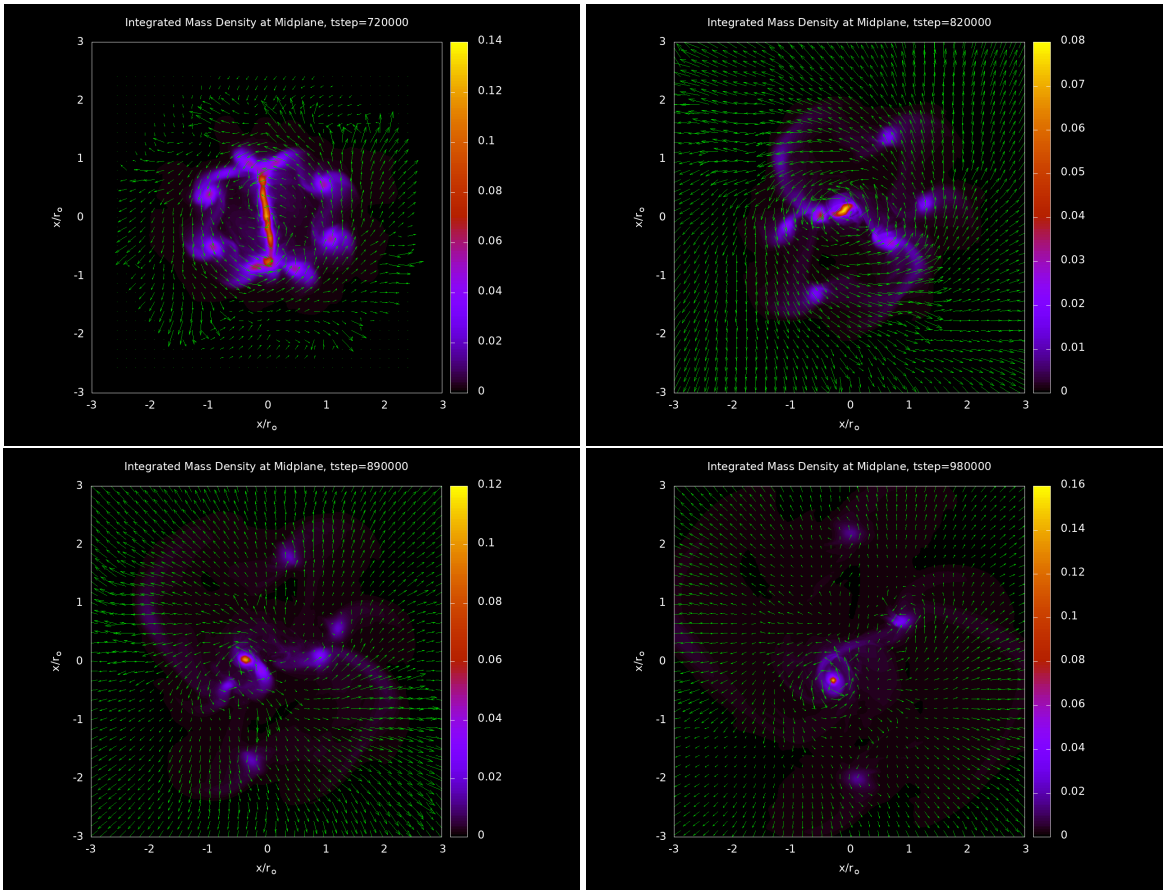

FIGURE 83. Integrated midplane density map with overlaid velocity vectors for the nonlinear evolution of the $M2$ model including fast cooling showing stellar bifurcation and subsequent evolution of the binary system. Distances are normalized to $r_\circ$ the location of density maximum in the equilibrium disk.

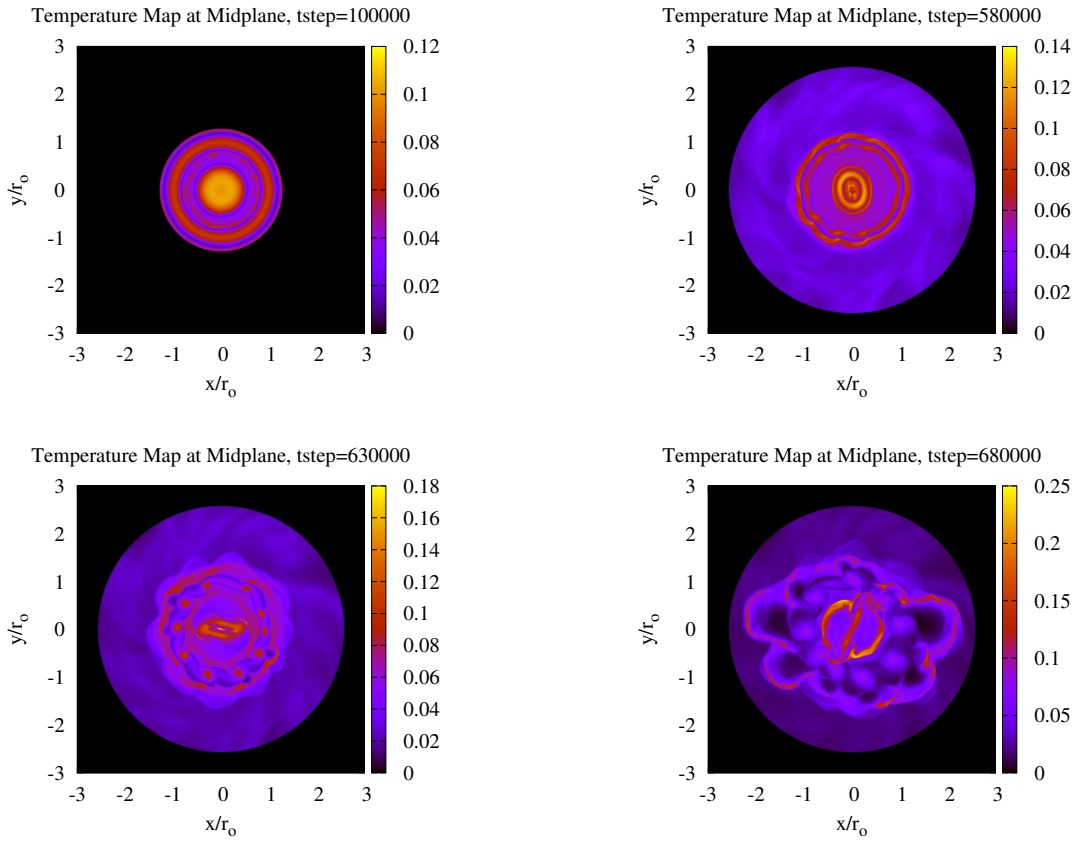

FIGURE 84. Midplane temperature maps for the nonlinear evolution of the $M2$ model including fast cooling showing the formation of the central stellar bar and fragmentation of the disk. Distances are normalized to $r_\circ$ the location of density maximum in the equilibrium disk.

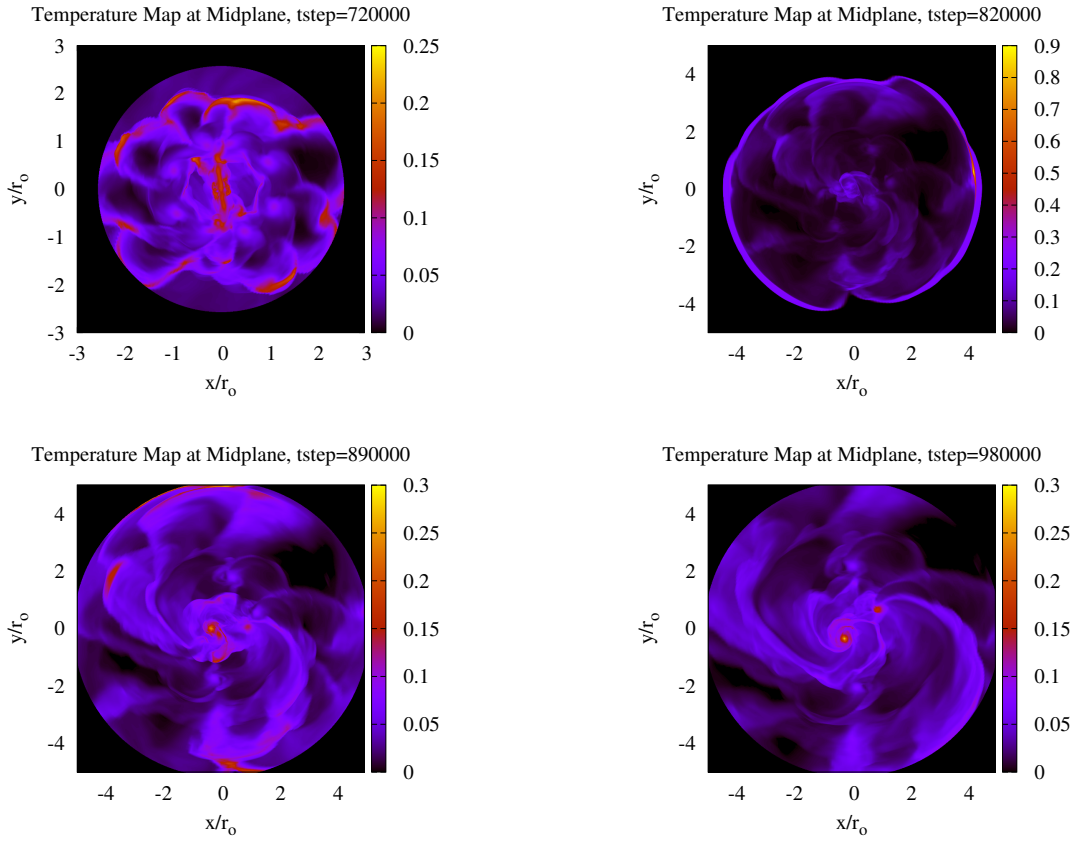

FIGURE 85. Midplane temperature maps for the nonlinear evolution of the $M2$ model including fast cooling showing the evolution of system. Distances are normalized to $r_\circ$ the location of density maximum in the equilibrium disk.

Table 11. Clump analysis for the M2 model including fast cooling

Clump	Max ρ	J-val	L-val	ΔJ	ΔL	ΔK	Volume	Mass
1	6.3875e-2	109	220	0-280	170-256	0-80	0.04464	0.5808
2	1.5583e-3	312	77	282-342	57-97	0-80	0.05403	0.1658
3	1.8279e-4	485	218	435-525	188-248	0-80	0.08362	0.03931
4	1.3930e-4	622	81	573-673	41-121	0-80	0.10717	0.03821

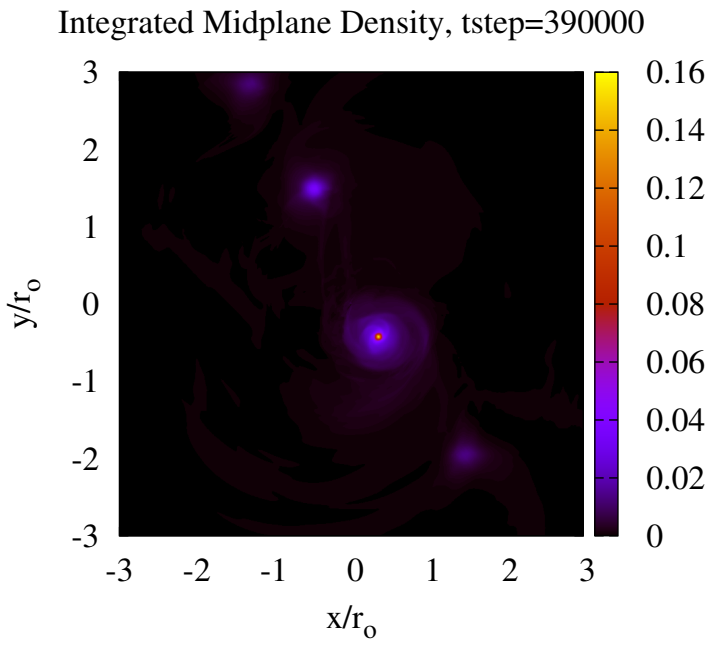

FIGURE 86. Integrated midplane density map of the M2 model including fast cooling after saturation of the barlike instability when the simulation was halted at $\tau_\circ = 2.30$ and $A_2 = 1.46$

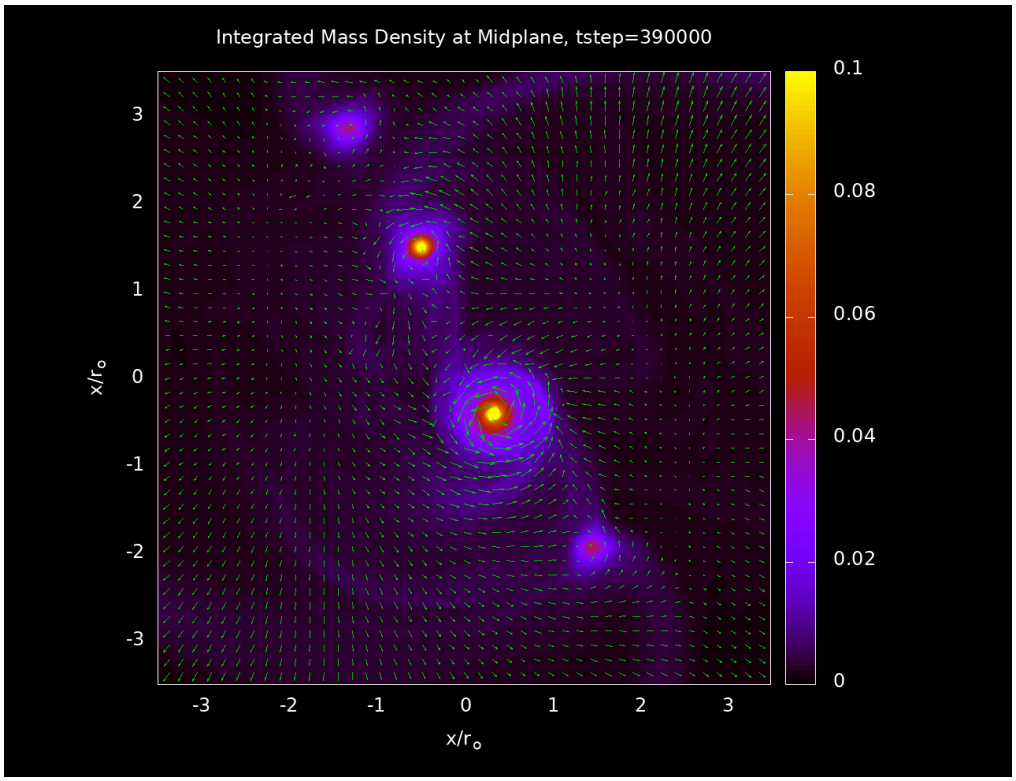

FIGURE 87. Integrated midplane density map with overlaid velocity vectors for the M2 model including fast cooling after saturation of the barlike instability when $\tau_\circ = 2.30$ and $A_2 = 1.46$

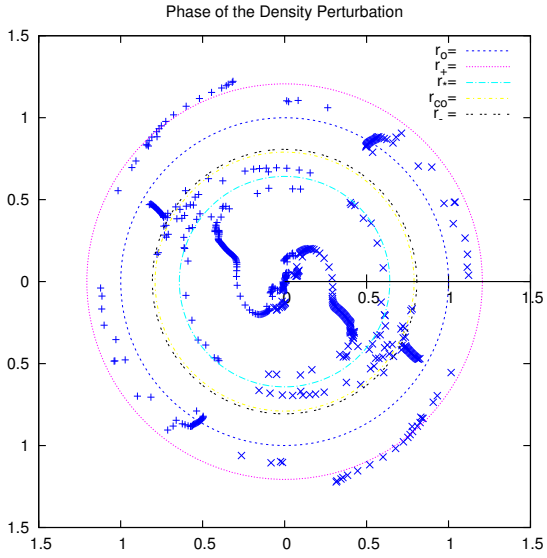

FIGURE 88. Constant phase loci for the $M2$ model including fast cooling showing $\delta\rho$ phase of the $m = 2$ component at $t/\tau_\circ =$. The equilibrium values for the outer edge of the star r_*, location of corotation r_{co}, inner edge of the disk r_-, location of density maximum in the disk $r_\circ$ and the disk outer edge r_+ are shown. Values are normalized by $r_\circ$.

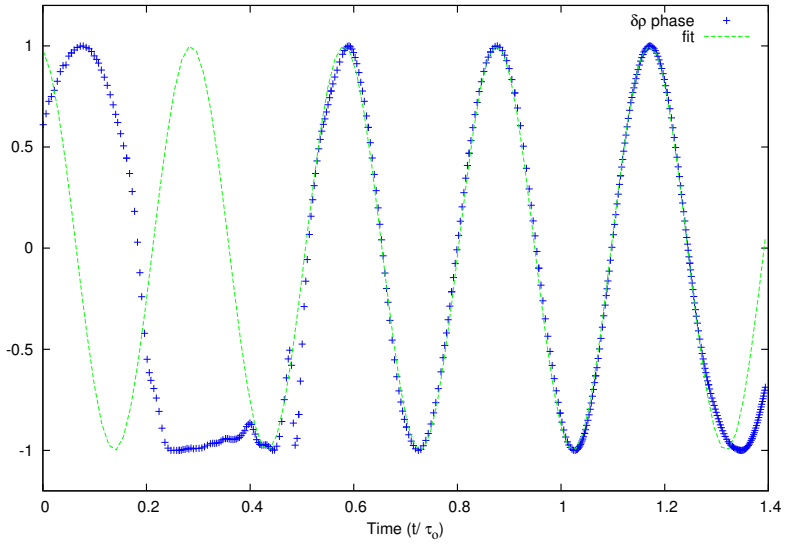

FIGURE 89. Phase angle plot for the $M2$ model including fast cooling showing the cosine of the $\delta\rho$ phase angle for the $m = 2$ component in blue taken inside the disk at $r/r_\circ = 1.0$. A fitting function $f(t) = cos(21.3 * x + 0.2)$ is plotted in green. Times are normalized by $\tau_\circ$.

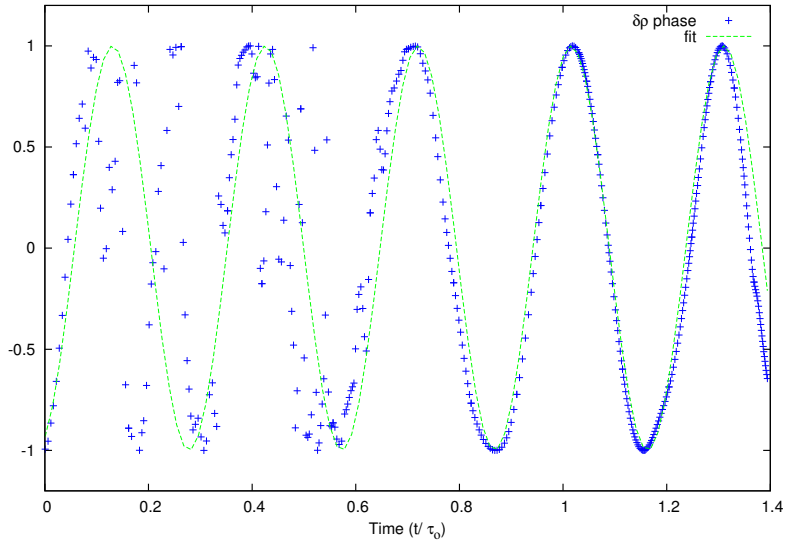

FIGURE 90. Phase angle plot for the $M2$ model including fast cooling showing the cosine of the $\delta\rho$ phase angle for the $m = 2$ component in blue taken inside the disk at $r/r_\circ = 0.32$. A fitting function $f(t) = cos(21.3 * x + 3.5)$ is plotted in green. Times are normalized by $\tau_\circ$.

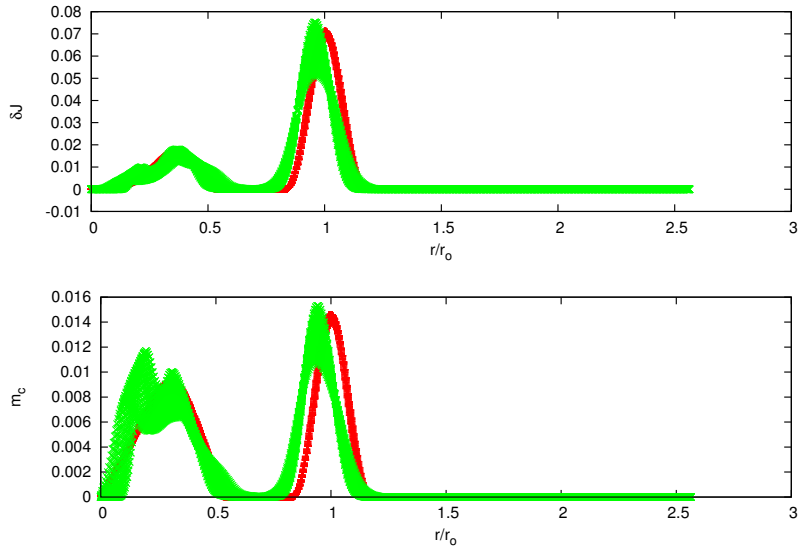

FIGURE 91. δJ and cylindrical mass fraction m_c for the $M2$ model including fast cooling at times $\tau_\circ = 0.16$ (red) and 1.28 (green).

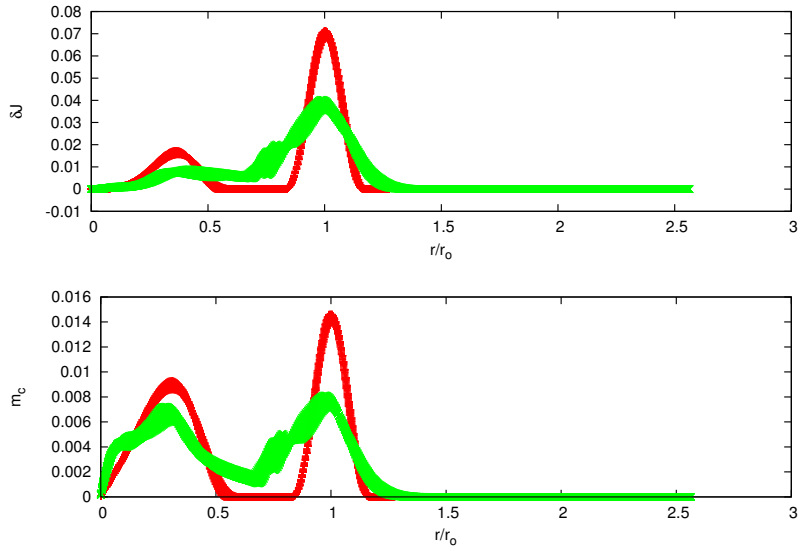

FIGURE 92. δJ and cylindrical mass fraction m_c for the $M2$ model including fast cooling at times $\tau_\circ = 0.16$ (red) and 1.37 (green).

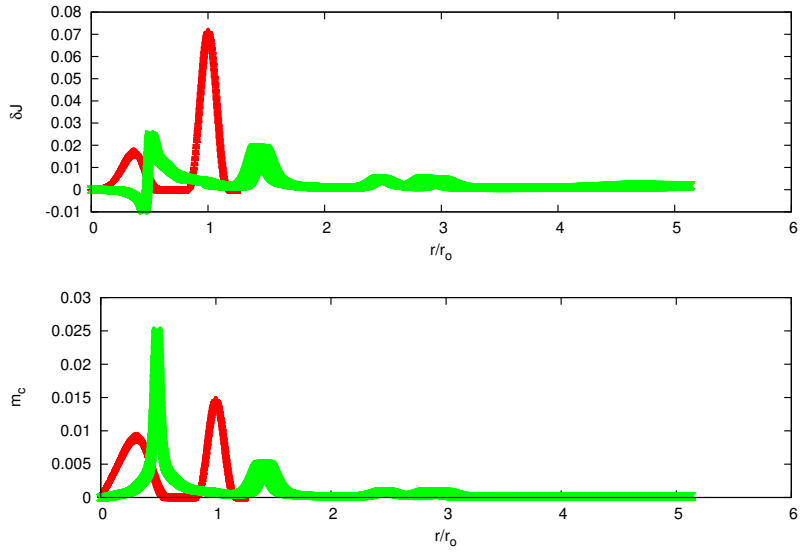

FIGURE 93. δJ and cylindrical mass fraction m_c for the $M2$ model including fast cooling at times $\tau_\circ = 0.16$ (red) and 2.3 (green).

CHAPTER V

DISCUSSION

Coupling of Stellar Modes with Disk Modes

An avenue of study that has not received much attention is how coupling of stellar oscillation modes with modes excited in circumstellar disks affects the stability properties of systems with massive disks. Coupling of stellar modes with disk modes opens the possibility of new classes of modes through which nonaxisymmetric instabilities might develop. For example, we find evidence in our current study that star-disk coupling could drive instability in slowly rotating stars, stars otherwise stable to dynamic nonaxisymmetric instabilities [220], [85]. Coupling of stellar and disk modes could also produce distinct new types of nonaxisymmetric instabilities, such as the one-armed modes driven by the *indirect* stellar potential discovered by [3], or it could lead to changes to the onset and nonlinear development of well-known stellar and disk modes. These and related possbilities have been addressed in only a handful of studies.

Yuan & Cassen (1985) studied the coupling of secularly unstable, but dynamically stable stellar f-modes with spiral arms excited in infinitesimally thin circumstellar disks. Yuan & Cassen considered the bar modes of Maclaurin spheroids while Imamura *et al.* (1995) and Lai (2001) considered $m \geq 2$ modes in polytropic stars. Yuan & Cassen, Imamura *et al.*, and Lai showed that f-modes coupled strongly to spiral arms driven at the inner Lindblad resonance and corotation in infinitesimally thin disks and that coupling could drive instability in stars which were beyond the neutral points of nonaxisymmetric modes found along sequences of increasing angular

momentum equilibrium stars (See aslo [68]). Coupling was considered significant when it drove instability on dynamic or near dynamic timescales. Yuan & Cassen, Imamura *et al.*, and Lai found that this occurred for disks with masses significant when compared to the masses of the central stars or when $\beta > 0.20$ when only barlike modes were considered [219], [103], [123].

Adams, Ruden, & Shu (1989) showed that one-armed spiral modes in massive disks could be excited if the disk mode coupled with the central star. In systems where the central star is driven off the center-of-mass of the system, its subesequent orbital motion leads to an indirect potential which couples back into the disk. The forcing drives a one-armed spiral in the disk. Adams, Ruden, & Shu considered point mass central stars in orbital motion and did not investigate how the star and disk coupled to drive the star off the center-of-mass of the system. Consequently, how the couple worked and so how the disk angular momentum was divided between the orbital and rotational angular momenta of the star was not determined. Questions of spin-down and spin-up of the central star could thus not be addressed [3].

Lin, Krumholz, & Kratter (2011) followed the collapse of two differentially rotating interstellar medium clouds. Collapse of differentially rotating nonmagnetic clouds and, perhaps, magnetic clouds leads naturally to the formation of rotating central stars surrounded by massive disks. Lin, Krumholz, & Kratter paid particular attention to star-disk coupling during collapse and how it affected the spin-down of the forming star. They found that one-armed modes did not spin the star down efficiently, rather, they drove the central star into orbital motion as found by Adams, Ruden & Shu (1989). Efficient spin-down was found for two-armed modes, however. The work was important, however, the parameter space of resolved star-disk systems

was not explored. Further work remains to be done to explore how coupling of disk modes and stellar modes is manifested in general astrophysical systems [131].

Dust and Planet Formation

For the core-accretion model of planet formation to be viable, during the earliest stages of planetesimal formation, micron-sized dust grains must collide and then combine to form larger particles in a process called binary agglomeration. However, it is unclear whether this mechanism can efficiently continue once particles reach centimeter to meter sizes. At this point, impact cratering and disruption could halt the process. The mechanical and chemical processes involved in grain agglomeration are poorly understood for particles in this size regime. Two colliding "rocks" of this size are just as likely, and possibly more likely, to shatter each other another apart as opposed to agglomerating together to form a larger object [209]. In addition, the slow growth for centimeter-decimeter sized particles via binary agglomeration process presents a major problem with the timescales associated with the formation of the giant planets. For gas giants to form via this process, rocky cores of several Earth masses must be formed in order to gravitationally capture sufficient gas to create the extensive atmospheres of the giant planets. The formation of these "cores" must be completed in less than a million years well before the disk gas is dispersed via accretion onto the parent star, photoevaporation, stellar winds, or close stellar encounters with other planetesimals completely halts or disrupts the planet formation process [96], [95]. Another proposed theory for gas giant planet formation relies on the disk having little to no turbulent motions such that the dust grains can settle into a thin sub-layer that might be dense enough to be gravitationally unstable to clumping [173], [73]. Whether the disk is turbulent or not is still an unresolved and greatly contested

issue. Unfortunately, even in the event that the disk is quiescent and the dust could settle into a thin sub-layer at the midplane, Weidenschilling (1980) has argued that a Kelvin-Helmholtz instability would develop between the dust-dominated layer at the midplane (which orbits at the Keplerian velocity) and the gas-dominated regions above and below the midplane (which orbit at sub-Keplerian velocities due to partial support by the internal pressure gradient) [208]. This instability might generate turbulence that would "kick-up" the dust and inhibit the gravitational clumping [31].

Many researchers in the field do not believe that disk instability is viable due to the fact that when they measure the Toomre-Q parameter, they generally find that $Q > 1.0$. This suggests that the disks are hot and stable. However, the Toomre-Q parameter was developed for infinitesimally think disks and may not be applicable to the stability of thick 3D disks nor nonaxisymmetric disks. In addition, instability does not require that the Toomre-Q parameter be small everywhere [141].

Temperatures, Shocks and Chrondrules

Chondrules, from the ancient greek *chrondros*, or grain, are small igneous rocks about 0.1-1.0 mm in diameter that were flash melted during their formation. Understanding the formation mechanism of chrondrules has remained an outstanding problem in astrophysics for over a century [64]. There have been several proposed theories that include planetesimal interactions with the young sun, planetesimal impacts, nebular shocks and lightning [182], [175] [147], [43], [45]. Among these proposed methods, the heating of chondrule precursors in nebular shocks is one of the more developed models for chondrule formation and is consistent with the meteoritic record [148]. However, gravitational instabilities leading to spiral arms drive strong shocks where high-density gas collides with lower density gas and can also be a source

of the heating needed for chondrule formation. Chondrules formed in this way are believed to form first 1 to 3 Myr of the Solar Nebulas evolution [19]. Chondrule precursors were flash melted at temperatures $T \approx 1700$ K were experienced by the precursors for a few minutes. The melts then cooled over hours, with the actual cooling time depending on chondrule type [178]. There are three basic types of chondrites in which almost all chondrules can be classified: carbonaceous, ordinary, and enstatite chondrites. For an in-depth discussion of chondrite classification and petrology, I refer the reader to the recent review articles by [94], [178], [110]. Ca-Al-rich Inclusions (CAIs) and Amoeboid Olivine Aggregates (AOAs) provide constraints on the environment of the early Solar Nebula. CAI's are thought to be among the first solids processed in the Solar Nebula with formation timescale of $0 - 0.3$ Myr. CAIs formed at pressures near 10^{-3} atm and at temperatures $T \approx 1400$ K. Some CAIs were completely melted and others were not [136]. It is estimated that half of all material accreted onto Earth each year is in the form of chondritic meteorites [93]. Chondrules, therefore constitute the primitive building blocks of terrestrial worlds. A theoretical description of the environments in which chondrules can form is a crucial step in understanding the formation and origin of our solar system.

For this discussion I focus on the shock wave model for chondrule formation [100], [44], [37]. Estimating that the shockfront in the non-cooling model is moving with speed $v = 15 - 20 r_\circ/\tau_\circ$ and using the kinetic theory of gas to estimate temperatures, and normalizations from table 1 for the Sol system, we find that $T = \frac{1}{3}\frac{m_p v^2}{k} \approx 550 - 940$ Kelvin.

Temperatures were calculated by dividing the internal energy density array $\epsilon(J, L, K)$ by the mass density array $\rho(J, L, K)$. With this definition,

$$\frac{\epsilon}{\rho} = \frac{kT}{(\gamma - 1)\mu m_p} \tag{5.1}$$

and

$$T = \frac{(\gamma - 1)\mu m_p}{k} \frac{\epsilon}{\rho} \tag{5.2}$$

To estimate dimensional temperatures, we can assume a gas composed of 75% hydrogen and 25% helium. A gas of hydrogen atoms (H) has $\mu = 1$, while a gas of helium atoms (He) has $\mu = 4$ which results in $\mu = 1.75$. The mass of a proton, $m_p = 1672.621910^{-27}$ g, $\gamma = 5/3$ and Boltzman's constant is $k = 1.380710^{-16}$ cm^2 g s^{-2} K^{-1}.

CHAPTER VI

FUTURE WORK

Understanding complex nonlinear systems such as those that lead to the formation of stars and planetary systems must be approached as an iterative task. Beginning with equilibrium configurations of pointmass stars surrounded by protoplanetary disks, we have slowly added layers of complication to the problem. Linear analyses were performed, followed by fully nonlinear evolution of the initial equilibrium configurations. Later, the pointmass approximation was relaxed and we developed equilibrium star and disk configurations whose evolution was followed into the linear and nonlinear regimes. To understand the formation and evolution of binary systems I proposed that we fully develop a binary module to be added into CHYMERA's algorithms.

Extension to Circumbinary Disks

The computer code CHYMERA was amended to perform nonlinear calculations of circumbinary disks - that is - disks surrounding two point-mass stars. This was done in a relatively simple way by directly calculating the force from one star on the other and using a leapfrog scheme to advance the binary star-system in time. Next, the binary stellar gravitational potential can be used to evolve the disk in time by superposition with the disk potential on the computational grid. The leapfrog algorithm is well suited for numerically integrating Newton's equations of motion over a long period of time starting from some initial conditions. The leapfrog scheme is often used in N-body dynamics codes and is well suited for these types of simulations

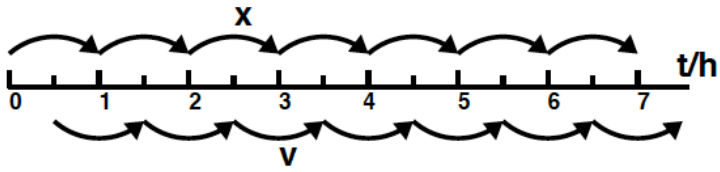

FIGURE 94. A flow chart which illustrates the second-order leapfrog integration scheme for the CHYMERA binary subroutine.

because (i) is it very simple to write (ii) it is a symplectic algorithm which gives it a "global" stability and (iii) it is a second-order method.

The leapfrog method is an elegant method for integrating Newtons laws of motion, which takes advantage of the property that dx/dt does not involve x itself and the equation for dv/dt does not involve v (assuming velocity independent forces). For a single degree of freedom, the equations of motion are

$$\frac{dx}{dt} = v \tag{6.1}$$

$$\frac{dv}{dt} = F(x) = -\frac{dU}{dt} \tag{6.2}$$

where $F(x)$ is the force on the particle when it is at position x, $U(x)$ is the potential energy and v is the velocity. The basic integration formula for the leapfrog integration is

$$x_{n+1} = x_n + hv_{n+1/2} \tag{6.3}$$

$$v_{n+3/2} = v_{n+1/2} + hFx_{n+1} \tag{6.4}$$

where n is the step number and h is the interval between timesteps. We show a simplified flow chart for the leapfrog algorithm in one-dimension in figure 94. You may immediately notice that without the $v_{1/2}$ term there is no clear way to make the algorithm work if we only know initial conditions x_0 and v_0. The easiest way to get around this is to simply use a Euler method to find the first half-step

$$v_{1/2} = v_0 + \frac{1}{2} hFx_0 \tag{6.5}$$

Despite the fact that this is a first order method, we only do this once and so our leapfrog scheme remains second order.

In addition to combining great simplicity with second order accuracy, the leapfrog algorithm has several other features that are highly desirable (i) it is time reversal invariant, (ii) it conserves angular momentum and (iii) it is symplectic (area preserving). To extend this algorithm to multiple dimensions is straight forward

$$x^i_{n+1} = x^i_n + hv^i_{n+1/2} \tag{6.6}$$

$$v^i_{n+3/2} = v^i_{n+1/2} + hF{x_{n+1}}^i \tag{6.7}$$

for $i = 1, ..., N$ coordinate dimensions.

The leapfrog algorithm was used to advance the two pointmass stars in space and time. Once a new position is calculated, we superimpose the two stars' point-like gravitational potential

$$\Phi_{tot*} = \Phi_* + \Phi_{bin} = -[\frac{\mathrm{G}M_*}{|\mathbf{r} - \mathbf{r}_*|} + \frac{\mathrm{G}M_{bin}}{|\mathbf{r} - \mathbf{r_{bin}}|}], \tag{6.8}$$

where Φ_{tot*} is the total potential from the two stellar components, Φ_{bin} is the potential from the secondary star, $\mathbf{r}$ is the field point, $\mathbf{r}_*$ is the position of the first stellar component, $\mathbf{r_{bin}}$ is the position of the secondary stellar component, with the potential from the disk. The perturbed disk self-gravity is again found by solving the Poisson equation. The potential from the two stars is superimposed with the disk component and used to evolve the fluid in the disk at cell for each timestep in the calculation.

Some issues arise with the point-particle approximation for the binary stars. At the location of any point particle, a singularity in the pontential will arise. To get around this, I softened the stars gravitational potential by assuming the stars to have a uniform density spread over several cells on the computational grid.

There are several issues that I can currently see with the binary module: (i) the stellar potential is superimposed with the disk potential to evolve the the the fluid forward in time, however, as the code is written now, the disk potential does not affect the stellar components. I have written preliminary code to achieve this, however, I could not yet convince myself that it was working properly and stability (e.g. computational stability of the algorithm) tests would need to be performed. (ii) An binary equilibrium code needs to be developed for our simulations to have any physical significance. As the code is currently written, we use the pointmass version of the Hachisu self-consistent filed algorithm [78]. This initial state is loaded into the CHYMERA nonlinear code. Then, the pointmass star is artificially broken into two components and the separation of the to components is chosen by the user. This in itself introduces energy to the system and starts off the simulation out of equilibrium. If the separation is small, then this should only act as a small perturbation away from equilibrium. However, if significant energy is added to the system, or the separation is large, then the physical significance of the simulation is questionable. Many tests

would need to be performed to determine what "small" means in this context, or better yet, a binary equilibrium code needs to be developed.

To isolate the properties of gravitational instabilities in circum-binary disks, a method of generating hydrostatic equilibrium density structures poses a significant challenge. It is important to begin with stable initial conditions to determine how instabilities grow and organize in the disk. Currently, no method of generating equilibrium density structures for binary systems exists due to their inherently non-axisymmetric structure. I would like to work toward deriving an analytical model for calculating these initial structures. Certain fluid quantities are invariant in the Euler equation governing fluid motion if the right assumptions are made. Using a new conserved variable (vorticity?), I hope to simplify the form of the equations used to derive time-independent equilibrium solutions. This, however, may not be possible. Completion of this task would constitute a major advancement in the study of circum-binary disks.

Non-Linear Circumbinary Disk Calculations – Preliminary Results

Here we present preliminary results from nonlinear pointmass binary star calculations using the newly developed algorithms that were incorporated into the CHYMERA code. The equilibrium properties for pointmass circumbinary disk calculations are given in Table 12. The model chosen had properties similar to the system binary system GGtau. In Figure 95 we show the integrated fourier amplitudes $\mathcal{A}_m$ for $m = 1$ to 8 in the disk midplane for model GG binary model. Times are normalized in units of $\tau_\circ$. The m-components of the density perturbation never reach steady exponential growth, however, the $m = 2$ maintains the highest amplitude throughout the simulation and eventually saturates around $A_2 = 1.0$. Again, even

m-modes saturate at a higher amplitude than odd-m with the exception of the $m = 1$ component.

In Figures 96 and 97 we show integrated midplane density maps of the nonlinear evolution of the GG model. Distances are normalized to $r_\circ$. In the upper left panel of 96 we see the disk just after perturbations have been applied. The presence of the pointmass binary system creates a dipole gravitational field and we see that this causes the disk to star pooling mass at points slightly ahead of a line connection the two stars in the upper right panel. We can also see that some mass has begun to pool in the gravitational well of the two stars. The dipole field has similar effects on the disk that the stellar bar mode does. It drives eccentricity changes in the disk. In the lower left panel we see that the disk has begun to develop two dense regions that are forming mass reservoirs. We can also see accretion from the disk onto the stars. In the lower right panel we can see that the mass reservoirs are beginning to accrete onto the two stars. In Figure 97 we can watch this accretion process continue until the two stars have accreted most of the disk mass. The new disk configuration resembles a two-armed spiral structure. One of the pointmass binary stars appears to accrete more material than the other. This could be related to the growth of the $m = 1$ component after the $m = 2$ saturates. In figures 98 and 99 we show integrated midplane density maps with overlaid velocity vectors for the nonlinear evolution of the GG model. Since the stars are not fully resolved, the velocity vectors in the stellar region do not have significance with respect ot the stars, they map the fluid motions.

Table 12. Equilibrium Properties of Pointmass Circumbinary Disks

M_*/M_d	β_d	j_{tot}	r_-/r_+	r_+	$r_\circ$	$\tau_\circ$	ρ_{max}	Ω_{max}
6.40	0.481	12.726	0.679	28.327	23.488	273.2	4.271E-03	81.660

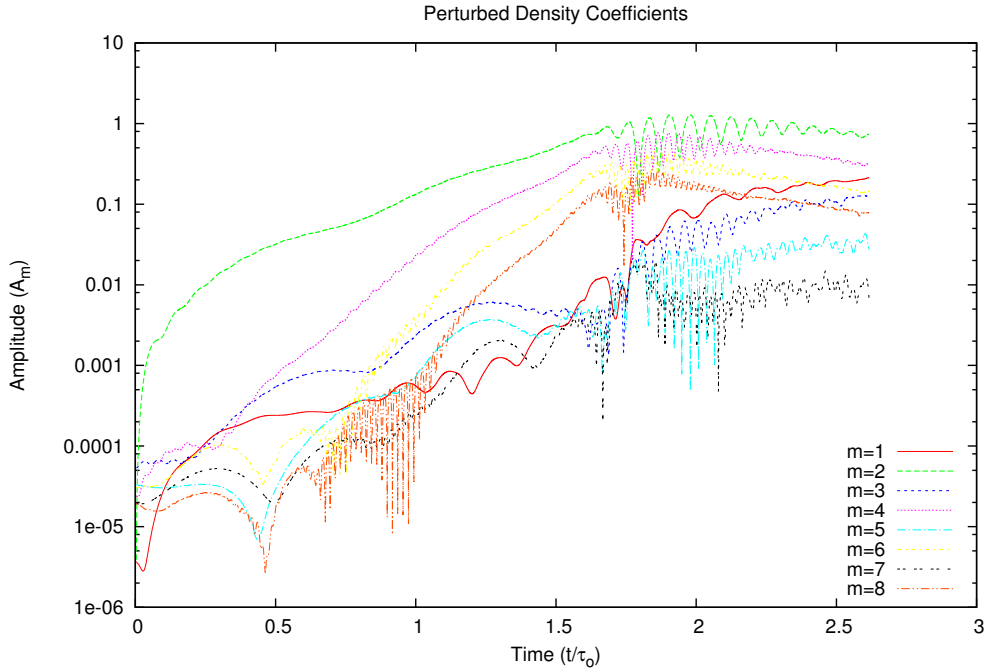

FIGURE 95. Integrated Fourier amplitudes $\mathcal{A}_m$ for $m = 1$ to 8 in the disk midplane for model GG binary model. Times are normalized in units of $\tau_\circ$, the rotation period for material at density maximum in the disk midplane.

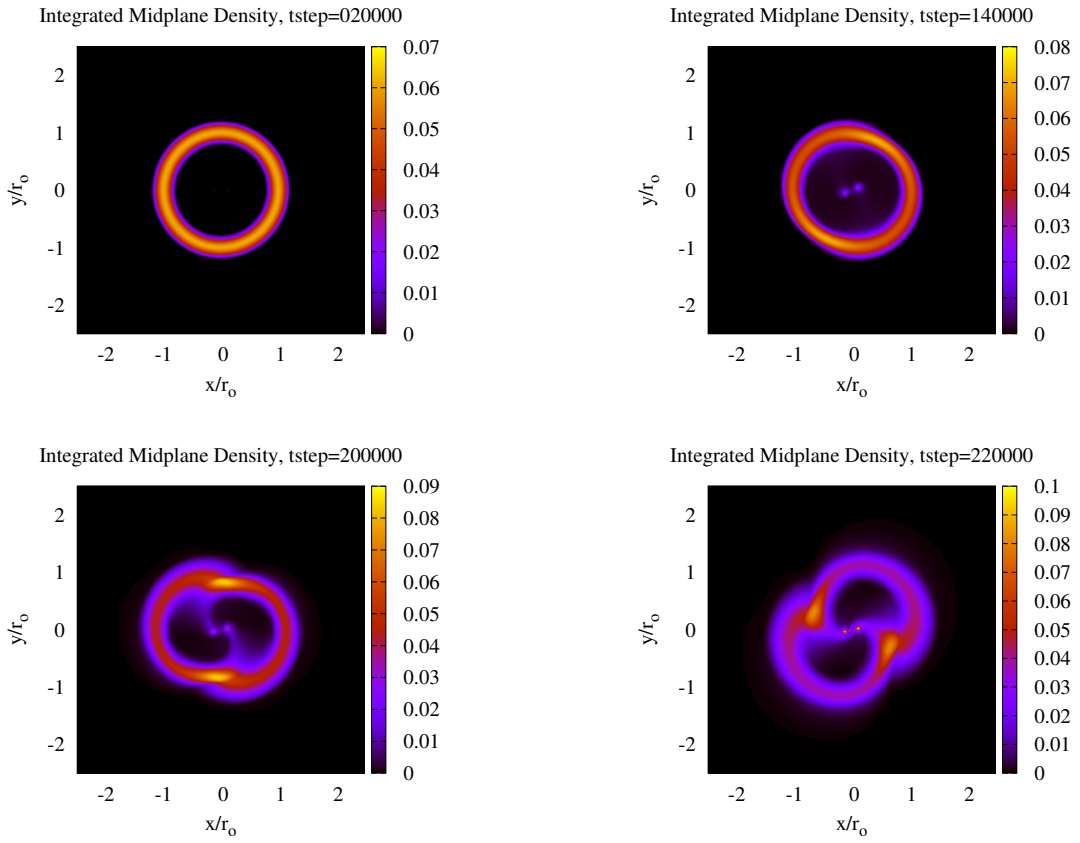

FIGURE 96. Integrated midplane density map of the nonlinear evolution of the *GG* model. Distances are normalized to $r_\circ$ the location of density maximum in the equilibrium disk.

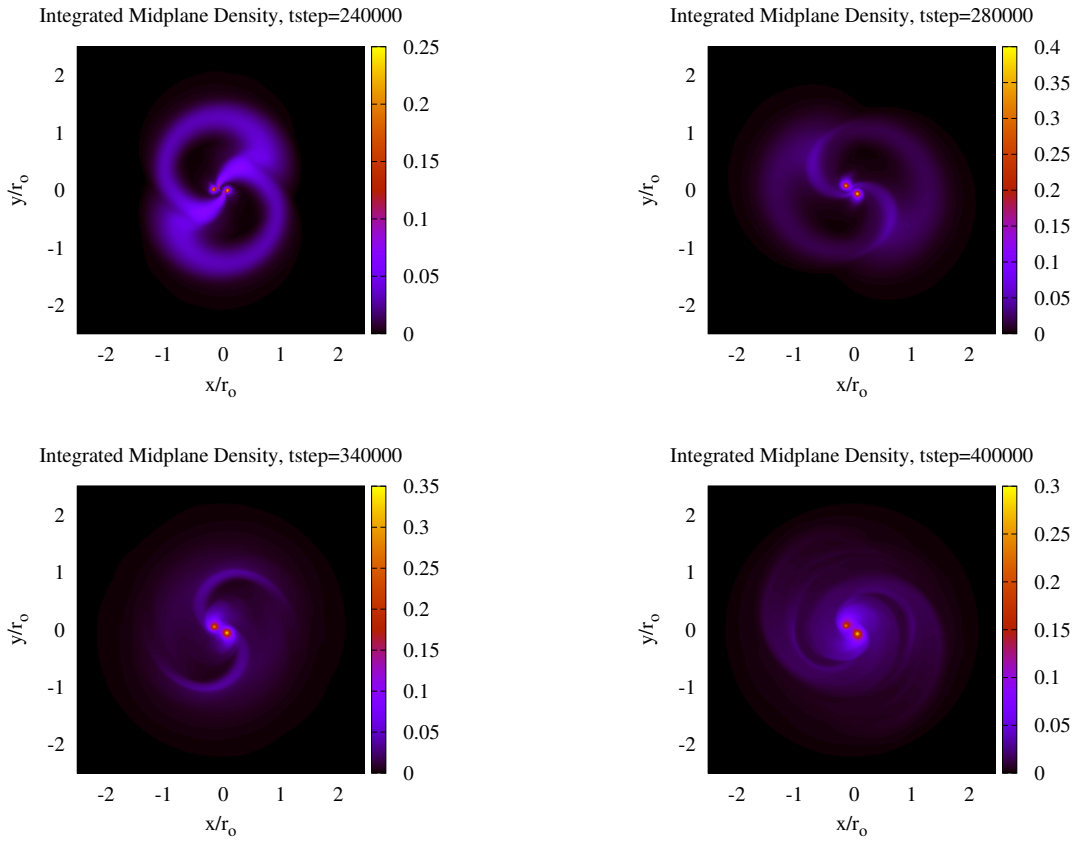

FIGURE 97. Integrated midplane density map of the nonlinear evolution of the *GG* model. Distances are normalized to $r_\circ$ the location of density maximum in the equilibrium disk.

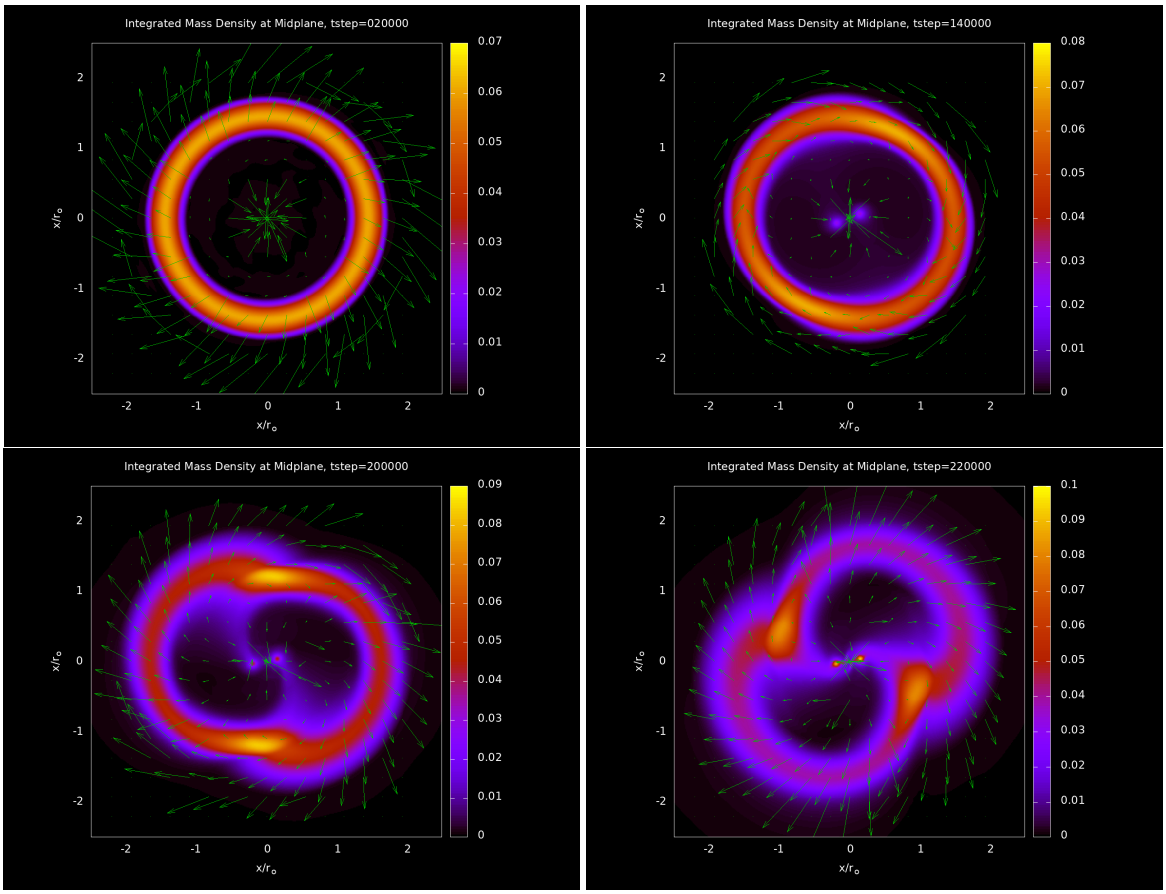

FIGURE 98. Integrated midplane density map with overlaid velocity vectors for the nonlinear evolution of the *GG* model. Distances are normalized to $r_\circ$ the location of density maximum in the equilibrium disk.

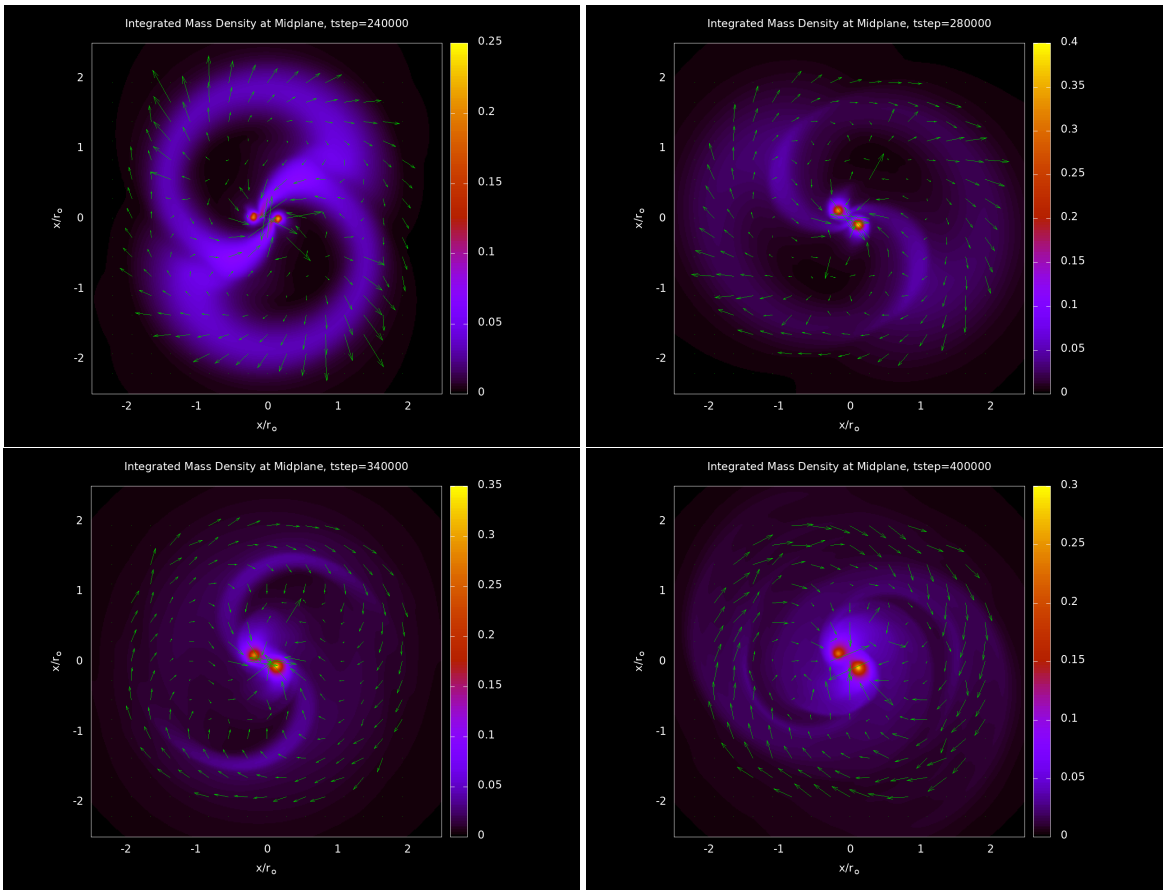

FIGURE 99. Integrated midplane density map with overlaid velocity vectors for the nonlinear evolution of the *GG* model. Distances are normalized to $r_\circ$ the location of density maximum in the equilibrium disk.

CHAPTER VII

SUMMARY AND CONCLUSIONS

This chapter is devoted to reporting the conclusions of my research and how the results of my work pertain to my initial research questions: Can the fission hypothesis produce short-period binary stars, and what initial conditions lead to the formation of binary stars and circumbinary planets?

From previous linear studies of circumstellar disks surrounding pointmass stars, an extensive library of equilibrium, and linear models was compiled covering the parameter space occupied by typical protostellar and protoplanetary disks. We examined equilibrium disk models varying three parameters: the ratio of the inner to outer equatorial radii, the ratio of star mass to disk mass, and the rotation law exponent q. We took the polytropic index $n = 1.5$ and examined the exponents $q = 1.5$ and 2, and the transitional $q = 1.75$. For each of these sets of parameters, we examined models with inner to outer radius ratios from 0.1 to 0.75, and star mass to disk mass ratios from 0 to 10^3. We numerically calculated the growth rates and oscillation frequencies of low-order nonaxisymmetric disk modes m = 1-5, modes with azimuthal dependence $\propto \mathrm{e}^{im\phi}$. Low-$m$ modes are found to dominate with the character and strength of instability strongly dependent on disk self-gravity. Representatives of each mode type were examined in detail, and torques and mass transport rates were calculated. Disk models were grouped into families defined by n and q, where family members were parameterized by r_-/r_+, the ratio of the inner and outer radii of the disk, and M_*/M_d, the ratio of the star to disk mass. Disk modes were identified and classified in terms of their morphological and dynamical properties. This previous work served as a foundation for understanding

nonaxisymmetric instabilities in protostellar disks and for informing how and why I chose the particular initial conditions for exploring the Fission hypothesis of binary star formation.

The fission model chosen for particular study has a central compressible star in rapid differential rotation. The star has the specific angular momentum distribution $h_M(\varpi) = 2m_\varpi$, the so-called L-distribution. By rapid rotation, we mean that the star has $\beta = T/|W|$ above the Maclaurin spheroid barlike mode secular instability threshold, $\beta_{sec} = 0.137$ (*e.g.,* see Tassoul 1978). The star, however, has β_* below the dynamic barmode instability threshold $\beta_{dyn} = 0.274$ where dynamic barlike instabilities have been shown to develop for incompressible Maclaurin spheroids [187]. In this case, the dynamically stable star according to the β_{dyn} criterion, may be driven unstable by the coupling of the secularly unstable stellar mode to the dynamically unstable disk mode [220], [103]. Alternatively, the disk may alter the central star configuration greatly enough to make the star unstable to the dynamic bar instability even though $\beta_* < \beta_{dyn}$ [131], [85]. We use $q = 1.5$ and the central star has ratio $r_p/r_e = 0.180$, $r_e/r_- = 0.790$, while the disk has $r_-/r_+ = 0.66$ and $\beta_d = .455$. The ratio of the stellar mass to disk mass is $M_*/M_d = 1.18$ where we have an approximately equal mass star and disk.

Based on our previous linear studies, the fission model $M2$ would be classified as an I^- mode and is expected to have the largest linear growth in the $m = 2, 3$ components of the density perturbation. The model parameters were chosen due in part because the disk is massive and expected to have a large effect on the star and due to the region of parameter space where the $m = 2$ coefficient is expected to dominate the disk leading to a two-fold symmetry conducive to the excitation of the barmode in the star and formation of a binary central object.

The *fission hypothesis* is not widely accepted by the astrophysics community as a viable way to produce close-binary stars due to the failure of past numerical studies [191], [135]. Based on previous nonlinear studies of solitary differentially rotating polytropic stars, the central star develops a nonaxisymmetric barmode instability which does not

fission due to the development of spiral arms. Torques from the spiral arms transfer angular momentum outward leading to spin-down of the central object.

Williams (1988) found that within $\approx 10\tau_{cen}$, a rapidly rotating polytrope of index $n = 0.8$ and $\beta = 0.31$ develops a central bar mode with trailing spiral arms. The trailing spiral arms exert a torque on the central object which slows its rotation. This resulted in a system with a slowly rotating central star plus a ring. Williams (1988) suggested that including cooling effects could drive the future evolution of the barmode and lead stellar fission [213].

Imamura (1999) investigated nonaxisymmetric instabilities in rapidly rotating polytropes with specific attention to the bar mode. Again, this study found that the barmode produces barlike distortions in the central region of the polytropes which trail into spiral arms. The spiral arms gave rise to self-gravitational torques which control the nonlinear evolution of the system. The self-gravitational torque was calculated using quasi-linear theory and then compared to fully nonlinear hydrodynamic simulations. Imamura (1999) found that (i) saturation of the bar mode is due to the self-interaction gravitational torque (ii) saturation occurs before fission can occur (iii) quasi-linear theory accurately predicts mass and other global properties of the bar (iV) bars will show two stages of evolution; a dynamic growth phase leading to saturation of the mode and a secular phase where the bar sheds angular momentum to the spiral arms. Imamura (1999) concluded that the self-

interaction torque saturates the growth of the barmode before it can lead to fission and hence the formation of close binary star systems [101]. Previous studies of the fission process did not include the effects a protostellar disk can have on the evolution of the stellar core, and therefore, dismissed significant physics which naturally take place in the stellar and planetary evolution process.

We investigated the affects of including circumstellar material into the calculation. Beginning from an equilibrium mass density and angular momentum structure where the fundamental quantities are unchanging in time, we perturbed the system and followed the evolution using linear and nonlinear methods. We find very good agreement between our linear and nonlinear models. In this way, less computationally expensive linear methods are a good predictor for nonlinear effects. Circumstellar disks produce an outward radial acceleration on material inside the inner edge of the protoplanetary disk. This tends to weaken the average inward pull due to the stellar gravitational field and increase tidal forces at points inside the star. This reduction of the inward force of gravity on the star lowers the threshold in β where dynamice barlike nonaxisymmetric instabilities develop compared to systems without circumstellar disk material.

The nonlinear evolution of the system can be broken down into four stages: (i) an initial settling phase while the instability is organizing in the system, (ii) a linear stage in the evolution where there is good agrement with linear calculations, (iii) a saturation stage characterized by the dominant component of the density perturbation reaching maximal amplitude where large scale changes to the density structure of the disk occur, and finally (iv) a stage beyond saturation where a new steady state occurs. In the absence of cooling, an $m = 2$ barmode instability develops in the central star with trailing spiral arms. Once the instability reached saturation amplitudes, the

star interacts with the disk and after $2.60\tau_{circ}$ when $A_2 = 1.47$ the system evolves into two unequal mass binary stellar objects which rotate on independent axes and orbit a common center of mass. This work serves as proof of concept that even in the absence of cooling, the fission model is a viable avenue of binary star formation when informed initial conditions are explored and circumstellar material is included. When the simulation was halted, the binary stars have a separation of roughly $1.6r_\circ$. The maximum density in the primary star is $\rho_{max} = 0.12$ and the maximum temperature is $T = 0.2$. Shockwaves produced when the star interacted with the disk resulted in maximum temperatures of $T = 0.7$ when $t/\tau_\circ = 1.7$ and $A_2 = 0.83$. The simulation was halted at $t/\tau_\circ = 2.60$ when a total of 5.2% of the material had flowed off the computational grid. At this point, we found that the two stellar components are unequal in mass with the primary stellar component containing roughly 46% of the initial mass of the system and the secondary component containing roughly 27%. The remaining 21.8% of the mass on the computational grid was contained in the disk filaments. To put these numbers into context, we use the conversion factors reported in Table 1 to convert polytrope units to dimensional units. If we use the conversion factors for a Sol-like system we find that evolution of the binary system occurs on very short timescales where $2.6\tau_\circ = 13.1$ years at this point the binary separation is 16 AU. However, if we use conditions similar to that of the system GGtau we find that $2.6\tau_\circ = 1,532.9$ years and the separation to be 144 AU.

We then considered the effects of radiative losses to the system using a constant cooling function Λ exploring the effects of three different cooling rates scaled to the characteristic timescales of the star and/or disk. We investigated how cooling changes the growth-rates of the fastest growing modes and what effect this has on the nonlinear evolution of the $M2$ system. When radiative losses are included, we find that fission

still occurs but the morphology of the system changes due to the loss of pressure support in the gas. This can change the value of r_-/r_+ for the system and push it into a region of parameter space where higher m components grow. Cooling does not strongly alter the properties of star-disk modes rather, cooling changed the outcome of simulations because it modified the structure of the background disk.

We explored the affects of weak cooling where $\tau_c = 5\tau_\circ = 15.2\tau_{cen}$. With this definition the volumetric cooling rate used in the energy equation becomes $\Lambda = \epsilon/5\tau_\circ$. Disk fragmentation is thought to occur when: (i) the Toomre Q-parameter is smaller than 1.6-1.7 somewhere in the disk, indicating that the disks are unstable to gravitational instabilities; and (ii) cooling is efficient. Recall that Gammie (2001) derived a cooling criteria for 2D thin disks which states that if the timescale for the local internal energy to dissipate is more or less equivalent to the local orbital timescale, clump production will follow [71]. The precise definition for *efficient* is not clear as it depends on numerical resolution, artificial viscosity, and Λ [142], [143], [145], [183]. Meru & Bate (2012) suggest that the critical cooling time falls in the range $\tau_c/\tau_\circ \sim$ 3-5. With this definition of the cooling rate, we did not expect to see based on the Gammie criterion, and no fragmentation occurred in the system. The linear stage of evolution occurs between $0.4 < t/\tau_\circ < 1.3$. Compared to the non-cooling case, exponential growth in the $m = 3$ component begins at $\tau_\circ = 0.6$ again, followed by the $m = 4$ near $\tau_\circ = 1.2$. The growth rate in the $m = 3$ component is larger with the addition of weak cooling compared to the case where no radiative losses were considered. We estimate that $m = 2$ grows at a rate of $\approx 10.8\tau_\circ^{-1}$ and $m = 3$ grows at a rate of $\approx 10.1\tau_\circ^{-1}$. At $t/\tau_\circ = 1.36$ when $A_2 = 0.33$, the star begins to develop a central bar with trailing spiral arms near the outer edge. The central bar becomes more compact/slender due to the loss of pressure support from cooling as compared to

the non-cooling case. When the simulation is halted at $t/\tau_\circ = 2.53$ when $A_2 = 1.68$, the system has evolved into two equal mass binary stars. The disk at this point is very diffuse. When weak cooling is included the odd-m Fourier components never reach the saturation amplitudes of the even-m components. This may account for the even symmetry of the system's evolution. When the simulation is halted, the binary stars sit at a separation of roughly $\varpi = 2.5r_\circ$. At $\tau_\circ = 2.53$ a total of 5.5% of the material had flown off the grid. At this point we find that the two stellar components are roughly equal in mass with the primary stellar component containing roughly 43% of the initial mass of the system and the secondary stellar component containing roughly 40%. The remaining 11.5% of the mass on the computational grid is contained in the disk filaments. We saw counterclockwise circulation in each of the stellar objects that forms nearly circular streamlines. At this point, the maximum density in the primary star was $\rho = 0.06$ and the maximum temperature was $T = 0.25$. Shockwaves produced by stellar interaction with the disk steepened when weak cooling was considered and formed a circular wave with very high temperatures $T = 3.5$ that spread away from the disk at speeds of about $v = 15/20r_\circ/\tau_\circ$. Temperatures reached in the shockwave were 14 times higher than that of the final stellar temperatures.

For the system with a moderate cooling rate, where $\tau_c = 1.7\tau_\circ = 5.0\tau_{cen}$, according to the Gammie criterion we could have expected to see fragmentation since the timescale for the local internal energy to dissipate on order of the local orbital timescale for both the star and the disk. Again, we find a $m = 3$ three-armed mode grows in tandem with the $m = 2$ mode. The system transitions into the linear phase of its evolution with steady exponential growth of the $m = 2$ component between $0.4 < t/\tau_\circ < 1.2$. The growth rate in the $m = 3$ component is larger with moderate cooling than weak cooling and on order with the $m = 2$ component until $\tau_\circ = 1.2$

when $m = 4$ starts growing exponentially. This could be evidence of mode mixing where power from one mode is transferred to another mode. Coupling between the even and odd modes may be responsible for the differences we see in the evolution of the system. We estimated that $m = 2$ grows at a rate of $\approx 12.3\tau_\circ^{-1}$ and $m = 3$ grows at a rate of $\approx 12.5\tau_\circ^{-1}$ but then changes to $\approx 9.2\tau_\circ^{-1}$ when the $m = 4$ starts growing. At $t/\tau_\circ = 1.94$ when $A_2 = 1.45$, the system evolves into to unequal mass binary pairs. With moderate cooling, fragmentation of the disk occurs, where disk fragments are later absorbed by the stars. Shockwaves launched by star-disk interactions steepen forming a circular wave with very high temperatures $T = 3.0$ 12 times higher than that of the final stellar temperatures. The model is halted at $\tau_\circ = 2.48$ after 4.7% of the mass has flowed off the grid and $A_2 = 1.61$. At this point the system has evolved into two unequal mass binary stars. There is counterclockwise circulation in each of the stellar objects that forms nearly circular streamlines. At this point, the binary stars sit at a separation of roughly $\varpi = 2.3r_\circ$. The maximum density in the primary star is $\rho = 0.2$ and the maximum temperature is $T = 0.25$. The primary stellar component contains roughly 49.7% of the initial mass of the system and the secondary stellar component containing roughly 32.8%. The remaining 12.8% of the mass on the computational grid is contained in the disk filaments.

For the fastest cooling rate tested, where $\tau_c = 1.0\tau_\circ = 3.0\tau_{cen}$, we expected disk fragmentation based on the Gammie criterion. The qualitative evolution of this model was markedly different in character than for the previous cooling rates tested. With fast cooling, the model spends less time in organizational/settling phase of its evolution as compared to the non-cooling, weak and moderate cooling cases. The system transitions into the linear phase of its evolution with steady exponential growth of the $m = 2$ component between $0.3 < t/\tau_\circ < 1.2$. Compared to the non-

cooling, weak and moderate cooling case, exponential growth in the $m = 3$ component briefly appears at $\tau_\circ = 0.6$ at which point growth dampens and at $t/\tau_\circ = 0.7$ growth in the $m = 7$ and $m = 8$ components begins. We estimate that $m = 2$ grows at a rate of $\approx 11.9\tau_\circ^{-1}$ and $m = 3$ briefly grows at a rate of $\approx 11.9\tau_\circ^{-1}$ but then changes character completely at which point the $m = 7$ and $m = 8$ components grow at a rate of $\approx 12.2\tau_\circ^{-1}$ and $\approx 12.1\tau_\circ^{-1}$, respectively. At $t/\tau_\circ = 1.16$ when $A_2 = 0.09$ the disk undergoes fragmentation corresponding to growth of the $m = 7$ and $m = 8$ components of the density perturbation. We see evacuation of the central star, a new feature of the fast cooling model. We speculate this is due to the rapid rotation combined with the fast cooling rate and that the star's outer edge and the disk inner edge $r_e/r_- = 0.79$ are very close to one another. This reduces the inward force of gravity in the star allowing disk to pull the stellar material outward. At the same time fast cooling is causing the loss pf pressure support before gravitational instability can organize in the system and balance the cooling with heat produced via shocks. The disk fragmented into ten clumps, and the evacuated stellar object folded over on itself forming a bar like object with two distinct dense regions. When the central star intersects with the disk, a shockwave is launched. This shockwave does not disrupt the disk fragments. The shockwave formed a circular wave with a high temperature of $T = 0.9$, temperatures 3 times higher than that of the final stellar temperatures. The model is halted at $\tau_\circ = 2.30$ after 6.5% of the mass has flowed off the grid when $A_2 = 1.46$. At this point, the maximum density in the primary star is $\rho = 0.16$ and the maximum temperature is $T = 0.3$. The system evolved into two unequal mass stellar sized objects which rotate on independent axes and show nearly circular stramlines. The stellar components are orbited by two remaining disk fragments. These fragments also have circulating stramlines and we speculate that these objects could be Jovian

planetary precursors formed via the disk instability method of planet formation. The primary stellar component contains roughly 58.1% of the initial mass of the system and the secondary stellar component contains roughly 16.6%. The two substellar clumps contain 3.9% and 3.8% of the initial mass of the system. The remaining 3.9% of the mass on the computational grid is contained in the disk filaments.

This work serves to show that the fission process is a viable method of forming not only multiple star systems, but planets around multiple star systems. In addition, this work shows that the disk instability theory of Jovian planet formation is a viable method of forming planetary precursors. This work is by no means a complete picture, but it demands that further studies endeavor to investigate this mechanism as an avenue for forming short-period binary star systems capable of harboring planets.

REFERENCES CITED

[1] Adams, F.C., Shu, F.H., & Lada, C.J. 1987a. The Disks of T Tauri Stars with Flat Infrared Spectra. *Bulletin of the American Astronomical Society*, **19**, p.1096.

[2] Adams, F.C., Lada, C.J., & Shu, F. H. 1987b. Spectral Evolution of Young Stellar Objects. *Astrophysical Journal*, **312**, p.788.

[3] Adams, F.C., Ruden, S.P., & Shu, F. H. 1989. Eccentric Gravitational Instabilities in Nearly Keplerian Disks. *Astrophysical Journal*, **347**, p.959.

[4] Albrecht, S., Winn, J.N., D.C., Fabrychy, Torres, G., & Setiawan, J. 2012. *The BANANA Survey: Spin-Orbit Alignment in Binary Stars.* From Interacting Binaries to Exoplanets: Essential Modeling Tools, Proceedings of the International Astronomical Union. Edited by M. T. Richards and I. Hubeny, IAU Symposium, Volume 282, p. 397-398.

[5] Alves, F.O., *et al.* . 2019. Gas flow and accretion via spiral streamers and circumstellar disks in a young binary protostar. *Science*, **366**(6461), 90–93.

[6] Andalib, S.W., Tohline, J.E., & Christodoulou, D.M. 1997. A Survey of the Principal Modes of Nonaxisymmetric Instability in Self-Gravitating Accretion Disk Models. *The Astrophysical Journal Supplement Series*, **108**, 471–487.

[7] Andrews, S., *et al.* . 2018. The Disk Substructures at High Angular Resolution Project (DSHARP). II. Characteristics of Annular Substructures. *The Astrophysical Journal Letters*, **869**(2), 27 pp.

[8] Andr, P. 2011. *Spectral Classification of Embedded Stars. In: Gargaud M. et al. (eds) Encyclopedia of Astrobiology.* Berlin, Heidelberg: Springer.

[9] Armitage, P.J. 2011. Dynamics of Protoplanetary Disks. *Annual Review of Astronomy and Astrophysics*, **49**, 195–236.

[10] Bai, XN., & Stone, J.M. *Non-ideal MHD Effects in Protoplanetary Disks.* American Astronomical Society, ESS meeting no.2, id.36.03.

[11] Baines, D., Oudmaijer, R.D., Porter, J.M., & Pozzo, M. 2016. On the binarity of Herbig Ae/Be stars. *Monthly Notices of the Royal Astronomical Society*, **367**, 737–753.

[12] Balbus, S. A. 2003. Enhanced Angular Momentum Transport in Accretion Disks. *Annual Review of Astronomy & Astrophysics*, **41**, 555–597.

[13] Balbus, S. A., & Hawley, J.F. 1991a. A Powerful Local Shear Instability in Weakly Magnetized Disks. II. Nonlinear Evolution. *Astrophysical Journal*, **376**, p.223.

[14] Balbus, S. A., & Hawley, J.F. 1998. Instability, turbulence, and enhanced transport in accretion disks. *Reviews of Modern Physics*, **70**, 1–53.

[15] Balbus, S.A., & Hawley, J.F. 1991b. A Powerful Local Shear Instability in Weakly Magnetized Disks. I. Linear Analysis. *Astrophysical Journal*, **376**, p.214.

[16] Barge, P., & Sommeria, J. 1995. Did planet formation begin inside persistent gaseous vortices? *Astronomy and Astrophysics*, **295**, L1–L4.

[17] Batalha, N.M., *et al.* . 2013. Planetary candidates observed by Kepler. III. Analysis of the first 16 months of data. *The Astrophyiscal Journal Supplementary Series*, **204**(2).

[18] Bate, M., Lodato, G., & Pringle, J.E. 2010. Chaotic star formation and the alignment of stellar rotation with disc and planetary orbital axes. *Monthly Notices of the Royal Astronomical Society*, **401**, 1505–1513.

[19] Bizzarro, M., Baker, J.A., & Haack, H. 2004. Mg isotope evidence for contemporaneous formation of chondrules and refractory inclusions. *Nature*, **431**, 275–278.

[20] Blum, J., & Wurm, G. 2000. Experiments on Sticking, Restructuring, and Fragmentation of Preplanetary Dust Aggregates. *Icarus*, **143**, 138–146.

[21] Boley, A., *et al.* . 2006. The Thermal Regulation of Gravitational Instabilities in Protoplanetary Disks. III. Simulations with Radiative Cooling and Realistic Opacities. *The Astrophysical Journal*, **651**, 517–534.

[22] Boley, A.C. 2007. *The Three-Dimensional Behavior of Spiral Shocks in Protoplanetary Disks*. Ph.D Thesis, Indiana University.

[23] Boley, A.C., Hartquist, T.W., Durisen, R.H., & Michael, S. 2007. The Internal Energy for Molecular Hydrogen in Gravitationally Unstable Protoplanetary Disks. *The Astrophysical Journal,*, **656**, L89–L92.

[24] Bonnell, I., & Bate, M. 1994. The Formation of Close Binary Systems. *Monthly Notices of the Royal Astronomical Society*, **271**(4), 999–1004.

[25] Brush, S. 1996. *A history of modern planetary physics*. New York: New York: Cambridge University Text. Accessed Online: https://archive.org/details/historyofmodernp0000brus/page/6/mode/2up.

[26] Burrows, C.J, *et al.* . 1996. Hubble Space Telescope Observations of the Disk and Jet of HH 30. *Astrophysical Journal*, **473**, p. 437.

[27] Cabritt, S. *The Origin of Jets: Observational Constraints vs. Theoretical Predictions*. JENAM-2007, "Our non-stable Universe", held 20-25 August 2007 in Yerevan, Armenia. Abstract book, id. 22-22.

[28] Cai, K. 2006. *3D Hydrodynamics Simulations of Gravitational Instabilities in Embedded Protoplanetary Disks*. Ph.D Thesis, Indiana University.

[29] Cai, K., *et al.* . 2006. The Effects of Metallicity and Grain Size on Gravitational Instabilities in Protoplanetary Disks. *The Astrophysical Journal*, **636**, L149–L152.

[30] Casseus, S., *et al.* . 2015. A Compact Concentration of Large Grains in the HD 142527 Protoplanetary Dust Trap. *The Astrophysical Journal*, **812**.

[31] Champney, J.M. 1995. A numerical turbulence model for multiphase flows in the protoplanetary nebula. *Physics of Fluids*, **7**, pp.1703.

[32] Chandrasakhar, S. 1958. *An Introduction to the Study of Stellar Structure*. New York: Dover Publications.

[33] Chandrasakhar, S. 1969. *Ellipsoidal Figures of Equilibrium*. New Haven: Yale University Press.

[34] Chandrasakhar, S. 1981. *Hydrodynamic and Hydromagnetic Instability*. New York: Dover Publications.

[35] Chini, R., Hoffmeister, V.H., Nasseri, A., Stahl, O., & Zinnecker, H. 2012. A spectroscopic survey on the multiplicity of high-mass stars. *Monthly Notices of the Royal Astronomical Society*, **424**, 1925–1929.

[36] Christodoulou, D.M., & Narayan, R. 1992. The Stability of Accretion Tori. IV. Fission and Fragmentation of Slender, Self-gravitating Annuli. *Astrophysical Journal*, **388**, p. 451.

[37] Ciesla, F., & Hood, L. 2002. The Nebular Shock Wave Model for Chondrule Formation: Shock Processing in a ParticleGas Suspension. *Icarus*, **158**, 281–293.

[38] Cieza, L.A., *et al.* . 2017. ALMA Observations of Elias 224: A Protoplanetary Disk with Multiple Gaps in the Ophiuchus Molecular Cloud. *The Astrophyiscal Journal Letters*, **851 L23**.

[39] Cohen, M., & Kuhi, L.V. 1979. Observational studies of star formation: conclusions. *Astrophysical Journal, Part 2 - Letters to the Editor*, **227**, L105–L106.

[40] Cuzzi, J.N., Dobrovolskis, A.R., & Champney, J.M. 1993. Particle-Gas Dynamics in the Midplane of a Protoplanetary Nebula. *Icarus*, **106**, 102–134.

[41] D'Angelo, G., Durisen, R.H., & Lissauer, J.J. 2010. *Giant Planet formation.* Exoplanets, edited by S. Seager. Tucson, AZ: University of Arizona Press.

[42] De Rosa, R.J., *et al.* . 2014. The VAST Survey III. The multiplicity of A-type stars within 75pc. *Monthly Notices of the Royal Astronomical Society*, **437**, 1216–1240.

[43] Desch, S. 2006. How to make a chondrule. *Nature*, **441**, 416–417.

[44] Desch, S., & Connoly, H.C. 2002. A model of the thermal processing of particles in solar nebula shocks: Application to the cooling rates of chondrules. *Meteoritics & Planetary Science*, **37**, 183–207.

[45] Desch, S.J., & Cuzzi, J.N. 2001. The Generation of Lightning in the Solar Nebula. *Icarus*, **143**, 87–105.

[46] Di Folco, E., *et al.* . 2014. GG Tauri: the fifth element. *Astronomy and Astrophysics*, **565**(1404).

[47] Duchene, G., & Kraus, A. 2013. Stellar Multiplicity. *Annual Review of Astronomy and Astrophysics*, **51**(1), 269–310.

[48] Durisen, R.H. 1973. Viscous Effects in Rapidly Rotating Stars with Application to White-Dwarf Models. Theory and Techniques. *Astrophyiscal Journal*, **183**, 205–214.

[49] Durisen, R.H. 1978. Incompressible fluid ellipsoids in halos. I. The second-harmonic oscillations of the Maclaurin spheroids. *Astrophysical Journal*, **224**, 826–834.

[50] Durisen, R.H., & Howard, E. 1984. Implications of recent numerical calculations for the fission theory of the origin of the Moon. *Icarus*, **58**(2), 153–158.

[51] Durisen, R.H., & Tohline, J.E. 1980. A Numerical Study of the Fission Hypothesis for Rotating Polytropes. *Space Science Reviews*, **27**(3-4), 267–273.

[52] Durisen, R.H., Gingold, R.A., Tohline, J.E., & Boss, A.P. 1982. The Binary Fission Hypothesis: A Comparison of Numerical Results. *Bulletin of the American Astronomical Society*, **14**, p.888.

[53] Durisen, R.H., Gingold, R.A., Tohline, J.E., & A.P., Boss. 1986. Dynamic Fission Instabilities in Rapidly Rotating N = 3/2 Polytropes: A Comparison of Results from Finite-Difference and Smoothed Particle Hydrodynamics Codes. *Astrophyiscal Journal*, **305**, p.281.

[54] Durisen, R.H., *et al.* . 2007. *Gravitational Instabilities in Gaseous Protoplanetary Disks and Implications for Giant Planet Formation.* Protostars and Planets V, B. Reipurth, D. Jewitt, and K. Keil (eds.), University of Arizona Press, Tucson, 951 pp., 2007., p.607-622.

[55] Dursen, R.H., *et al.* . *Dynamic Instability of Barlike Modes.* Birth and Evolution of Binary Stars, Poster Proceedings of IAU Symposium No. 200 on The Formation of Binary Stars, held 10-15 April, 2000, in Potsdam, Germany. Edited by Bo Reipurth and Hans Zinnecker, 2000, p. 187.

[56] Dutrey, A., Gullotau, S., & Simon, M. 1994. Images of the GG Tauri rotating ring. *Astronomy and Astrophysics*, **286**, 149–159.

[57] Dyson, F.W. 1893. *The potential of an anchor ring.*

[58] Eisner, J.A., & J.M., Carpenter. 2003. Distribution of Circumstellar Disk Masses in the Young Cluster NGC 2024. *The Astrophysical Journal*, **598**(2), 1341–1349.

[59] Eisner, J.A., & J.M., Carpenter. 2006. Massive Protoplanetary Disks in the Trapezium Region. *The Astrophysical Journal*, **641**(2), p. 1162.

[60] Eriguchi, Y., & Hachisu, I. 1982. New Equilibrium Sequences Bifurcating from Maclaurin Sequence. *Progress of Theoretical Physics*, **67**(3), 844–851.

[61] Eunkyu, h., *et al.* . 2014a. Exoplanet Orbit Database. II. Updates to Exoplanets.org. *Publications of the Astronomical Society of the Pacific*, **126 827**.

[62] Eunkyu, H., *et al.* . 2014b. Exoplanet Orbit Database. II. Updates to Exoplanets.org. *Publications of the Astronomy Society of the Pacific*, **126**(943), 827. accessed online.

[63] Fabrycky, D., & Tremaine, S. 2007. Shrinking Binary and Planetary Orbits by Kozai Cycles with Tidal Friction. *The Astrophysical Journal*, **669**(2), 1298–1315.

[64] Farrington, O.C. 1915. *Meteorites, their structure, composition, and terrestrial relations.* Chicago: Lakeside Press.

[65] Fleming, T.P., Stone, J.M., & Hawley, J.F. 2000. The Effect of Resistivity on the Nonlinear Stage of the Magnetorotational Instability in Accretion Disks. *The Astrophysical Journal*, **530**, 464–477.

[66] Forgan, D., & Rice, K. 2011. The Jeans mass as a fundamental measure of self-gravitating disc fragmentation and initial fragment mass. *Monthly Notices of the Royal Astronomical Society*, **417**, 1928–1937.

[67] Forgan, D., Rice, K., Cossins, P., & Lodato, G. 2011. The nature of angular momentum transport in radiative self-gravitating protostellar discs. *Monthly Notices of the Royal Astronomical Society*, **410**, 994–1006.

[68] Friedman, J.L., & Schutz, B.F. 1978. Secular instability of rotating Newtonian stars. *Astrophysical Journal*, **222**, 281–296.

[69] Furlan, E., *et al.* . 2006. A Survey and Analysis of Spitzer Infrared Spectrograph Spectra of T Tauri Stars in Taurus. *The Astrophysical Journal Supplement Series*, **165**(2).

[70] Gammie, C.F. 1996. Linear Theory of Magnetized, Viscous, Self-gravitating Gas Disk. *Astrophysical Journal*, **462**, p.725.

[71] Gammie, C.F. 2001. Nonlinear Outcome of Gravitational Instability in Cooling, Gaseous Disks. *The Astrophysical Journal*, **553**, 174–183.

[72] Gillion, M., *et al.* . 2017. Seven temperate terrestrial planets around the nearby ultracool dwarf star TRAPPIST-1. *Nature*, **542**, 456–460.

[73] Goldreich, P., & Ward, W.R. 1973. The Formation of Planetesimals. *Astrophysical Journal*, **183**, 1051–1062.

[74] Goldreich, P., Goodman, J., & Narayan, R. 1986. The stability of accretion tori. I - Long-wavelength modes of slender tori. *Monthly Notices of the Royal Astronomical Society*, **221**, 339–364.

[75] Goodman, J., & Narayan, R. 1988. The stability of accretion tori. III - The effect of self-gravity. *Monthly Notices of the Royal Astronomical Society*, **231**, 97–114.

[76] Goodwin, S.P., Kroupa, P., Goodman, A., & Burkert, A. 2014. *The Fragmentation of Cores and the initial Binary Population.* Protostars and Planets V. Protostars and Planets V is a book collection of various contributed papers.

[77] Greene, T.P., *et al.* . 1994. Further mid-infrared study of the Ophiuchi cloud young stellar population: Luminosities and masses of pre-mainssequence stars. *The Astrophysical Journal*, **434**, 614–626.

[78] Hachisu, I. 1986. A Versatile Method for Obtaining Structures of Rapidly Rotating Stars. *Astrophysical Journal Supplement*, **61**, p.479.

[79] Hachisu, I., & Eriguchi, Y. 1982. Bifurcation and Fission of Three Dimensional, Rigidly Rotating and Self-Gravitating Polytropes. *Progress of Theoretical Physics*, **68**(1), 206–221.

[80] Hachisu, I., & Eriguchi, Y. 1984. Fission sequence and equilibrium models of rigidity rotating polytropes. *Astrophysics and Space Science*, **99**, 71–74.

[81] Hadley, K., & Imamura, J.N. 2011. Nonaxisymmetric instabilities of self-gravitating disks. I toroids. *Astrophysics and Space Science*, **334**, 1–26.

[82] Hadley, K., Fernandez, P., Imamura, J.N., Keever, E., & Tumblin, R. *Nonaxisymmetric instabilities of self-gravitating disks: Linear and quasi-linear regimes*. FIRST STARS IV - FROM HAYASHI TO THE FUTURE -. AIP Conference Proceedings, Volume 1480, pp. 361-363 (2012).

[83] Hadley, K., *et al.* . 2014. Nonaxisymmetric instabilities of self-gravitating disks. II. Linear and quasi-linear analyses. *Astrophysics and Space Science*, **353**, 191–222.

[84] Hadley, K., Dumas, W., Imamura, J., Keever, E., & Tumblin, R. 2015. Nonaxisymmetric instabilities of self-gravitating disks. III. Angular momentum transport. *Astrophysics and Space Science*, **359**, 23 p.

[85] Hadley, K., *et al.* . 2019. Nonaxisymmetric instabilities and star-disk coupling I. Moderate mass disks. *Astrophysics and Space Science*, **364**, 22 p.

[86] Haghighipour, N. 2003. Gas Drag Induced Enhancement of the Growth-Rate of Planetesimals. *Bulletin of the American Astronomical Society*, **35**, p.1046.

[87] Hansen, C.J., Kawaler, S.D, & Trimble, V. 2004. *Stellar Interiors - Physics Principles, Structure and Evolution*. New York: Springer.

[88] Hartigan, P., & Kenyon, S.J. 2003. A Spectroscopic Survey of Subarcsecond Binaries in the Taurus-Auria Dark Cloud with the Hubble Space Telescope. *Astrophysical Journal*, **583**, 334–357.

[89] Hawley, J.F., & Stone, J.M. 1998. Nonlinear Evolution of the Magnetorotational Instability in Ion-Neutral Disks. *The Astrophysical Journal*, **501**, 758–771.

[90] Hawley, J.F., Smarr, L.L., & Wilson, J.R. 1984. A numerical study of nonspherical black hole accretion. II - Finite differencing and code calibration. *Astrophysical Journal Supplement Series*, **55**, 211–246.

[91] Hayashi, C. 1981. Structure of the Solar Nebula, Growth and Decay of Magnetic Fields and Effects of Magnetic and Turbulent Viscosities on the Nebula. *Progress of Theoretical Physics Supplement*, **70**, 35–53.

[92] Herbig, G.H., & Bell, K.R. *Third Catalog of Emission-Line Stars of the Orion Population*. Third catalog of emission-line stars of the Orion population., by G.H. gerbig and K.R. Bell. Lick Observatory Bulletin no. 1111, Santa Cruz: Lick Observatory, Jun 1988, 90 p.

[93] Hewins, R.H. 1997. CHONDRULES. *Annual Review of Earth and Planetary Sciences*, **25**, 61–83.

[94] Hewins, R.H., *et al.* . 2005. Experimental Constraints on Chondrule Formation. *Chondrites and the Protoplanetary Disk ASP Conference Series*, **341**.

[95] Hollenbach, D.J., & Tielens, A.G.G.M. 1999. Photodissociation regions in the interstellar medium of galaxie. *Reviews of Modern Physics*, **71**, 173–230.

[96] Hollenbach, D.J., Yorke, H.W., & Johnstone, D. 2000. *Disk Dispersal around Young Stars*. Protostars and Planets IV (Book - Tucson: University of Arizona Press; eds Mannings, V., Boss, A.P., Russell, S. S.), p. 401-428.

[97] Huang, J., *et al.* . 2018a. The Disk Substructures at High Angular Resolution Project (DSHARP). I. Motivation, Sample, Calibration, and Overview. *The Astrophysical Journal Letters*, **869**(2), 15 pp.

[98] Huang, J., *et al.* . 2018b. The Disk Substructures at High Angular Resolution Project (DSHARP). III. Spiral Structures in the Millimeter Continuum of the Elias 27, IM Lup, and WaOph 6 Disks. *The Astrophysical Journal Letters*, **869**(2), 15 pp.

[99] Hut, P. 1981. Tidal evolution in close binary systems. *Astronomy and Astrophysics*, **99**, 126–140.

[100] Iida, A., Nakamoto, T., Susa, H., & Nakagawa, Y. 2001. A Shock Heating Model for Chondrule Formation in a Protoplanetary Disk. *Icarus*, **153**, 430–450.

[101] Imamura, J., Durisen, R.H, & Pickett, B. *The Bar Mode Instability: Gravitational Torques and Bar Formation*. Star Formation 1999, Proceedings of Star Formation 1999, held in Nagoya, Japan, June 21 - 25, 1999, Editor: T. Nakamoto, Nobeyama Radio Observatory, p. 203-204.

[102] Imamura, J., Friedman, J.L., & Durisen, R.H. 1985. Secular stability limits for rotating polytropic stars. *Astrophyiscal Journal*, **294**, 474–478.

[103] Imamura, J., *et al.* . 1995. Nonaxisymmetric Secular Instabilities Driven by Star/Disk Coupling. *Astrophysical Journal*, **444**, p.363.

[104] Imamura, J., Durisen, R., & Pickett, B.K. 2000. Nonaxisymmetric Dynamic Instabilities of Rotating Polytropes. II. Torques, Bars, and Mode Saturation with Applications to Protostars and Fizzlers. *The Astrophysical Journal*, **528**, 946–964.

[105] Isella, A., *et al.* . 2016. Ringed structures of the HD 163296 protoplaneary disk revealed by ALMA. *Physical Review Letters*, **117**.

[106] Izidoro, A., *et al.* . 2015. Accretion of Uranus and Neptune from inward-migrating planetary embryos blocked by Jupiter and Saturn. *Astronomy & Astrophysics*, **582**, 16 pp.

[107] Jeans, J. 1929. *The Universe Around Us.* Cambridge, England: The MacMillan Company.

[108] Jeans, J.H. 1919. The origin of binary systems. *Monthly Notices of the Royal Astronomical Society*, **79**, p. 408.

[109] Jin, L. 1996. Damping of the Shear Instability in Magnetized Disks by Ohmic Diffusion. *Astrophysical Journal*, **457**, p.798.

[110] Jones, R.H.I. Grossman, J.N., & Rubin, A.E. 2005. Chemical, Mineralogical and Isotopic Propeties of Chondrules: Clues to their Origin. *Chondrites and the Protoplanetary Disk ASP Conference Series*, **341**.

[111] Kant, I. 1755. *Universal Natural History and the Theory of the Heavens: Essay on the Constitution and the Mechanical Origin of the Whole Universe according to Newtonian Principles.* Canada: Richer Resource Publications. Translated by Ian Johnston, 1998, Vancouver Island University.

[112] Kenyon, S.J., & Hartmann, L. 1987. Spectral Energy Distributions of T Tauri Stars: Disk Flaring and Limits on Accretion. *Astrophysical Journal*, **323**, p.714.

[113] Kenyon, S.J., & Hartmann, L. 1995. Pre-Main-Sequence Evolution in the Taurus-Auriga Molecular Cloud. *Astrophysical Journal Supplement*, **101**, p.117.

[114] Kiuchi, K., Shibata, M., Montero, P., & Font, J. 2011. Gravitational waves from the Papaloizou-Pringle instability in black hole-torussystems. *Physical Review Letters*, **25**(106).

[115] Klahr, H., & Bodenheimer, P. 2003a. *The Formation of a Planet in the Eye of a Hurricane – A Three Phase Model for Planet Formation.* American Astronomical Society, DPS meeting 35, id.25.01; Bulletin of the American Astronomical Society, Vol. 35, p.961.

[116] Klahr, H.H., & Bodenheimer, P. 2003b. Turbulence in Accretion Disks: Vorticity Generation and Angular Momentum Transport via the Global Baroclinic Instability. *The Astrophysical Journal*, **582**, 869–892.

[117] Klahr, H.H., & Henning, T. 1997. Particle-Trapping Eddies in Protoplanetary Accretion Disks. *Icarus*, **128**, 213–229.

[118] Kojima, Y. 1986. The Dynamical Stability of a Fat Disk with Constant Specific Angular Momentum. *Progress of Theoretical Physics*, **75**, 251–261.

[119] Kojima, Y. 1989. Non-axisymmetric unstable modes of a differentially rotating torus. *Monthly Notices of the Royal Astronomical Society*, **236**, 589–602.

[120] Kozai, Y. 1962. Secular perturbations of asteroids with high inclination and eccentricity. *Astronomical Journal*, **67**, 591–598.

[121] Kunz, M.W., & Balus, S.A. 2004. Ambipolar diffusion in the magnetorotational instability. *Monthly Notices of the Royal Astronomical Society*, **348**, 355–360.

[122] Kurtovic, N., *et al.* . 2018. The Disk Substructures at High Angular Resolution Project (DSHARP). IV. Characterizing Substructures and Interactions in Disks around M ultiple Star Systems. *The Astrophysical Journal Letters*, **869**(2), 13 pp.

[123] Lai, D. 20001. Secular bar-mode evolution and gravitational waves from neutron stars. *AIP Conference Proceedings*, **575**, 246–257.

[124] Landau, L.D., & Lifshitz, E.M. 1987. *Fluid Machanics*. London: Pergamon Press.

[125] Laughlin, G., & Bodenheimer, P. 1994. Nonaxisymmetric Evolution in Protostellar Disks. *Astrophysical Journal*, **436**, p.335.

[126] Lebovitz, N.R. 1972. On ths fission theory of binary stars. *Astrophysical Journal*, **175**, p.171.

[127] Lebovitz, N.R. 1974. The Fission Theory of Binary Stars. II. Stability to Third-Harmonics Disturbances. *Astrophysical Journal*, **190**, 121–130.

[128] Lee, JE, *et al.* . 2017. Formation of wide binaries by turbulent fragmentation. *Nature Astronomy*, **1**(0172).

[129] Leinart, C., Richichi, A., & Martin, H. 1997. Binaries among Herbig Ae/Be stars. *Astrotronomy and Astrophysics*, **318**, 472–484.

[130] Lin, D.N.C., & Pringle, J.E. 1987. A viscosity prescription for a self-gravitating accretion disc. *Monthly Notices of the Royal Astronomical Society*, **225**, 607–613.

[131] Lin, MK., Krumholz, M.R., & Kratter, K.M. 2011. Spin down of protostars through gravitational torques. *Monthly Notices of the royal Astronomical Society*, **416**, 580–590.

[132] Lissauer, J.J. 1987. Timescales for planetary accretion and the structure of the protoplanetary disk. *Icarus*, **69**, 249–265.

[133] Lodato, G., & Rice, W.K.M. 2004. Testing the locality of transport in self-gravitating accretion discs. *Monthly Notices of the Royal Astronomical Society*, **351**, 630–642.

[134] Lovelace, R.V.E., Li, H., Colgate, S.A., & Nelson, A.F. 1999. Rossby Wave Instability of Keplerian Accretion Disks. *The Astrophysical Journal*, **513**, 805–810.

[135] Lozier, J.L., Michale, S., Durisen, R.H., & N., Imamura J. Fission of Rapidly Rotating Protostars.

[136] MacPherson, G.J., & Huss, G.R. 2005. Petrogenesis of Al-rich chondrules: Evidence from bulk compositions and phase equilibria. *Geochimica et Cosmochimica Acta*, **69**, 3099–3127.

[137] Mayer, L., Wadsley, J. Quinn, T., & Stadel, J. 2004. *Giant Planet Formation from Disk Instability. Cooling and Heating.* Extrasolar Planets: Today and Tomorrow, ASP Conference Proceedings, Vol. 321, held 30 June - 4 July 2003, Institut D'Astrophysique de Paris, France. Edited by Jean-Philippe Beaulieu, Alain Lecavelier des Etangs and Caroline Terquem.

[138] Mayer, L., Wadsley, J., Quinn, T., & Stadel, J. 2005. Gravitational instability in binary protoplanetary discs: new constraints on giant planet formation. *Monthly Notices of the Royal Astronomical Society*, **363**, 641–648.

[139] Mayor, M., & Queloz, D. 1995. A Jupiter-mass companion to a solar-type star. *Nature*, **378**(6555), 355–359.

[140] Mejia, A.C. 2004. *The Thermal Regulation of Gravitational Instabilities in Disk Around Young Stars.* Ph.D Thesis, Indiana University.

[141] Mejia, A.C., Durisen, R.H., Pickett, B.K., & Cai, K. 2005. The Thermal Regulation of Gravitational Instabilities in Protoplanetary Disks. II. Extended Simulations with Varied Cooling Rates. *The Astrophysical Journal*, **619**, 1098–113.

[142] Meru, F., & Bate, M.R. 2010. Exploring the conditions required to form giant planets via gravitational instability in massive protoplanetary discs. *Monthly Notices of the Royal Astronomical Society*, **406**, 2279–2288.

[143] Meru, F., & Bate, M.R. 2012. On the convergence of the critical cooling time-scale for the fragmentation of self-gravitating discs. *Monthly Notices of the Royal Astronomical Society*, **427**, 2022–2046.

[144] Meyer, D.M.A., Kuiper, R., Kley, W., Johnston, K.G., & Vorobyov, E. 2018. Forming Spectroscopic Massive Protobinaries by Disk Fragmentation. *Monthly Notices of the Royal Astronomical Society*, **473**(3), 3615–3637.

[145] Michael, S., Steiman-Cameron, T.Y., Durisen, R.H., & Boley, A.C. 2012. Convergence Studies of Mass Transport in Disks with Gravitational Instabilities. I. The Constant Cooling Time Case. *The Astrophysical Journal*, **746**, 11 p.

[146] Moeckel, N., & Bally, J. 2007. Capture Formed Binaries via Encounters with Massive Protostars. *The Astrophysical Journal*, **656**, 275–286.

[147] Morris, M.A., & Desch, S.J. 2010. Thermal Histories of Chondrules in Solar Nebula Shocks. *The Astrophysical Journal*, **722**, 1474–1494.

[148] Morris, M.A., Weidenschilling, S.J., & Desch, S.J. 2016. The effect of multiple particle sizes on cooling rates of chondrules produced in large-scale shocks in the solar nebula. *Meteoritics & Planetary Science*, **51**, 870–883.

[149] Nakano, T., & Umebayashi, T. 1986. Dissipation of magnetic fields in very dense interstellar clouds. I. Formulation and conditions for efficient dissipation. *Monthly Notices of the Royal Astronomical Society*, **218**, 663–684.

[150] Noaz, S. 2016. The Eccentric Kozai-Lidov Effect and Its Applications. *Annual Reviews in Astronomy & Astrophysics*, **54**, 441–489.

[151] Noh, H., Vishniac, E.T., & Cochran, W.D. 1992. An Examination of the M = 1 Instability in a Low-Mass Protoplanetary Disk. *Astrophysical Journal*, **397**, p.347.

[152] Norman, M.L., & Winkler, K.H. 1986. NATO Advanced Research Workshop on Astrophysical Radiation Hydrodynamics.

[153] Offner, S.S.R., *et al.* . 2016. The turbulent origin of outflow and spin misalignemnt in multiple stars. *The Astrophysical Journal Letters*, **827 L11**(1).

[154] Ostricker, J.P., & Peebles, P.J.E. 1973. A Numerical Study of the Stability of Flattened Galaxies: or, can Cold Galaxies Survive? *Astrophysical Journal*, **186**, 467–480.

[155] Paczynski, B. 1978. A model of self-gravitating accretion disk. *Acta Astronautica*, **1978**, 91–109.

[156] Papaloizou, J.C., & Savonije, G.J. 1991. Instabilities in self-gravitating gaseous discs. *Monthly Notices of the Royal Astronomical Society*, **248**, 353–369.

[157] Papaloizou, J.C.B., & Pringle, J.E. 1984. The dynamical stability of differentially rotating discs with constant specific angular momentum. *Monthly Notices of the Royal Astronomical Society*, **208**, 721–750.

[158] Papaloizou, J.C.B., & Pringle, J.E. 1987. The dynamical stability of differentially rotating discs with constant specific angular momentum. *Monthly Notices of the Royal Astronomical Society*, **225**, 267–283.

[159] Papaloizou, J.C.B., Larwood, J.D., Nelson, R.P., & Turquem, C. 2007. *Precessing warped discs in close binary systems*. In: Meyer-Hofmeister E., Spruit H. (eds) Accretion Disks New Aspects. Lecture Notes in Physics, vol 487. Springer, Berlini.

[160] Paploizou, J.C.B., & Lin, D. 1989. Nonaxisymmetric Instabilities in Thin Self-gravitating Rings and Disks. *Astrophysical Journal*, **344**, p.645.

[161] Paploizou, J.C.B., & Pringle, J.E. 1984. The dynamical insatbility of differentially rotating discs with contant spaific angular momentum. *Monthy Notices of the Royal Astronomical Society*, **208**(4), 721–750.

[162] Perez, L.M., Andrea, I., Carpenter, J.M., & Chandler, C.J. 2014. Large-scale Asymmetries in the Transitional Disks of SAO 206462 and SR 21. *The Astrophysical Journal Letters*, **783**.

[163] Perez, L.M., *et al.* . 2016. Spiral density waves in a young protoplanetary disk. *Science*, **353**, 1519–1521.

[164] Pickett, B.K. 1995. *Three Dimensional Hydrodynamics of Protostars and Protostellar Disks*. Ph.D Thesis, Indiana University.

[165] Pickett, B.K., Durisen, R.H., & Davis, G. 1996. The Dynamic Stability of Rotating Protostars and Protostellar Disks. I. The Effects of the Angular Momentum Distribution. *Astrophysical Journal*, **458**, P.714.

[166] Pickett, B.K., Cassen, P., Durisen, R.H., & Link, R. 1998. The Effects of Thermal Energetics on Three-dimensional Hydrodynamic Instabilities in Massive Protostellar Disks. *The Astrophysical Journal*, **504**, 468–491.

[167] Pickett, B.K., Cassen, P., Durisen, R.H., & Link, R. 2000. The Effects of Thermal Energetics on Three-dimensional Hydrodynamic Instabilities in Massive Protostellar Disks. II. High Resolution and Adiabatic Evolutions. *The Astrophysical Journal*, **529**, 1034–1053.

[168] Pickett, B.K., *et al.* . 2003. The Thermal Regulation of Gravitational Instabilities in Protoplanetary Disks. *The Astrophysical Journal*, **590**, 1060–1080.

[169] Raghavan, D., *et al.* . 2010. A Survey of Stellar Families: Multiplicity of Solar-type Stars. *The Astrophysical Journal Supplement*, **190**(1), 42 pp.

[170] Reipurth, B., *et al.* . 2014. *Multiplicity in Early Stellar Evolution.* In Protostars and Planets VI. Protostars and Planets VI is a book collection of various contributed papers.

[171] Rice, W.K.M., Lodato, G., & Armitage, P.J. 2005. Investigating fragmentation conditions in self-gravitating accretion discs. *Monthly Notices of the Royal Astronomical Society: Letters*, **364**, L56–L60.

[172] Roxburgh, I. W. 1965. On the Fission Theory of the Origin of Binary Stars. *Astrophysical Journal*, **143**(1), 111–120.

[173] Safronov, V.S., & Zvjagina, E. V. 1969. Relative Sizes of the Largest Bodies during the Accumulation of Planets. *Icarus*, **10**, 109–115.

[174] Sana, H., James, G., & Gosset, E. 2010. The massive star binary fraction in young open clusters III. IC 2944 and the Cen OB2 association. *Monthly Notices of the Royal Astronomical Society*, **416**(2), 817–831.

[175] Sanders, I.S., & Scott, E.R.D. *Origin of Chondrules, Chondrites and Cores.* 75th Annual Meeting of the Meteoritical Society, held August 12-17, 2012 in Cairns, Australia. Published in Meteoritics and Planetary Science Supplement, id.5177.

[176] Santos, N.C., *et al.* . 2017. Observational evidence for two distinct giant planet populations. *Astronomy & Astrophysics*, **603**(A30).

[177] Schwarz, R., Funk, B., & Bazs, . 2016. New prospects for observing and cataloguing exoplanets in well-detached binaries. *Monthly Notices of the Royal Astronomical Society*, **460**, 3598–3609.

[178] Scott, E.R.D., & Krot, A.N. 2005. Chondritic Meteorites and the High-Temperature Nebular Origins of Their Components. *Chondrites and the Protoplanetary Disk ASP Conference Series*, **341**.

[179] Shakura, N.I., & Sunyaev, R.A. 1973. Black Holes in Binqary Systems. Observational Appearance. *Astronomy & Astrophysics*, **24**, 337–355.

[180] Shariff, K. 2009. Fluid Mechanics in Disks Around Young Stars. *Annual Reviews of Fluid Mechanics*, **41**, 283–315.

[181] Shu, F.H., Adams, F.C., & Lizano, S. 1987. Star formation in molecular clouds: observation and theory. *Annual Reviews of Astronomy and Astrophysics*, **25**, 23–81.

[182] Shu, F.H., Shang, H., & Lee, T. 1996. Toward an Astrophysical Theory of Chondrites. *Science*, **271**, 1545–1552.

[183] Steiman-Cameron, T.Y., Durisen, R.H. andBoley, A.C., Michael, S., & McConnell, C.R. 2013. Convergence Studies of Mass Transport in Disks with Gravitational Instabilities. II. The Radiative Cooling Case. *The Astrophysical Journal*, **768**, 14 p.

[184] Stoeckly, R. 1965. Polytropic Models with Fast, Non-Uniform Rotation. *Astrophysical Journal*, **142**, 208–228.

[185] Strom, S.E. 1972. Optical and Infrared Observations of Young Stellar Objects - an Informal Review. *Publications of the Astronomical Society of the Pacific*, **84**(502), p.745.

[186] Swedenborg, E. 1954. *Principia Rerum Naturalium: English translation.* London: Swedenborg Institute. accessed online.

[187] Tassoul, JL. 1978. *The Theory of Rotating Stars.* Princeton, New Jersey: Princton University Press.

[188] Tazzari, M., *et al.* . 2021. The first ALMA survey of protoplanetary discs at 3 mm: demographics of grain growth in the Lupus region. *Monthly Notices of the Royal Astronomical Society*, **506**, 5117–5128.

[189] Tobin, J.J., *et al.* . 2016. A triple protostar system formed via fragmentation of a gravitationally unstable disk. *Nature*, **538**, 483–486.

[190] Tohline, J.E. 1980. Fragmentation of Rotating Protostellar Clouds. *The Astrophysical Journal*, **235**, 866–881.

[191] Tohline, J.E. 2002. The Origin of Binary Stars. *Annual Review of Astronomy and Astrophysics*, **40**, 349–385.

[192] Tohline, J.E., & Durisen, R.H. *An Update on Binary Formation by Rotational Fission.* The Formation of Binary Stars, Proceedings of IAU Symp. 200, held 10-15 April 2000, in Potsdam, Germany, Edited by Hans Zinnecker and Robert D. Mathieu, 2001, p. 40.

[193] Tohline, J.E., Durisen, R.H., & McCollough, M. 1983. The Growth of Bar Structure in a Rapidly Rotating Fluid. *Bulletin of the American Astronomical Society*, **15**, p.963.

[194] Tohline, J.R., & Hachisu, I. 1990. The Breakup of Self-gravitating Rings, Tori, and Thick Accretion Disks. *Astrophysical Journal*, **361**, p.394.

[195] Tokovinin, A. 2014. From Binaries to Multiple. I. Data on F and G Dwarfs within 67 pc of the Sun. *The Astronomical Journal*, **147**(4).

[196] Toomre, A. *Gravitational Interactions Between Galaxies (invited Paper).* The Formation and Dynamics of Galaxies: Proceedings from IAU Symposium no. 58 held in Canberra, Australia, August 12-15, 1973. Edited by John R. Shakeshaft. International Astronomical Union. Symposium no. 58, Dordrecht; Boston: Reidel, p.347.

[197] Toomre, A. 1964. On the gravitational stability of a disk of stars. *Astrophysical Journal*, **139**, 1217–1238.

[198] Toomre, A., & Toomre, J. 1972. Galactic bridges and tails. *Astrophysical Journal*, **178**, 623–666.

[199] Tremaine, S., & Davis, S.W. 2014. Dynamics of warped accretion discs. *Monethly Notices of the Royal Astronmical Society*, **441**(2), 1408–1434.

[200] Trevor, D., *et al.* . 2016. A Neptune-sized transiting planet closely orbiting a 510-million-year-old star. *Nature*, **534**, 658–661.

[201] Tribick, A., & contributors. 2020 (7). *MIT Open Exoplanet Catalogue.* http://www.openexoplanetcatalogue.com/. An open source database of all discovered extrasolar planets.

[202] Tsiganis, K. 2015. Planetary science: How the Solar System didn't form. *Nature*, **528**, 202–204.

[203] Tumblin, R., Fernandez, P., Hadley, K., Imamura, J.N., & Keever, E. *Nonaxisymmetric instabilities of self-gravitating disks: Angular mometum transport.* FIRST STARS IV - FROM HAYASHI TO THE FUTURE -. AIP Conference Proceedings, Volume 1480, pp. 361-363 (2012).

[204] van der Marel, N., *et al.* . 2016. Gas Cavities inside Dust Cavities in Disks Inferred from ALMA Observations. *Young Stars & Planets Near the Sun, Proceedings of the International Astronomical Union, IAU Symposium*, **314**, 139–142.

[205] Walter, F.M., *et al.* . 1988. X-Ray Sources in Regions of Star Formation. III. Naked T Tauri Stars Associated with the Taurus-Auriga Complex. *Astronomical Journal*, **96**, p.297.

[206] Wardle, M. 2004. Star Formation and the Hall Effect. *Astrophysics and Space Science*, **292**, 317–323.

[207] Weidenschilling, S. J. 1977. Aerodynamics of solid bodies in the solar nebula. *Monthly Notices of the Royal Astronomical Society*, **180**, 57–70.

[208] Weidenschilling, S. J. 1980. Dust to planetesimals: Settling and coagulation in the solar nebula. *Icarus*, **44**, 172–189.

[209] Weidenschilling, S.J., & Cuzzi, J.N. *Formation of Planetesimals in the Solar Nebula*. Protostars and Planets III Editors, Eugene H. Levy, Jonathan I. Lunine; with the editorial assistance of M. Guerrieri and M.S. Matthews ; with 91 collaborating authors; Publisher, University of Arizona Press, Tucson, Arizona, 1993.

[210] White, R. J., *et al.* . 1999. A Test of Pre-Main-Sequence Evolutionary Models across the Stellar/Substellar Boundary Based on Spectra of the Young Quadruple GG Tauri. *Astrophysical Journal*, **520**, 811–821.

[211] Williams, H.A., & Tohline, J.E. 1987a. Linear and Nonlinear Dynamic Instability of Rotating Polytropes. *Astrophysical Journal*, **315**, p.594.

[212] Williams, H.A., & Tohline, J.E. 1987b. A Second Order, Three-Dimensional Hydrodynamic Computer Code. *Bulletin of the American Astronomical Society*, **19**, p.744.

[213] Williams, H.A., & Tohline, J.E. 1988. Circumstellar Ring Formation in Rapidly Rotating Protostars. *Astrophysical Journal*, **334**, p.449.

[214] Williams, J.P., & Cieza, L.A. 2011. Protoplanetary Disks and Their Evolution. *Annual Review of Astronomy and Astrophysics*, **49**, 67–117.

[215] Wu, Y., Murray, N.W., & Ramshaim, J.M. 2018. Hot Jupiters in Binary Star Sysytems. *The Astrophysical Journal*, **670**, p.820.

[216] Yang, S.X. 1992. Ph.D Thesis, Indiana University.

[217] Yen, HW., *et al.* . 2016. Gas gaps in the protoplaneatry disk around the young protostar HL Tau. *The Astrophyiscal Journal Letters*, **820 L25**.

[218] Youdin, A. 2011. The Exoplanet Census: A General Method Applied to Kepler. *The Astrophysical Journal*, **742**(1), 13 pp.

[219] Yuan, C., & Cassen, P. 1985. Protostellar angular momentum transport by spiral density waves. *Icarus*, **64**, 435–447.

[220] Yuan, C., & Cassen, P. 1994. Resonantly Driven Nonlinear Density Waves in Protostellar Disks. *The Astrophysical Journal*, **437**, 338–350.

[221] Zhang, X., Liu, B., Lin, D., & Li, H. 2014. Migration and Growth of Protoplanetary Embryos. I. Convergence of Embryos in Protoplanetary Disks. *The Astrophysical Journal*, **797**.